



**AFRL-RZ-WP-TR-2009-2087**

# **REDUCED ORDER MODELING METHODS FOR TURBOMACHINERY DESIGN**

**Jeffrey M. Brown**

**Structures Branch  
Turbine Engine Division**

**MARCH 2009  
Interim Report**

**Approved for public release; distribution unlimited.**

*See additional restrictions described on inside pages*

**AIR FORCE RESEARCH LABORATORY  
PROPULSION DIRECTORATE  
WRIGHT-PATTERSON AIR FORCE BASE, OH 45433-7251  
AIR FORCE MATERIEL COMMAND  
UNITED STATES AIR FORCE**

## NOTICE AND SIGNATURE PAGE

Using Government drawings, specifications, or other data included in this document for any purpose other than Government procurement does not in any way obligate the U.S. Government. The fact that the Government formulated or supplied the drawings, specifications, or other data does not license the holder or any other person or corporation; or convey any rights or permission to manufacture, use, or sell any patented invention that may relate to them.

This report was cleared for public release by the USAF 88<sup>th</sup> Air Base Wing (88 ABW) Public Affairs Office (PAO) and is available to the general public, including foreign nationals. Copies may be obtained from the Defense Technical Information Center (DTIC) (<http://www.dtic.mil>).

AFRL-RZ-WP-TR-2009-2087 HAS BEEN REVIEWED AND IS APPROVED FOR PUBLICATION IN ACCORDANCE WITH ASSIGNED DISTRIBUTION STATEMENT.

\*//Signature//

---

DR. JEFF BROWN  
Structures Branch  
Turbine Engine Division  
Propulsion Directorate

//Signature//

---

DR. CHARLES CROSS, Chief  
Structures Branch  
Turbine Engine Division  
Propulsion Directorate

\*//Signature//

---

JEFFREY M. STRICKER  
Chief Engineer  
Turbine Engine Division  
Propulsion Directorate

This report is published in the interest of scientific and technical information exchange and its publication does not constitute the Government's approval or disapproval of its ideas or findings.

\*Disseminated copies will show “//Signature//” stamped or typed above the signature blocks.

<b>REPORT DOCUMENTATION PAGE</b>				<i>Form Approved</i> <i>OMB No. 0704-0188</i>	
The public reporting burden for this collection of information is estimated to average 1 hour per response, including the time for reviewing instructions, searching existing data sources, gathering and maintaining the data needed, and completing and reviewing the collection of information. Send comments regarding this burden estimate or any other aspect of this collection of information, including suggestions for reducing this burden, to Department of Defense, Washington Headquarters Services, Directorate for Information Operations and Reports (0704-0188), 1215 Jefferson Davis Highway, Suite 1204, Arlington, VA 22202-4302. Respondents should be aware that notwithstanding any other provision of law, no person shall be subject to any penalty for failing to comply with a collection of information if it does not display a currently valid OMB control number. <b>PLEASE DO NOT RETURN YOUR FORM TO THE ABOVE ADDRESS.</b>					
<b>1. REPORT DATE (DD-MM-YY)</b> March 2009		<b>2. REPORT TYPE</b> Interim		<b>3. DATES COVERED (From - To)</b> 07 March 2006 – 30 March 2009	
<b>4. TITLE AND SUBTITLE</b>  REDUCED ORDER MODELING METHODS FOR TURBOMACHINERY DESIGN				<b>5a. CONTRACT NUMBER</b> IN HOUSE	
				<b>5b. GRANT NUMBER</b>	
				<b>5c. PROGRAM ELEMENT NUMBER</b> 62203F	
<b>6. AUTHOR(S)</b>  Jeffrey M. Brown				<b>5d. PROJECT NUMBER</b> 3066	
				<b>5e. TASK NUMBER</b> 12	
				<b>5f. WORK UNIT NUMBER</b> 306612WC	
<b>7. PERFORMING ORGANIZATION NAME(S) AND ADDRESS(ES)</b>  Turbine Engine Division, Structures Branch (AFRL/RZTS) Air Force Research Laboratory , Propulsion Directorate Wright-Patterson Air Force Base, OH 45433-7251 Air Force Materiel Command United States Air Force				<b>8. PERFORMING ORGANIZATION REPORT NUMBER</b>  AFRL-RZ-WP-TR-2009-2087	
<b>9. SPONSORING/MONITORING AGENCY NAME(S) AND ADDRESS(ES)</b>  Air Force Research Laboratory Propulsion Directorate Wright-Patterson Air Force Base, OH 45433-7251 Air Force Materiel Command United States Air Force				<b>10. SPONSORING/MONITORING AGENCY ACRONYM(S)</b> AFRL/RZTS	
				<b>11. SPONSORING/MONITORING AGENCY REPORT NUMBER(S)</b> AFRL-RZ-WP-TR-2009-2087	
<b>12. DISTRIBUTION/AVAILABILITY STATEMENT</b> Approved for public release; distribution unlimited.					
<b>13. SUPPLEMENTARY NOTES</b> PAO Case Number: 88ABW-2008-1263; Clearance Date: 11 December 2009. This is a dissertation submitted in partial fulfillment of the requirements for the degree of Doctor of Philosophy at Wright State University, Dept. of Mechanical and Materials Engineering, Dayton, OH.					
<b>14. ABSTRACT</b> Design of structural components is constrained by both iteration time and prediction uncertainty. Iteration time refers to the computation time each simulation requires and controls how much design space can be explored given a fixed period. A comprehensive search of the space leads to more optimum designs. Prediction uncertainty refers to both irreducible uncertainties, such as those caused by material scatter, and reducible uncertainty, such as physics-based model error. In the presence of uncertainty, conservative safety factors and design margins are used to ensure reliability, but these negatively impact component weight and design life. This research investigates three areas to improve both iteration time and prediction uncertainty for turbomachinery design. The first develops an error-quantified reduced-order model that predicts the effect of geometric deviations on airfoil forced response. The second research area develops a Probabilistic Gradient Kriging approach to efficiently model the uncertainty in predicted failure probability caused by small sample statistics. The third area develops CMS modeling methods.					
<b>15. SUBJECT TERMS</b> Force response, mistuning, reduced-order, turbomachinery, probabilistic, component mode synthesis, Integrally bladed Rotor, modeling, simulation, kriging, Gaussian stochastic process					
<b>16. SECURITY CLASSIFICATION OF:</b>			<b>17. LIMITATION OF ABSTRACT:</b> SAR	<b>18. NUMBER OF PAGES</b> 262	<b>19a. NAME OF RESPONSIBLE PERSON (Monitor)</b> Dr. Jeffrey M. Brown <b>19b. TELEPHONE NUMBER (Include Area Code)</b> (937) 255-7223
<b>a. REPORT</b> Unclassified	<b>b. ABSTRACT</b> Unclassified	<b>c. THIS PAGE</b> Unclassified			

# Contents

<b>1</b>	<b>Introduction</b>	<b>1</b>
1.1	The Turbine Engine . . . . .	1
1.1.1	High Cycle Fatigue . . . . .	4
1.1.2	Airfoil Forced Response . . . . .	6
1.1.3	Mistuning . . . . .	8
1.2	Review of Relevant Mistuning Research . . . . .	11
1.2.1	Lumped Parameter Model Mistuning Studies . . . . .	11
1.2.2	Advanced Physics-based Reduced-Order Mistuning Model Development . . . . .	16
1.2.3	Probabilistic Efforts in Mistuning Modeling . . . . .	22
1.3	Review of Probabilistic Analysis and Epistemic Uncertainty Quantification Research . . . . .	26
1.3.1	Model Error Quantification Research . . . . .	28
1.3.2	Statistical Uncertainty Quantification Research . . . . .	34
1.4	Summary of Research Need . . . . .	39
1.5	Research Summary . . . . .	40
<b>2</b>	<b>Reduced-Order Model Development for Airfoil Forced Response</b>	<b>49</b>
2.1	Introduction . . . . .	50

2.2	Reduced-Order Airfoil Geometry Model . . . . .	53
2.3	Standard Blade-Alone Forced Response Reduced-Order Model . . . . .	55
2.4	Error Quantif ed Reduced-Order Model . . . . .	57
2.5	Numerical Results . . . . .	60
2.5.1	Reduced-Order Geometry Model Results . . . . .	61
2.5.2	Standard and Error-Quantif ed Reduced-Order Model Results . . .	62
2.5.2.1	Frequency Results . . . . .	62
2.5.2.2	Modal Force Results . . . . .	65
2.5.2.3	Forced Response Results . . . . .	67
2.5.3	Approximation Error Root Cause and Improved Physical Model . .	69
2.6	Conclusion . . . . .	71
<b>3</b>	<b>Probabilistic Gradient Kriging to Efficiently Predict Failure Probability</b>	
	<b>Confidence Intervals</b>	<b>91</b>
3.1	Introduction . . . . .	92
3.2	Theory . . . . .	95
3.2.1	Probabilistic Analysis with Statistical Parameter Uncertainty . . . .	95
3.2.2	Kriging Approximation . . . . .	97
3.2.3	Probabilistic Gradient Kriging . . . . .	100
3.3	Demonstration Problems . . . . .	106
3.3.1	Fatigue Crack Growth . . . . .	106
3.3.2	Burst Margin of a Disk . . . . .	112
3.4	Conclusion . . . . .	113
<b>4</b>	<b>Application of Component Mode Synthesis Methods for Modeling Geo-</b>	
	<b>metric Mistuning in Integrally Bladed Rotors</b>	<b>125</b>
4.1	Introduction . . . . .	127

4.2	Theory . . . . .	133
4.2.1	Nominal-Mode Reduced-Order Mistuning Model . . . . .	133
4.2.2	Geometric Mistuning with Component Mode Synthesis Methods . .	140
4.2.2.1	Nominal-Mode Approximation with Geometrically-Perturbed FEM Airfoil Modal Stiffnesses . . . . .	143
4.2.2.2	Nominal-Mode Approximation with Approximate Air- foil Modal Stiffness Perturbation . . . . .	144
4.2.2.3	Nominal-Mode Approach with Non-Nominal Mode Ex- pansion . . . . .	146
4.2.2.4	Non-Nominal Mode Approach with Geometrically-Perturbed FEM Mode Shapes . . . . .	147
4.2.2.5	Non-Nominal Mode Approach with Approximate Per- turbed Mode Shapes . . . . .	149
4.3	Results . . . . .	151
4.3.1	Nominal Mode Approach with Geometrically-Perturbed FEM Air- foil Modal Stiffnesses . . . . .	153
4.3.2	Nominal Mode CMM with Approximate Airfoil Modal Stiffness Perturbation . . . . .	158
4.3.3	Nominal Mode Approach with Non-nominal Mode Expansion . . .	161
4.3.4	Non-Nominal Mode Approach with Geometrically-Perturbed FEM Mode Shapes . . . . .	164
4.3.5	Geometric Component Mode Mistuning with Approximate Per- turbed Mode Shapes . . . . .	165
4.4	Computational Time . . . . .	171
4.5	Conclusions . . . . .	173

<b>5 Conclusion</b>	<b>224</b>
<b>Bibliography</b>	<b>227</b>

# List of Figures

1.1	Turbojet Engine Schematic . . . . .	44
1.2	Example Goodman Diagram . . . . .	45
1.3	Integrally Bladed Rotor . . . . .	45
1.4	Example Campbell Diagram . . . . .	46
1.5	Tuned Response (solid line) versus Mistuned (Dotted) . . . . .	47
1.6	Dye and Henry Spring-Mass Model . . . . .	48
2.1	Mode Fifteen and Mode Sixteen . . . . .	72
2.2	Airfoil Surface Deviation (Blade 1) . . . . .	73
2.3	Total Variance Explained by Principal Components . . . . .	74
2.4	Airfoil Frequency Variation . . . . .	75
2.5	Frequency Prediction Comparison (Mode 16) . . . . .	76
2.6	Correlation of PC Mode Parameters and Residual (Mode 16) . . . . .	77
2.7	Maximum Error Calculation for Airfoil Frequency . . . . .	78
2.8	Airfoil Modal Force Variation . . . . .	79
2.9	Modal Force Prediction Comparison (Mode 15) . . . . .	80
2.10	Maximum Error Calculation for Airfoil Modal Force (Mode 15) . . . . .	81
2.11	Maximum Error Calculation for Airfoil Modal Force . . . . .	82
2.12	Airfoil Forced Stress Variation . . . . .	83



2.13	Forced Stress Prediction Comparison (Mode 15) . . . . .	84
2.14	Maximum Error Calculation for Airfoil Forced Stress . . . . .	85
2.15	Sensitivity Convergence Plot . . . . .	86
2.16	Step Size Sensitivity Variation . . . . .	87
2.17	Frequency Comparison for Single PCA Mode Variation . . . . .	88
2.18	First PCA Mode Frequency Perturbation . . . . .	89
2.19	Modal Stiffness Approximation Results - Mode 11 . . . . .	90
3.1	Cyclic Load Mean and Standard Deviation Sampling Distributions . . . . .	116
3.2	RS and PGK Approximation Comparison, $\Delta\sigma$ . . . . .	117
3.3	Kriging and PGK Approximation Comparison, $\Delta\sigma$ . . . . .	118
3.4	FCG: PGK and RS Predicted vs. MCS Actual . . . . .	119
3.5	FCG: Kriging and RS Predicted vs. MCS Actual . . . . .	120
3.6	Fatigue Crack Growth Failure Probability Distribution . . . . .	121
3.7	Burst Margin: PGK and RS Predicted vs. MCS Actual . . . . .	123
3.8	Burst Margin: PGK and Kriging Predicted vs. MCS Actual . . . . .	124
4.1	ADLARF Rotor . . . . .	176
4.2	Geometrically Perturbed Airfoil Substructure (100x Magnification) . . . . .	177
4.3	ADLARF Rotor FEM . . . . .	178
4.4	ADLARF Model Aft Flange Boundary Conditions . . . . .	179
4.5	NMA- $\lambda_{FEM}$ versus FEM Maximum Forced Response Prediction . . . . .	180
4.6	NMA - $\lambda_{FEM}$ versus Full Model Maximum Forced Response - Mode 11 . . . . .	181
4.7	Blade-to-Blade Response at Maximum Response at Peaks - Mode 11 . . . . .	182
4.8	Blade-to-Blade Response at Maximum Response at 4319 Hz. - Mode 11 . . . . .	183
4.9	Blade-to-Blade Response at Maximum Response at 4331 Hz. - Mode 11 . . . . .	184
4.10	NMA- $\lambda_{FEM}$ versus Full Model Maximum Forced Response - Mode 13 . . . . .	185

4.11	Blade-to-Blade Response at Maximum Response at Peaks- Mode 13 . . . .	186
4.12	Blade-to-Blade Response at Maximum Response at 4794 Hz. - Mode 13 . .	187
4.13	Blade-to-Blade Response at Maximum Response at 4797 - Mode 13 . . . .	188
4.14	NMA- $\lambda_{FEM}$ versus Full Model Maximum Forced Response - Mode 17 . .	189
4.15	Blade-to-Blade Response at Maximum Response at Peaks - Mode 17 . . . .	190
4.16	Blade-to-Blade Response at Maximum Response at 6474 Hz. - Mode 17 . .	191
4.17	Blade-to-Blade Response at Maximum Response at 6480 - Mode 17 . . . .	192
4.18	Modal Stiffness Approximation Results - Mode 11 . . . . .	193
4.19	Comparison of Approximate NMA Approaches - Mode 11 . . . . .	194
4.20	Modal Stiffness Approximation Results - Mode 13 . . . . .	195
4.21	Comparison of NMA Approaches - Mode 13 . . . . .	196
4.22	Modal Stiffness Approximation Results - Mode 17 . . . . .	197
4.23	Comparison of NMA Approaches - Mode 17 . . . . .	198
4.24	Comparison of NMA- $\lambda_{FEM}$ and NMA-NNME- $\lambda_{FEM}$ Results - Mode 11 .	199
4.25	Blade-to-Blade NMA- $\lambda_{FEM}$ versus NMA-NNME- $\lambda_{FEM}$ Results - Mode 11	200
4.26	NMA- $\lambda_{FEM}$ versus NMA-NNME- $\lambda_{FEM}$ Maximum Forced Response Results- Mode 13 . . . . .	201
4.27	NMA- $\lambda_{FEM}$ versus NMA-NNME- $\lambda_{FEM}$ Blade-to-Blade Results - Mode 13	202
4.28	NMA- $\lambda_{FEM}$ versus NMA-NNME- $\lambda_{FEM}$ Maximum Forced Response Re- sults - Mode 17 . . . . .	203
4.29	NMA- $\lambda_{FEM}$ versus NMA-NNME- $\lambda_{FEM}$ Blade-to-Blade Results - Mode 17	204
4.30	CMS $A_k$ Vector Nominal vs. Non-Nominal - Blade 9 - M13 . . . . .	205
4.31	NNMA versus FEM Maximum Forced Response Results . . . . .	206
4.32	NNMA versus FEM Maximum Forced Response Results- Mode 11 . . . .	207
4.33	Blade-to-Blade NNMA Response Comparison at Maximum Response- Mode 11 . . . . .	208

4.34	NNMA versus FEM Maximum Forced Response - Mode 13 . . . . .	209
4.35	NNMA versus FEM Maximum Forced Response - Mode 17 . . . . .	210
4.36	Approximate Mode Shape MAC Values (Modes 1-20) . . . . .	211
4.37	Approximate Mode Shape MAC Values (Modes 21-40) . . . . .	212
4.38	Reduced Airfoil Substructure Mass Matrix . . . . .	213
4.39	NNMA- $\lambda_a$ - $\phi_a$ versus NMA- $\lambda_a$ Maximum Forced Response Results- Mode 11 . . . . .	214
4.40	NNMA- $\lambda_{FEM}$ - $\phi_a$ versus NMA- $\lambda_{FEM}$ Maximum Forced Response Results- Mode 11 . . . . .	215
4.41	NNMA- $\lambda_a$ - $\phi_a$ versus NNMA- $\lambda_a$ - $\phi_{FEM}$ Maximum Forced Response Results- Mode 11 . . . . .	216
4.42	NNMA- $\lambda_a$ - $\phi_a$ versus NMA- $\lambda_a$ Maximum Forced Response Results- Mode 13 . . . . .	217
4.43	NNMA- $\lambda_{FEM}$ - $\phi_a$ versus NMA- $\lambda_{FEM}$ Maximum Forced Response Results- Mode 13 . . . . .	218
4.44	NNMA- $\lambda_a$ - $\phi_a$ , versus NNMA- $\lambda_a$ - $\phi_{FEM}$ Maximum Forced Response Results- Mode 13 . . . . .	219
4.45	NNMA- $\lambda_a$ - $\phi_a$ versus NMA- $\lambda_a$ Maximum Forced Response Results- Mode 18 . . . . .	220
4.46	NNMA- $\lambda_{FEM}$ - $\phi_a$ versus NMA- $\lambda_{FEM}$ Maximum Forced Response Results- Mode 18 . . . . .	221
4.47	NNMA- $\lambda_a$ - $\phi_a$ , versus NNMA- $\lambda_a$ - $\phi_{FEM}$ Maximum Forced Response Results- Mode 18 . . . . .	222
4.48	Solution Time Comparison . . . . .	223

# List of Tables

3.1	Fatigue Crack Growth Parameters . . . . .	115
3.2	Fatigue Crack Growth Statistics . . . . .	115
3.3	Fatigue Crack Growth Approximation Metrics . . . . .	115
3.4	Burst Margin Parameters . . . . .	122
3.5	Burst Margin Statistics . . . . .	122
4.1	ADLARF Nominal Airfoil Frequencies . . . . .	175

REDUCED ORDER MODELING METHODS  
FOR TURBOMACHINERY DESIGN

A dissertation submitted in partial fulfillment of the  
requirements for the degree of  
Doctor of Philosophy

By

JEFFREY M. BROWN  
B.S., Georgia Institute of Technology, 1994  
M.S., Wright State University, 1998

---

2008  
Wright State University

WRIGHT STATE UNIVERSITY  
SCHOOL OF GRADUATE STUDIES

October 31, 2008

I HEREBY RECOMMEND THAT THE DISSERTATION PREPARED UNDER MY SUPERVISION BY Jeffrey M. Brown ENTITLED Reduced-Order Modeling Methods for Turbomachinery Design BE ACCEPTED IN PARTIAL FULFILLMENT OF THE REQUIREMENTS FOR THE DEGREE OF Doctor of Philosophy.

---

Ramana V. Grandhi, Ph.D.  
Dissertation Director

---

Ramana V. Grandhi, Ph.D.  
Director, Engineering Ph.D. Program

---

Joseph F. Thomas, Jr., Ph.D.  
Dean, School of Graduate Studies

Committee on  
Final Examination

---

Ramana V. Grandhi, Ph.D.

---

Joseph C. Slater, Ph.D., P.E.

---

Ravi Penmetsa, Ph.D.

---

Mo-how H. Shen, Ph.D.

---

Charles J. Cross, Ph.D.

# Abstract

Brown, Jeffrey M., Ph.D., Department of Mechanical and Materials Engineering, Wright State University, 2008. *Reduced Order Modeling Methods for Turbomachinery Design*.

Design of structural components is constrained by both iteration time and prediction uncertainty. Iteration time refers to the computation time each simulation requires and controls how much design space can be explored given a fixed period. A comprehensive search of the space leads to more optimum designs. Prediction uncertainty refers to both irreducible uncertainties, such as those caused by material scatter, and reducible uncertainty, such as physics-based model error. In the presence of uncertainty, conservative safety factors and design margins are used to ensure reliability, but these negatively impact component weight and design life. This research investigates three areas to improve both iteration time and prediction uncertainty for turbomachinery design. The first develops an error-quantified reduced-order model that predicts the effect of geometric deviations on airfoil forced response. This error-quantified approximation shows significant improvements in accuracy compared to existing methods because of its bias correction and description of random error. The second research area develops a Probabilistic Gradient Kriging approach to efficiently model the uncertainty in predicted failure probability caused by small sample statistics. It is shown that the Probabilistic Gradient Kriging approach is significantly more accurate, given a fixed number of training points, compared to conventional Kriging

and polynomial regression approaches. It is found that statistical uncertainty from small sample sizes leads to orders of magnitude variation in predicted failure probabilities. The third research area develops non-nominal and nominal mode Component Mode Synthesis methods for reduced-order modeling of the geometric effects on rotor mistuning. Existing reduced-order methods approximate mistuning with a nominal-mode, or design intent, basis and airfoil modal stiffness perturbation. This assumption introduces error that can be quantified when compared to a finite element model prediction of a geometrically perturbed rotor. It is shown that the nominal-mode approach can produce significant errors, whereas the non-nominal approach accurately predicts blade-to-blade mistuned response.



# Acknowledgments

First and foremost, I would like to thank my advisor, Dr. Ramana Grandhi, for his support and guidance throughout this project. Without his encouragement, this project would not have come to fruition. I look forward to many years of friendship and productive collaboration. I began this effort to transform myself from a design engineer to a research engineer, and I feel have accomplished that. Hopefully the committee agrees.

I am grateful to Drs. Slater, Penmetsa, Shen, and Cross, who have agreed to serve on my committee and provide their feedback. I have enjoyed learning from them as both teachers and colleagues. I also look forward to a long fruitful working relationship with each of them.

I would like to thank Alysoun Taylor, who had the unenviable task of editing my written work. Any coherence of this document is thanks in large part to her. She also provided valuable support navigating the many administrative tasks associated with completion of the program requirements.

I would like to thank the Dayton Area Graduate Study Institute (DAGSI) for the financial support to pursue my degree. Without it, I may have never began.

I would like to thank Dr. Jeremy Daily for his support and friendship during our joint travels through the Ph.D. program. When he told me that he thought he failed the first of three candidacy exams, I was relieved that I wasn't the only one. I will always remember our months of studying for the exams, interspersed with games of bang-qui.

I would like to thank Dr. Brian Beachkofski for his support and technical advice. Having someone to talk to who had gone through the process—and made it out with remnants of sanity—was very encouraging.

Finally, I would like to thank my wife and best friend, Angela. I have probably talked to her more than anybody about the minute details of my research. She dutifully absorbed these rants and was the perfect sounding board. I'm sorry for all the constraints that this effort has put on our life. It has ended not a moment too soon with the new happy constraints of our son Rowan and our new daughter due in January.

Dedicated to

Christopher James Brown

# 1 Introduction

Chapter 1 gives the reader foundational information on the research subject. Section 1.1 provides an overview of the turbine engine, including its primary components and design challenges, with emphasis on the High Cycle Fatigue (HCF) failure mode and conventional industrial design approaches for HCF avoidance. Section 1.2 reviews four decades of research related to mistuned response relevant to the methods developed in Chapter 4, *Application of Component Mode Synthesis Methods for Modeling Geometric Mistuning in Integrally Bladed Rotors*. Section 1.3 summarizes technical efforts relevant to the developed model and statistical uncertainty quantification methods described in Chapter 2, *Reduced-Order Model Development for Airfoil Forced Response*, and Chapter 3, *Probabilistic Gradient Kriging to Efficiently Predict Failure Probability*.

## 1.1 The Turbine Engine

Since their development in the early 1940s, turbine engines have powered great social, economic, and military advancements. From the ability of aircraft turbine engines to convey travelers with great speed, to power generation turbines responsible for nearly all the world's electricity, turbine engine are remarkable machines. Their development represents the most significant advancement to the world's military Air Forces, beginning with the Messerschmidt 262 and extending to today's F-22 Raptor, powered by the super cruising

F119 engine. Turbine technology has come incredibly far in the past seventy years, but there are still technological barriers to leap that will result in even more capable commercial, industrial, and military applications. These future advancements will lead to lower fuel burn rates, higher speeds, and greater reliability.

Three main component modules combine to create the turbine engine schematic shown in Figure 1.1. Starting at the air intake, the compressor section increases incoming air pressure and temperature using rotating airfoils to move flow through an ever decreasing annulus. At the end of the compressor, high pressure and temperature air moves to the second module, the combustor, through a diffuser that enhances combustor mixing. The combustor injects fuel into the airflow which is ignited and further increases temperatures, pressures, and flow velocity. The combustion gases flow through a nozzle into the third engine module, the turbine. As the hot gas passes the turbine airfoils, rather than compressing the flow, there is expansion and work extraction. Turbine work is then passed through a shaft to rotate the compressor. This continuous process accelerates air through the engine, resulting in the opposite reaction of forward thrust.

Each successive turbine engine advancement must overcome incredible design challenges imposed by the operational physics. The interaction of aerodynamics, thermodynamics, structural dynamics, and material mechanics are common to each engine component and require thorough analysis. Extreme ranges of temperatures, pressures, and loading must be endured by each component. Components can rotate between 10000–20000 RPM, for military fighter aircraft engines, imparting tens of thousands of G's on each airfoil, thermal gradients between cooled and uncooled surfaces can be several hundred degrees Fahrenheit, and parts must be tolerant to damage from ingested objects, including birds. As a compounding challenge, pursuit of more efficient and high performance engine components drives designs towards lighter, thinner, yet still durable components. Considering that engines are designed for thousands of hours of usage, it is not an understatement that

the turbine engine is an extreme engineering challenge.

To ensure engine reliability, a number of component failure modes must be designed out of operational probability. Low Cycle Fatigue (LCF) is caused by the successive loading and unloading of rotating components as the engine accelerates and decelerates through its operational range. This loading generates stresses that surpass the elastic limit of the material and can result in failures at well under 10,000 cycles. Creep failures affect components that experience long hold times at high temperatures such as turbine airfoils and disks. Creep will cause radial growth of the disk and airfoils, eventually leading to component overstress or case impact. Thermomechanical fatigue (TMF) combines creep and LCF in a nonlinear relationship that leads to more rapid failure than each causes independently. Airfoil oxidation is caused by the hot gas path reaction with metal and ceramic components and leads to reduced component strength and erosion.

Each of these failure modes pose significant challenges to the design community, but they share a risk management advantage. Risk management is the practice employed by engine maintenance organizations to ensure that operational risks are held to acceptable levels and includes on-wing inspections, engine data analysis, and full engine tear-down reviews. These practices can identify precursors of failure events and lead to replacement and repair of components to ensure reliable operations. Each failure mode in the previous paragraph develops slowly and progresses at predictable rates, allowing for successful risk management.

Unfortunately, not all failure modes develop slowly. Rotor burst is a rare failure event caused by over-stressing the disk beyond its ultimate strength. The main risk of these events are over-speed conditions, but because of accurate steady stress prediction tools and engine controls, this failure mode has been virtually eliminated. Airfoil flutter is an aeromechanical phenomena encountered when the aerodynamic damping dramatically drops because of the interaction of airfoil vibration and unsteady aerodynamic pressures. The loss of

damping results in stresses that rise to dramatic levels that result in rapid failure. Though a significant challenge even today, flutter occurs at a limited number of operating conditions, which can be determined during design and developmental testing.

Related to flutter is another forced response phenomenon that has led to a significant number of operational failures, airfoil HCF. This has been a significant focus of research over the last decade and is a primary subject of this research with direct relevance to the efforts in Chapter 2 and 4.

### **1.1.1 High Cycle Fatigue**

Between 1982 and 1996, HCF accounted for 56% of all Air Force Class A engine-related failure events [1]. Class A failures are those that result in loss of human life or at least one million dollars in damage. In 1994, HCF required expenditure of 850,000 maintenance man-hours for repair, replacement, and inspections. This failure mode has been so pervasive because of the inability to accurately predict airfoil forced response with physics-based simulation, uncertainty in material capability, and an inability to effectively risk manage the failure mode. Unlike other failure modes, HCF failure can occur seemingly at random with no prior warning.

HCF is a damage mechanism characterized by elastic stress cycling over a large number of cycles until failure. Frequently, HCF failures are characterized as those beyond 10,000 cycles. When engine conditions result in significant alternating stresses, to be detailed in Subsection 1.1.2, there is a risk of HCF damage. While damage can be accumulated per cycle and summed using Miner's rule, this is generally not done in airfoil design because of the uncertainty in operational stress magnitudes and the rate at which HCF cycles are accumulated. HCF vibration frequencies for airfoils can be anywhere from several hundred to many thousand cycles per second. With such high frequency response, incredible sums

of damage cycles can be accumulated in a single aircraft mission.

Instead of damage summation, HCF design relies on a failure state defined when the resonant amplitudes exceed the endurance limit of the material. The endurance limit is an experimentally determined value of stress at which HCF damage is not accumulated and is a function of the material, alternating and steady stresses, and number of cycles to failure. There exist many failure theories for these conditions, of which the most widely used is the Goodman limit. Traditionally,  $10^7$  cycles define the number of cycles to failure. A Goodman Diagram, Figure 1.2, is used to plot the division between infinite and finite life. The  $x$ -axis is the steady stress value and the  $y$ -axis is the alternating stress value with a line connecting the two axes defining the boundary between the lower area, infinite life region, and upper area, finite life region. The  $x$ -intercept is conventionally located at the material ultimate strength and the  $y$ -intercept is the stress amplitude at HCF failure under the zero mean stress condition. In this plot, points are included that represent the nodal stresses from a finite element model to show which locations have exceeded the Goodman limit.

Consider an engine that experiences a resonance condition at 15,000 Hz. If the alternating stress is just above the specified endurance limit, going from the undamaged state to failure would occur in less than twelve minutes. Given that aircraft missions are on the order of hours, an undamaged engine can fail before development of a failure precursor that can be identified through risk management practice. This is one cause for the high failure rates seen in past decades and the reason why designing for HCF avoidance is critical.

Because of the significance of HCF to fleet failure rates and the risk management challenge it poses, accurately predicting HCF risks and reducing them through design is of paramount importance. For current materials, prediction of the HCF fatigue life variation can be effectively accomplished with empirical models. These empirical models can be developed with relatively inexpensive material coupons and fatigue testing machines. Conversely, the component stresses cannot be effectively determined by empiricism because



each test would require the manufacture of a full Integrally Bladed Rotor (IBR) at cost of several hundred thousand dollars each. Physics-based forced response prediction tools are therefore required to ensure robustness of future engine components susceptible to HCF..

### **1.1.2 Airfoil Forced Response**

Prediction of airfoil forced responses that cause HCF failures remains one of the most difficult turbine engine design challenges. While HCF in turbine engines can strike anywhere, the primary challenge and largest risk is associated with rotating airfoils in the compression section. The compression section is composed of rotors and stators. Rotors are composed of the rotating disk and airfoil subcomponents that function together to compress the incoming airflow. There are two varieties of rotors, inserted-blade and integrally bladed. Figure 1.3 shows an IBR, sometimes called a Blisk (bladed-disk), that is either machined from a single metal forging or manufactured through welding individual airfoils to the outer diameter of the disk. This approach was developed in the mid-1980s to reduce weight and increase efficiency, but a side effect was the reduction of friction damping inherent in inserted-blade dovetail contact conditions. Because of this, IBRs are more susceptible to large amplitude vibration and HCF. There are also inherent repair challenges with IBRs because individual damaged blades can no longer be easily replaced.

Airfoil forced response is driven by the interaction between rotating airfoils and stators. Stators are stationary airfoils within the compression section that participate in the air compression process and redirect airflow to be compressed by the next downstream rotor section. Behind each stator airfoil are pressure distortions in the flow field. As each rotor airfoil passes from the stator passage, the area between two stators, the airfoil goes from a high pressure to reduced pressure region. Because stators and airfoils are symmetrically spaced around the engine circumference, the rotation of airfoils past stators imparts a har-

monic excitation force on the airfoil. The harmonic excitation frequency is a function of the number of stators and the rotor speed. A given rotor stage in the engine can be impacted by the harmonic excitation of both upstream and downstream stator and rotor stages, leading to the potential for very complex harmonic loading, but in general the upstream stator is the most critical excitation source.

When the excitation frequency nears and eventually equals a rotor airfoil resonant frequency, the forced response dramatically increases. Resonant frequencies are a fundamental dynamic characteristic of a component, along with the mode shape, and are determined by component geometry, material properties, and boundary conditions. A structure excited at one of its given resonant frequencies will have an unbounded response in the absence of damping and have a displacement field given by the corresponding mode shape. The magnitude of the displacement field is a function of the modal loading and system damping. The modal loading, or modal force, is the inner product of the loading vector with the mode shape vector, or eigenvector. Damping is provided by the structural properties of the material, the mechanical connections of the component, and the structural interaction with the aerodynamic loading. As alluded to, IBRs lack damping from the mechanical interface found in inserted-blade rotors, and there is limited damping associated with the monolithic metal alloys used in IBRs.

Because prediction of alternating stress is computationally expensive, airfoil HCF design practices have relied heavily on resonance avoidance to ensure reliability. The primary tool used to accomplish this is the Campbell Diagram (Figure 1.4), which determines coincidence of excitation and airfoil frequencies at multiple airfoil resonant frequencies and engine order (EO) excitations. The EO excitation is the number of pulses an airfoil receives per revolution and is plotted on the diagram as lines that begin at the origin and slope upward to the right. For example, if there are ten stators preceding a rotating stage, it will see a ten engine order excitation. The nearly horizontal lines beginning at the  $y$ -axis

represent the airfoil mode frequencies. The slight upward slope of these lines is caused by the stress stiffening of the structure, resulting in higher frequencies as RPM increases. It is also common for these lines to curve downward because of increasing temperature with respect to speed that reduces the material stiffness. Where the engine order lines cross with the airfoil mode lines, a resonant condition will exist at the defined RPM on the  $x$ -axis. Design practice is structured to avoid resonances at critical operation conditions such as idle, cruise, and maximum speed.

Until only recently, resonant stresses were not predicted as part of design practice. Instead, the avoidance approach was used and supplemented by extensive engine testing to determine high stress modes. Such an approach led to costly redesign efforts to move problem modes out of the operating range. Also, with the advent of low-aspect ratio airfoils and their associated higher modal density, it became increasingly difficult to avoid critical resonances. Because of this, and because of improvements in computational capability, physics-based prediction of forced response amplitude has been increasingly used in design. These physics-based tools include finite element models (FEMs) coupled to unsteady aerodynamic computational fluid dynamic (CFD) loads and methods to predict mistuned rotor response. Mistuning prediction capabilities are a primary subject of this research, in particular, advancing the ability accurately predict and quantify uncertainty of mistuned response.

### **1.1.3 Mistuning**

Standard analysis procedures in engineering practice conduct computations on nominal, or design intent, geometries. In some cases the analysis may consider blue print tolerances to investigate sensitivities. For IBR forced response, analysis of the nominal geometry is referred to as a tuned analysis to infer that all the airfoils of the rotor have identical natural

frequencies. While this was standard practice for many years, it has been well known since the early 1970s that rotor airfoils are not exact nominal geometries and, in fact, each airfoil has slightly different geometry within inspection tolerance limits. Variation in the airfoil geometries is caused by manufacturing deviations and usage effects such as erosion, foreign object damage (FOD), and airfoil blending repair operations. These random geometries are responsible for variations in airfoil frequencies, changes in mode shapes, and a breakdown of the rotor's cyclic symmetry.

Cyclic symmetry refers to a nominal, and therefore tuned, rotor's periodic geometric configuration. In such a configuration, the entire model can be identically represented by a repeated sector that is rotated  $n_b$  times through an angle equal to  $2\pi/n_b$  where  $n_b$  is the number of sectors. The assumption of cyclic symmetry can greatly reduce the size of rotor models because only the single sector model is required. Cyclic constraints are used as boundary conditions between the adjacent faces of the sector model to provide results equal to a full rotor model. Cyclically symmetric components are characterized by multiple response harmonics and repeated natural frequencies. These harmonics physically represent the disk nodal diameters which are lines of zero displacement that cross the rotor.

In the presence of random airfoil geometries, cyclic symmetry breaks down, resulting in changes in the nodal diameter response and the splitting of repeated roots. Instead of a single repeated root there will be  $n_b$  blade, closely spaced natural frequencies. A single excitation frequency near the tuned repeated natural frequency will then excite multiple modes. The magnitude of each mode's amplitude is a function of its proximity to the excitation frequency, the modal forcing of the mode, and modal damping. The superposition of the modal response from the multiple excited modes can lead to the localization of modal energy in a small set of blades. Combination of these modes can, and does, lead to forced response results greater than an excitation of the tuned model. Figure 1.5 shows a typical result forced response function (FRF) from a mistuned rotor where each dotted curve rep-

resents and individual blade's response and the solid line is the tuned response where each blade has the same forced response.

It should be clear that mistuning is a stochastic phenomenon governed by the airfoil variations of each individual IBR. This complicates the tasks of quantifying IBR forced response and requires use of conservative design margins or predictions of the stochastic behavior. In fact, a significant body of research has focused on predicting the theoretical maximums of mistuning which can lead to amplification factors beyond 5x [2]. Stochastic behavior prediction is much more valuable because reliability can be explicitly quantified, the effect of design changes can be determined, and less restrictive bounds can be used for mistuning.

The following section, 1.2, begins with a literature review of the key research efforts in predicting rotor mistuned forced response and relevant stochastic modeling efforts. From this review, areas of needed research will be identified to improve the current state-of-the-art in mistuning prediction. Section 1.3 proceeds with a review of model and statistical uncertainty quantification research, which are relevant to mistuning as well as other turbomachinery failure mechanisms.

It is found that the development of reduced-order models has not considered the quantifiable uncertainty of the approximation. A significant contribution would be to develop an uncertainty-quantified approximation approach for airfoil forced response. Second, it is found that nominal-mode approximation of mistuned response is the dominant method for mistuning approximation, the uncertainty this creates has not been studied, nor have non-nominal mode reduced-order approaches been developed based on Component Mode Synthesis (CMS) solutions. Secondly, it is found that methods to quantify physics-based model error have not been widely developed. Third, it is found that the uncertainty in probability density function statistics from small sample sets, and their impact on failure probability confidence intervals, have not been extensively researched, particularly for sample-based

failure probability calculations.

## **1.2 Review of Relevant Mistuning Research**

This section reviews the last 40 years of mistuning research and highlights efforts relevant to the remainder of the dissertation. The first subsection reviews research efforts that studied mistuned rotors with lumped stiffness, mass, and damping models and determined the significance of the problem as well as insights into key parameters. The review continues with a subsection on recent efforts to develop reduced-order finite element model-based mistuning models. The third subsection reviews methods to probabilistically predict mistuned response. From this review of efforts, the need for additional research is defined.

### **1.2.1 Lumped Parameter Model Mistuning Studies**

Seminal efforts in computational and empirical mistuning were conducted by Ewins [3]. In his 1969 publication, an analytical model of coupled lumped masses was constructed to represent a five-bladed disk with various magnitudes of frequency splitting, i.e. mistuning. By varying the magnitude of the splitting and damping, he achieved results showing that forced response stresses varied between 60% and 120% of the tuned response. He further showed that the ratio of frequency splitting to damping could be used to define mistuned response across a range of selected values. Using a thirty-bladed rotor with mistuning applied by attaching shims of various thickness to the blade tips, Ewins empirically showed very close qualitative agreement for the 1<sup>st</sup> bending mode of a selected subset of airfoils. Going further, the paper recommends a blade frequency arrangement strategy to reduce the overall forced response and, as later verified, virtually eliminate mistuned amplifications [4]. This single paper covered many of the concepts that would be refined over the next 40 years.

Other significant works in the early era of mistuning analysis continued to use analytical lumped parameter models. Considering the computational capabilities of the time, this was a necessity. Dye and Henry modeled a 43-bladed Spey low pressure compressor rotor as a sequence of masses coupled through springs to adjacent masses, representing blade-to-blade coupling, and also coupled to ground through a spring to represent disk stiffness [5]. This model, shown in Figure 1.6, and slight modifications of it have been and will continue to be widely used by numerous researchers. Empirical quantification of the model parameters for the Spey rotor was conducted to determine values for the springs, and subsequent analysis showed impacts of disk-to-blade stiffness ratios, damping value, and mistuning distributions. This effort set the example for accounting for blade frequency deviation through probability distributions, specifically with a truncated Gaussian distribution, and also showed a now classic plot of maximum mistuning amplification as a function of mistuning percentage. These plots show an almost parabolic increase and decrease in mistuning amplifications at low mistuning values, followed by a consistent tapering off at higher mistuning deviations. Dye and Henry predicted mistuning amplification at nearly twice the tuned response, far greater than the original effort of Ewins.

Whitehead derived a maximum amplification equation for mistuned response that was the beginning of many future efforts to develop this capability [2]. His derived value of  $0.5(1 + \sqrt{n_b})$ , when applied to the 43-bladed Spey rotor, equates to an amplification of almost four times the tuned response. The developed model considered only aerodynamic coupling of blades and was formulated to couple each blade with all other blades on the rotor. The combined efforts of Ewins, Dye and Henry, and Whitehead created a strong foundation for further researchers, and many of their findings are still quite valuable to understanding mistuning.

The following two decades saw continued refinement of lumped parameter models for mistuning prediction. El-Bayoumy and Srinivasan treated the disk as an axisymmetric plate

with tapered thickness to more accurately represent disk design geometries [6]. This effort was exceptional in that it showed figures of the mistuned mode shapes for a 24-bladed rotor as an approach to determine the highest responding mistuned blade. Such information would be valuable during the instrumentation of demonstration hardware to ensure measurement of maximum stresses. They concluded that the maximum response blade was located near the tuned system frequency rather than an extreme mistuned blade. Additional results showed, for the investigated mistuning pattern, mistuning amplifications for the high stress blade of approximately 48%. The ability to identify the mistuning pattern will be a key issue of the non-nominal and nominal mode mistuning approximation analyses in Chapter 4.

Sogliero and Srinivasan used the same model but investigated the impact of the mistuned response of a random fleet of rotors on the expected time to failure [7]. This is the unique in that it is the first instance where a probabilistic mistuning study was used for reliability quantification. A sample of 24 blade frequencies was selected from a Gaussian distribution to generate a random rotor response and this was repeated for 10 random rotors. Four blade frequency populations were investigated, which had standard deviations ranging from 2 Hz. to 15 Hz., with an average value of 391 Hz. Results showed that the 2 Hz. standard deviation had the lowest life and improved at each increase in variation. The effort also showed that the distribution of life followed approximately the Weibull distribution and that, for coefficients of variation above 1.25%, the mistuned life exceeded the tuned life. The use of the Weibull distribution to model mistuned response would continue to be used and investigated almost 40 years later [8].

Kaza and Kielb developed a model that incorporated both structural mistuning and aero coupling for flutter prediction [9]. Aerodynamic loading for each airfoil was predicted using two-dimensional unsteady cascade theories and provided the first attempt at using physics-based prediction of aerodynamic loads for mistuned response prediction. Even



today, use of realistic loading is typically ignored in mistuning assessments. The effort primarily investigated the impact of mistuning on flutter and concluded that a moderate amount of intentional mistuning can reduce flutter occurrence.

Griffin and Hoosac developed a model representing each rotor sector as three lumped masses connected by springs to represent the disk, platform, and airfoil [10]. Sector-to-sector structural coupling was through springs connecting the disk masses and aerodynamic damping was represented with elements connecting airfoil masses. The effort conducted several analyses investigating the impact of normally distributed blade frequencies on response. A significant finding was that the distribution of response was not normally distributed, which impacts results from statistical perturbation techniques to be discussed in Subsection 1.2.3, which assume normally distributed response. Results also showed significant mistuning located at the frequency of the tuned mode, which corroborated prior results [6]. In contrast to the prior effort of Sogliero and Srinivasan [7], the study showed that maximum mistuned response did not decrease at large standard deviation values for mistuning. This is not an uncommon event in the use of lumped parameter models with specific dynamic properties and loading conditions. The paper concludes with fleet management strategies that show that reduced mistuned response can be achieved by sorting blades into closely matched frequency groups or a dual population of high and low frequency airfoils.

Afolabi modified the Dye and Henry model to incorporate two degrees-of-freedom (DOF) airfoils and constructed 30-bladed models with blade frequencies selected from a Gaussian distribution [11]. In his work, it was found that the minimum and maximum response blades were most often found with blades having the largest deviation from the tuned frequencies, again, in contrast with previous work. This phenomenon is validated experimentally on a 33-bladed rotor where all airfoils were strain gaged, and it was concluded that when limited instrumentation is available, gages should be placed on the extreme fre-

quency airfoils. Again, it is desired to predict blade-to-blade mistuning patterns. This has significance for Chapter 4 where this capability is assessed for nominal and non-nominal mistuning approximation methods.

Griff n would later develop a modification to the two-mass problem that represented aerodynamic coupling between airfoils with a spring-dashpot element [12]. The structural parameters of the model were chosen so that they gave results similar to a nominal finite element model and the aerodynamic parameters were calculated using a NASA-developed aerodynamic code. The statistical variation of the structural parameters was set to correspond to bench test measurements of a set of airfoils. When compared to empirical results, the theoretical model matched data for the first two modes very well, with a significant difference for the third mode. Of special importance, while comparing experimental results to theoretical, the authors account for the variation in experimental results caused by strain gage errors that result from variations in strain gage ratios. This is the first known effort to account for the impact of mode shape variations in such an analysis. Their empirical investigation showed that the standard deviation in the ratio of the strain to displacement varied from 8 to 13 percent for the first three modes, which is substantially larger than the typical 1 to 2 percent standard deviation of frequency. This indicates that the nominal-mode mistuning approximation should be investigated further because of the demonstrated large variation in mode shape.

Wie and Pierre applied perturbation methods for free and forced vibrations to investigate significant mistuning factors [13]. Their investigations showed that mistuning was dependent on coupling strength and that for a small mistuning to coupling ratio, i.e. strong coupling, the system responds as a perturbation of the tuned system. For the weak coupling case the system responded as a perturbation of the decoupled mistuned system where small mistuning greatly impacts response.

A of lumped parameter mistuning research has identified two significant issues relevant

to the new methods developed in this dissertation. First, the prediction of blade-to-blade stresses is important to the design process. Also, mode shapes vary to a larger degree than frequencies, which impacts the accuracy of the nominal-mode mistuning approximation discussed in the following subsection.

### **1.2.2 Advanced Physics-based Reduced-Order Mistuning Model Development**

The lumped parameter mistuning models were vital for creating a basic understanding of mistuned response but they could not accurately predict rotor mistuned response. An obvious problem was that they could only investigate a small set of modes and they were coarse approximations of actual design geometry. It would take time for advancements in computational power and finite element modeling tools for more rigorous methods to be applied.

A foundation for mistuning work that would come decades later was established by Craig and Bampton in almost the same year that the initial analytical mistuning studies were beginning [14]. Their article defined an approach for substructuring based on constraint modes at substructure interfaces and the fixed-interface normal modes of the interior DOF. The defined method was the Craig-Bampton (C-B) Component Mode Synthesis (CMS) approach which was computationally efficient, easily implemented, and would be widely adopted by commercial finite element modeling codes. Irretier would use the CB-CMS approach to model a simple 2-D mistuned bladed disk model and demonstrate the process of using a finite element method to produce required response substructures [15].

A modified CMS technique, applicable to modern day design practice, was shown by Castanier, et al. [16]. The approach used cyclic-sector finite element predictions of modal quantities, stiffness, and mass matrices for use in a modified CMS approach that used

disk-induced constraint modes. Use of disk-induced constraint modes limits interface DOF and reduces the assembled substructure size and solution time. The modified CMS technique further assumes that mistuned response can be approximated by linear combination of nominal, i.e. tuned, modes. This limits the method to perturbation of airfoil frequencies, and ignores geometric mistuning effects on constraint modes and cantilevered substructure mode shapes. Results compared favorably to analytical case studies [17]. The analytical case studies used a full FEM that applied airfoil Young's modulus mistuning to represent mistuning. As such, the airfoil substructures maintained their nominal mode shapes and the full models themselves were only an approximation of geometric mistuning. This is significant and the work in Chapter 4 will conduct a validation of the nominal approach using a geometrically perturbed full model. In the original validation study, accuracy was degraded by excessive interface stiffness caused by the disk-induced constraint mode assumption, and an iterative approach to artificially adjust mistuned modal stiffnesses was employed for solution improvement. The approach has been widely used by the turbomachinery industry, and software development led to mistuning prediction software, known as REDUCE. The approach is also referred to as a Component Mode Mistuning (CMM) approach. Later, the REDUCE CMS method was modified by Bladh et al. to account for shroud interfaces [18].

Bladh et al. developed a C-B CMS approach that used a Secondary Modal Analysis Technique (SMART) to further reduce assembled substructure matrices size [19, 20]. Because the approach is based on C-B CMS, the interface stiffness between substructures is more accurately represented. The resulting model will have a larger set of DOF compared to REDUCE, but the SMART approach conducts an eigenanalysis of the C-B reduced matrices to create a second reduced basis. The SMART results are used in a mistuning projection technique to accurately predict mistuning with fewer DOF because of the more accurate constraint mode stiffness modeling. As with REDUCE, validation was conducted with a

full FEM that applied various Young's modulus values for each airfoil to represent mistuning.

Recent work by Lim, Bladh, Castanier, and Pierre researched the impact of an aspect geometric mistuning [21]. It specifically addresses the impact of large geometric deformations caused by Foreign Object Damage (FOD) and how the deformed shape of a single blade impacts forced response. The solution approach uses a CMS approach and divides the rotor into two substructures, a tuned bladed disk and the set of mistuned airfoils. In the formulation, all the DOF in the mistuned airfoil component are treated as interface DOF. This can lead to large reduced-order models when all the blades are mistuned. By considering the case of a single FOD deformed airfoil, the model order is greatly reduced. The two subcomponents in the model are coupled through attachment modes created by applying unit forces to the interface region of the tuned bladed disk. The authors noted that these attachment modes can lead to matrix ill-conditioning and numerical instability due to the fact that displacement values of the attachment modes are much less than those of normal modes. Also, the attachment and normal modes may not be independent.

To overcome the numerical challenges caused by the attachment modes, Lim, Castanier, and Pierre developed a reduced-order modeling approach based on the mode acceleration method based on static mode condensation [22]. In this approach the mistuned system is transformed to a reduced basis space of the tuned system modes and a set of static deflection shapes that account for mistuning. These static deflection shapes can be obtained without the need to conduct a more expensive modal analysis. Again, in this case a single blade deformed by a FOD impact was addressed, which reduced the number of static analyses to conduct. Both papers were exceptional as the first approach to handle geometric effects of a mistuned system. They were constrained to the impact of large geometric effects on a single blade and conducted a deterministic analysis.

Petrov, Sanliturk, and Ewins developed an alternate reduced-order mistuning model [23].

This model represents mistuned rotors as a summation of the dynamic stiffness matrix of the tuned matrix plus a mistuning matrix. The matrix inversion operation required in the solution is efficiently solved using Sherman-Morrison-Woodbury identity that simplifies the inverse computations for two added matrices. The mistuning matrix is reduced by considering a subset of the full model that include DOF where mistuning is applied and where response quantities are known. With this approach, if airfoil geometries are varied then all the airfoil surface DOF are required, which could become computationally expensive. To avoid this, the authors proposed using a few active DOF per blade and using lumped mass, stiffness, and damping elements to act as representative mistuning elements. It was also noted by the authors that the accuracy of the model was reliant on the tuned system modes and it therefore shares the nominal-mode assumption of the REDUCE and SNM approaches. Petrov and Ewins would use this mode to conduct analysis of the worst mistuning patterns in rotors [24].

During the development of the CMS simulation approaches at the University of Michigan, efforts at Carnegie Mellon were developing alternate approaches for reduced-order mistuning models from tuned FEM results. Yang and Griffin developed an approach based on the receptance method [25]. This effort was based on a method by Menq, Griffin, and Bielak that was applied to beam element tuned analysis [26]. The receptance method is similar to that of CMS in that the response of a set of connected substructures is predicted by how it reacts at the interface. The non-interface DOF are expressed in some manner at the interface DOF. Yang and Griffin's effort represented the response of the rotor as rigid-body interface displacements and tuned clamped-free blade modes. The approach was demonstrated on a two-dimensional FEM representing a rotor, and mistuning in the model was represented as elastic modulus changes to the airfoils. This approach is similar to the REDUCE approach, though the REDUCE uses disk-induced displacements to couple the modeshapes. Use of rigid-body modes at the interface led to overly-stiff response

and development of the receptance approach was not continued.

Soon after this, Yang and Griffin would develop a new reduced-order modeling technique [27, 28]. Their approach created the reduced model through transformation of the full system model to a modal basis of tuned modes. In this case the rotor is treated as a single structure. The number of reduced DOF is determined by how many tuned modes are retained. The response of the mistuned system is approximated by a weighted sum of the nominal modes that are determined by solving the modal eigenvalue problem. Mistuning is introduced by perturbing the modal stiffness and mass matrix that results from the new basis transformation. For computational simplicity and efficiency, these perturbations are a Young's modulus perturbation proportional to the percentage frequency mistuning of each airfoil. This model is attractive because it can be constructed from a cyclic sector finite element model, results in a small reduced order model, and accurately accounts for blade-disk interface stiffness. The method was demonstrated on a two-dimensional rotor model with mistuning represented by changing the elastic modulus of the airfoils. Again, as with previous efforts, the validation problem itself was only an approximation of geometric mistuning. The developed method was implemented in software called Subset of Nominal Modes (SNM) and has been widely used in the turbomachinery industry. The efforts in Chapter 4 will apply the nominal-mode approximation to a geometrically perturbed IBR and quantify the method's uncertainty.

Feiner and Griffin would introduce a modification to the subset of nominal modes approach [29]. In their article, the authors formulated a method to approximate the mistuning matrix, which requires the stiffness and mass matrix from a FEM, with blade-alone frequency deviations. The method allows mistuning predictions based on either FEM predicted or measured frequencies without the need for a FEM generated stiffness and mass matrix. The method was demonstrated on a two-dimensional rotor example where mistuning was represented by changing the blade length, density, and elastic modulus. The

assumptions in the model are that a single, isolated family of modes is involved in the response, the strain energy is primarily in the blades, the frequencies are closely spaced, and the blade mode shapes are equivalent. The authors conclude that these assumptions are valid for the fundamental, i.e, low order modes. Examples were shown where the method proved inaccurate at higher modes. This model would be later used as a tool for mistuning identification, the process of determining a rotor's stiffness, mass, and damping properties based on measured frequency response data [30, 31]. The developed method was implemented in software called Fundamental Mistuning Model (FMM) and has been widely used in the turbomachinery industry.

Sinha expanded the SNM approach for geometric mistuning and labeled the approach Multiple Modal Domain Analysis (MMDA) [32]. His work is significant and relates to Chapter 4 in that it develops a method to explicitly account for geometric mistuning. The approach represents the blade geometry variation through a spatial statistics model as shown by Garzon et al. [33]. The MMDA approach uses nominal system tuned modes and tuned modes of rotors having perturbed geometry based on the spatial statistical analysis. The spatial statistical analysis produces a set of principal component modes that define the geometric deviations with a reduced basis. The perturbed geometries consist of the nominal geometry with the addition of each retained principal component mode. The ROM dimension is the number of tuned modes retained multiplied by the number of retained principal component modes. This is still an approximate basis for the airfoil modeshapes since the actual geometry of the airfoils is not used to generate the modal basis. The approach uses results from a cyclic sector analysis and sector DOF are transformed to the new basis through pre- and post-multiplying matrices. The approach was demonstrated on a geometrically-perturbed academic rotor and showed excellent accuracy for a single mode. It was not shown that a nominal mode approximation would not work for the considered mode.



While MMDA is an effective ROM, there can still be large computational costs associated with the transformation of physical sector DOF to the new basis, particularly when there are a large number of DOF in the disk. It also requires full model solutions from multiple sector models. The CMS approach would alleviate these problems by partitioning the substructures so that DOF associated with the disk would not need to be solved for each retained geometry model. The approach also is an approximate basis that may not efficiently provide accurate solutions with a limited number of retained modes. Sinha's work also did not demonstrate the use of the nominal-mode approximation for the problem, and therefore did not fully demonstrate the need to account for non-nominal modes. Therefore, there remains a significant need to develop a CMS approach, as in Chapter 4, that demonstrates nominal and non-nominal approximation of geometric mistuning.

### **1.2.3 Probabilistic Efforts in Mistuning Modeling**

Several previously mentioned research efforts have modeled blade frequency variations as probability density functions and used Monte Carlo sampling to predict mistuned forced response variation. Use of Monte Carlo sampling can require a significant number of simulations in order to confidently predict the mistuned forced response distribution, and researchers have pursued methods to accelerate the prediction. In general, these efforts have been demonstrated on lumped parameter systems.

Sinha developed one of the earliest probabilistic methods to predict the distribution of mistuned response [34]. His approach was to formulate the dynamic response of a discrete model of a mistuned rotor as function of tuned and perturbed response to obtain a closed form solution for the perturbed response. By assuming that the stiffness variations used to represent mistuning were Gaussian and independent, the response of the mistuned system would also be normal because the displacement prediction is based on a linear combination

of the mistuning variations. Sinha found that the accuracy was dependent on the level of damping with inaccuracies found in low damping examples.

Wei and Pierre conducted statistical analysis using multiple approaches on the same discrete parameter model [35]. Their work included the application of a hybrid statistical perturbation technique that consisted of Monte Carlo sampling using a perturbed modal response model that provided input to a modal superposition forced response model. A second approach directly predicted the perturbed forced response without the modal analysis requirement. Both allow the use of higher order perturbation methods while reducing the computational resources needed for the full-order model. Example applications showed that the hybrid and analytical prediction approaches were accurate under specified conditions of damping and mistuning levels.

Recently, Mingnolet, Lin, and LaBorde developed a new perturbation method resulting in an analytical formulation of the mistuning probability density function [36]. Full definition of the applied adaptive perturbation method is given in a prior paper [37]. When applied to a discrete mistuning model, the method was able to more accurately predict the probability density function over a wider range of mistuning conditions than previous efforts.

While perturbation methods have significant computational advantages, results have shown that their accuracy can degrade depending on the mistuning parameters of the system. Researchers have developed alternate approaches to approximate the probability density function of mistuned systems using stochastic basis vector approaches applicable to a wider range of mistuning parameters. Bay, Nair, Bhaskar, and Keane developed such an approach using preconditioned stochastic Krylov vectors and a Bubnov-Galerkin method to compute the coefficients of the vector participation. Examples, using a discrete representation of a mistuned system, showed accurate results for the first two statistical moments and the mean of the maximum blade amplitude. It was shown that the method provided more

accurate results than linear perturbation methods but still had accuracy problems when the statistical variation, as a function of excitation frequency, was highly nonlinear. This could be a result of the use of only three Krylov vectors to represent the response. Also, the method does not predict the full distribution of response [38]. Sinha used a polynomial chaos approach, which is related to the previous effort but uses Hermite polynomials [39]. It was found for a discrete mistuning model that the third-order polynomial chaos expansion yielded accurate statistics of the forced response.

Capiez-Lernout and Soize developed a nonparametric model of random uncertainties for mistuned bladed disks and used a FEM-based model for prediction [40]. This approach begins with the nominal-mode C-B CMS reduction of a bladed disk using tuned system modes of the disk sector and blade subcomponents. The blade subcomponent modal stiffnesses are treated as random and with their matrix entities governed by a defined nonparametric probability function. This probability function includes dispersion parameters that include a non-physical parameter as a technique to account for model errors and can be used to assess the sensitivity to random data and prediction error. A follow on effort by the authors modified these dispersion based on an estimate from three geometric parameters [41]. The accuracy of this approach is difficult to assess since the dispersion parameters are non-physical and are intended to represent multiple forms of uncertainty. The methods in Chapter 2 develop an explicit approach to quantify geometric variation on modal stiffness, as well as blade mode shape.

Scarselli and Lecce investigated the use of a range of non-deterministic approaches to predict mistuned rotor response [42]. They demonstrated the approaches on a twenty-bladed rotor modeled by three-dimensional finite elements. Mistuning was introduced through variation in the elastic modulus of each blade. A three layer artificial neural network model was used to approximate response. A network was constructed using sixty-seven training sets and the results were quite poor. Results from one thousand training sets

resulted in better results for the lowest frequency mode but poor results for all other modes. The authors concluded that further improvements to neural networks would be required for mistuning applications. The authors also demonstrated a Genetic Algorithm (GA) optimization to maximize mistuning amplification. A prior effort used this same approach to minimize mistuning [43].

Li, Castanier, Pierre, and Ceccio applied an experimental Monte Carlo approach to predict the population of mistuned response [44]. The experimental approach involved a single 24-bladed test rotor subjected to many varying forces that were used to represent frequency mistuning variation. The required force variation is determined by predicting a forced response caused by structural variations and recasting the dynamic equations to solve for the forces with the known displacements. These forces then were applied to the test rotor over a range of random mistuning patterns to experimentally gather the distribution in response. Experimental results were compared to reduced-order model predictions using the structural frequency variations. While in many cases the comparison of the distributions did show differences, the experimental approach did a surprisingly good job at capturing the 99<sup>th</sup> percentile response.

Lee, Castanier, and Pierre assessed the use of several probabilistic methods on a two DOF per blade lumped parameter model [8]. This included the First-Order Reliability Method (FORM), Second-Order Reliability Method (SORM), Advanced Mean Value (AMV) Method, Moving Least Squares Response Surface, radius-based importance sampling, and statistically accelerated Monte Carlo. Many of these approaches have been widely used in probabilistic applications. The accelerated Monte Carlo involves the use of a three-parameter Weibull distribution to model the statistical behavior. It was found that FORM, SORM, AMV, and response surface method were unable to predict the distribution of maximum mistuned response, regardless of the standard deviation of frequency variation. This is not unexpected as the performance function of the mistuned response is quite chaotic. The

radius-based importance sampling approach was computationally expensive because of the large number of variables. The accelerated Monte Carlo method, based on the assumption that the distribution of the maximum mistuned response can be modeled by a Weibull, gave good results. Fifty mistuning simulations were used to determine the three Weibull parameters and this distribution compared well with results from 500 Monte Carlo simulations.

Each of these efforts are significant in the development of methods to probabilistically predict mistuning, but they have not addressed two significant factors. First they have not explicitly accounted for geometric variation in the analysis. A method will be developed for this in Chapter 2. Second, they have not addressed model and statistical uncertainty in the analysis. Model uncertainty refers to the discrepancy between the reduced-order model and the full-order model that it is representing, and the statistical uncertainty refers to the lack of knowledge of the true population statistics of a random parameter. There are other uncertainties of relevance, such as the discrepancy between the full-order model and experimental data, but these are not addressed here. A model uncertainty quantification approach is considered in Chapter 2 and statistical uncertainty is considered in Chapter 3. The following section reviews efforts in both model and statistical uncertainties.

## **1.3 Review of Probabilistic Analysis and Epistemic Uncertainty Quantification Research**

Probabilistic analysis propagates design parameter input variations through a physics-based model to predict variation in response. Input are conventionally defined with Probability Density Functions (PDF) and the output are response statistics and PDF. It is an alternative to deterministic analysis processes that account for variations through experience based safety factors. While deterministic approaches have been used with success, they are

typically over conservative. Today's increasing demand for lower cost, higher performance systems, has led to the demand for improved methods. The probabilistic approach can more accurately model variation and lead to reduced conservatism yet maintain system safety. It has also been demonstrated that the experienced-based safety factors of a deterministic approach do not guarantee safety, particularly for new systems which may operate beyond our historical experience. The probabilistic approach allows for assessment of safety in these new operating regimes.

A probabilistic analysis can be divided into three stages, definition of input uncertainty, physics-based model definition, and probability integration. The definition of input uncertainty typically refers to defining PDF for input parameters, but there are also non-probability based methods for quantification such as Bayesian [45], fuzzy sets [46], evidence theory [47], and information gap [48]. The physics-based model is either the same model used in the deterministic design process or frequently a surrogate model of the process such as a response surface. The probability integration method propagates the impact of the input distributions through the physics-based model, and there are many approaches to do so. A common approach is Monte Carlo analysis which randomly samples the input distributions, calculates the physics-based model response, and over many samples predicts the response distribution.

While uncertainty is accounted for in the definition of input variation through PDF, uncertainty in a probabilistic analysis is also present in the physics-based model and probability integration method. There is uncertainty in the physics-based model caused by both the analytical form and the solution's numerical discretization. Probabilistic integration is also uncertain based on the approach used to approximate the multi-dimensional integration of the failure domain. For example, Monte Carlo analyses uncertainty is a function of the number of random samples and the systems failure probability. Even the definitions of design parameter uncertainty with PDF is uncertain when small statistical samples are used

for their development.

Uncertainty in the probabilistic analysis can be categorized as either aleatory or epistemic. Aleatory, or irreducible, uncertainty is the natural variation of a parameter, such as the variation in material fatigue properties due to grain size, shape, and location. Because exact grain properties of a specific object are unmeasurable without destructive evaluation, these properties are unknown to the analyst. Epistemic, or reducible, errors are caused by a lack of information that could be obtained if constraints of time and cost were removed. For example, uncertainty in design parameter PDF can be reduced through collection of additional data points, and model error can be reduced by including higher order terms in the analytical form.

Understanding the uncertainties at all stages of the probabilistic analysis process is necessary for confident application to practical design. Most research in probabilistic methods have considered aleatory uncertainties, but a growing body of research has been focused on accounting for epistemic uncertainty in the analysis process. For the purpose of this review, the epistemic efforts are divided into physics-based model error quantification and statistical uncertainty quantification. This division also reflects the content of this dissertation. Chapter 2 develops an approach to account for physics-based model error and Chapter 3 addresses statistical uncertainty quantification. These chapters expand on prior works in the area, reviewed in the following subsections.

### **1.3.1 Model Error Quantification Research**

Thacker et al. defined a conceptual framework for computer simulation verification and validation which encompasses the need for model error quantification [49]. In their work, they defined the need for validation metrics for a model prediction and suggested a simple metric based on the function  $e = y - y^*$ , where  $y$  is experimental data,  $y^*$  is the model prediction,

and  $e$  is the error. Proposed metrics included the expected value of the error,  $E(e)$ , error variance,  $V(e)$ , error probabilities,  $P(e > 0)$ , or hypothesis tests such as  $E(e > 0)$ . Their work also considered model calibration, defined as the process of adjusting model parameters to improve agreement between model output and experimental measurements. They reference a statistical model calibration approach developed by Kennedy and O'Hagan as a potential approach [50]. The work concludes with recognition that variation in model input parameters can be established and propagated through simulation approaches such as sampling-based methods (Monte Carlo, Latin Hypercube, etc.) and sensitivity based methods (First Order Reliability Method (FORM) [51], Advanced Mean Value [52], Adaptive Importance Sampling etc. [53]).

Kennedy and O'Hagan developed an approach to statistically account for the error between a model and experiments [50]. They based their model on Gaussian stochastic process models of deterministic computer code output, a method developed by Sacks et al. [54]. Kennedy and O'Hagan modeled the relationship between computer code output and experiments as

$$z_i = \rho\eta(x_i, \theta) + \delta(x_i) + e_i \quad (1.1)$$

where  $z_i$  are empirical observations,  $\rho$  is an unknown regression parameter,  $\eta(\cdot, \cdot)$  is a Gaussian stochastic process model representing predicted response as a function of measured variables,  $x_i$ , and calibration parameters,  $\theta$ . The model inadequacy function  $\delta(\cdot)$  is a Gaussian stochastic process model of the difference between  $z_i$  and  $\eta(\cdot, \cdot)$ , and  $e_i$  is experimental observation error. This problem is formulated in a Bayesian framework where prior information is defined for  $\theta$  and  $\rho$ . Given new information from experiments,  $z_i$ , a Bayesian update is conducted that adjusts the calibration data to a posterior distribution that accounts for the new information. The calibration parameters are selected by the analyst prior to this



analysis and require the definition of an appropriate prior. Both of these requirements are subject to uncertainty. The method developed in Chapter 2 uses a frequentist approach to calibrate the model, avoiding the challenge of prior definition, and also uses an analytical method to determine which design parameters should be calibration parameters.

Ditlevsen suggested that the model uncertainty should be related directly to the basic variables in the first journal issue of *Structural Safety* in 1982 [55]. Thoftt-Christensen and Murotsu suggested that model uncertainty be taken into account by adding non-physical random variables to the probabilistic calculation [56]. The error variables are added as subjectively defined second order moments. There are clear computational simplicities with this approach but the subjective nature of the quantification has inherent disadvantages. The method developed in Chapter 2 will provide a quantitative approach to define the model error variation.

Several efforts have been conducted on quantifying the discretization error associated with numerical models. Alvin incorporated mesh discretization error into a response surface model [57]. The response surface includes variation in design parameters and the fidelity of the computational mesh. His work extends the process of Richardson's extrapolation [58, 59] that bases discretization error estimates on successive numerical solutions. It requires results from more than two grid densities to verify the convergence rate for the extrapolation. In probabilistic solutions that vary design parameters, this convergence analysis would need to be done at each variation, which would significantly increase the computational cost of the analysis. Alvin's method developed a response surface model that did not consider every parameter value in the analysis, and instead both mesh size and the parameters were change in a Design of Experiment discretization of the design space. This limits the number of reanalysis required yet covers the grid density errors across the design space. The method was successfully demonstrated on a dynamic simulation of a one-dimensional bar. Kammer et al. extended this approach using a rational

function, rather than the polynomial basis of the Alvin's original work [60]. The approach allowed accurate extrapolation with a coarser mesh in the numerical analysis. It is recognized that this technique does not address all forms of epistemic error, such as the model form error.

It was posed by Helton that both aleatory and epistemic uncertainty could be addressed within an evidence theory framework [61]. This approach was advanced by Bae et al. who presented that aleatory uncertainties are appropriately handled by classical probability methods whereas epistemic uncertainties are suited to evidence theory [62]. Their work also developed a cost effective algorithm to predict the possibility bounds from the evidence analysis. In evidence theory, input variables are defined as bounded belief and plausibility values. Belief bounds capture the expected range of a parameter and plausibility bounds comprise the larger range of possible parameter values. The method's predicted output bounds the potential response based on belief, plausibility, and possibility. This approach is useful in the presence of large uncertainties from various sources, but does not specifically address model error quantification.

Logan et al. developed an approach to quantify parametric, model form, and numerical discretization error based on the independent assessment of each [63]. The authors assume that each term can be assessed independently but recognized that this is generally not the case. The uncertainty is accounted for at the integral level, that is, a top-down approach that does not consider the uncertainties at each of the components of the model. Three of the four the defined components of uncertainty, experimental data, numerical discretization, and model parameter, are quantified using independent approaches. The remaining error is then classified as model error.

Faccone et al. created a procedure to assess the uncertainty in experimental evaluation of turbine engine IBR forced response [64]. Their effort is of particular interest since it develops an approach to model uncertainty of airfoil response models. Chapter 2 develops an

alternate approach that could augment the overall uncertainty analysis process developed in the reference. Their approach models both experimental, sensor, and FEM modeling uncertainty. The work models a sensor's measurement uncertainty as a perturbation of a nominal value by the product of a normally distributed random variable,  $\epsilon_s = N(0, \sigma_s)$ , where  $\sigma_s$  is the sensor standard deviation, and a sensor noise parameter defined as a percentage of the maximum response amplitude. The authors recognize that a more rigorous definition for  $\epsilon_s$  may be needed when considering a given sensor type to account for its specific characteristics. The process also accounts for uncertainty associated with the sensor's location as a random perturbation on the surface position. Model uncertainty is accounted for by comparing experimental mode shapes,  $\phi_i^{(e)}$ , and model predicted mode shapes,  $\phi_i^{(m)}$ , using a linear combination of the  $i^{th}$  model predicted mode shape and its frequency-wise immediate neighbors through a set of weights  $(w_{i-1}, w_i, w_{i+1})$ . The paper concludes that modeling uncertainties reduce the confidence associated with experimental response measurement. They recognize that several other model uncertainties should be accounted for, such as localized geometric variations. The method developed in Chapter 2 develops exactly such an approach.

Hasselmann developed an approach to create a model validation metric for transient dynamic model results [65]. The metric is based on an PCA analysis of two matrices of transient response data, one experimental and one predicted. The left singular vectors, diagonal matrix of singular values, and right singular vectors are used to define a set of normalized PCA metrics. This approach avoids the need for modal matching between experimental and analytical PCA vectors and also reduces the number of metrics needed to characterize the modeling uncertainty. The statistics of the metrics can also be used to model uncertainty in a physical simulation.

Vinai et al. developed a statistical method for model uncertainty quantification that accounted for the variation in model accuracy at changing operating conditions [66]. Their

approach quantified the error between experiment and model as a function of testing conditions and used a statistical clustering approach to divide the region into three separate regions that showed the same statistical properties. These statistical properties are used to create error PDF for each region and can be used to estimate the physical model's uncertainty in each region. The use of parameter specific error is related to the approach taken in Chapter 2 to quantify uncertainty. In Chapter 2, a more rigorous statistical analysis is applied that identifies both bias and random error as a function of specific design parameters, not just regions of the design space.

Red-Horse and Benjamin posed an approach to model uncertainty where random variables are comprised of PCE approximated equivalence classes constrained by the available information [67]. Rather than conventional PDF to define random parameters, their work used a probability triple,  $(\Omega, S, P)$ , comprised of the sample space,  $\Omega$ , a sigma algebra of subsets of  $\Omega$ ,  $S$ , and a probability measure,  $P$ . Both the input parameters and response are expanded with PCE. The method results in variables effectively bounded by upper and lower bound CDF that define parameter and response uncertainty. In their example, expert opinion information was used to develop the uncertainty in the parameters.

Vittal and Hajela developed two approaches for calculating probabilistic confidence intervals from response surface methods [68]. In this, they are specifically addressing the error associated with the approximate fit of the surface. This work is related to that of Chapter 2 as they are both quantifying the error associated with an approximate model. Their first method used three defined limit states to obtain upper, mean, and lower failure probability values at a design point of interest. The second approach was a closed form solution to predict confidence intervals for predicted reliabilities obtained using the Mean-Value First Order Second Moment (MV-FOSM) method. Each of the proposed methods is applicable to quadratic response surface approximations based on DOE stratification of the sample space. Their work accounted for uncertainty in the regression parameters of the

response surface caused by the lack of fit of the response surface.

From the review of these prior works, it is identified that a new model error quantification approach is needed. The approach should objectively quantify error rather than relying on subjective expert judgment. It should model the error as a function of design parameter to account for variations in error across the design space. Developing an approach to model the error associated with local geometry deviations will also contribute to the confidence in turbomachinery dynamic response testing. The efforts in Chapter 2 accomplish these goals.

### **1.3.2 Statistical Uncertainty Quantification Research**

Statistical uncertainty quantification has been researched to a limited degree. In probabilistic analysis, random variables are described as probability density functions defined by distribution type (e.g. normal, lognormal) and statistics (e.g. mean, standard deviation). It is typically assumed that the statistics are known without uncertainty, that is, you have ideally quantified the population statistics. In reality, because of the limited data sets used to quantify distributions, uncertainty exists.

Bayesian analysis is a classical approach for modeling uncertainty in the statistics of variable design parameters [45]. With it, unknowns, such as a population mean, are treated as random variables. The unknowns are defined as Bayesian priors and are typically based on subjective expert judgment. When new data is collected, the Bayesian methodology updates the prior estimation based on the likelihood function of the new data to produce a posterior distribution that reflects the current state of knowledge. Monte Carlo Chain Monte (MCMC) analysis is frequently used to draw samples from the posterior distribution in an efficient manner [69]. A common criticism of Bayesian analysis is in the ambiguity involved with definition of the prior information. A less common criticism is that when

conducting a probabilistic analysis for the purpose of failure probability prediction, a single value is predicted based on the failure limit and the posterior distribution. From an engineering perspective, there is value in accounting for the uncertainty in the parameters of the statistics, sometimes called hyperparameters, in such a way that either a distribution of failure probability or confidence bound is predicted.

Early works in propagating statistical uncertainty were based on approximate reliability methods using the safety index. Der Kiureghian and Liu demonstrated the prediction of mean, median, maximum likelihood estimates, and bounds of a safety index from uncertain statistical parameters [70].

Wirshing posed a first-order expansion of the failure probabilities to predict bounds of the failure probability [71]. It is based on the FORM prediction of failure probability. The upper and lower bound is computed at a selected confidence level,  $\alpha$ , and used to determine a distance offset from the expected MPP by a linear approximation. The approach is computationally efficient, but the accuracy is dependent on the linearity of the limit state. As a first approximation, the approach is valuable.

Torng and Thacker posed a probabilistic method to assess reliability for structural problems with uncertainties due to estimation, modeling, and human error [72]. They defined that aleatory uncertainties are reflected in the calculated reliability, whereas epistemic uncertainties are reflected in confidence bounds. They proposed that an iterative procedure and a fast convolution method calculate the aleatory reliability and that, for the epistemic uncertainties, a nested approach predict confidence bounds. The nested approach uses random sampling from the distribution defining the variation in statistical model. This is sometimes referred to as an “outer-loop” sample with an “inner-loop” reliability analysis that predicts failure probability based on the sampled statistic. The authors recommended modeling aleatory uncertainty with probability distributions and statistical uncertainty, from lack of data, applied classical statistical confidence bound methods to the small data sets to

get objectively defined hyperparameters. This approach is also used in Chapter 3.

Torng and Thacker soon developed an alternate approach that conducted the nested probabilistic analysis using an approximation function based on probabilistic sensitivity factors [73]. Probabilistic sensitivity factors are calculated at the Most Probable Point (MPP) of the standard normal space that identifies the shortest distance between the origin and the limit state. Effectively these are the sensitivities of the safety index,  $\beta$ , with respect to a deviation in a random statistic. When assuming a linear limit state,  $\beta$  is transformed to a failure probability based on the standard normal distribution. The variation of  $\beta$  with respect to variation in random parameters is approximated as a Taylor series expansion at the converged MPP value and the probabilistic sensitivities. This is an approximate approach as the perturbations away from the converged MPP value will no longer lie on the limit state.

Mehta et al. assessed the uncertainty quantification approaches of Torng and Thacker in addition to a first-order approach developed by Wirshing, full nested MCS, and a regression approach where the response function is approximated with a response surface [74]. They also posed to combine both model and statistical uncertainty into a single quantity, a design interval. Statistical uncertainty was quantified with classical statistical confidence bound methods. The regression approach approximates the computationally expensive performance function and inner-loop MCS is based on the approximation. They concluded that the full nested outer- and inner-loop approach is the most accurate but had obvious computational costs, and that the approximate methods were efficient but had potential accuracy issues.

Venkataraman et al. developed several approaches to calculate confidence bounds for the safety index,  $\beta$  [75]. The first used a nested MCS approach with Latin hypercube sampling at both levels. The second used a single MCS to calculate failure probability and sensitivities of the failure probability to the distribution parameters. Sensitivities are then

used to develop a local linear approximation of  $\beta$  using a linear Taylor's series expansion. The sensitivities were calculated numerically via Karamchandani's approach so each sensitivity calculation does not require re-evaluating the limit state function [76]. Chapter 3 expands on this approach and uses gradient-enhanced Kriging as a failure probability approximation. The third approach uses response surface approximation fitted to the limit state function at MCS sampling points. It is based on a method developed by Melchers and Ahammed that approximates the limit state function values at all the failed MC sample points with a linear hypersurface [77]. This explicit form of the limit state function can then be used for calculating the confidence limits of  $\beta$  or failure probabilities using the FORM. The fourth method shown was a nested FORM approach where a linear expansion of  $\beta$  at the MPP is used to approximate the reliability index at a confidence interval,  $\beta_\alpha$ . This process is repeated until convergence to a limit state condition. The developed approaches were demonstrated on a cantilever beam example and showed that all four methods predict confidence bounds within a few percent of each other.

Picheny et al. developed a method for predicting an MCS-predicted conservative estimate of failure probability based on the uncertainty in sample statistics using a single MCS simulation [78]. Their approach focused on providing a conservative estimate of the input statistics, as defined by Cumulative Distribution Functions (CDFs), and using a single MCS reliability calculation to predict the conservative estimate. They found that using conservative estimates of the CDFs were overly conservative when compared to a bootstrapping simulations and that bootstrapping was only acceptable when large data sets (e.g. 100 values) were available. These conservative estimates of CDF show the challenge of using subjective information for uncertainty quantification.

Cruse and Brown developed an efficient approach to propagate Bayesian statistical uncertainty by approximating the inner-loop failure probability calculation using a failure probability response surface [79]. This surface was a function of the statistical parameters



and was developed using a Design of Experiments (DOE) training set of MCS-predicted failure probabilities. While the quadratic response surface used was effective in the example problem, complex responses may require advanced approximation tools. Further, since each surface training point requires a full MCS, accurate and efficient regression techniques for a given set of training points are desired. The method developed in Chapter 3 extends this approach by using a more advanced surface regression approach.

Bichon et al. discussed the application of Bayesian inference coupled with Efficient Global Reliability Analysis (EGRA) to problems with statistical uncertainty [80]. The approach is based on using EGRA as a surrogate model for failure probability as a function of statistical parameter [81]. EGRA locates multiple points on the limit state throughout the uncertain space and uses the points to construct a Gaussian stochastic process model that provides a global approximation for the entire limit state. With this surrogate, uncertainties in hyperparameters defined as Bayesian priors are efficiently propagated to a distribution of failure. An adaptive importance sampling approach is used calculate the probability of failure from the Gaussian process model.

From the review of these prior works, it can be seen that a new method for statistical uncertainty quantification is needed. The approach should not subjectively model uncertainty to provide defensible estimates of error. The method should not rely on the safety index as a failure probability approximation since the approach is susceptible to unquantified error. The approach should also accurately create a surrogate model for failure probability that is more efficient than traditional response surface methods. These requirements are all met by the developments in Chapter 3.

## 1.4 Summary of Research Need

Based on the review of the existing research, advances to reduced-order mistuning modeling, model uncertainty quantification, and statistical uncertainty quantification can make significant contributions to turbomachinery design.

Advanced to reduced-order mistuning modeling would address the current limitations of nominal-mode methods. Their first limitation is that they rely on nominal-mode approximation of response and use airfoil modal stiffness perturbations to represent mistuning. This approximation does not account for the geometric deviation on mode shapes, and for modes where this is significant, errors will be introduced. Airfoil geometric deviations alter their structural mode shapes the nominal mode approximation introduces a quantifiable error. The errors that this introduces have not been quantified in the existing body of research since validation studies have only considered Young's modulus mistuning. Development of a geometric mistuning model, as in Chapter 4, will improve accuracy and improve integration with the design process.

A geometric mistuning approach has been developed by Sinha [32], but it has its own limitations. First, while an effective ROM, there can still be large computational costs associated with the transformation of physical sector DOF to the new basis, particularly when there are a large number of DOF in the disk. Second, it requires full model solutions from multiple, potentially large, sector models. Third, the approach is an approximate basis that is not the most efficient basis for the solution. Finally, Sinha's work also did not demonstrate the use of the nominal-mode approximation for the problem, and therefore did not fully demonstrate the need to account for non-nominal modes. A CMS approach, developed in Chapter 4, would alleviate these problems by partitioning the substructures so that DOF associated with the disks would not need to be solved for each retained geometry model.

The developed geometric mistuning model of Chapter 4 includes approximation of airfoil substructure modal response. In the development of approximations, there will always be errors. There is also a need to develop approximate models for blade-alone response that provide input to mistuning models and account for their approximation error. From the review of prior works, it is identified that a new model error quantification approach is needed. The approach should objectively quantify error rather than relying on subjective expert judgment. It should model the error as a function of design parameter to account for variations in error across the design space. Developing an approach to model the error associated with local geometry deviations will also contribute to the confidence in turbomachinery dynamic response testing. The efforts in Chapter 2 accomplish these goals.

From the review of these prior works, it can be seen that a new method for statistical uncertainty quantification is needed. The approach should not subjectively model uncertainty to provide defensible estimates of error. The method should not rely on the safety index as a failure probability approximation since the approach is susceptible to unquantified error. The approach should also accurately create a surrogate model for failure probability that is more efficient than traditional response surface methods. These requirements are all met by the developments in Chapter 3.

## **1.5 Research Summary**

Design of structural components is constrained by both iteration time and prediction uncertainty. Iteration time refers to the computation time each simulation requires and controls how much of the design space can be explored given a fixed period. Prediction uncertainty refers to both irreducible uncertainties, such as those caused by material scatter, and reducible model uncertainty, such as the simulation error of the physics-base model. In the presence of uncertainty, conservative safety factors and design margins are used to ensure

structural integrity, but that also negatively impact component weight and design life. This research investigates three areas to improve both iteration time and uncertainty quantification for turbomachinery design.

The first develops two reduced-order models that predict the effect of geometric deviations on airfoil forced response. A Principle Component Analysis approach is used to create a reduced-basis set of geometric perturbations that also statistically characterized the deviations. The first reduced-order response model is based on eigensensitivity calculations of the modal response with respect to the reduced geometry basis and a first-order Taylor series expansion. The second reduced-order model accounts for the approximation error between the Taylor series approximation and full models. A small set of randomly generated full-order model solutions are used to quantify the discrepancy between full and approximate solutions. A regression analysis between the reduced-basis set of geometry perturbations and the discrepancy is used to quantify both bias and random uncertainty of the approximation. When included in the eigensensitivity approximation of modal response, this error-quantified approximation shows significant improvements in accuracy, because of its bias correction, and description of uncertainty, through the remaining random error.

The second research area develops a Probabilistic Gradient Kriging approach to efficiently model the uncertainty of failure probability predictions caused by the sampling error from small sample statistics. A Kriging approximation based on both failure probability values and gradients is used as a reduced-order model of failure probability as a function of statistical parameter. Probabilistic gradients are obtained through a numerical approximation that obtains sensitivities without the need for costly finite difference approximations based on additional probabilistic simulations. It is shown that the Probabilistic Gradient Kriging approach is significantly more accurate for a given number of training points when compared to conventional Kriging and polynomial regression approaches. It

is further found that the impact of statistical uncertainty from small sample sizes can lead to uncertain failure probabilities that can be an order of magnitude greater than the true value.

Reduced-order methods have been developed that rapidly predict mistuned rotor response by approximating mistuning with a nominal-mode basis and airfoil modal stiffness perturbation. Nominal-mode approximation assumes that the geometry of each airfoil is identical and the geometric perturbations that alter modal stiffness do not perturb mode shape. This work investigates the accuracy of that approximation and develops several Component Mode Synthesis based reduced-order mistuning models that explicitly account for geometric deviations using both nominal and non-nominal mode shape approaches. The first represents the prevailing industry method and uses nominal-mode substructure reduction with airfoil substructure modal stiffnesses perturbed using geometrically-perturbed cantilevered airfoil finite element models. This approach demonstrates effective qualitative predictions that identify relative mistuning amplification but, when compared to analytical results from a geometrically-perturbed integrally bladed rotor model, shows significant ( $\sim 20\%$ ) errors in maximum predicted mistuning amplification. For blade-to-blade response prediction at specific frequencies, dramatic ( $>100\%$ ) errors are demonstrated. The second approach uses nominal-mode substructure reduction and mistuned airfoil modal stiffness perturbations from reduced-order modal methods. The reduced-order airfoil model reduces computational time while enabling qualitative mistuning prediction. The third method uses nominal-mode substructure reduction, mistuned modal stiffnesses from geometrically-perturbed airfoil finite element models, and expands results with a non-nominal Craig-Bampton matrix for each airfoil. Though improvements in quantitative prediction of maximum response frequency and response amplitudes are found for all modes, the method was inconsistent. The fourth approach uses non-nominal mode substructure reduction and expansion using non-nominal Craig-Bampton matrices generated

from geometrically-perturbed finite element models. This approach demonstrates excellent prediction of peak mistuning amplification and blade-to-blade response with prediction errors below 1%. A fifth approach uses reduced-order modal methods to approximate the non-nominal Craig-Bampton matrices. Use of these approximate mode shapes is found to significantly improve accuracy compared to the nominal-mode assumption but that overall performance is dominated by accurate frequency approximation. It is concluded that for rapid qualitative analysis, nominal-mode mistuning analysis with approximate mistuned modal stiffnesses should be used, for improved accuracy with additional computational expense approximate non-nominal mode mistuning analysis should be used, and with greater solution time and need for quantitative accuracy, geometrically perturbed finite element model results should be used in non-nominal Craig-Bampton reduction and expansion.

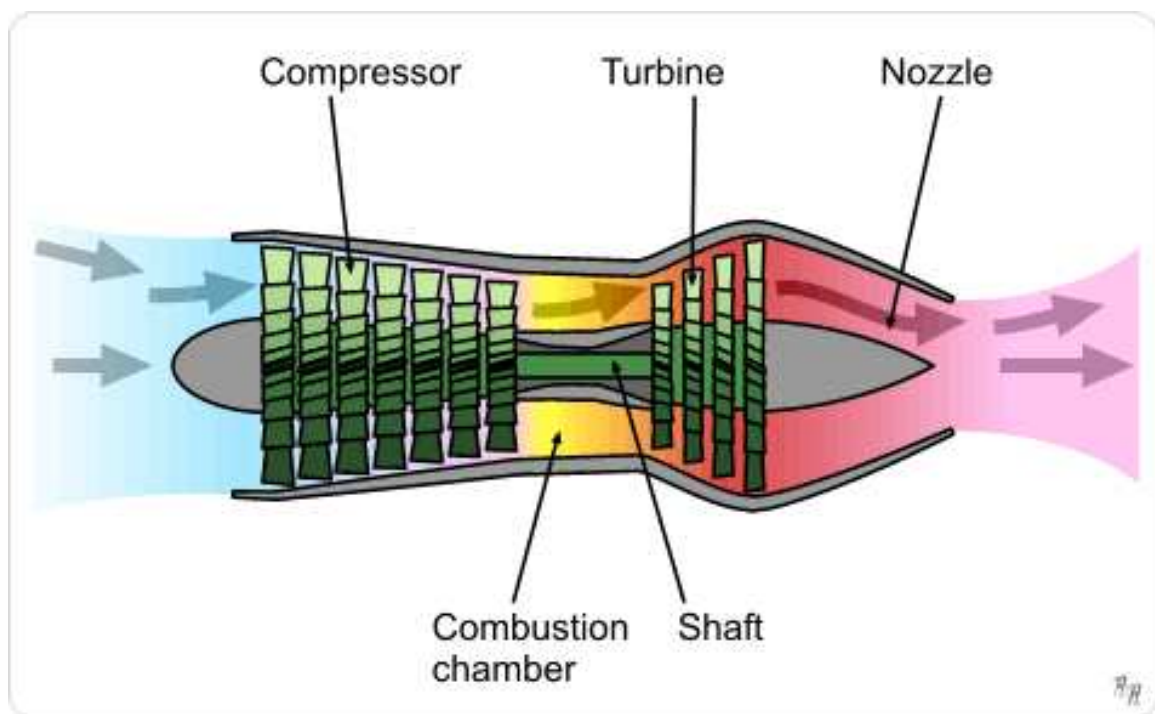


Figure 1.1: Turbojet Engine Schematic

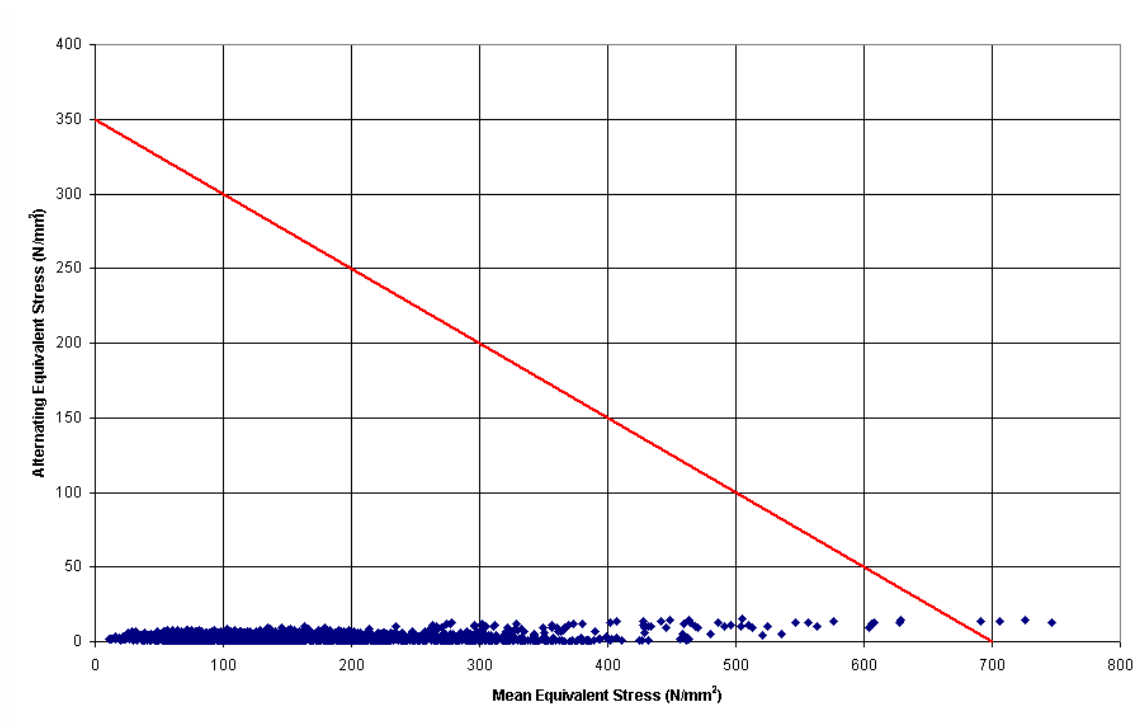


Figure 1.2: Example Goodman Diagram



Figure 1.3: Integrally Bladed Rotor



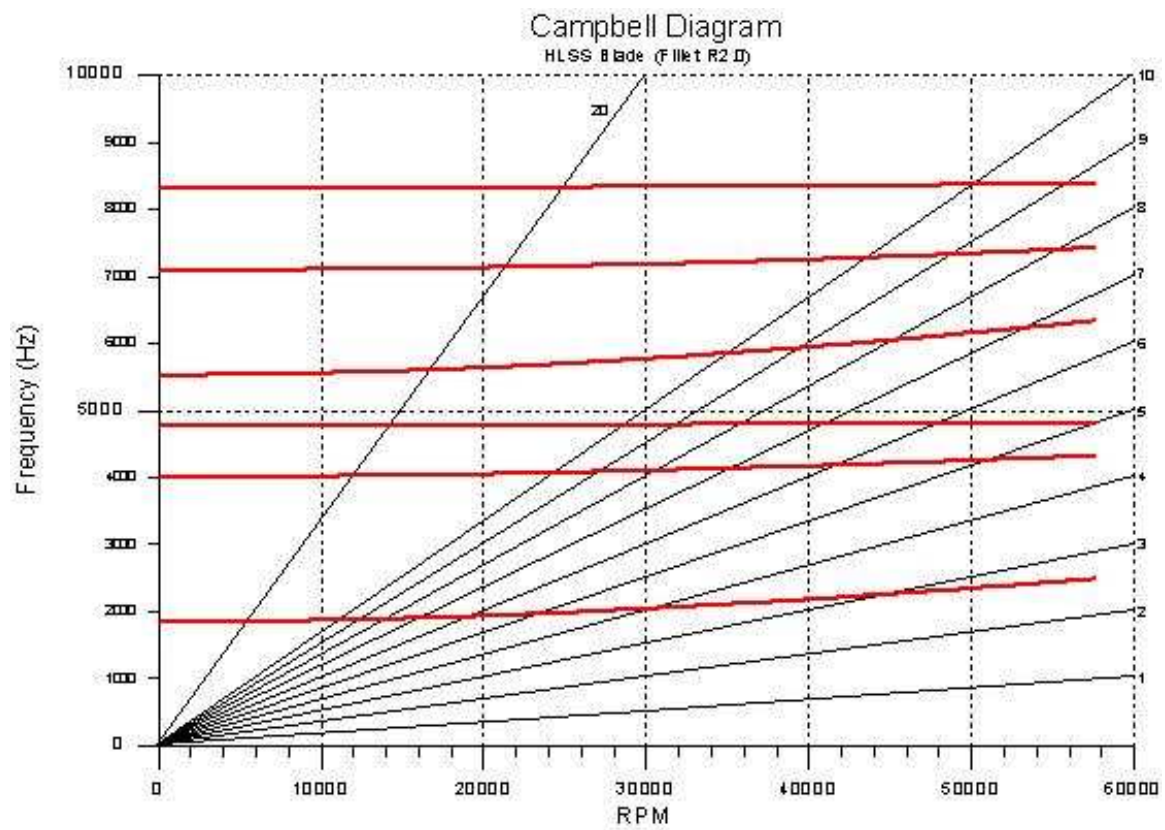


Figure 1.4: Example Campbell Diagram

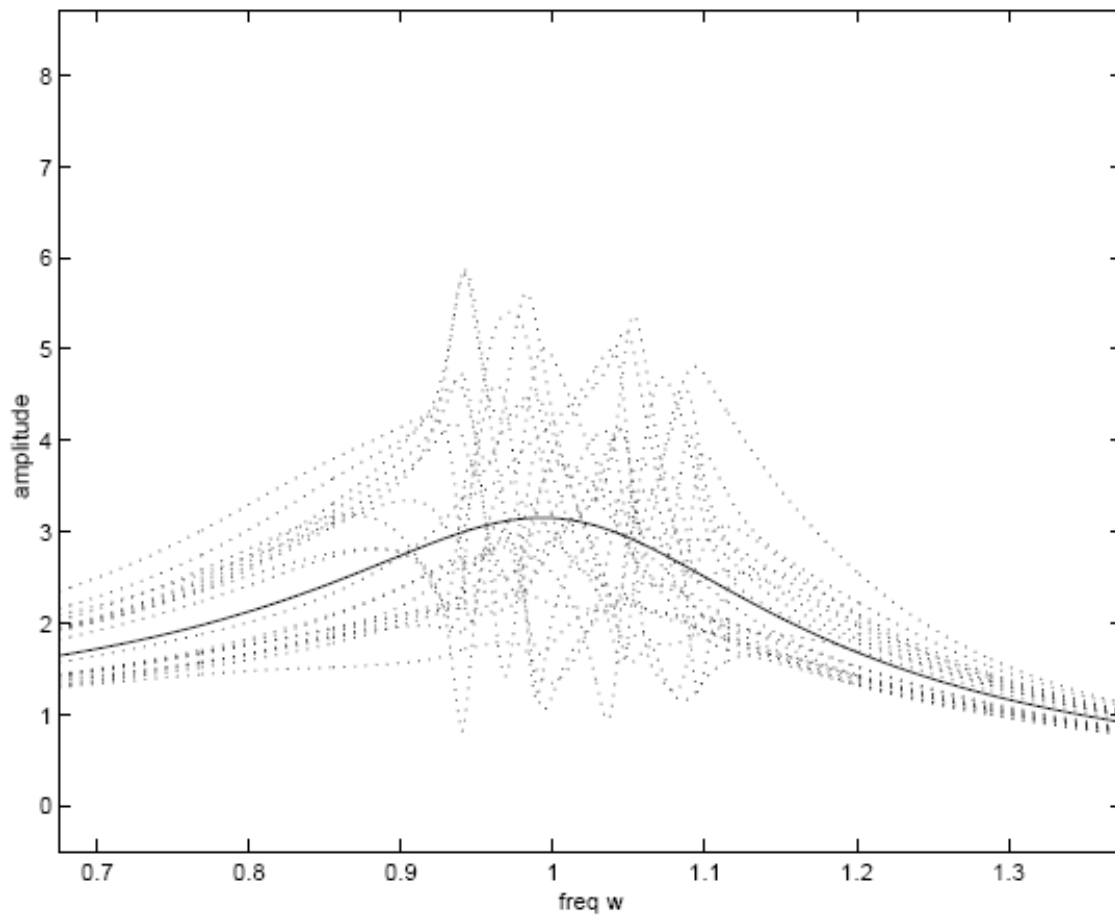


Figure 1.5: Tuned Response (solid line) versus Mistuned (Dotted)

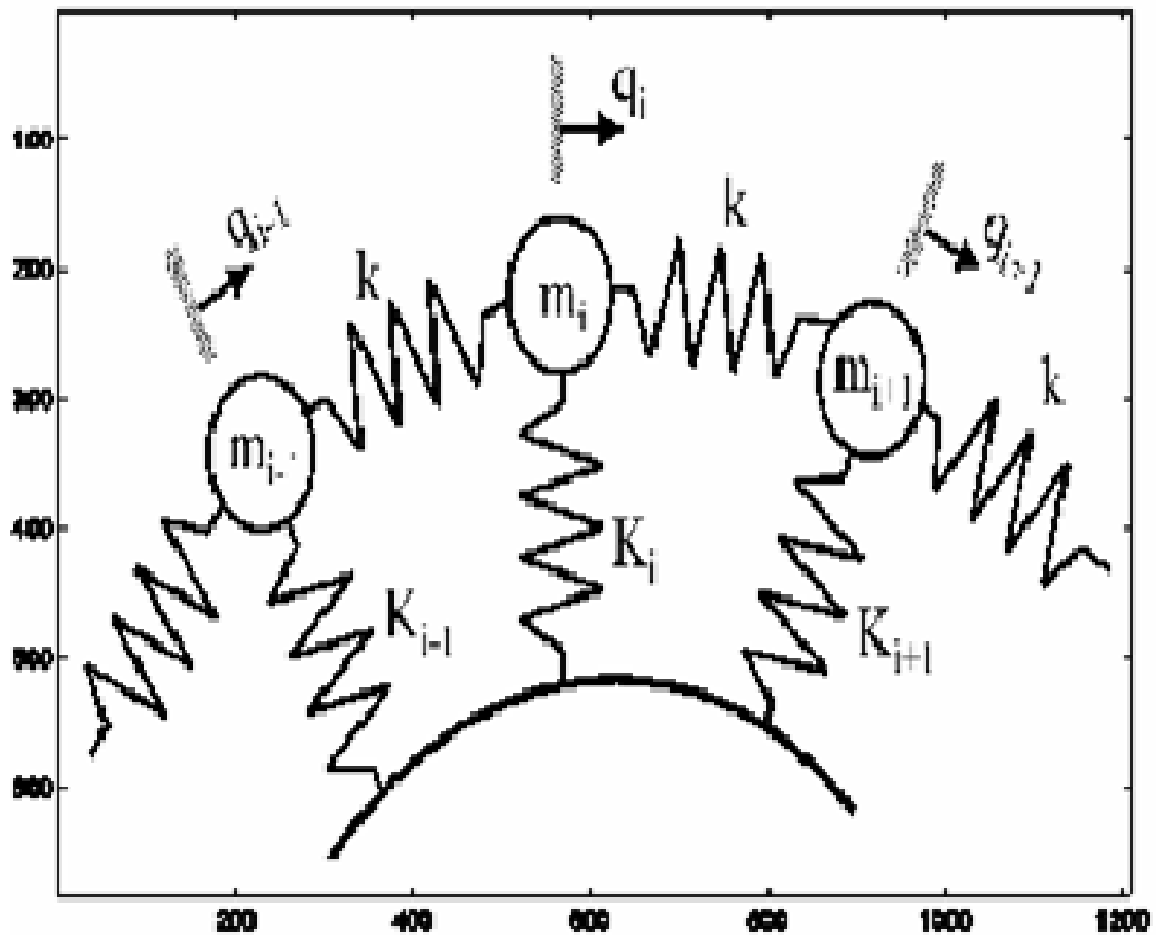


Figure 1.6: Dye and Henry Spring-Mass Model

## **2 Reduced-Order Model**

# **Development for Airfoil Forced Response**

### **Abstract**

Two new reduced-order models are developed to accurately and rapidly predict geometry deviation effects on airfoil forced response. Both models have significant application to improved mistuning analysis. The first developed model integrates a Principal Component Analysis approach to reduce the number of defining geometric parameters, semi-analytic eigensensitivity analysis, and first-order Taylor series approximation to allow rapid as-measured airfoil response analysis. A second developed model extends this approach and quantifies both random and bias error between the reduced and full model. Adjusting for the bias significantly improves reduced-order model accuracy. The error model is developed from a regression analysis of the relationship between airfoil geometry parameters and reduced-order model error, leading to physics-based error quantification. Both models are demonstrated on an advanced fan airfoil's frequency, modal force, and forced response.

## 2.1 Introduction

Effective airfoil dynamic response analysis ensures rotor reliability and requires prediction of resonance avoidance margin, forced response, and mistuning. Standard practices predict dynamic response using Finite Element Models (FEMs) of design intent geometries. While sufficient for some cases, this standard approach does not explicitly consider airfoil structural response variations caused by random manufacturing deviations from design intent geometries. Because hundreds or thousands of these simulations would be required to assess effects from random variations, a new more efficient airfoil modal and forced response prediction process is required.

Existing literature contains a significant body of work developing efficient mistuned rotor forced response predictions using reduced-order models (ROMs) [19, 16, 29, 12, 23, 25]. These efforts have shown strong amplification of rotor forced response caused by small perturbations in blade-to-blade frequency. While effective, these prior models are limited in two significant ways. First, they assume that airfoil frequencies vary but airfoil mode shapes remain nominal. This assumption enables computational efficiencies but geometric deviations clearly alter blade-to-blade mode shapes, thus altering each blade's modal force, and impacting mistuned response. Their second limitation is the required experimentally obtained blade-to-blade frequency variation input. Such empirical measures are subject to error, particularly for Integrally Bladed Rotors (IBRs) and the known challenge to isolate their individual airfoil frequencies from the rotor system response. These experimental results also are not connected to airfoil geometric parameters that can be controlled in the design process for acceptable frequency scatter manufacturing. Because of these limitations, physics-based ROMs of airfoil modal and forced response that explicitly account for geometric deviations are needed that provide accurate input to existing mistuning models and include frequency scatter in design. Further, since existing mistuning prediction meth-

ods do not consider mode shape variation, a ROM is needed to show the significance of mode shape variation on forced response and lead to future improved mistuning analysis tools.

ROM development begins with an approach to create a reduced set of geometry parameters defining manufacturing variation. Previous efforts in reduced-order airfoil geometry modeling include Garzon and Darmofal's use of Principal Component Analysis (PCA) [33]. The PCA approach is a common statistical method that creates a reduced basis space through an eigenanalysis of the covariance between parameter deviations [82]. The research demonstrated the effectiveness of the technique for turbomachinery applications. An alternate approach was demonstrated by Capiez-Lernout et al. in their development of a technique characterizing manufacturing tolerances for mistuned bladed disk with a dispersion parameter [41]. This ad-hoc estimation of the geometry effects on response does not directly depend on measured geometry but does have computational advantages. Because the PCA approach is directly related to measured deviations, it is applied in this ROM development.

With a reduced geometry model determined, development of a reduced-order response method remains. Taylor series approximations are an attractive method assuming that the required sensitivities can be efficiently calculated. Methods to rapidly predict sensitivities of modal response, or eigensensitivities, have been developed by Fox and Kapoor for unique eigenproblems and Friswell for cyclic symmetry problems [83, 84]. These equations are semi-analytic and allow sensitivity calculation from a single FEM solution with efficiency improvements described later. Such approaches have been widely used in optimization applications, but not for airfoil modal response approximation over the range of manufacturing deviations considered in this effort.

With these existing tools the first of two airfoil response ROMs, the standard ROM, is developed. First, PCA is used to create a reduced basis set of the manufacturing deviations.

Eigensensitivities are then efficiently calculated semi-analytically with respect to this new basis, and these are used in a first-order Taylor series modal response approximation. These approximate modal quantities are then used in a modal domain forced response analysis. When combined, the integrated approaches lead to an exceptionally efficient and accurate model.

Though accurate, as with all approximations, there is error. Model errors have been widely recognized as critical to the design and analysis process and the need for its accounting has been outlined in several professional editorial policy papers [85, 86]. In this research a second ROM is developed, an error-quantified ROM, that captures the error developed in the model reduction process. This *a posteriori* error model requires a linear regression model of the errors obtained between a limited number of full model and standard ROM comparisons. Results from the model are able to reduce the standard ROM error and quantify the approximate model uncertainty.

It is noted that these models do not account for the impact of geometric deviations on unsteady aerodynamic loading. While this may be an important factor in the prediction of forced response, the development of a reduced-order model for aerodynamics is an ongoing challenge not considered in this research.

The following sections develop the two ROMs. How measured airfoil deviations are reduced to a practical number of parameters with PCA is defined in Section 2.2. Section 2.3 develops the standard reduced-order modal and forced response models, and Section 2.4 introduces the error-quantified ROM. These sections are followed by results from a real-world component that show the significance of geometric deviations from design intent and demonstrate the accuracy of both developed models. The application of these new tools provide improved input to existing mistuning prediction models, show the effect of geometrically induced mode shape variation on forced response, and create a model that can be used for future mistuning tool developments.

## 2.2 Reduced-Order Airfoil Geometry Model

In the past, deviations from design intent have been checked with templates and manual gages. Such devices are pass-fail tools providing no quantitative response information back to the engineer. Because of the rotor response sensitivity to geometric variations, new measurement techniques are desired. One approach uses coordinate measurement machines (CMMs) that collect data through a geometry traversing probe that obtains spatial data points at regular intervals. Each measured airfoil may provide thousands of measured data points. Assessing the sensitivity of each of these locations to perturbation would require significant computational resources, hence the need for a reduced-order geometry model retaining a limited set of parameters quantifying geometry deviations. PCA is attractive given its ease of implementation and the creation of minimum a set of retained basis vectors to represent fully correlated geometry variations.

PCA is implemented by storing  $n$  measured three-dimensional coordinate data points in vector  $\mathbf{x} \in \mathbb{R}^{3n}$ . A set of  $p$  measured airfoils results in matrix,  $\mathbf{X} \in \mathbb{R}^{3n,p}$ . Since we are interested in variations from the average blade, the mean value of each row is subtracted from each member of the row to give a matrix of measured deviations,  $\Delta\mathbf{X}$ , where each element is

$$\Delta x_{i,j} = x_{i,j} - \bar{x}_i \quad i = 1, 2, \dots, 3n; j = 1, 2, \dots, p \quad (2.1)$$

where  $\bar{x}_i$  is the average of the  $i^{th}$  row. It is important to note that the average,  $\bar{x}_i$ , is not necessarily the original design intent. Also, subtracting the row mean from each element makes the expected value of each row zero. The first-order covariance matrix of  $\Delta\mathbf{X}$  defines the statistical relationship between a measurement point deviation and all other points, and its eigensolution leads to eigenvectors that can be used to form a new subspace optimally representing variation. This is written in standard eigenproblem form



$$Cov(\Delta\mathbf{X})\Psi = \Psi\mathbf{D} \quad (2.2)$$

where  $\mathbf{D}$  and  $\Psi$  are the eigenvalue and eigenvector matrices, respectively. The eigenvectors are the principal components modes of the measured data, and the eigenvalues are the principal component variances that indicate the data variance each principal component captures. Based on these eigenvalues, graphical and statistical methods can be used to retain a limited set of basis vectors. Also of importance, the principal components are orthogonal, and therefore, uncorrelated statistically. The PCA transforms a large set of correlated parameters into a small set of uncorrelated parameters.

Transformation of the measured deviations,  $\Delta\mathbf{X}$ , to the principal component basis requires the linear operation

$$\mathbf{Z} = \Psi^T[\Delta\mathbf{X}] \quad (2.3)$$

where the eigenfunction matrix is multiplied by the deviation matrix to give the z-score matrix,  $\mathbf{Z} \in \mathbb{R}^{m,p}$  with  $m$  the number of retained principal component modes. These scores are effectively regression coefficients for the new principal component basis and define the participation of each PCA mode in each measured geometry. The above algorithm, Eq. 2.1-2.3, is the covariance method of PCA and the columns of  $\mathbf{Z}$  represent the Karhunen-Loeve transformation.

How these z-scores and principal component modes are integrated into a reduced-order forced response model is described in the following section.

## 2.3 Standard Blade-Alone Forced Response

### Reduced-Order Model

The approach used in this ROM development is Taylor Series approximation using first-order sensitivities. Sensitivity calculations can be computationally expensive when calculated numerically via finite difference methods that require a FEM evaluations for each design parameter. This work proposes to use semi-analytic methods that replace the costly calculations of the process, i.e. decomposing the stiffness and mass matrix and solving the matrix eigenvalue problem.

Combining the semi-analytic sensitivity methods defined in [87] with the reduced-order geometry model results from Section 2.2 leads to the following principal component mode response sensitivities

$$\frac{\partial \lambda_i}{\partial \psi_j} = \phi_i^T \left( \frac{\partial \mathbf{K}}{\partial \psi_j} - \lambda_i \frac{\partial \mathbf{M}}{\partial \psi_j} \right) \phi_i \quad (2.4)$$

$$\frac{\partial \phi_i}{\partial \psi_j} = \sum_{g=1}^r c_{ig} \phi_g \quad (2.5)$$

where  $i$  identifies the vibration mode number,  $j$  the principal component mode number, and where  $r$  is the total number of retained vibration modes. The constant terms are calculated

$$c_{ig} = \frac{\phi_g^T \left( \frac{\partial \mathbf{K}}{\partial \psi_j} - \lambda_g \frac{\partial \mathbf{M}}{\partial \psi_j} \right) \phi_i}{(\lambda_g - \lambda_i)} \quad (2.6)$$

$$c_{ii} = -\frac{1}{2} \phi_i^T \frac{\partial \mathbf{M}}{\partial \psi_j} \phi_i \quad (2.7)$$

where  $\lambda_i$  and  $\phi_i$  are eigenvalue and mass-normalized eigenvector,  $\mathbf{K}$  and  $\mathbf{M}$  are mass and stiffness matrices, and  $\psi_j$  are retained principal component modes. The stiffness and mass

matrix derivatives are numerically computed through nominal and perturbed finite element models. Forced response sensitivity can also be calculated directly, but is not done so here because of the need to explicitly retain frequency and mode shape sensitivities for use as input to mistuning and modal force predictions.

Prediction of modal stress sensitivity requires the derivative of the strain-displacement equation. Differentiating this equation with respect to the  $j^{th}$  principal component mode gives

$$\frac{\partial \sigma_i}{\partial \psi_j} = \mathbf{D}\mathbf{B}\frac{\partial \phi_i}{\partial \psi_j} + \mathbf{D}\frac{\partial \mathbf{B}}{\partial \psi_j}\phi_i \quad (2.8)$$

where  $\mathbf{D}$  is the elasticity matrix,  $\mathbf{B}$  is the strain-displacement matrix, and  $\sigma_i$  is the stress vector of the  $i^{th}$  vibration mode. As with the mass and stiffness matrices, the sensitivity of the strain-displacement matrix is calculated numerically.

Once the sensitivities have been computed, the standard ROM eigenvalues and eigenvectors are computed with a first-order Taylor series expansion. The approximations are

$$\tilde{\lambda}_i = \lambda_i^0 + \sum_{j=1}^m \frac{\partial \lambda_i}{\partial \psi_j} d\psi_j \quad (2.9)$$

$$\tilde{\phi}_i = \phi_i^0 + \sum_{j=1}^m \frac{\partial \phi_i}{\partial \psi_j} d\psi_j \quad (2.10)$$

where  $\lambda_i^0$  and  $\phi_i^0$  are the average eigenvalue and eigenvector results and the tilde symbol annotates an approximation. The increment  $d\psi_j$  is the  $j^{th}$  z-score value for a given measured airfoil. A first-order approximation was chosen over higher-order methods because of its simplicity and its accurate performance in the demonstration problem. Further work exploring the use of higher-order methods does have merit should a situation be found where the current approach has unacceptable accuracy.

The forced response ROM is based on modal domain transformation of the equation of motion using the approximate values for eq. 2.9 and 2.10 while assuming harmonic forcing

and motion

$$(-\omega_f^2 + i2\tilde{\lambda}_i\omega_f\zeta_i + \tilde{\lambda}_i^2)\tilde{\alpha}_i = \tilde{\phi}_i^T \mathbf{f} \quad (2.11)$$

where  $\omega_f$  is the forcing frequency,  $\zeta_i$  the modal damping,  $\tilde{\phi}_i^T \mathbf{f}$  the approximate modal force, and  $\tilde{\alpha}_i$  the approximate modal coordinates

$$\tilde{\alpha}_i = \frac{\tilde{\phi}_i^T \mathbf{f}}{(\tilde{\lambda}_i^2 - \omega_f^2) + i(2\tilde{\lambda}_i\omega_f\zeta_i)} \quad (2.12)$$

which gives the participation of the  $i^{th}$  approximate mode. The approximate displacement vector,  $\tilde{\mathbf{u}}$ , is computed in the approximate modal domain

$$\tilde{\mathbf{u}} = \tilde{\Phi} \tilde{\boldsymbol{\alpha}} \quad (2.13)$$

where the algebra represents modal summation.

While the ROM presented in this section does reduce the costly modal analysis procedures from expensive matrix computations to simple arithmetic, there is error introduced in the approximation. The next section describes how to improve this model using the developed error-quantification technique.

## 2.4 Error Quantified Reduced-Order Model

Models in general have an unquantified error between their result and the true value. Accounting for this error and providing an error bound on the result ensures proper model application. This section develops an approach to quantify the error between the eigensensitivity-based approximate models developed in Section 2.3 and full FEM solutions. This quantification includes analysis for reducible errors related consistently to design parameter

variations, i.e. bias, and random errors that are irreducible without modifying the model form. This error quantification approach is used to reduce error instead of pursuing higher-order approximation methods to avoid the complexity and to develop the error quantifying approach that is applicable to even these more advanced approximations.

The developed error model is an *a posteriori* model that requires comparison of a limited number,  $k$ , of full solutions to the standard ROM. These models are referred to as training models that provide the error analysis data. The error is quantified as the discrepancy vector between standard ROM and full model results.

$$\delta_k = f(\mathbf{z}_k) - \tilde{f}(\mathbf{z}_k) \quad k = 1, 2, \dots, p \quad (2.14)$$

where the functions represent the simulation of a modal response at the  $k^{th}$  vector of z-scores defining an airfoil, and the tilde represents the standard ROM approximation. Analysis of the relationship between the vector  $\delta$  and the components of  $\mathbf{z}_k$  determines the existence of a physical relationship between principal component mode magnitude and discrepancy. A discrepancy model as a function of z-scores is constructed from the regression analysis

$$\delta = \mathbf{F}\beta + \varepsilon \quad (2.15)$$

where  $\mathbf{F}$  is a matrix of defined regression functions,  $\beta$  is a vector of unknown regression coefficients, and  $\varepsilon$  is a normally distributed zero mean error term. In the error-quantified ROM the regression functions are components of the  $\mathbf{Z}$  matrix that defines the airfoil geometries. As an example, the matrix form for a regression model that includes a constant and all linear terms is

$$\mathbf{F} = \begin{bmatrix} 1 & \mathbf{Z}_{1,1} & \mathbf{Z}_{1,2} & \cdots & \mathbf{Z}_{1,p} \\ 1 & \mathbf{Z}_{2,1} & \mathbf{Z}_{2,2} & & \\ \vdots & & & \ddots & \\ 1 & & & & \mathbf{Z}_{m,p} \end{bmatrix} \quad (2.16)$$

where the first column is the regression coefficient for the constant model term,  $b_0$ . Should the discrepancy data show nonlinear characteristics, additional non-linear regression terms can be added. The regression coefficients are determined so that the error between the regression model and the data is minimized through solution of the linear least-squares problem

$$(\mathbf{F}^T \mathbf{F})^{-1} \mathbf{F}^T \delta = \begin{bmatrix} b_0 \\ b_1 \\ \vdots \\ b_m \end{bmatrix} \quad (2.17)$$

where the  $b$  values are the most likely estimates of the regression coefficient vector,  $\beta$ . The error term,  $\varepsilon$ , should be uncorrelated, normally distributed with zero mean and constant variance for statistical modeling assumptions to be met that allow confidence interval prediction. The linear model developed from eq. 2.15 is added to the approximate model developed in Section 2.3 to develop the error-quantified ROM for the  $p^{th}$  airfoil

$$\tilde{\lambda}_i = \lambda_i^0 + \sum_{j=1}^n \frac{\partial \lambda_i}{\partial \psi_j} d\psi_j + (\mathbf{z}_p^*)^T \beta + \varepsilon_p \quad (2.18)$$

$$\tilde{\phi}_i = \phi_i^0 + \sum_{j=1}^n \frac{\partial \phi_i}{\partial \psi_j} d\psi_j + (\mathbf{z}_p^*)^T \beta + \varepsilon_p \quad (2.19)$$

where  $\mathbf{z}_p^*$  is the vector of z-scores for the  $p^{th}$  airfoil with the addition of a leading value

of one to account for the constant  $b_0$  term. Because the error terms are modeling error as the difference between full FEM and standard ROM, the addition of these terms reduces the error. Predictor variables, members of  $\beta$ , are only included in the model if they show statistical significance to the error. An advantage of this process is that the PCA produces an orthogonal set of predictor variables which simplifies determination of the parameter significance. These error-quantified modal quantities are then used in an error-quantified forced response solution using the modal domain approach from the previous section.

## 2.5 Numerical Results

The sensitivity of blade-alone modal and forced response to geometric deviations from design intent and the effectiveness of both the standard ROM and error-quantified ROM is shown on an advanced sixteen-bladed low aspect ratio IBR. This IBR, the Advanced Damping Low Aspect Ratio Fan (ADLARF), has been rigorously studied under the GUIDe Consortium, a joint government, university, and industrial program to fund research in turbomachinery forced response [88, 89, 90]. Because airfoil geometry measurements are not available for this rotor, measured deviations from a related industrial IBR fan stage are used. Full FEMs of the as-measured models of the sixteen airfoils are used to assess sensitivity to variations from design intent, create the error model training data, and quantify the accuracy of the two developed ROMs. While these ROMs do not directly provide mistuning results, they provide the required data for previously referenced mistuning models that account for structural coupling.

Modal calculations were made with a blade-alone finite element fan blade model. The blade approximately spans 12 inches with a 9 inch chord length. The model contains linear hexahedral elements with an element edge length of 0.25 inches, resulting in 7722 degrees-of-freedom, uses common Ti 6Al-4V material properties, and all degrees of freedom are

fixed at the blade root. This is a high quality, but not fully converged model, that was used to reduce computational requirements during the development process. A more rigorous converged mesh analysis was conducted to ensure that the unconverged model does not impact any of the research conclusions. The converged model had nearly 50,000 degrees-of-freedom and frequency variation results for the as-measured models, for the twentieth and most complex mode, were within a maximum of 0.02 percent between the investigated and converged model. This demonstrated that the geometric deviations had nearly the same percentage effect on response variation regardless of mesh density.

Results are obtained from the first twenty modes, covering responses from first flex at 360 Hz. to approximately 7,000 Hz. Figure 2.1 shows the mode shapes for the fifteenth and sixteenth mode, which are discussed in greater detail in subsection 2.5.2. The models were created parametrically with the coordinate measurement machine data points used as the parameters. With this model, airfoil geometry variations were automatically generated through a script file and mesh topology remained consistent with each model. Post processing was also conducted through scripting to ensure error-free result tabulation.

### **2.5.1 Reduced-Order Geometry Model Results**

An available set of compressor airfoil measured geometry deviations and the ADLARF nominal geometry provided representative as-measured geometry. Figure 2.2 shows one measured geometry deviation profile representative of the remaining airfoils, both as a blade surface contour plot and a three dimensional surface plot. Correlation between surface deviation across the blade is evident and shows that a reduced-order geometry model should account for spatial correlation. The measurement also shows negative deviations near the tip and positive deviations near the base. Such a pattern could be developed from variations in the vertical alignment of the part during manufacture. The probability distri-



bution of the set of all measured deviations is non-Gaussian, has a mean value of nearly zero, a standard deviation of 0.003 in., a minimum of -0.015 in., and maximum of 0.011 in.

PCA of the sixteen measured blades generates fifteen principal components,  $\Psi \in R^{3n,15}$ . Figure 2.3 shows the percentage total variance of each principal component mode, and it is shown that the first fifteen modes capture all measured deviations. As expected, the modes are ordered by decreasing variance modeling. Because fifteen features fully describe the blade geometry deviations, there is a significant computational cost reduction associated with the Taylor series approximations. If PCA had not reduced the geometry deviation degrees-of-freedom to fifteen, one sensitivity calculation would be needed for each FEM surface node degree-of freedom, requiring nearly 2,700 simulations.

## **2.5.2 Standard and Error-Quantified Reduced-Order Model**

### **Results**

The ROMs developed in Sections 2.2 and 2.3 are demonstrated on the as-measured rotor. Each subsection first includes results showing the full FEM predicted response variations of the sixteen as-measured airfoils. These results justify the need to account for geometrically induced variations. The subsections then continue to show the ROM's accuracy in predicting blade-to-blade variations for a selected critical mode, provides the training data used to determine the model bias and random error, and the two ROM's maximum errors over the first twenty modes.

#### **2.5.2.1 Frequency Results**

The IBR frequency variation predicted from the sixteen as-measured airfoils for the first twenty modes, normalized by the average frequency, is shown in the Figure 2.4 box-and-whisker plot. A box-and-whisker plot displays the four quartiles of data for each data set,

displaying the median as the horizontal dash bisecting the rectangular box into the first upper and lower data quartiles. The dashed vertical lines attached to these boxes show the upper and lower second quartiles. Additional symbols are for outlier data. Results show the largest frequency variation interval covering greater than  $\pm 2\%$  of the average value for sixteenth mode with the mean range of variation for all modes nearly  $\pm 1\%$ . It is seen that the normalized frequency deviation does not appear to significantly increase with increasing mode number because of the normalization. The absolute variation in frequency does increase with mode number. Further analysis of the coefficient of variation, the data mean divided by its standard deviation, does show an increasing trend in normalized variation.

While these are small deviations, they are in a range shown to lead to maximum mistuning amplifications. The close proximity of blade-to-blade frequencies causes multiple mode excitations at a single forcing frequency and summation of modal energy. Mistuning response will be highly sensitive to the exact pattern, so accurate prediction of each blade frequency is required. The predicted frequency variations can provide the necessary input to existing mistuned forced response ROMs and avoids experimental frequency measurement. Explicit geometric modeling also physically links design parameters to the frequency variations that lead to mistuned amplification. Understanding gained through these ROMs can lead to design changes or manufacturing process controls that will lead to improved IBR reliability.

Figure 2.5 shows the comparison between the predicted blade-to-blade IBR frequencies from the full finite element model, standard ROM, and the error-quantified ROM. Results for the sixteenth mode are shown because it had the largest frequency scatter in the first twenty modes, as seen in the box-and-whisker plot contained in Figure 2.4, and also has the largest error between full model and standard ROM predictions as shown in Figure 2.7. Even though Figure 2.5 shows the ROMs at their worst, it is seen that the standard ROM does an admirable job predicting blade-to-blade frequency deviations and captures

the blade-to-blade trend in frequency deviation. Because mistuning is highly sensitive to frequency magnitudes, a reduced error model is still desirable. Results show that the error-quantified ROM greatly improved accuracy. The airfoils with the greatest error from the standard ROM, three, four, eight, ten, fifteen, and sixteen show a marked improvement with the error-quantified ROM.

The input for the bias and random error terms of the error-quantified ROM was constructed from the *a posteriori* discrepancy analysis between full FEM and standard ROM. Figure 2.6 shows the errors for the sixteenth mode plotted against the z-scores of the retained principal component modes. There is a clear linear correlation between the residual value and the z-score magnitude of the twelfth principal component mode, while all other modes appear randomly distributed. This linear relationship was seen for all twenty modes. Because there is a predictable trend between the residual and twelfth principal component mode magnitude, the error quantified reduced-order model from eq. 2.18 and 2.19 will account for model bias and improve accuracy. Each mode has its own regression coefficients based on that mode's data. The remaining error not accounted for as bias can be included in the random error parameter of the error-quantified ROM.

It is noted that standard regression modeling practice avoids validating the model with the data used to create the regression model. This practice was not followed for the results shown. This is acceptable because the strong linear relationship in the data shows that the result is more than a just a random phenomenon. Nonetheless, a set of 50 randomly generated airfoil geometries based on the statistics from the PCA analysis were analyzed with the full FEM and ROMs. These results did not change any of the conclusions based on the sixteen as-measured airfoils and show that the error-quantified model is applicable to the larger domain of random airfoils.

Figure 2.7 shows the maximum percent error between the two ROMs and the full FEM for all twenty vibration modes. This maximum error is obtained for each mode by comput-

ing the absolute difference between each ROM and full model, dividing by the full model value for each of the sixteen airfoils, and plotting only the maximum of these sixteen error results. This is again a worst case look at the models and the average blade error of the ROMs is significantly lower as can be seen in Figure 2.5. Figure 2.7 shows that while the standard ROM had a maximum percent error below 0.5% for the first 10 modes and below 1% for all but one of the remaining modes, the error-quantified ROM predicted much improved results nearly identical to the full model. Error percentages from the error-quantified ROM for the first twenty modes are below 0.1% error. The figure shows that the error-quantified ROM reduced the maximum percent error for all the first twenty modes by well over 75%. While the standard ROMs accuracy may be considered sufficient, the high sensitivity of mistuned response to variations on the order of its error indicates that the error-quantified model may be more appropriate.

### **2.5.2.2 Modal Force Results**

While frequency deviation has been a subject of study because of its relevance to frequency-based mistuning ROMs, mode shape deviation has received limited investigation. In this section the mode shape variations are not shown directly, instead the useful heuristic of modal force deviations are shown because of its role in forced response prediction. Modal force, the inner product of the mode shape and loading vectors, is the quantity on the right hand side of the modal equation of motion, and its variation has a 1:1 correspondence to forced displacement variation. Nominal unsteady loading predictions for a defined harmonic from a related IBR were used in the modal force calculation.

A modal force variation box-and-whisker plot for the as-measured IBR is shown in Figure 2.8. It is evident that these deviations are much larger than the frequency scatter. The first significant variation in modal force is shown at the fifth mode with an upper bound 29% larger than the average value. Considering the set of the first twenty modes, several

modes are observed with upper bounds near 20%, with mode fifteen notable for a 55% upper bound. These significant variations in modal force directly impact variation in airfoil forced response and these are not explicitly accounted for in current design or mistuning analysis practices. These variations are in addition to those blade-to-blade stress variations caused by mistuning, that should be accounted for to reliably predict forced response variations, and demonstrate the need for a eigenvector response ROM that accounts for geometry variation.

Figure 2.9 shows the blade-to-blade comparison between the full FEM, the standard, and error-quantified ROMs for the fifteenth mode modal force prediction. The fifteenth mode was selected because the as-measured airfoil results for this mode had the largest modal force variation, shown in Figure 2.8, and also has the largest error between standard ROM and full models as seen in Figure 2.11. Again, this shows the two ROMs at their worst. As seen in Figure 2.9, the standard ROM accurately captures the trend of modal force variation. The error-quantified ROM improves the approximation for nearly all airfoils, in particular the third, fourth, eighth, tenth, fifteenth, and sixteenth airfoil. These airfoils are the same that were shown to have the largest frequency error, also had the largest modal force error, and were also effectively accounted for by the error-quantified ROM.

The discrepancy calculated between the standard ROM and full FEM modal force solutions of the as-measured IBR are plotted with respect to the airfoil z-scores in Figure 2.10. Again as with the frequency results, principal component mode twelve shows a linear relationship between the error and airfoil z-score value. When compared to the frequency residuals of Figure 2.6, the linear relationship is still obvious but with more random variation.

Figure 2.11 illustrates the maximum error between the full FEM and ROMs for the first twenty modes. This maximum error is obtained for each mode by computing the absolute difference between standard ROM and full model, dividing by the full model value for each

of the sixteen airfoils, and plotting only the maximum of the sixteen errors. It is initially observed that the errors are significantly larger than for frequency, but this is not unexpected as the variations in modal force are significantly larger. For the first twenty modes, the standard ROM performs adequately with more than half the modes below 5% and most remaining modes below errors below 10% with the exception of the thirteenth, fifteenth and nineteenth modes. The error-quantified ROM reduces the error for these modes in addition to significant error reduction for the fifth mode. The error-quantified ROM reduces the error for these modes by over 50%. In general it is seen that the error-quantified model is providing a reduced benefit to the ROM when compared to the frequency results, but still enables more accurate modal force prediction for the first twenty modes within 6% of full model results. The remaining error can be accounted for with the error-quantified ROM random error term.

### **2.5.2.3 Forced Response Results**

While the variation in modal force is a significant contributor to forced response, it only accounts for variations in mode shape displacements. Variations in modal stress and frequency will also impact forced response variation and this section's results account for those effects. The maximum forced stress variation box-and-whisker plot is shown in Figure 2.12. Considering the set of the first twenty modes, several modes are observed with upper bounds near 20%, with mode fifteen notable for a 68% upper bound.

Comparison of these plots to the modal force variation results of Figure 2.8 shows similar magnitudes of variation for each mode but closer inspection shows differences on many modes. Mode nine's upper bound on airfoil forced response is 38% greater than average airfoil while its modal force upper bound was 19%. Mode fifteen shows a 68% increase in upper bound stress while the modal force upper bound variation for the mode was 55%. These 19% and 13% increase in stress upper bounds is caused by variations in the maxi-

imum modal stress caused by geometric deviations. This demonstrates the importance of accounting for modal stress variations in the developed ROMs.

The maximum forced stress blade-to-blade prediction is compared between the standard ROM, error-quantified reduced-order ROM, and full model in Figure 2.13. The fifteenth mode was selected because the as-measured results for this mode, shown in Figure 2.8, had the largest forced response scatter and also has the largest error between full models and standard ROM, shown in Figure 2.14. Figure 2.13 shows that the standard ROM does a good job representing the full model results, and accurately captures the blade-to-blade trend in forced stress values. The figure also shows that the error-quantified ROM improves the approximation for all airfoils, in particular the third, fourth, eighth, tenth, fifteenth and sixteenth airfoil.

The *a posteriori* training data used to create the error quantified reduced-order model is not shown but is almost identical to Figure 2.10.

Figure 2.14 plots the maximum error between the ROMs and the full models for the first twenty modes. For these modes, the standard ROM does well with most errors below 5%, with the exception of modes five, fifteen, and sixteen. The error-quantified ROM reduces the error for many of the larger errors in this range, particularly modes five, fifteen, and sixteen where error is reduced by nearly 50%. In general it is seen that the error-quantified model is not as effective in correcting for bias as it was for frequency, but still enables forced response force prediction for the first twenty modes within 5% of full model results. The remaining random error can be accounted for with the random error term.

### 2.5.3 Approximation Error Root Cause and Improved Physical Model

The results showed a modeling error which was identified and accounted for by the EQ modeling approach. While an acceptable approach, it is still beneficial to increase the accuracy of the approximation through an improvement in the physics of the approximation. The need for improvements in accuracy becomes evident from the results in Chapter 4. An approximation improvement was enabled by investigating the accuracy of the semi-analytical calculated sensitivities. In addition, the variation in frequency sensitivities and values across the design parameter space are investigated to show the nonlinearity of modal response across the range and show the applicability of the linear approximation.

After a thorough investigation it was found that errors in the approximation were associated to a non-converged finite difference step size in the semi-analytic sensitivity calculations. The semi-analytical approach is based on approximating the change in frequency by projecting the stiffness,  $\Delta K$ , and mass matrix,  $\Delta M$ , variations to the modal domain using the unperturbed mode shape,  $\phi_i$ . This approximation is accurate when the difference between  $\phi_i$  and  $\Delta\phi_i$  is small. At very small step sizes the difference between  $\phi_i$  and  $\Delta\phi_i$  is indeed small. A numerical finite difference approach for modal sensitivity calculations were less sensitive to step size. It was found, for the 1<sup>st</sup> mode, with the numerical finite difference approach that the variation in response with respect to changes in the geometric parameters is nearly linear. As such, use of large step sizes in the numerical approach produced accurate results. Figure 2.15 shows the convergence plot between the numerical and semi-analytical sensitivity calculations for the first bending mode. It is seen that the numerical approach predicts the same sensitivity regardless of step size, whereas the semi-analytical approach converges on the sensitivity at a step size of 0.00025. The standard ROM was constructed using a step size of 0.05 and the error in sensitivity is evident. Even



with these sensitivity errors, the standard ROM was able to predict the full FEM results with good accuracy. With the corrected sensitivities, the results are very similar to the EQ ROM. While the variation in response for the 1<sup>st</sup> mode was nearly linear, this was not the case for higher modes.

The variation of frequency sensitivity with step size for the 11<sup>th</sup> mode is shown in Figure 2.18. Results from the 11<sup>th</sup> mode are selected because it will be investigated further in Chapter 4. The figure shows, unlike the 1<sup>st</sup> mode results of Figure 2.15 that the sensitivity is not constant at various step sizes. This in part is due to the fact that a larger range of geometry variation has been considered. This variation in sensitivity indicates that the linear approximation will have increased error away from the forward differencing location.

As a final analysis of approximation error, Figure 2.17 shows compares the linear approximation and FEM results for the 11<sup>th</sup> mode given the perturbation of only the 1<sup>st</sup> principal component model. The forward differencing point was taken at a step size of 0.05 and it is seen that between 0 and 0.05, the accuracy of the approximation is excellent. Below 0 step size and above 0.05 it is shown that the approximation underpredicts the FEM frequency. This nonlinear response is responsible for the remaining errors in the 11<sup>th</sup> mode approximation. The comparison of the approximate to FEM frequencies for the 11<sup>th</sup> mode are shown in Figure 4.18 and the consistent underprediction of the approximation is evident. This demonstrates a need for improved approximation approaches that account for the nonlinear variation of modal response with respect to geometric parameters.

It is concluded that the semi-analytic sensitivities accurately predict sensitivities at a reduced computational cost compared to a numerical approach. The numerical approach is still clearly attractive because it is not dependent on the assumption of equality of  $\phi_i$  and  $\Delta\phi_i$ . Because of this, and the reduction in geometric parameters that reduces the computational requirements of a numerical approach, the numerical approach is used in Chapter 4. Use of the semi-analytical approach will be more valuable when a larger number of finite

difference calculations would be required. This could occur when a larger number of retained PCA modes are required or multipoint approximations are used. It is also concluded that nonlinear approximations are required for improved approximation accuracy. Linear approximations are used in Chapter 4, which will further identify the need for improved modal approximations.

## 2.6 Conclusion

This effort demonstrated the impact of geometry deviations from design intent on the modal and forced response behavior of airfoils. Significant variations were shown in frequency and these variations are significant to mistuned rotor response. The ability to predict these efficiently with the developed ROMs can significantly improve current mistuning analysis and design procedures. It was shown that mode shape variations were more sensitive than frequency variations and these led to large variations in forced response. These variations are not currently accounted for in design, but the developed ROMs begin the process to do so. The ROMs are based on PCA reduction in geometry parameters and an eigensensitivity-based approximation to reduced response solution times. The error between this model and full models was quantified, and a linear regression model was demonstrated to quantify which parameter was contributing to error. Knowledge of this relationship led to an improvement in the model accuracy.

Further analysis of the errors led to the identification of physics-based model errors that were reduced through the use of numerical rather than semi-analytic sensitivity calculations. It was also identified that improvements to accuracy can be made in the future by considering the nonlinear variation of the modal response. The results in Chapter 4 will demonstrate the need for such improvements.

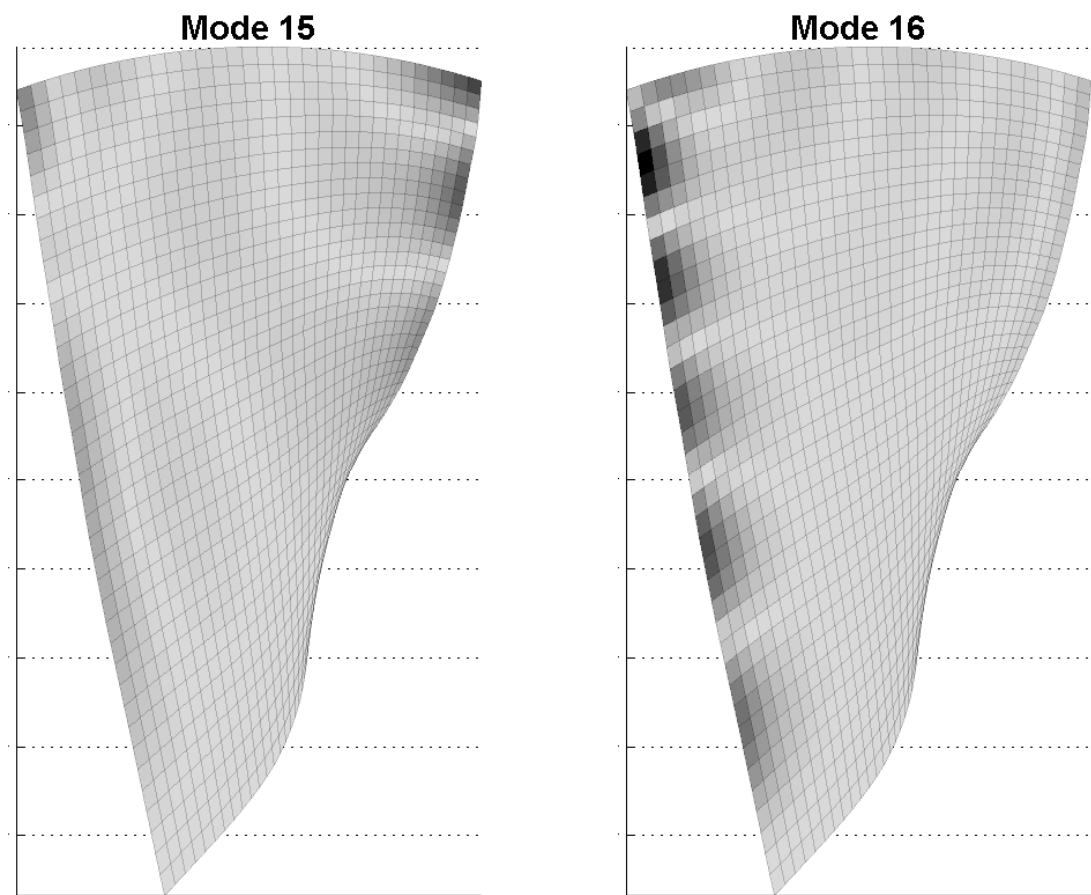


Figure 2.1: Mode Fifteen and Mode Sixteen

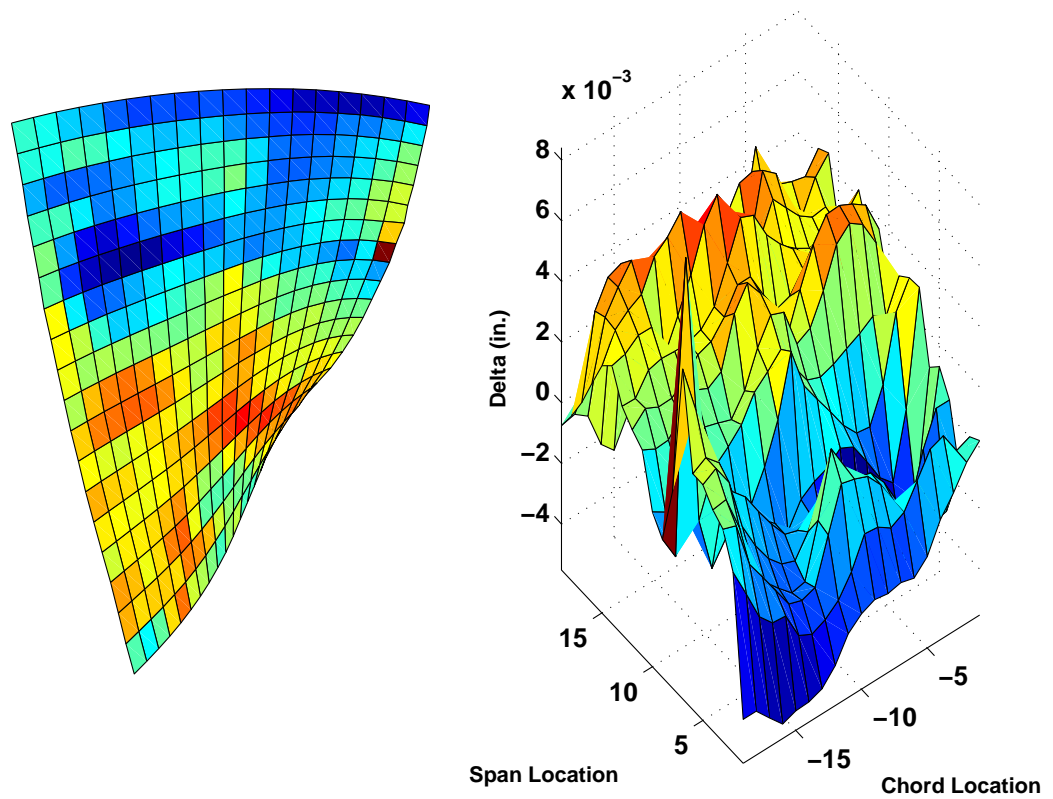


Figure 2.2: Airfoil Surface Deviation (Blade 1)

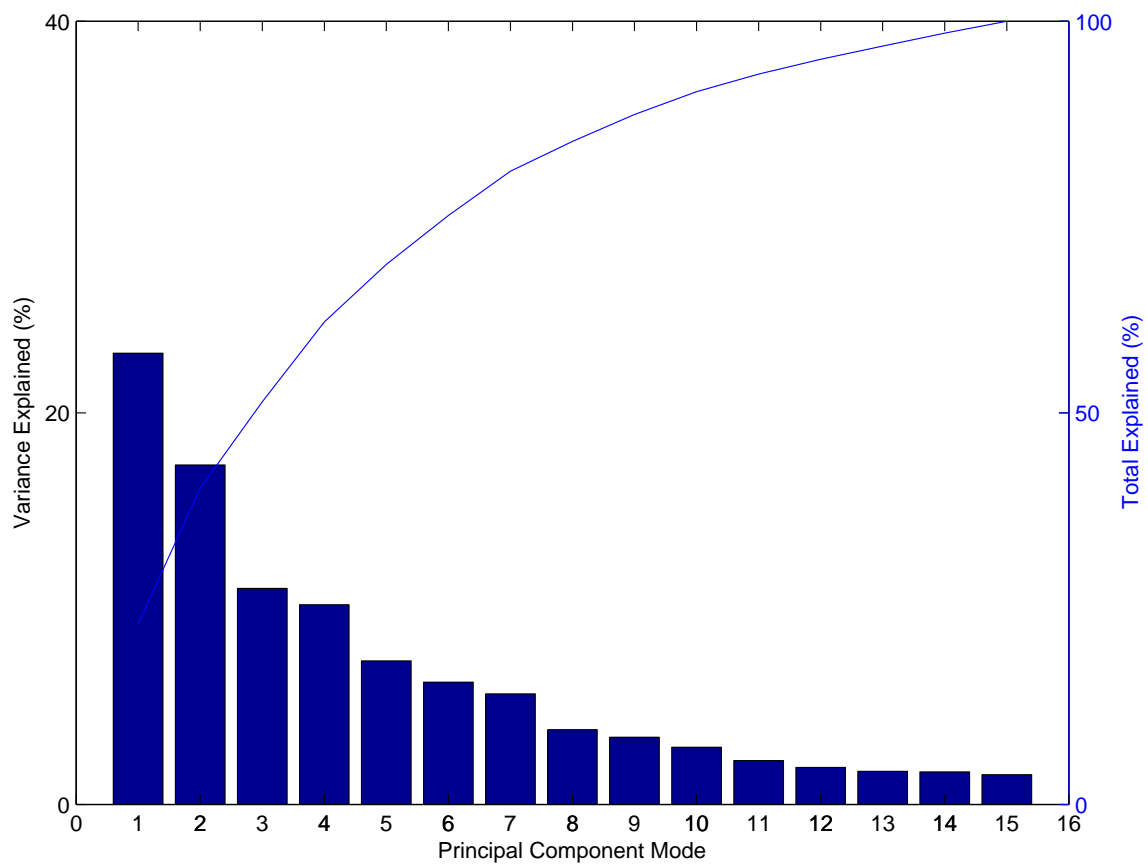


Figure 2.3: Total Variance Explained by Principal Components

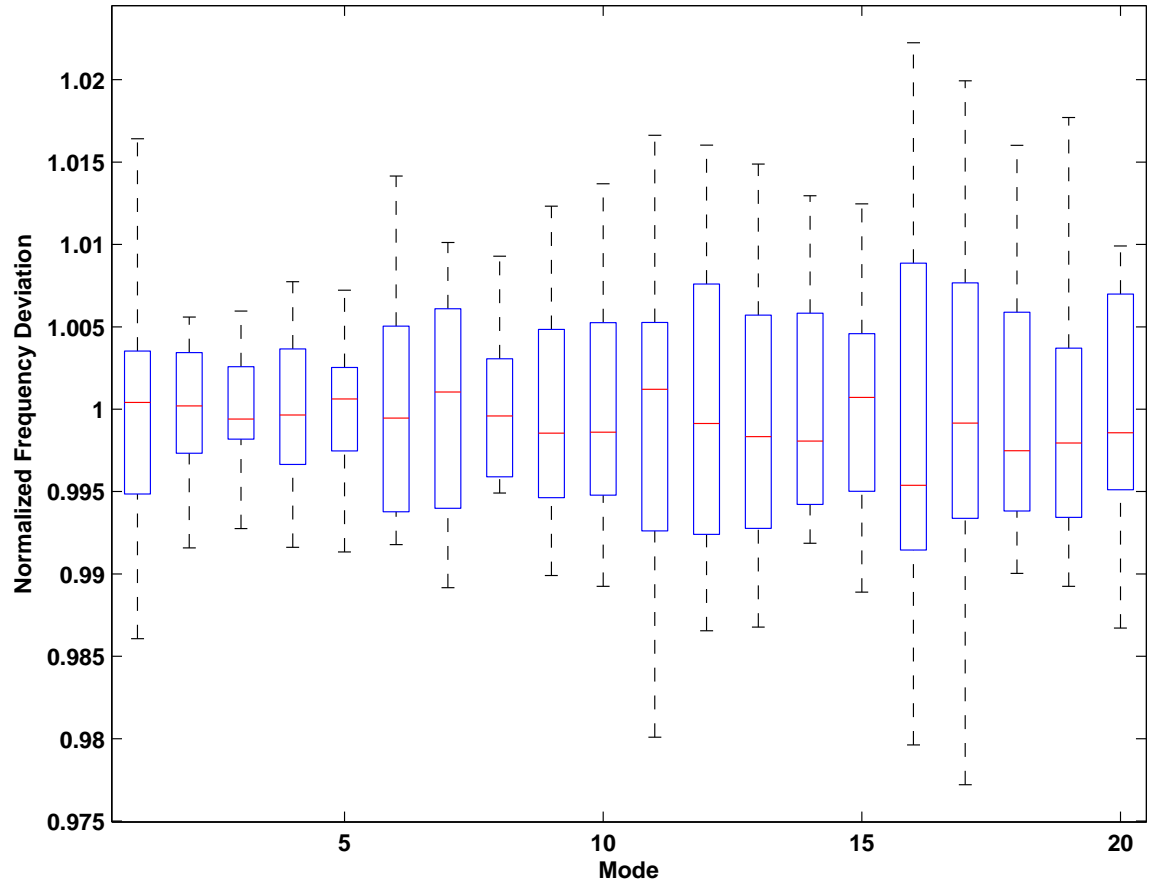


Figure 2.4: Airfoil Frequency Variation

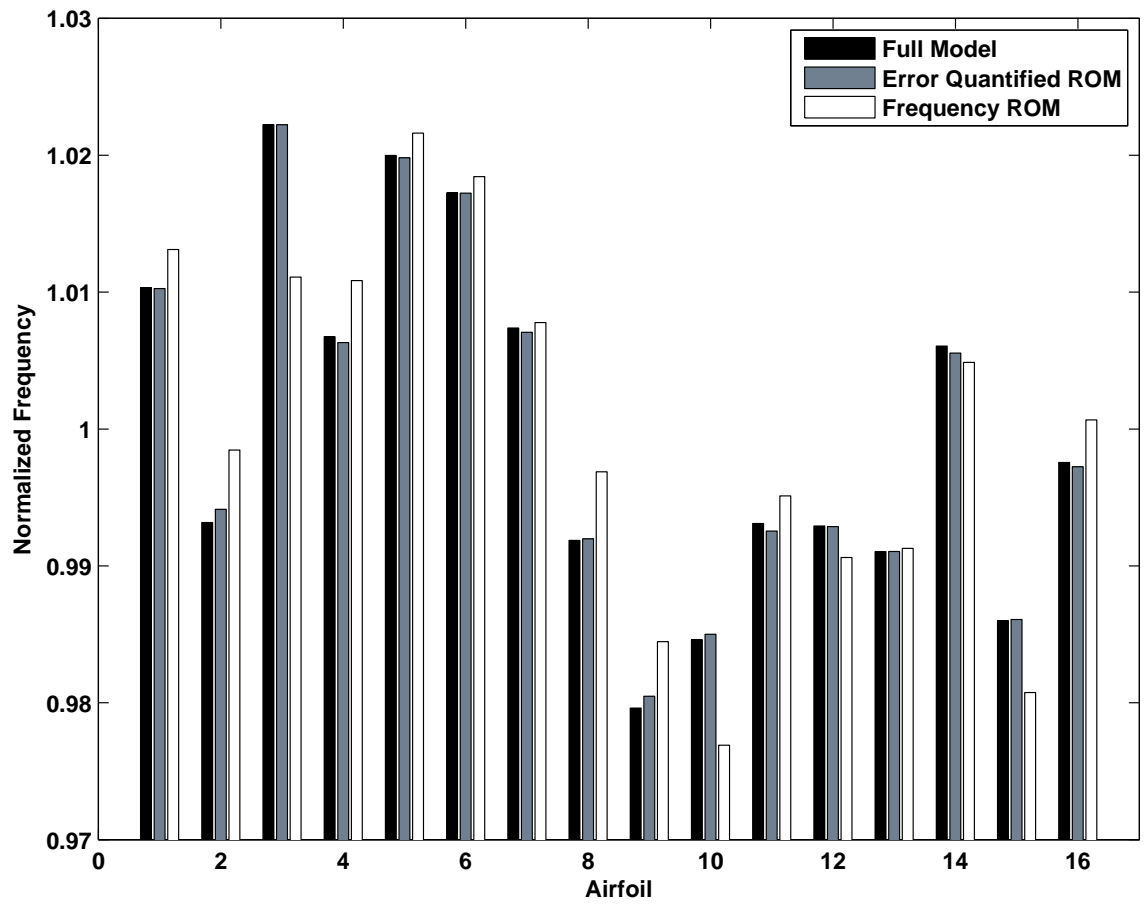


Figure 2.5: Frequency Prediction Comparison (Mode 16)

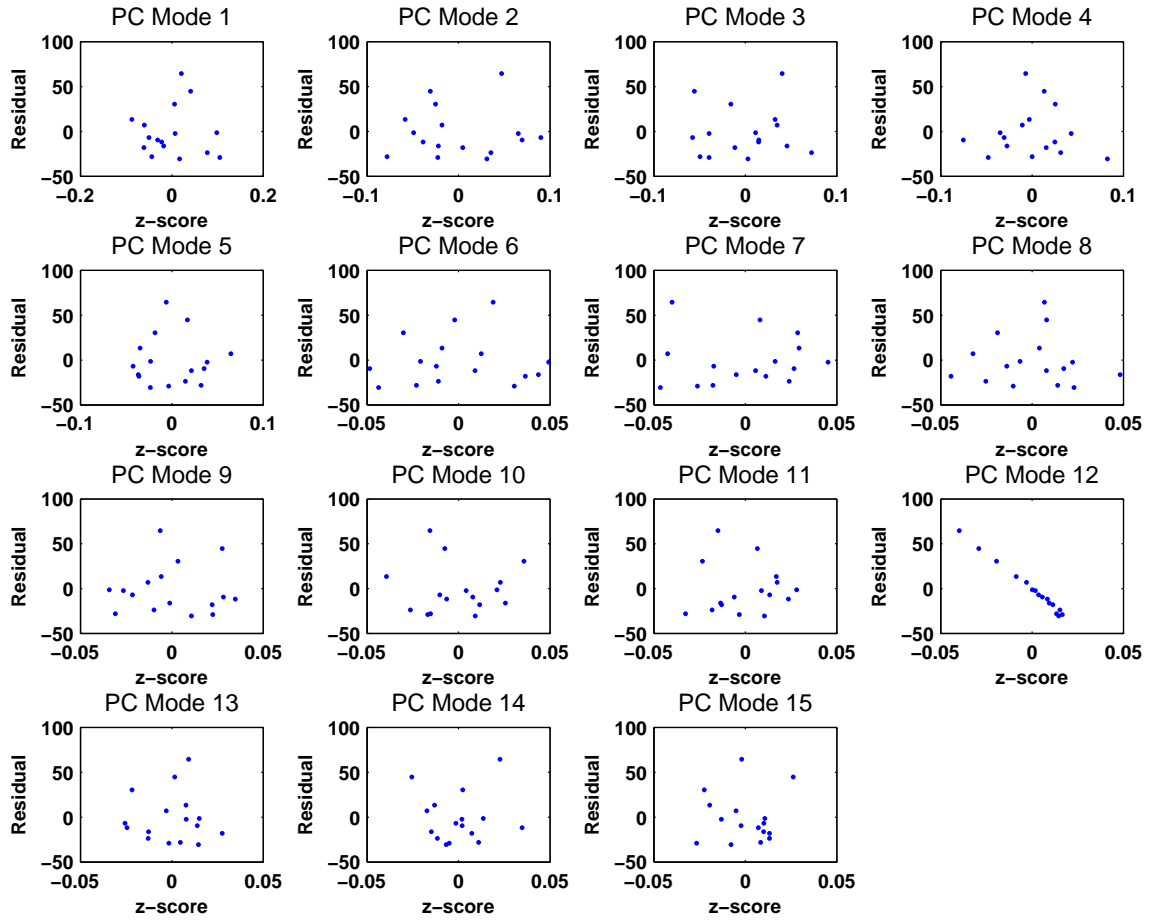


Figure 2.6: Correlation of PC Mode Parameters and Residual (Mode 16)



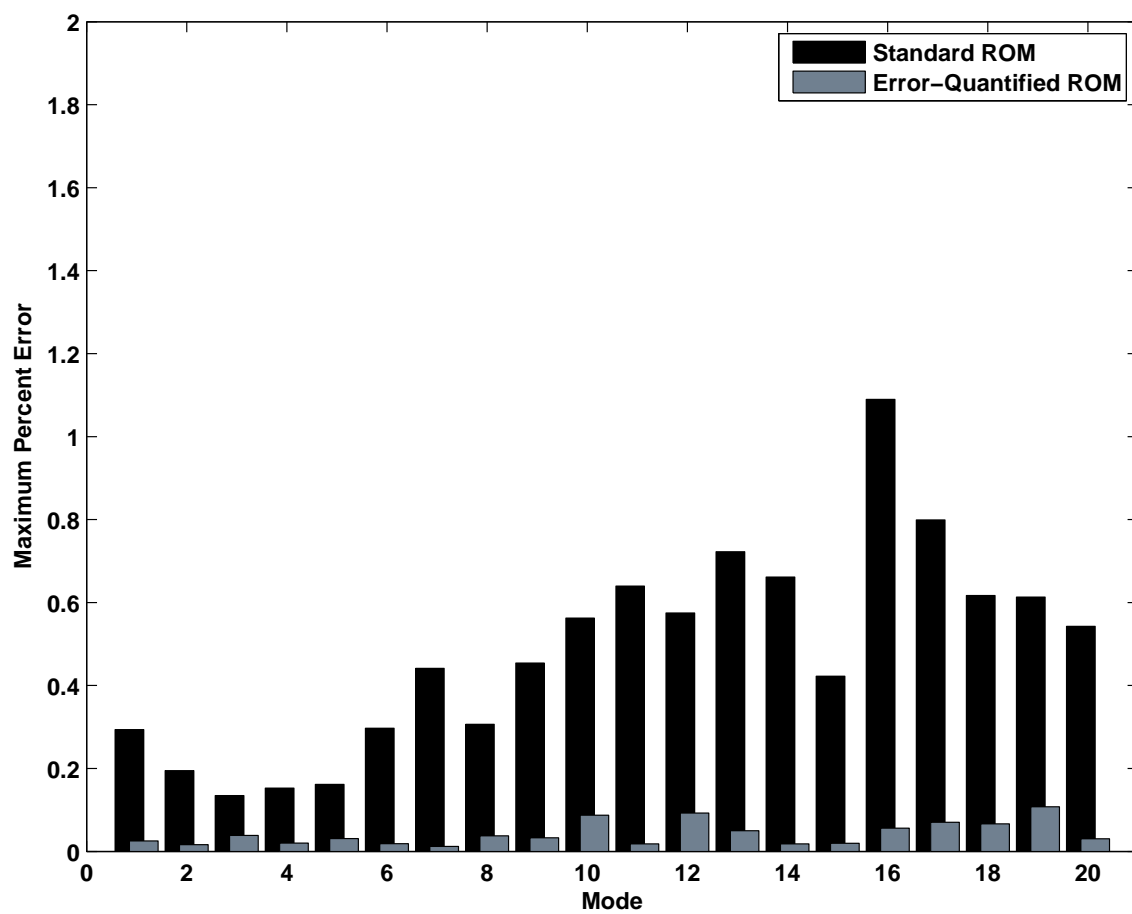


Figure 2.7: Maximum Error Calculation for Airfoil Frequency

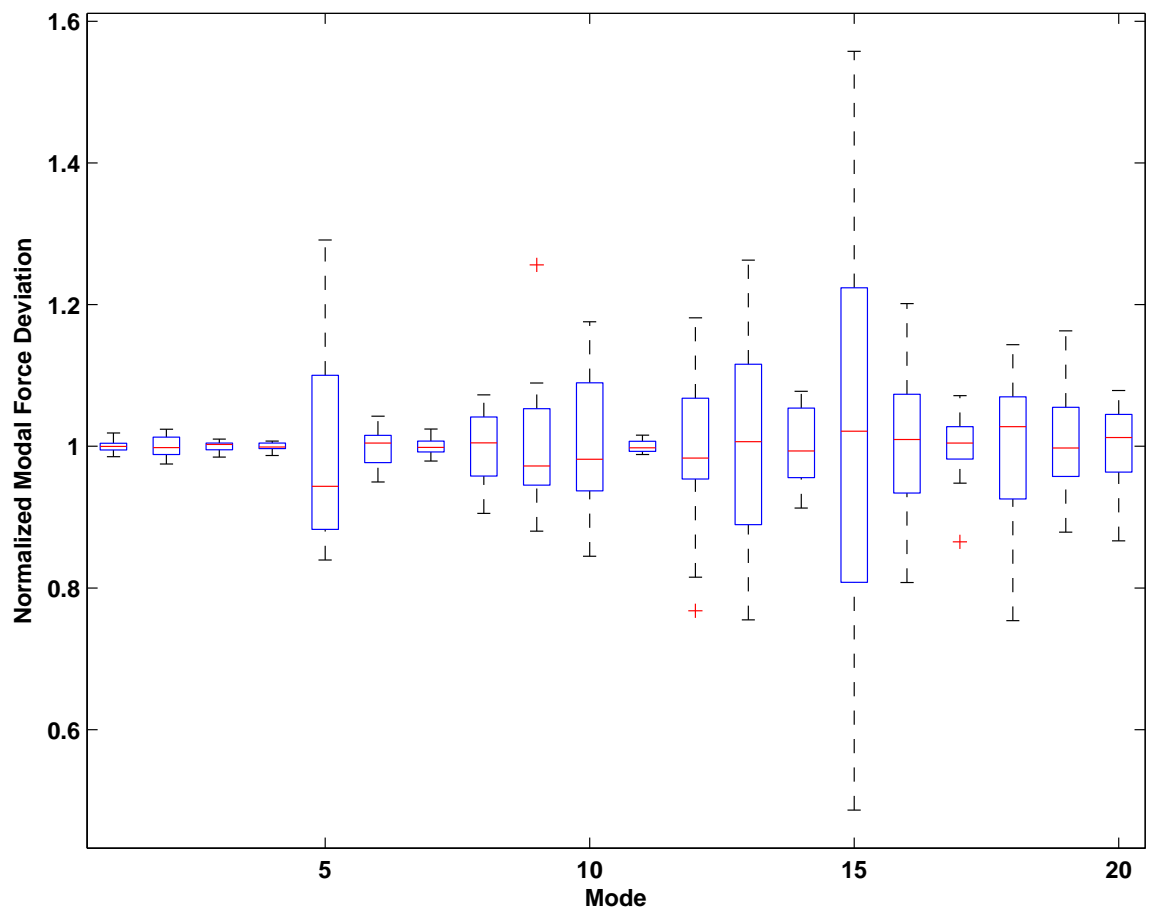


Figure 2.8: Airfoil Modal Force Variation

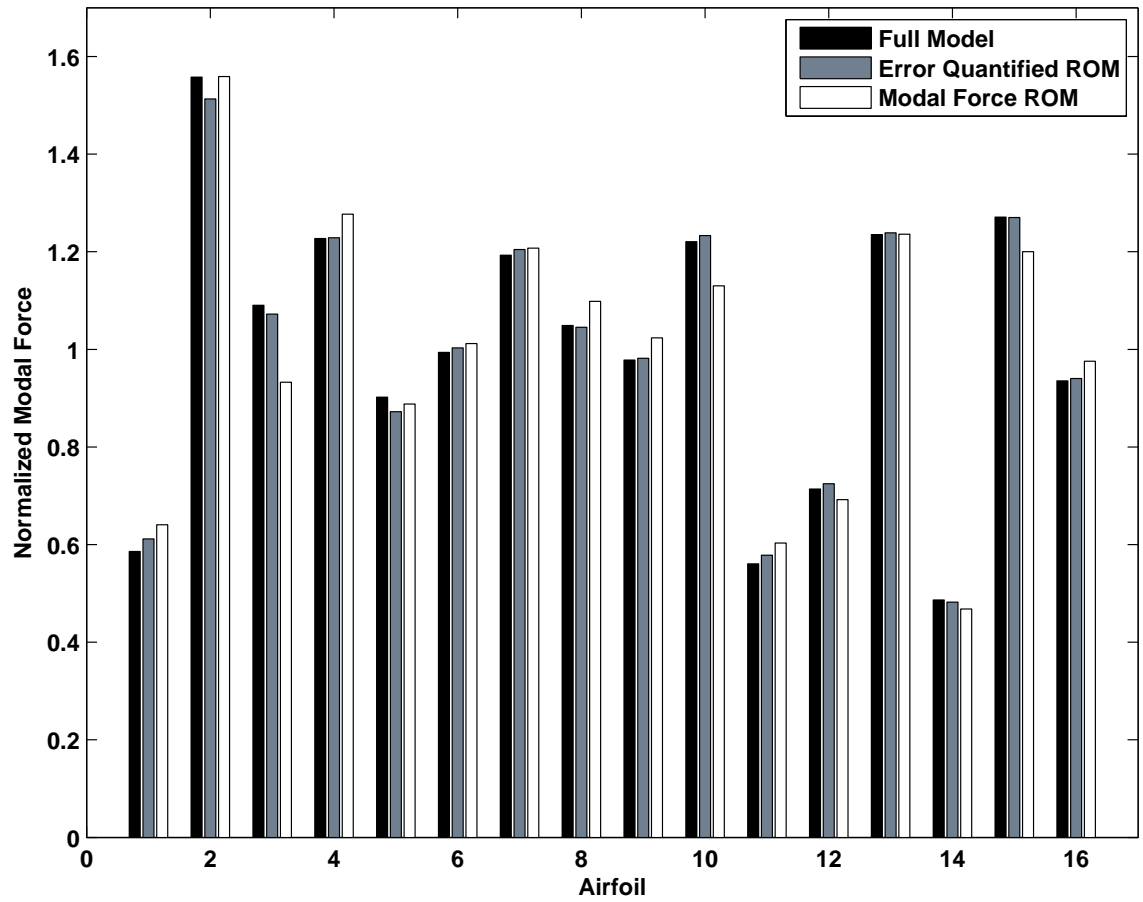


Figure 2.9: Modal Force Prediction Comparison (Mode 15)

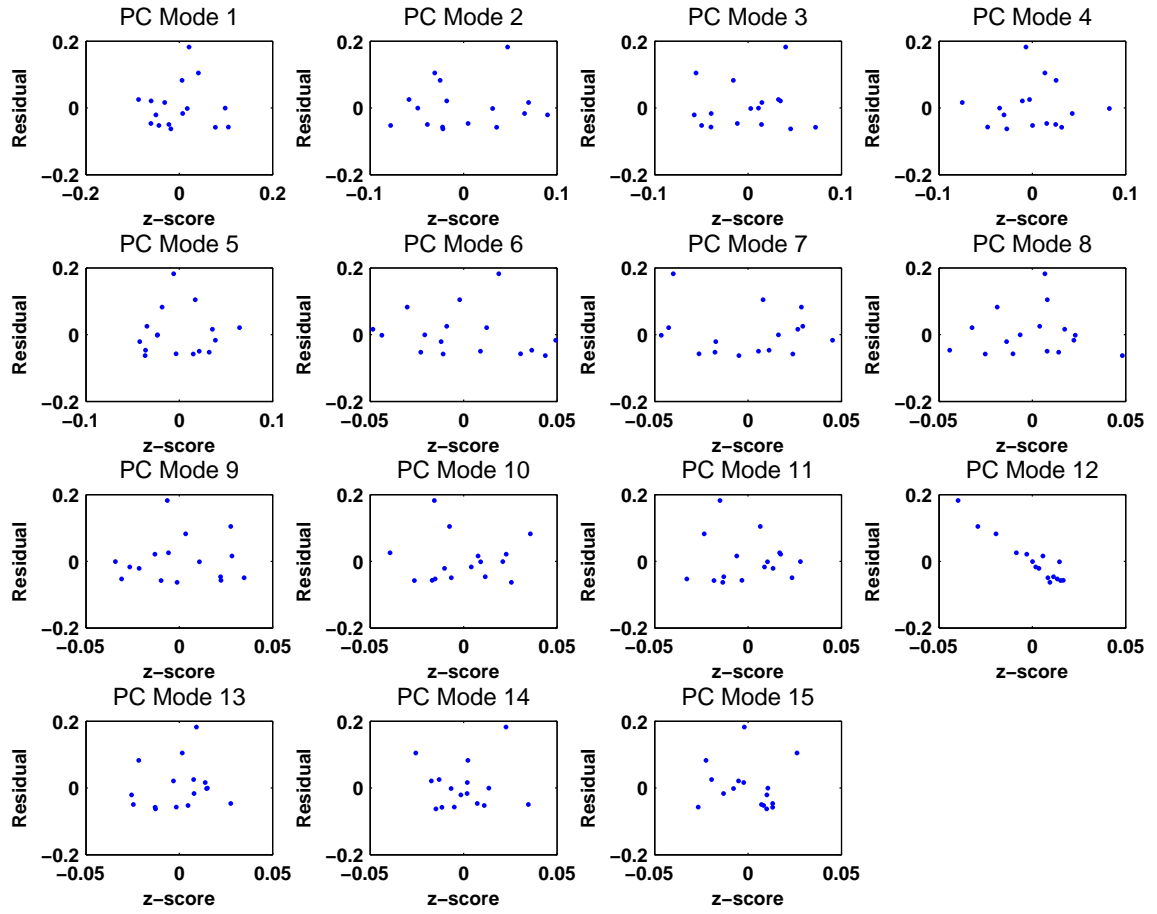


Figure 2.10: Maximum Error Calculation for Airfoil Modal Force (Mode 15)

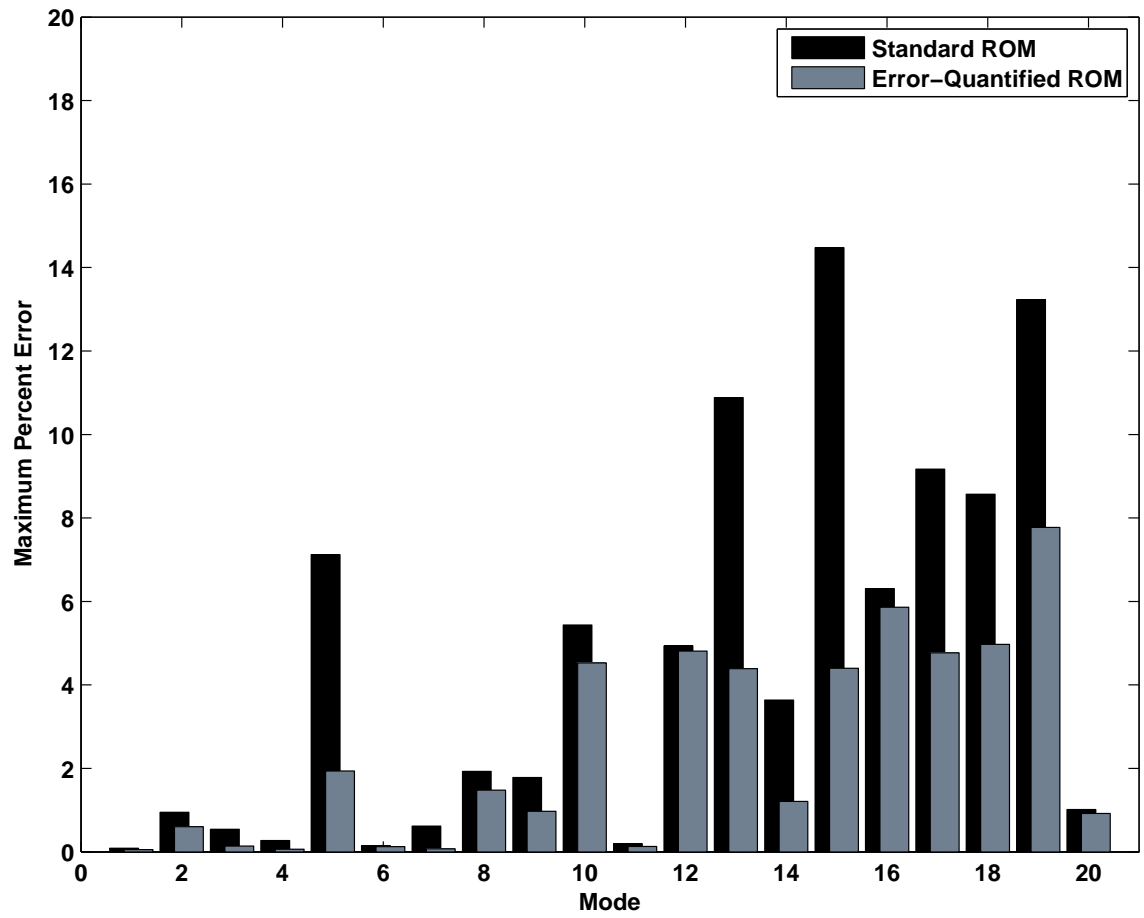


Figure 2.11: Maximum Error Calculation for Airfoil Modal Force

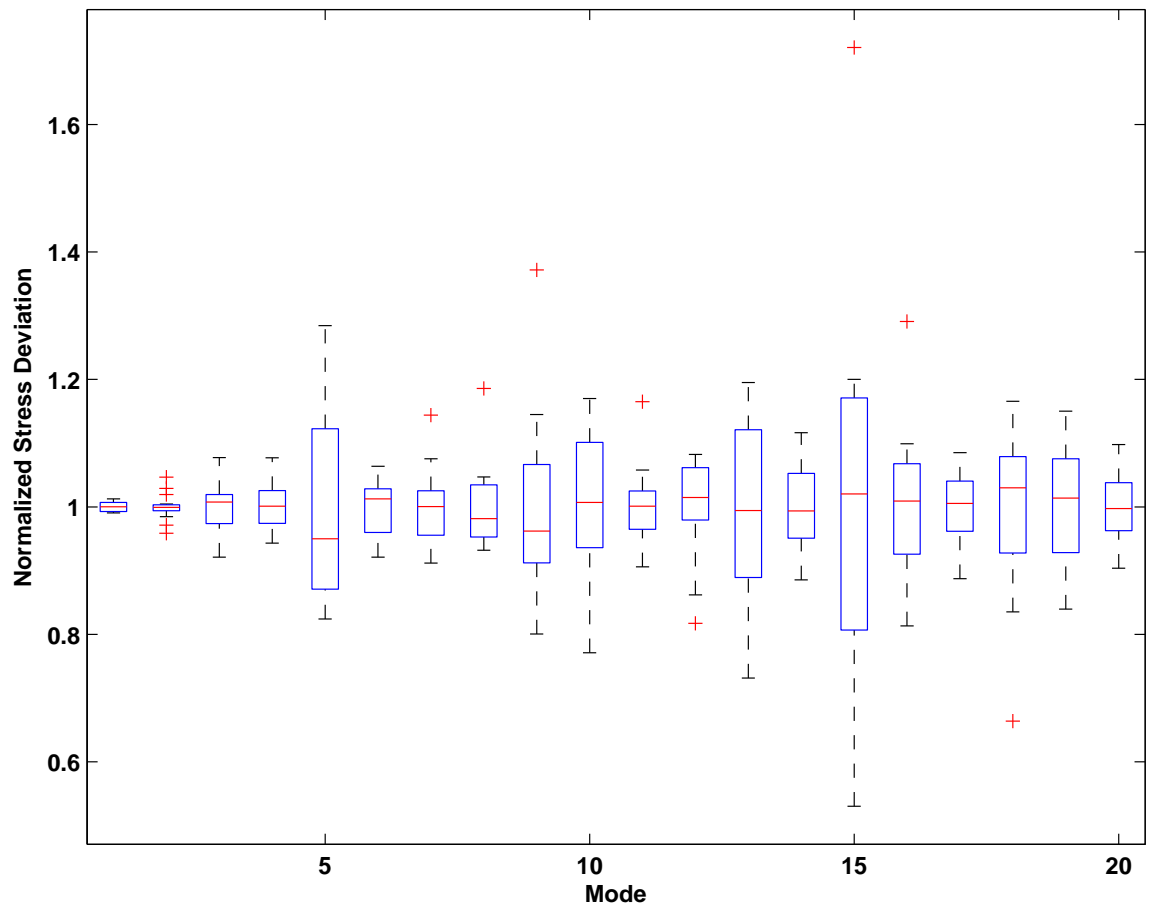


Figure 2.12: Airfoil Forced Stress Variation

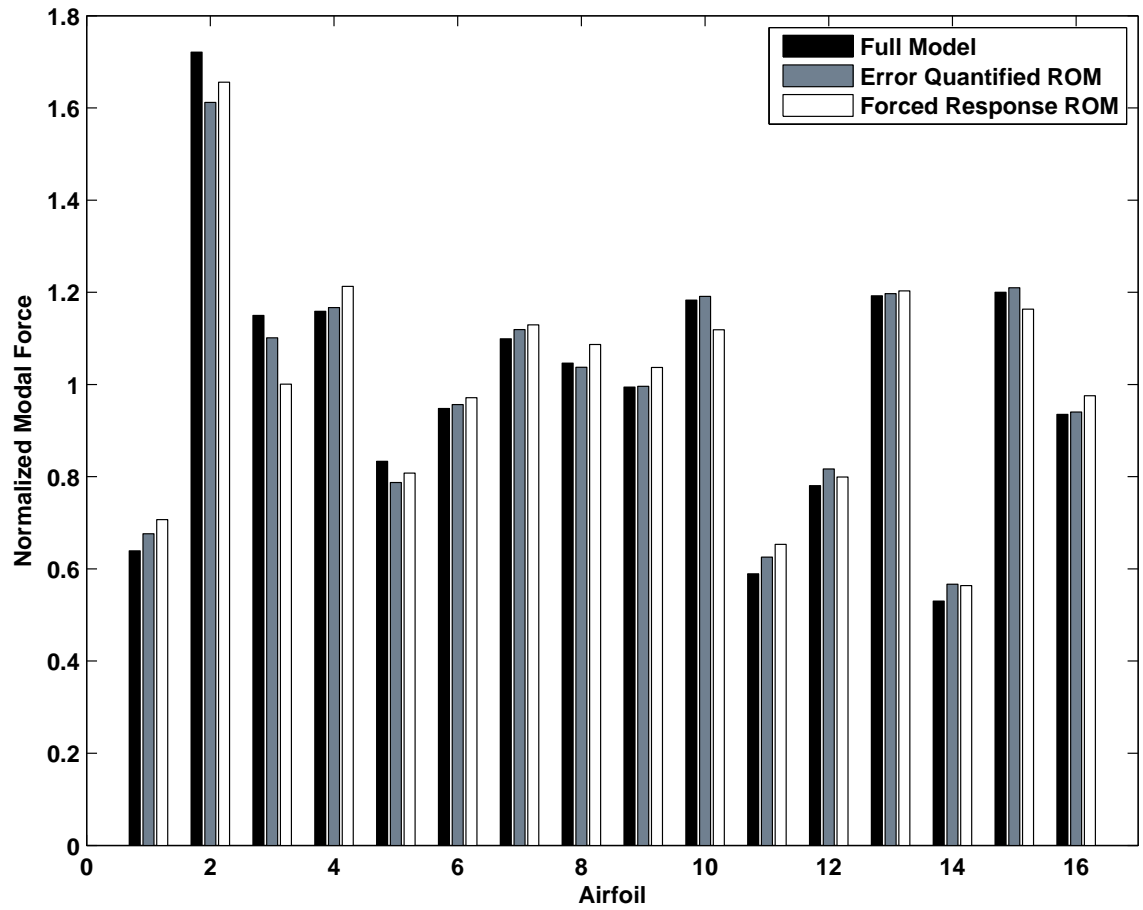


Figure 2.13: Forced Stress Prediction Comparison (Mode 15)

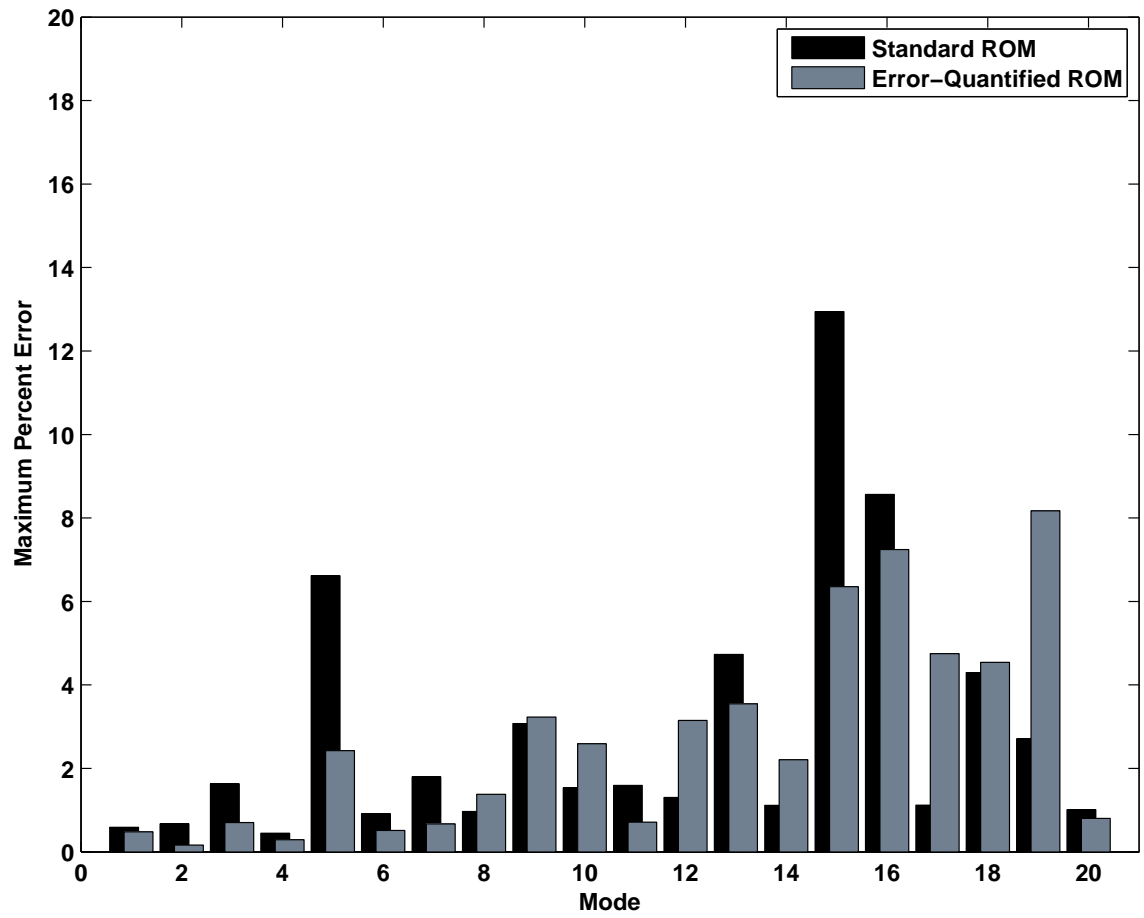


Figure 2.14: Maximum Error Calculation for Airfoil Forced Stress



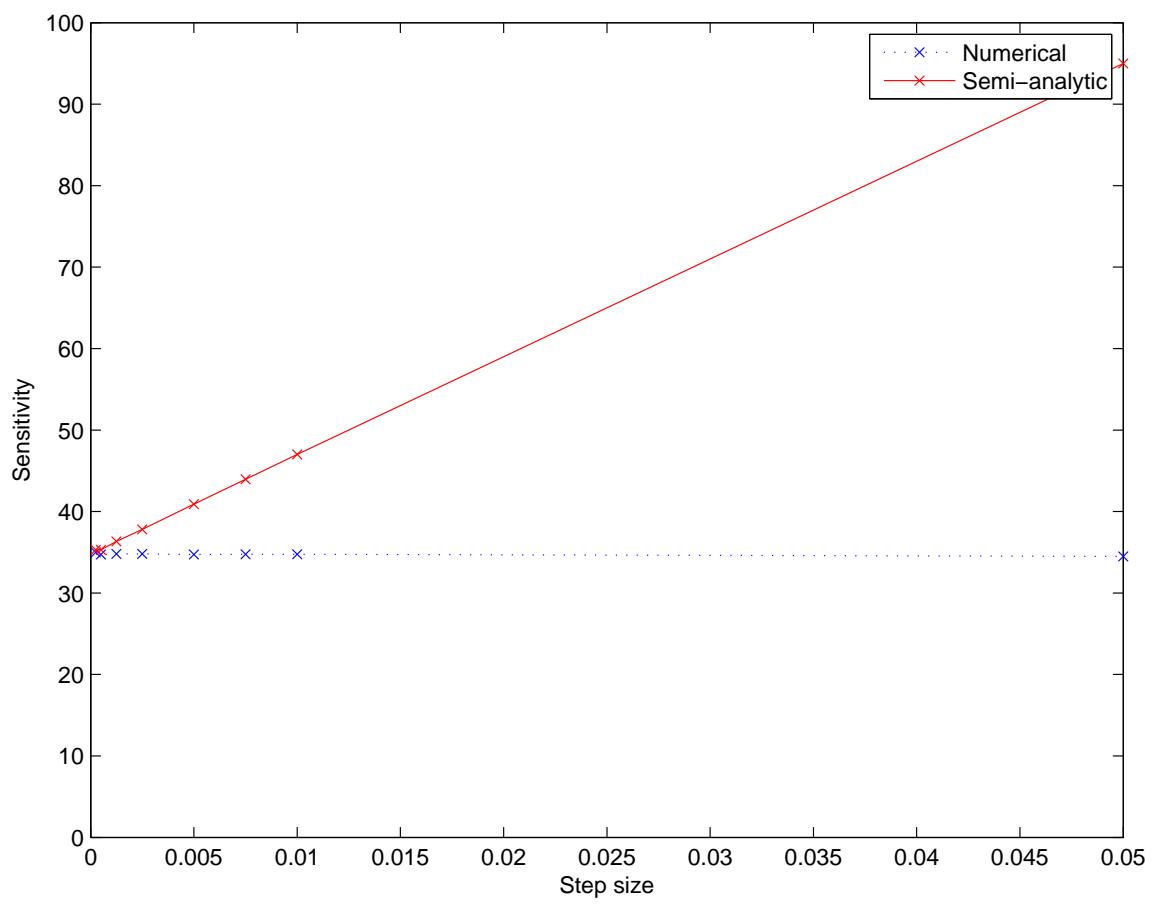


Figure 2.15: Sensitivity Convergence Plot

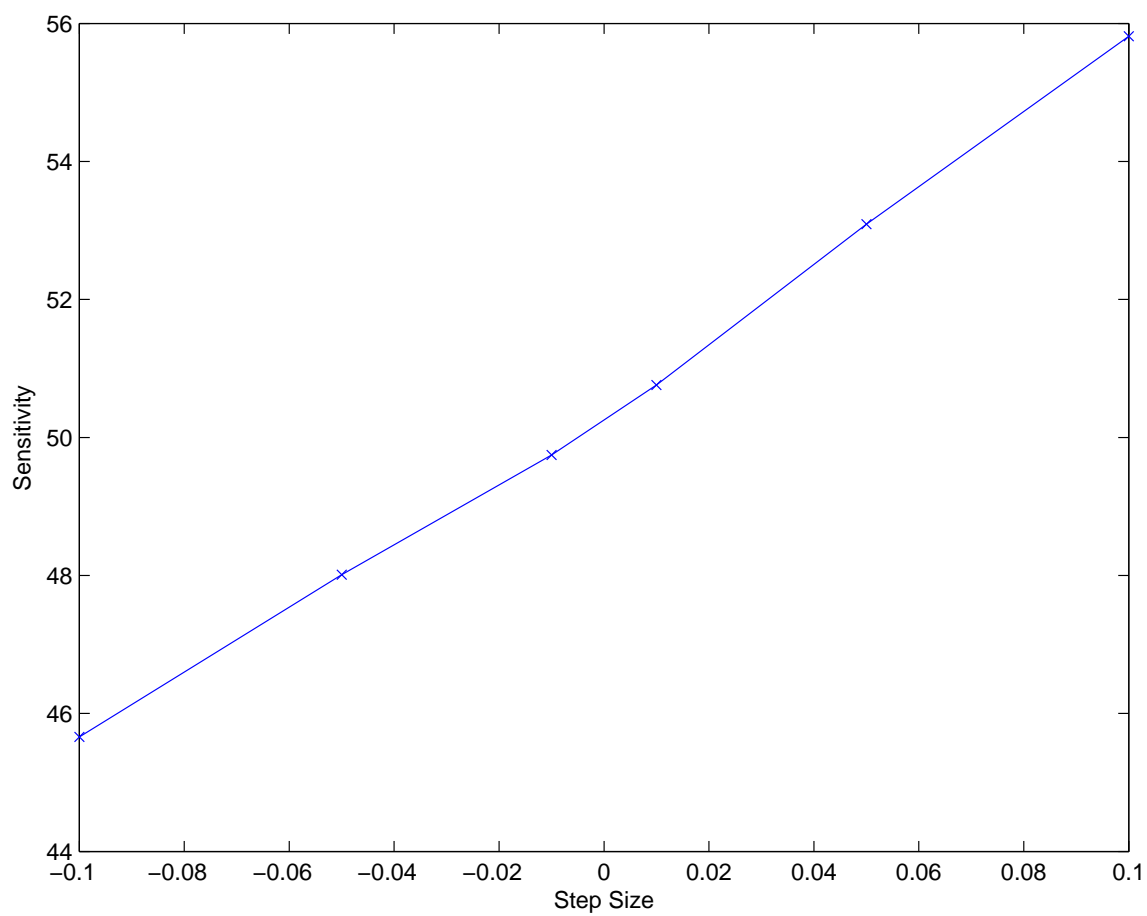


Figure 2.16: Step Size Sensitivity Variation

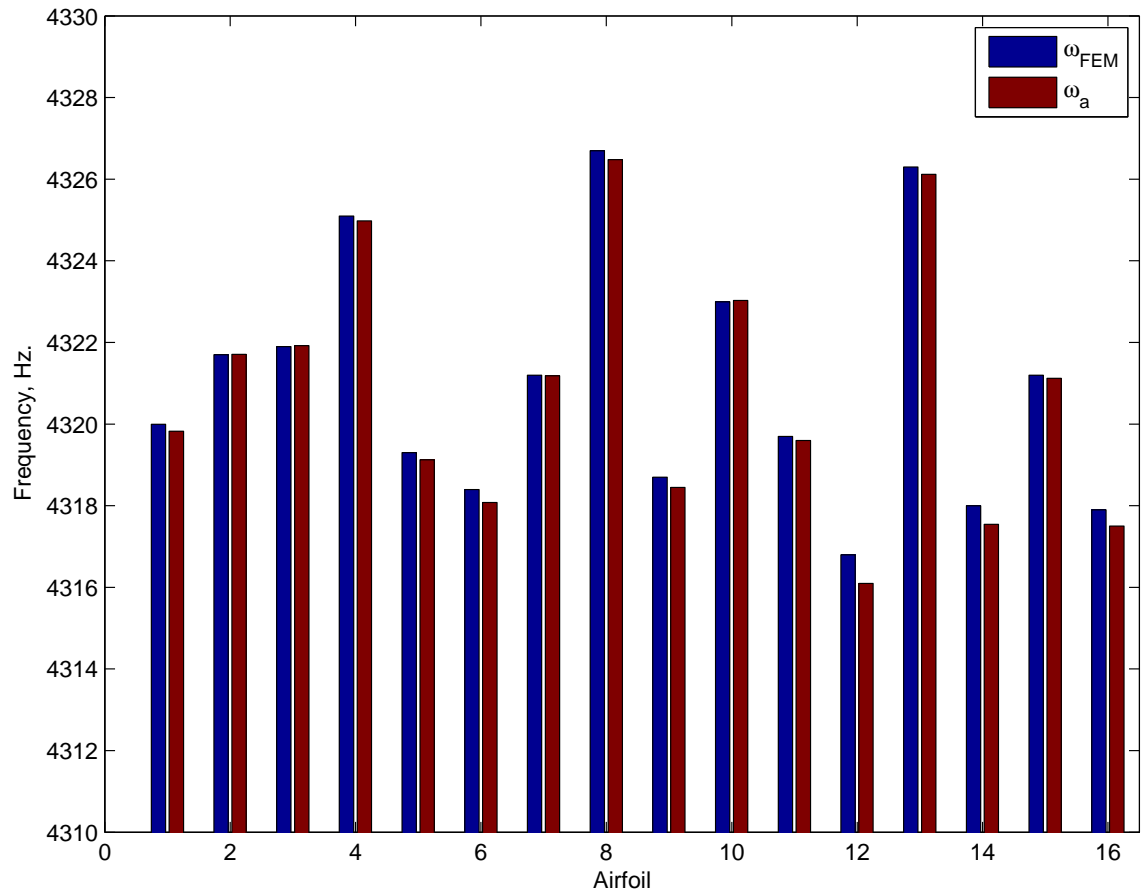


Figure 2.17: Frequency Comparison for Single PCA Mode Variation

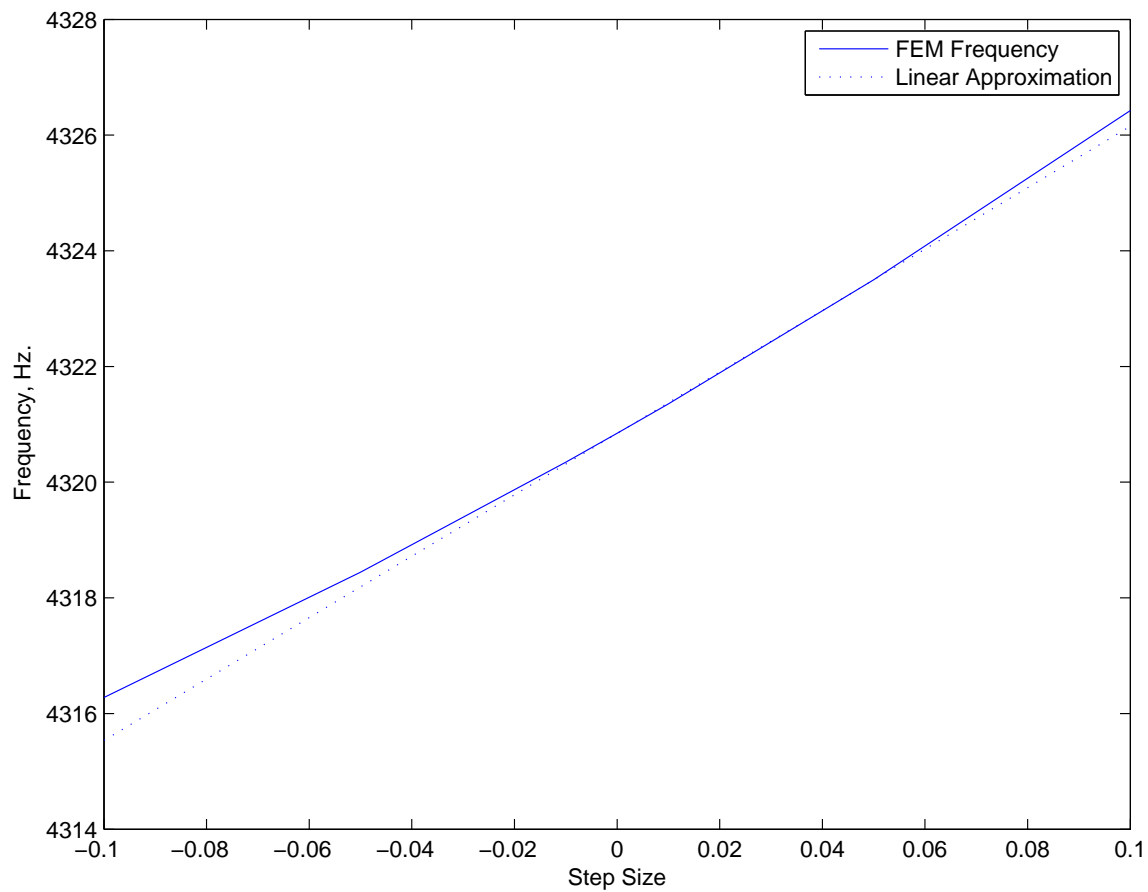


Figure 2.18: First PCA Mode Frequency Perturbation

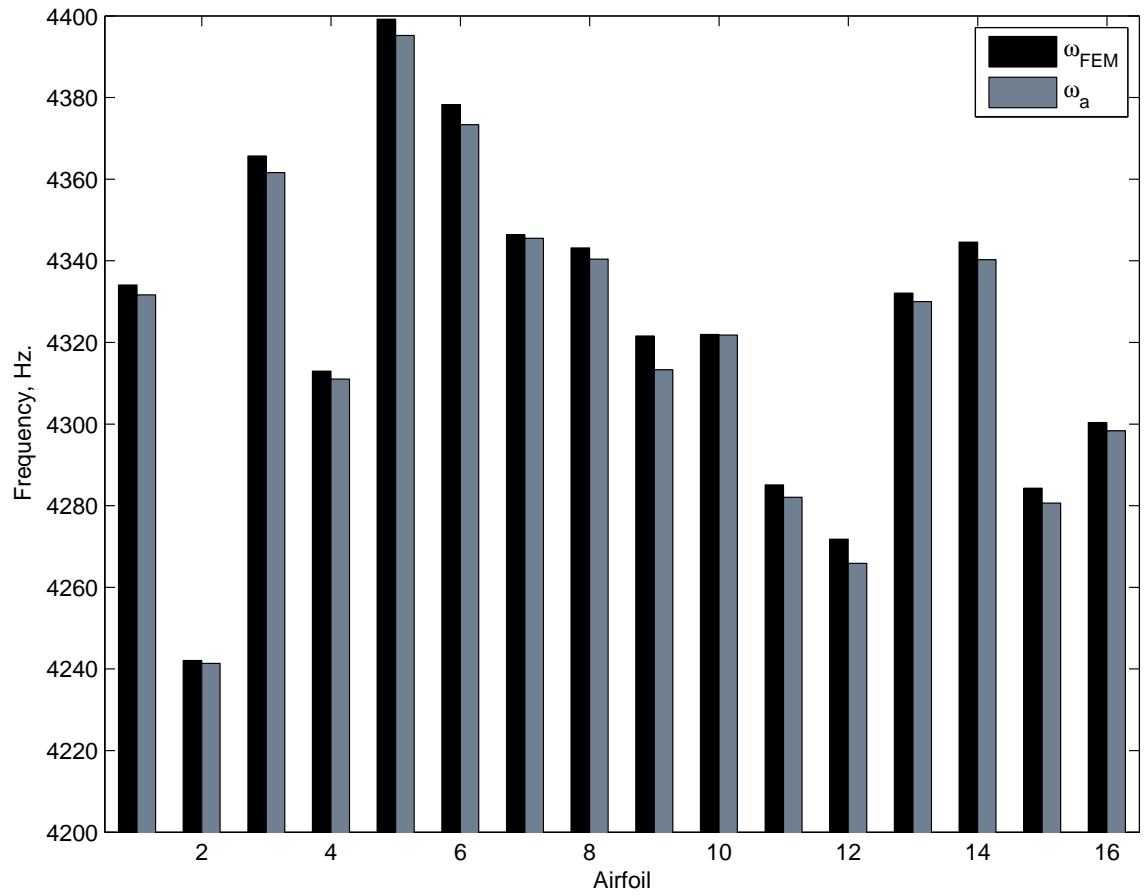


Figure 2.19: Modal Stiffness Approximation Results - Mode 11

# **3 Probabilistic Gradient Kriging to Efficiently Predict Failure Probability Confidence Intervals**

## **Abstract**

Probabilistic methods predict response variations caused by the randomness of a system's defining parameters. While it is generally assumed that the parameter statistics are known absolutely, they are usually an estimate taken from a small sample. The inherent variability of this process creates an uncertainty in the sample statistics that is quantified with a sampling distribution and statistical confidence intervals. Because probabilistic failure calculations are based on these uncertain statistics, the predicted failure probability itself becomes uncertain. Calculating the failure probability distribution requires a computationally expensive nested inner- and outer-loop reliability calculation. This work develops a failure probability approximation method for the inner-loop to efficiently quantify the effect of statistical parameter uncertainty on failure probability distributions and confidence bounds. The new failure probability approximation approach, Probabilistic Gradient Kriging, is based on an augmented Kriging approach that uses both the function values and efficiently calculated probabilistic sensitivities. Fatigue crack growth and rotor burst

demonstration problems are used to compare the polynomial response surface method, Kriging, and the new Probabilistic Gradient Kriging method. Results show that the new method can fit surfaces extremely well, reduce approximation error by an order of magnitude, and enable efficient statistical parameter uncertainty propagation. It is also shown that the uncertainty in statistical estimates from small samples can cause dramatic variations in predicted failure probability and should be accounted for to ensure system reliability.

### 3.1 Introduction

Probabilistic analysis methods predict reliability from a probability-based definition of a system's defining parameters. These parameters are described as probability density functions (PDFs) defined by distribution type and statistical parameters. It is typically assumed that the statistical parameters are known without uncertainty and that the population statistics have been ideally quantified. In reality, because of the limited data sets used to quantify statistical parameters, there is quantifiable uncertainty between sample and population statistics. This uncertainty can be modeled using a frequentist or Bayesian approach that leads to probability or likelihood definitions of the statistical parameters. The impact of this additional level of uncertainty can be calculated using a nested reliability calculation that requires outer-loop samples from the statistical uncertainty and inner-loop samples from conditionally defined PDFs of the system's defining parameters. Over many samples, the failure probability distribution is predicted from which confidence bounds can be quantified. The nested Monte Carlo Simulation (MCS) can be computationally expensive, since each outer-loop sample is itself a MCS. Clearly there is a need for a more efficient approach.

Early works in propagating statistical uncertainty were based on reliability methods using the safety index. Der Kiureghian and Liu demonstrated the prediction of mean, median,

maximum likelihood estimates, and bounds of a safety index from uncertain statistical parameters [70]. Torng and Thacker calculated safety index bounds at specified confidence intervals using an iterative approach and, in a later effort, approximated the variation of the safety index using linear Taylor series expansion [72, 73]. The works both showed significant sensitivity of the safety index to uncertainty in statistical parameters. Mehta et. al. assessed these approaches in addition to a first-order approach developed by Wirshing [71], full nested MCS, and a regression approach where the response function is approximated with a response surface [74]. They concluded the full nested outer- and inner-loop approach to be the most accurate but had the obvious computational costs, and that the approximate methods were efficient but had potential accuracy issues. Venkataraman et. al. developed several approaches to calculate confidence bounds for the safety index that included nested MCS with a safety index conversion, local approximation of the safety index using MCS and approximate sensitivities, a linear response surface approximation of MCS sampling points, and a nested two-loop First Order Reliability Method (FORM) [75]. Each method was shown to predict a result within a few percentage points of each other.

These prior works based their reliability calculations on safety index calculations. While acceptable for many problems where a Most Probable Point (MPP) can be located and the limit state approximated with a first or second order surface, the use of MCS of failure probability can be more generally applied. The limitation of this approach is the cost required for MCS of the inner-loop of the nested calculation. Picheny et. al. developed a method for predicting a MCS predicted conservative estimate of failure probability based on the uncertainty in sample statistics using a single MCS simulation [78]. Their approach focused on providing a conservative estimate of the input statistics and using a single MCS reliability calculation to predict the conservative estimate. While valuable, the distribution is not predicted and the conservative estimate may not accurately reflect the true confidence interval. Cruse and Brown developed an efficient approach to propagate Bayesian statistical



uncertainty by approximating the inner-loop failure probability calculation using a failure probability response surface [79]. This surface was a function of the statistical parameters and developed using a Design of Experiments (DOE) training set of MCS predicted failure probabilities. While the quadratic response surface used was effective in the example problem, complex responses may require advanced approximation tools. Further, since each surface training point requires a full MCS, accurate and efficient regression techniques for a given set of training points are desired.

This effort develops a new failure probability approximation approach that accurately and efficiently computes probabilistic confidence intervals from uncertain statistical parameters. The new method is called Probabilistic Gradient Kriging, or the PGK method. PGK is an approximate surface approach that fits both function values and augmenting model information. In this work, the function values are failure probabilities and the augmenting data are failure probability sensitivities. Efficiency is enabled by using sampling-based probabilistic sensitivity calculations that calculate both failure probability and failure probability sensitivity to statistical parameters using a single MCS sample set. The new method is compared to response surface and Kriging approximations of the failure probability surface. It is shown that the PGK approach is significantly more accurate than either of these two approximations, with the sum squared error reduced by at least an order of magnitude. The failure probability approximations are then used to calculate failure probability confidence intervals based on the uncertain statistical parameters. The method is demonstrated on both a fatigue crack growth model and rotors burst margin problem. It is shown that the uncertainty in statistical estimates from small samples can cause dramatic variations in predicted failure probability and that sample statistic uncertainty should be accounted for to ensure system reliability.

## 3.2 Theory

The first subsection describes probabilistic analysis with statistical parameter uncertainty and the method of describing the statistical parameter distribution. The second subsection reviews Kriging approximation which is the basis of the PGK method. The third subsection describes the PGK method, how gradients are included in the Kriging model, and how probabilistic gradients are calculated from a single MCS sample.

### 3.2.1 Probabilistic Analysis with Statistical Parameter Uncertainty

Conventional probabilistic analysis is used to predict failure probability,  $p_f$ , represented as

$$p_f = \int \cdots \int_{g(x) < z} p_x(x) dx \quad (3.1)$$

where  $p_x$  is a joint PDF of random parameters,  $x$ ,  $g(x)$  is the limit state function, and  $z$  is a failure value. The joint PDF is defined by, and therefore conditional upon, its statistical parameters. The uncertainty in statistical parameters due to small sample sizes can be modeled by considering this conditional statement and leads to a failure probability conditional on the statistical moments,  $\phi$ , of the random parameters

$$p_f|\phi = \int \cdots \int_{g(x) < z} p_{x|\phi}(x|\phi) dx \quad (3.2)$$

where  $\phi$  is a vector of statistical parameters defining the joint PDF and  $p_{x|\phi}(x|\phi)$  is the conditional distribution of  $x$  with respect to its statistical parameters. In this work, the uncertainty of  $\phi$  is considered and modeled as a random variable,  $p_\phi(\phi)$ , and its effect can be propagated by integrating Eq. 3.2 across the domain of  $\phi$ ,

$$E [p_f|\phi] = \int \cdots \int \left[ \int \cdots \int_{g(x) < z} p_{x|\phi}(x|\phi) dx \right] p_\phi(\phi) d\phi \quad (3.3)$$

where the inner integral can be approximated with a MCS failure probability calculation at a given  $\phi$  and the outer integral can be approximated with sampling from  $p_\phi(\phi)$ . The result is an expected value of failure probability. The distribution of failure probability can be constructed by numerically sampling random values of  $p_\phi(\phi)$  and solving the inner integral for failure probability. Confidence intervals and other summary statistic can be determined from this distribution.

A description of  $p_\phi(\phi)$  is required to complete eq. 3.3. There are several approaches for this including Bayesian and frequentist. For this work a frequentist approach is used because its mathematically simple, more commonly used in the engineering community, and amenable to the demonstration problem distributions. The developed PGK method is equally applicable to either method. For the frequentist approach,  $p_\phi(\phi)$  is calculated from statistical inferencing methods used to predict confidence intervals. For normally distributed data, the mean is normally distributed

$$p_\mu(\mu) \approx N\left(\mu_x, \frac{\sigma_x}{\sqrt{n}}\right)$$

where  $\mu_x$  is the sample mean,  $\sigma_x$  is the sample standard deviation, and  $n$  the number of samples. For small sample sizes, the distribution follows a t-distribution

$$\frac{\mu - \mu_x}{\sigma_x / \sqrt{n}} \approx t_{n-1}$$

where  $n - 1$  are the number of degrees of freedom. This same result is achieved with a Bayesian approach where a non-informative prior is used with the likelihood function of the data. For standard deviation, the distribution from small sample sizes follows a chi-squared

distribution

$$\frac{(n-1)\sigma_x^2}{\chi_{n-1}^2} \quad (3.4)$$

where  $\chi_{n-1}^2$  is the chi-squared distribution for  $n-1$  degrees of freedom. Confidence bounds on lognormally distributed data can be determined by taking the exponential of the results the above sampling distribution equations. There are many frequentist approaches for predicting confidence intervals for various distribution type.  $\bar{x}$  is the sample mean,  $\sigma$  the population standard deviation,  $s$  the sample standard deviation,  $z_\alpha$  the standard normal variable,  $t_\alpha$  the  $t$ -distribution, and  $s$  and only the simplest is used here for demonstration. The PGK method is suitable for all forms of statistical parameter uncertainty quantification. The primary function of PGK is to approximate failure probability variation with respect to statistical parameters. The following section begins the explanation of the approach.

### 3.2.2 Kriging Approximation

Conventional Response Surface (RS) methods fit polynomials to function values at selected training sites. Typically training site locations are selected through a design of experiments (DOE) approach. The general form of the RS is

$$y(x) = \sum_{j=1}^{n_k} \beta_j f_j(x) + \epsilon(x) \quad (3.5)$$

where  $x$  are the approximation locations,  $\beta_j$  are regression coefficients,  $f_j(x)$  are regression functions,  $n_k$  are the number of regression functions, and  $\epsilon$  a normally distributed, zero mean, constant standard deviation error parameter. The error term accounts for the discrepancy between the approximation and the training site function values and is generally not accounted for in further analysis other than surface fit metrics such as  $R^2$ . The  $R^2$

metric, the coefficient of determination, is a relative quantity that measures the proportion of data set variability modeled by the approximation. RS methods are particularly useful when fitting replicated experimental data because the surface approximates the data in a least squares sense. In the case of fitting output from computer simulations, it is generally true that each training site has a single function value and therefore an interpolating surface can be more accurate. Sacks et al. proposed a method to more effectively model deterministic computer responses frequently referred to as the Design and Analysis of Computer Experiments (DACE) [54]. This method itself is at its foundation a Kriging approach first introduced by Krige [91].

Kriging modifies the traditional RS technique by including a stochastic process model of the surface error:

$$y(x) = \sum_{j=1}^{n_k} \beta_j f_j(x) + Z(x) \quad (3.6)$$

where  $Z(x)$  is a Gaussian stochastic function with a zero mean and  $\sigma_z^2$  variance. By including the stochastic error function, the surface interpolates through training points rather than approximates as in RS methods. The Gaussian stochastic function is calculated as

$$Z(x) = r^T R(y - f\beta) \quad (3.7)$$

where  $R$  and  $r$  are correlation functions,  $y$  are training point function values, and  $(y - f\beta)$  the error between training site function values and the polynomial approximation. For the developed PGK method, it is important to select the product power exponential correlation function:

$$R(x^i, x^j) = \prod_{k=1}^{n_d} \exp\{-\theta_k |x_k^i - x_k^j|\} \quad (3.8)$$

where  $R$  is  $n_t \times n_t$ ,  $n_t$  the number of training sites,  $n_d$  the dimension of the design space,  $\theta_k$  a vector of correlation parameter, and  $x_k^i$  and  $x_k^j$  are training site locations. Its selection is important to PGK because its analytical derivative can be easily determined which will be shown in the following subsection. Several prior efforts using gradient Kriging have used this same correlation function.

Vector  $r^T$  is the  $1 \times n_t$  correlation between the training sites and a test site location:

$$r^T(x) = [R(x^0, x^1), R(x^0, x^2), \dots, R(x^0, x^{n_t})] \quad (3.9)$$

where test site,  $x^0$ , is an approximate solution location. The regression coefficients,  $\beta_j$ , are calculated as

$$\hat{\beta}_j = (f^T R^{-1} f)^{-1} f^T R^{-1} y \quad (3.10)$$

where  $\hat{\beta}_j$  is the maximum likelihood estimate of the regression coefficients. An appropriate  $\theta$  value is computed, as shown in Santner [92], by maximizing its negative log-likelihood function,  $L$ , over the sample points using the functions

$$L(\sigma, R, \theta) = \frac{-[n \ln(\sigma^2) + \ln |R|]}{2} \quad (3.11)$$

$$\sigma_z^2(\theta) = (y - f\beta)^T R^{-1} (y - f\beta) \quad (3.12)$$

where  $\sigma_z$  is the data variance. The maximization of  $L$  can require a complex multi-dimensional search process. This can be particularly challenging when the number of training sites becomes large because the inversion of  $R$  becomes expensive. With the PGK approach in the following subsection, this cost increases substantially as the size of  $R$  increases with number of augmenting models.

As formulated, the Kriging approximation is based only on training site function values. Using additional model information at the training sites, such as gradients, is a likely approach to improve approximation accuracy for a given number of training sites. The following subsection describes the use of gradients in the Kriging model and how these gradients are calculated at training sites with no additional computational cost.

### 3.2.3 Probabilistic Gradient Kriging

In the original work of Sacks, it was posed that multiple models could provide training site information for Kriging. A specific case that has clear advantages would be to use function value and gradient models at training sites. Prior researchers have demonstrated this gradient augmented Kriging on engineering applications. Chung and Alonso applied the approach to a 2-D CFD optimization problem and showed significant accuracy improvements [93]. Liu and Batill investigated augmenting Kriging with gradients and compared the approach to a Kriging approximation using additional function values generated from training site sensitivities and linear Taylor series expansion [94]. They found the augmented Kriging approach more accurate and did not have the additional challenges with selecting an appropriate step size to create additional function values. These works provide motivation to apply the gradient augmented Kriging technique to the approximation of failure probability surfaces.

Gradient Kriging augments the function values and regression functions with gradient information. In this case, the augmented training point input to the model,  $y_a$ , and augmented regression functions,  $f_a$ , are

$$y_a = [y_0(x), \dots, y_{n_p}(x)] \quad (3.13)$$

where  $y_0(x)$  are the function values,  $y_p(x)$  are the partial derivative values for the  $p^{th}$

partial derivative models,  $1 \leq p \leq n_p$ , where  $p$  are the number of partial derivatives. Each component of  $y_p(x)$  has partial derivatives with respect to each component of  $x_d$ ,  $1 \leq d \leq n_d$ , where  $n_d$  is the dimension of  $x$ . When only first partial derivatives are included, as is done in the demonstration problems,  $y_a$  becomes

$$y_a = \left[ y(x), \frac{\partial y(x)}{\partial x_1}, \frac{\partial y(x)}{\partial x_2}, \dots, \frac{\partial y(x)}{\partial x_{n_d}} \right]. \quad (3.14)$$

Similarly, the function and augmenting function values are

$$f_a = [f_0(x), \dots, f_{n_p}(x)] \quad (3.15)$$

and for only first partial derivative augmentation

$$f_a = \left[ f(x), \frac{\partial f(x)}{\partial x_1}, \frac{\partial f(x)}{\partial x_2}, \dots, \frac{\partial f(x)}{\partial x_{n_p}} \right] \quad (3.16)$$

The vector of regression coefficients are then

$$\hat{\beta}_a = (f_a^T R_a^{-1} f_a)^{-1} f_a^T R_a^{-1} y_a \quad (3.17)$$

where  $R_a$  is the augmented correlation matrix that includes covariances between each derivative and function model.

$$Cov \{y_0(x^i), y_p(x^j)\} = \sigma_z^2 \frac{\partial R(x^i, x^j)}{\partial x_p} \quad (3.18)$$

$$Cov \{y_q(x^i), y_p(x^j)\} = \sigma_z^2 \frac{\partial^2 R(x^i, x^j)}{\partial x_q^i \partial x_p^j} \quad (3.19)$$

where  $q$  also references the partial derivative models,  $1 \leq q \leq n_p$ , and  $x^i$  and  $x^j$  are training site values,  $1 \leq i \leq n_d, 1 \leq j \leq n_d$ .  $R_a$  will be an  $n_m \times n_m$  matrix of submatrices where



$n_m$  is the number of models,  $1 + n_p$ . Each submatrix is an  $n_t \times n_t$  matrix of correlations. Eqs. For a two-dimensional surface using a function model and its two partial derivatives,  $R_a$  is

$$R_a = \begin{bmatrix} R(i, j) & -\sigma_z \frac{\partial R(i, j)}{\partial x_1} & -\sigma_z \frac{\partial R(i, j)}{\partial x_2} \\ -\sigma_z \frac{\partial R(i, j)}{\partial x_1} & \sigma_z \frac{\partial^2 R(i, j)}{\partial x_1 \partial x_1} & \sigma_z \frac{\partial^2 R(i, j)}{\partial x_1 \partial x_2} \\ -\sigma_z \frac{\partial R(i, j)}{\partial x_2} & \sigma_z \frac{\partial^2 R(i, j)}{\partial x_1 \partial x_2} & \sigma_z \frac{\partial^2 R(i, j)}{\partial x_2 \partial x_2} \end{bmatrix} \quad (3.20)$$

where  $\sigma_z$  is the constant variance term. When the number of models and training points becomes large, computation of the inverse of  $R_a$  can be computationally costly. For the demonstration problems, the largest matrix was  $2500 \times 2500$  which did not contribute significantly to computational time, but it is a potential limitation for problems with high numbers of training sites. The partial derivative terms require the derivative of the correlation function. As stated, the product power exponential function, Eq. 3.8, is used because it is easily differentiated:

$$\frac{\partial R(i, j)}{\partial x_p} = -2\theta_p (x_p^i - x_p^j) \sigma_z^2 R(i, j) \quad (3.21)$$

$$\frac{\partial^2 R(i, j)}{\partial x_p \partial x_p} = \left( -2\theta_p + 4\theta_p^2 (x_p^i - x_p^j)^2 \right) \sigma_z^2 R(i, j) \quad (3.22)$$

$$\frac{\partial^2 R(i, j)}{\partial x_q \partial x_p} = 4\theta_q \theta_p (x_q^i - x_q^j) (x_p^i - x_p^j) \sigma_z^2 R(i, j). \quad (3.23)$$

The regression function matrix becomes

$$f = \begin{bmatrix} F_0 & \cdots & 0 \\ \vdots & \ddots & \\ 0 & & F_{n_p} \end{bmatrix} \quad (3.24)$$

$$F_0 = \begin{bmatrix} 1 & x_1^1 & \cdots & x_1^{n_k} \\ \vdots & \vdots & \vdots & \vdots \\ 1 & x_{n_t}^1 & \cdots & x_{n_t}^{n_k} \end{bmatrix}, F_1 = \begin{bmatrix} 0 & 1 & 0 & \cdots & 0 \\ \vdots & \vdots & \vdots & \vdots & \vdots \\ 0 & 1 & 0 & \cdots & 0 \end{bmatrix}, F_{n_p} = \begin{bmatrix} 0 & \cdots & 0 & 1 \\ \vdots & \vdots & \vdots & \vdots \\ 0 & \cdots & 0 & 1 \end{bmatrix} \quad (3.25)$$

where each regression function matrix is  $n_t \times n_k$  and for illustration constant and linear polynomials regression functions included.

The maximum likelihood of  $\theta$  is calculated using  $R_a$ . The correlation vector for test sites,  $r_a$ , requires the correlation between test and training sites for each of the models:

$$r_a^T(x) = \left[ r(i, j), \frac{\partial r(i, j)}{\partial x_q}, \frac{\partial r(i, j)}{\partial x_p} \right] \quad (3.26)$$

with derivative terms calculated with eq. 3.21. Augmenting the surface model with gradient information should lead to accuracy improvements when approximating the failure probability surface but, without further method development, the computational cost of the sensitivity calculations could limit method effectiveness. To be truly attractive, the PGK method should not incur additional function value computation costs such as those required for numerical finite difference calculations.

Calculating the required probabilistic sensitivities with a numerical finite difference approach would require  $1 + n_d$  MCS predictions at each training site. This would add significant cost to PGK and instead an approximate approach is used based on a single MCS sample at each training site. Karamchandani developed an approach to calculate failure probability sensitivities to statistical parameters using a single MCS sample set [76]. The approach is based on the numerical simulation of failure probability which derives from the analytical failure calculation:

$$p_f = \int_{-\infty}^{\infty} I(x) f_x(x) dx \quad (3.27)$$

where  $I(x)$  is an indicator variable with a 0 value for a safe condition and 1 for a failure state. Through MCS, the integral is approximated as

$$p_f = \frac{1}{N} \sum_{j=1}^N I(x_j) \quad (3.28)$$

where  $N$  is the number of samples. A perturbation of  $p_f$  from a change in a statistical parameter can be approximated using the ratio of the density functions for the sample points in the failure region,

$$p_f(\phi_i + \Delta\phi_i) \approx \frac{1}{N} \sum_{j=1}^n I(x_j) \frac{f(x_j | \phi_i + \Delta\phi_i)}{f(x_j | \phi_i)} \quad (3.29)$$

where  $\Delta\phi_i$  is a small distance away from a nominal statistic used in the MCS. This perturbed  $p_f$ , which has been calculated without a MCS simulation, can then be used with the nominal  $p_f$  in a finite difference sensitivity calculation

$$\frac{\partial p_f}{\partial \phi_i} \approx \frac{p_f(\phi_i + \Delta\phi_i) - p_f(\phi_i)}{\Delta\phi_i} \quad (3.30)$$

to predict approximate sensitivities. This sensitivity method is subject to bias and variance errors. The variance of the sensitivity was derived by Karamchandanhi et al.,

$$Var\left(\frac{\partial p_f}{\partial \phi_i}\right) = \frac{1}{N^2} \sum_{j=1}^N I(x_j) \left[ \frac{f(x_j | \phi_i + \Delta\phi_i) - f(x_j | \phi_i)}{f(x_j | \phi_i) \Delta\phi_i} \right]^2 - \frac{1}{N} \left( \frac{\partial p_f}{\partial \phi_i} \right)^2$$

This approach assumes that the Monte Carlo samples from  $f(x_j | \phi_i + \Delta\phi_i)$  are the same as those from  $f(x_j | \phi_i)$ . Failure to satisfy this assumption will lead to bias errors. The

bias is reduced with small  $\Delta\phi_i$  but variance increases.

Analytical approaches for failure probability sensitivities have been developed that could reduce this effect [95] but are not used here as the numerical approach is more easily implemented and the sensitivity variance does not significantly effect the PGK accuracy. Substitution of (3.30) into (3.14) leads to the efficiency of PGK in addition to its improved accuracy.

There are several issues to be considered with the application of PGK. First, the MCS results at each training site are not unique computer results as is normally the case with Kriging models. This uncertainty is associated with the sampling uncertainty of MCS and can be reduced, as it is in the demonstration problems, with an appropriate sample size. The uncertainty from the MCS is at least an order of magnitude smaller than those shown from the uncertainty in sample statistics. Second, the failure probability approximation has more variables than a typical response approximation. Each response approximation variable has multiple statistics associated with it and therefore the failure probability approximation will be a  $s$ -dimensional surface where  $s$  is the total number of statistical parameters. Third, there is error between the PGK approximation and the true failure surface. This error can be reduced with additional training data and the distribution of the  $\theta$  parameter can be used to establish a confidence on the surface  $f_t$ . Finally, the method does require multiple MCS which can be costly. A regression model or other reduced-order model of the limit state function is therefore still considered necessary for practical application.

In summary, this work proposes to calculate probabilistic confidence intervals from uncertain statistical parameters. The uncertainty in statistics is quantified using a frequentist statistical inferencing approach. The variation in failure probability as a function of the statistical parameters is predicted using an Kriging approach augmented with gradient information. These gradients are efficiently calculated using a single MCS sample at each training point. The PGK approach is then used to approximate the inner-loop of the nested

reliability problem and enables efficient prediction of failure probability confidence intervals. This approach is demonstrated in the following section.

### 3.3 Demonstration Problems

The developed methodology will be demonstrated on a fatigue crack growth and a disk burst margin model.

#### 3.3.1 Fatigue Crack Growth

The response function for the crack growth example is

$$N_f = \frac{\left(a_f^{1-m/2} - a_i^{1-m/2}\right)}{c(1.1215\Delta\sigma)^m \pi(1-m/2)} \quad (3.31)$$

with statistical values defined in Table 3.1. The number of samples in Table 2 was chosen so that each contributed significantly to the variation in failure probability. For example, if 15 samples were used for the Paris constant, its effect on failure probability variation would be negligible. Using the population statistics from the table and 2 million MCS samples the predicted failure probability is 0.0022. For initial demonstration purposes that facilitate a surface plot, population statistics are used for all but the cyclic load variable. In the case of one random variable, there are two predictors in the approximate model, one for each statistic, i.e. the mean and standard deviation. A small sample of ten data points is drawn from the population and used to estimate the cyclic load statistics and confidence intervals. The sample distribution from a typical ten sample data set is shown in Figure 3.1. These figures show the wide range in possible statistical values from the ten sample points. The 95% upper bound on the standard deviation is 21.53, more than twice the actual population standard deviation, while the mean upper bound is 107.30.

Approximating variation in failure probability as a function of statistical uncertainty requires selection of training sites. For demonstration, a full factorial two-level design is used that selects points at the lower 0.025% and upper 0.975% values of the each statistic's confidence interval. These four corner points of the design space do not allow an indication of surface curvature from function values alone. This is done with the intention of demonstrating the effectiveness of the developed PGK model when compared to the traditional RS approach.

To construct the RS approximation of failure probabilities, a conventional approach would be to conduct a step-wise analysis of the significant modeling variables and track the adjusted  $R^2$  value. In the four training site example, there are too few values to require this, and instead a full linear model with interaction terms is used that perfectly interpolates the training site data. The applied RS model is

$$p_f = b_o + b_1\mu_{\Delta\sigma} + b_2\sigma_{\Delta\sigma} + b_{12}\mu_{\Delta\sigma}\sigma_{\Delta\sigma} \quad (3.32)$$

where  $\{b_o, b_1, b_2, b_{12}\}$  are the regression coefficients and  $\mu_{\Delta\sigma}$  and  $\sigma_{\Delta\sigma}$  are the mean and standard deviation of the cyclic load random parameter. While in conventional RS usage, this model is over-fitting the data, this is actually advantageous in this example because there is insignificant variation in the training site data and the RS interpolates the data as does PGK. In a case where the number of Monte Carlo simulations was small and the uncertainty grew with respect to the sample statistic uncertainty, the RS approach would have the benefit of creating a best fit of the variation at all the training sites.

The PGK model is based on the same four training sites and uses only the constant regression term,  $b_o$ , and correlation data of training site error to model the function values. While the model could have used the same model shown in Eq. 3.32, which would reduce the error at the training sites, it is not done so in this example to demonstrate the PGK abil-

ity to effectively model the failure probability variation with few modeling assumptions. Instead, the approach allows the data to determine the form of the approximation. The approach does require the selection of a form of the correlation function and for this and all examples, the product power exponential function is used because of the ease in taking its analytical derivative. Other forms of correlation function, such as the Gaussian, are not significantly different than the product power exponential and it has not been shown that certain functions are superior to others. For the demonstration problems, the maximum likelihood estimate of the correlation parameter,  $\theta$ , is determined through a simple random walk search of parameter values. The random walk begins with an initial condition of ones for  $\theta$ . Each vector entry was then randomly perturbed by a uniformly distributed value between -1 and 1. If the new random values for  $\theta$  increase the negative log-likelihood function, Eq. 14, then it is retained as the initial condition for continued random perturbations. This process was continued until convergence.

Failure probability approximations are validated on a 10 x 10 grid of equally spaced test points that span the statistical confidence intervals. Results for the cyclic load variable are shown as a contour plot of the failure surface in Figure 3.2. The surface is represented by five cross sections equally distributed across the standard deviation dimension. The failure probability increases nonlinearly as both mean and standard deviation increase to a maximum of 0.0412 with a minimum of 0.0001. It is instructive to recall that the failure probability based on the population statistics is 0.0022, showing the maximum failure probability is more than 1500% greater when considering the bounds of the statistical confidence intervals. The linear RS approximation interpolates the corner training points and matches the trend of the failure surface but clearly does not match the surface curvature. On the other hand, the PGK approach utilizes the gradient information with excellent results, following the surface across the confidence interval region. The  $R^2$  metric is used to compare the fit of the approximation to the test data. It is calculated,

$$R^2 = 1 - \frac{SS_{err}}{SS_{tot}} \quad (3.33)$$

where  $SS_{err}$  is the sum of squared error,

$$SS_{err} = \sum_{i=1}^{n_v} (y_i - f_i)^2 \quad (3.34)$$

and  $SS_{tot}$  is the total sum of squares

$$SS_{err} = \sum_{i=1}^{n_v} (y_i - \bar{y})^2 \quad (3.35)$$

where  $n_v$  is the number of test sites,  $y_i$  are the function values at the test sites, and  $f_i$  are the approximation values at the test sites. The  $R^2$  value for the RS is 0.7001 while the PGK model is 0.9969. The  $SS_{err}$  is also compared with the RS model (0.0024) and PGK (1.67E-5.) Both measures show a substantial improvement with the PGK method.

The PGK approach is also compared to a standard Kriging approach in Figure 3.3. The results for the Kriging approximation are poor, even when compared to the linear RS, because of the sparsity and location of training data. The  $R^2$  value of the Kriging model is 0.3754, and the  $SS_{err}$  is 0.0036, which are both significantly worse than the RS model. Inquiring into the construction of the Kriging model shows why the fit is poor. Based on the assumed correlation function, and the optimized correlation parameters,  $\theta$ , the center region of the approximation loses all relationship to the training site regression error. Therefore, the approximation is left with only the regression term of the Kriging model, which is the constant term,  $b_o$ , in this model. This leaves a flat plane in the interior of the design space that is the average of all four data point values. The Kriging approximation could be improved by including additional regression terms of the RS model and would likely produce a superior result. Also, the selection of training points at the corners of the the



design space is an inefficient approach for Kriging since its accuracy is highest in regions surrounding the training points. By using corner points, a majority of the region around the training point is not considered. This same inefficiency is faced by the PGK method yet it still produces accurate results.

The remaining three random variables are all individually analyzed to identify any challenges prior to continuing to the full model approximation. The results are summarized in Tables 3.2 and 3.3. Again, in all cases PGK shows a dramatic improvement in the fit. Variation in the statistics of initial crack size,  $a_i$ , showed the most significant impact on failure probability with a maximum of 0.0504. The surface is the most linear of the variables investigated, seen by the 0.9221  $R^2$  for the RS method which is still inferior to the 0.9948  $R^2$  of PGK. The Paris constant had the smallest impact on failure probability variation, which was still over a 250% increase from nominal. For all parameters, PGK reduced the  $SS_{err}$  by at least an order of magnitude and maintained an  $R^2$  above 0.975 when approximating failure probability as a function of one parameter.

While these results are encouraging and give a visual representation of the approximate surface, the actual application of method is meant for the multidimensional approximation. For the demonstration problem with four random parameters, an 8-parameter hypersurface approximation is required. A two-level full factorial design would require 256 training sites which is more than desired considering the inefficiency of this approach for Kriging and PGK. Instead an Latin hypercube sample (LHS) design is used that effectively distributes training points throughout the design space. For the demonstration, 25 training points are used. The approximation was tested at 500 full MCS test sites also selected using LHS.

A stepwise regression was implemented to retain the significant linear, interaction, and quadratic terms of a response surface approximation. The stepwise regression is a numerical process that determines retained predictive variables based on a sequence of statistical tests. A forward selection approach was applied that begins with no predictors in the model

and successively adds variables and retains them if meeting specified significance levels. For this, a significance level of 0.05 was used to include the predictor. When predictors are added, previously included parameters change in significance and they are removed from the model when the significance increases beyond 0.1. The result of this regression retained 12 predictors

$$p_f = b_o + b_1\mu_{\Delta\sigma} + b_2\sigma_{\Delta\sigma} + b_3\mu_{a_i} + b_4\sigma_{a_i} + b_5\mu_{K_{IC}} + b_{14}\mu_{\Delta\sigma}\sigma_{a_i} + b_{24}\sigma_{\Delta\sigma}\sigma_{a_i} + \dots$$

$$\dots + b_{31}\mu_{a_i}\mu_{\Delta\sigma} + b_{38}\mu_{a_i}\sigma_{K_{IC}} + b_{22}\sigma_{\Delta\sigma}^2 + b_{55}\mu_c^2 \quad (3.36)$$

and is composed of linear, interaction, and quadratic terms. The  $R^2$  value for the fit of this surface to the 25 training points is 0.9859 and its adjusted  $R^2$  is 0.973994. The adjusted  $R^2$  modifies the  $R^2$  to account for the number of retained predictor variables in the model, debiting the value for each retained predictor. The adjusted  $R^2$  is

$$1 - (1 - R^2) \frac{n_t - 1}{n_t - n_p - 1} \quad (3.37)$$

where  $n_t$  is the number of training points and  $n_p$  is the number of predictor variables. The purpose of the adjusted  $R^2$  value is to prevent over-fitting the training points since retention of more predictor variable always increases  $R^2$ .

Results of the surface fitting are included in Table 3.3 and show a maximum failure probability of 0.1214, an almost 4500% increase from the true population value. Figure 3.4 compares the PGK and RS predicted values versus the 500 full MCS results. The PGK approximation of the failure surface maintained excellent fit of the data with an  $R^2$  of 0.9831, while linear RS managed only 0.7306. Similarly, Figure 3.5 shows the Kriging

model compared to the RS model. The Kriging model in this case achieved an  $R^2$  of 0.8254, which shows that in the multidimensional case with LHS sampling that Kriging was a better approximation than the RS. These results show that the PGK method can be effectively used to efficiently approximate failure probability uncertainty caused by small sampling uncertainty for the fatigue crack growth problem.

With the PGK approximation available as the inner-loop of the nested reliability calculation, the outer-loop sampling of the statistical uncertainty can be efficiently conducted. The histogram of 100,000 outer-loop samples is shown in Figure 3.6. Without the failure probability approximation, and using the 2 million sample inner-loop MCS, this prediction would require a total of 200 billion function calls. The 95% upper bound of this distribution is 0.0428, nearly a 1600% increase in the population failure probability. These results show the significance of accounting for the sample statistic uncertainty to ensure robust designs.

### 3.3.2 Burst Margin of a Disk

Disk burst margins ensure rotating disk integrity from potential overstress conditions. The margin is calculated using

$$M_b = \sqrt{\frac{(MUF)(UTS)}{\frac{\rho\omega^2(R^3 - R_o^3)}{3g(R - R_o)}}} \quad (3.38)$$

where the parameters and population statistics are defined in Table 3.4. Using these statistics, a limit  $M_b$  value of 0.39, and 2 million MCS samples, the predicted failure probability is 0.0168. Small samples were drawn from each of the Table 3.4 variables with the exception of  $\rho$ , the material density. The material density's uniform distribution does not allow for conventional confidence interval calculations, though they can be calculated with other methods. The small sample statistics are shown in Table 3.5.

RS, Kriging, and PGK methods are used to approximate the variation in failure prob-

ability caused by the statistical uncertainty. Twenty-five training points were randomly selected in the design space using LHS. The RS method used constant, linear, and the 14 most significant interaction terms while the Kriging and PGK again used only a constant regression term. Five hundred full MCS test points were used for the comparison between the approximations. Figure 3.7 shows the comparison of PGK versus RS. The RS method shows significant error and is clearly unusable while the PGK approximation performed well with a  $R^2$  value of 0.92. Figure 3.8 compares PGK and Kriging and though Kriging is superior to RS, it still shows considerable error with an  $R^2$  value of 0.28.

Using the PGK approximation of failure probability, the sample statistics in Table 3.5, and a 100,000 MCS samples, the 95% upper bound on failure probability is 0.3731, a 2250% increase over the true population failure probability. Again, it is shown that statistical parameter uncertainty can play a dramatic role in the computation of failure probability computation.

### 3.4 Conclusion

A method has been proposed to efficiently approximate the variation in predicted failure probabilities in the presence of random parameter statistical uncertainty. This method is used to approximate the inner-loop of a nested reliability calculation. The proposed PGK method is based on a Kriging model augmented with probabilistic sensitivity information. Efficiency of the approach is maintained through the use of numerical sensitivities that do not require multiple Monte Carlo simulations at each training site. Two demonstration problems were provided to show the accuracy of the PGK method. The fatigue crack growth example achieved  $R^2$  values above 0.97 and reduced error compared to a conventional RS by at least an order of magnitude. The disk burst margin showed similar accuracy improvements. Both examples demonstrated the significance of sampling uncer-

tainty on predicted failure probabilities and show that sample statistic uncertainty should be accounted for to ensure system reliability.

$N_f$ , cycles to failure	computed
$a_i$ , initial crack size	$LN(0.1, 0.005)$
$a_f$ , final crack size	$\frac{1}{\pi} \left( \frac{K_{IC}}{1.1215\Delta\sigma} \right)^2$
$\Delta\sigma$ , cyclic load	$LN(100, 10)$
$c$ , Paris constant	$LN(1.2E-10, 1.2E-11)$
$K_{IC}$ , fracture toughness	$N(60, 6)$
$m$ , Paris law exponent	3

Table 3.1: Fatigue Crack Growth Parameters

	$n_s$	$\bar{x}_{0.025}$	$\bar{x}$	$\bar{x}_{0.975}$	$s_{0.025}$	$s$	$s_{0.975}$
$\Delta\sigma$ , cyclic load	10	90.28	97.95	107.304	6.8534	10.75	21.53
$a_i$ , initial crack size	15	0.0072	0.0099	0.0156	0.0027	0.0053	0.0142
$c$ , Paris constant	4	9.46E-11	1.10E-10	1.36E-10	2.99E-12	6.70E-12	5.10E-11
$K_{IC}$ , fracture toughness	10	55.34	59.49	63.54	3.99	5.807	10.46

Table 3.2: Fatigue Crack Growth Statistics

	$R_{RS}^2$	$R_{PGK}^2$	$SSE_{RS}$	$SSE_{PGK}$	$p_f \text{ max}$
$\Delta\sigma$ , cyclic load	0.7001	0.9969	2.44E-3	1.67E-4	0.0412
$a_i$ , initial crack size	0.9221	0.9948	6.06E-4	7.13E-5	0.0504
$c$ , Paris constant	0.7476	0.9771	3.91E-5	2.62E-6	0.0072
$K_{IC}$ , fracture toughness	0.7602	0.9765	9.00E-4	1.00E-4	0.0104
Hypersurface	0.6794	0.9831	2.23E-3	1.58E-4	0.1214

Table 3.3: Fatigue Crack Growth Approximation Metrics

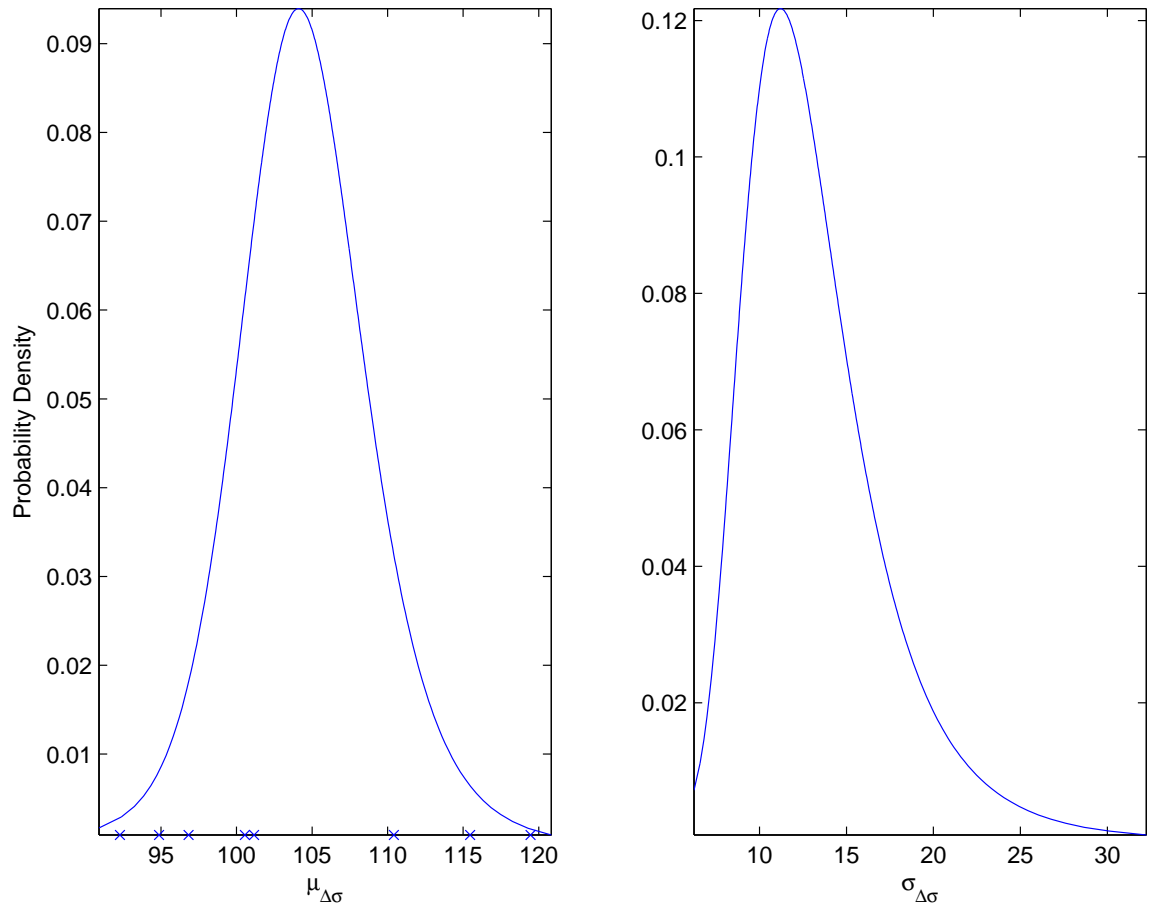


Figure 3.1: Cyclic Load Mean and Standard Deviation Sampling Distributions

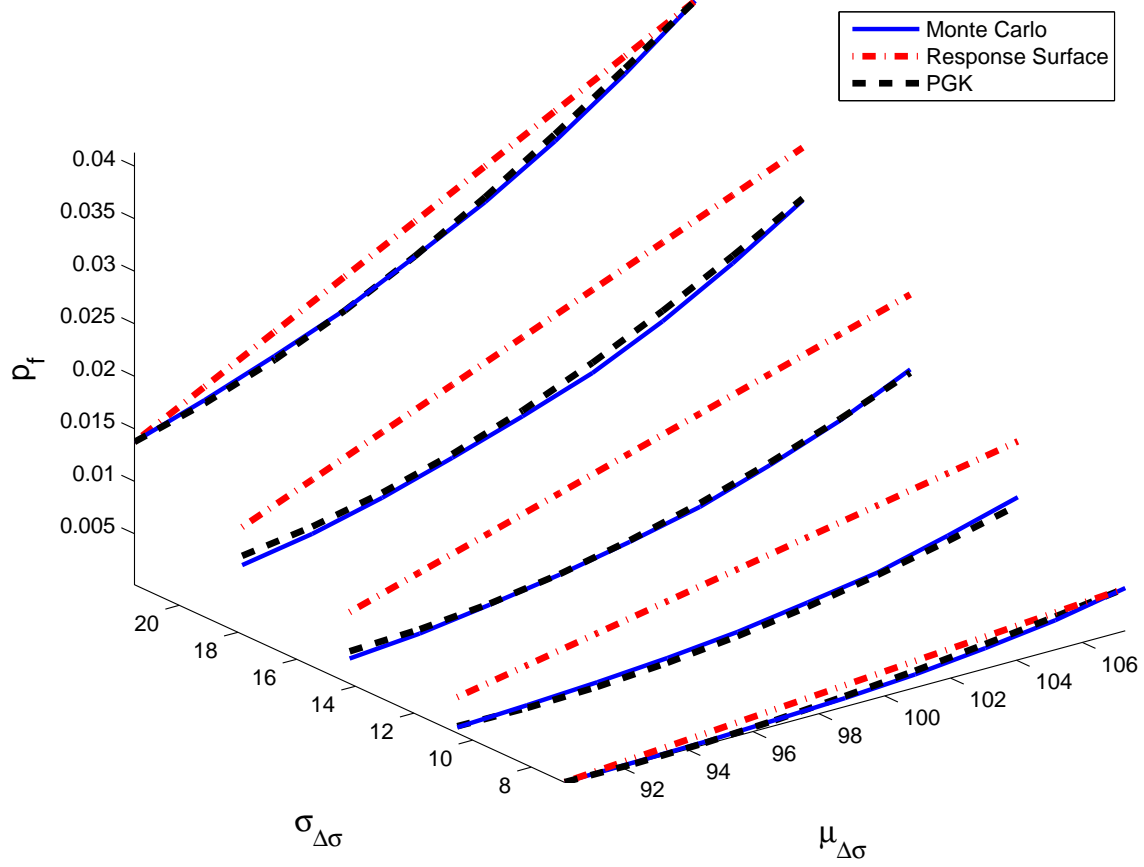


Figure 3.2: RS and PGK Approximation Comparison,  $\Delta\sigma$



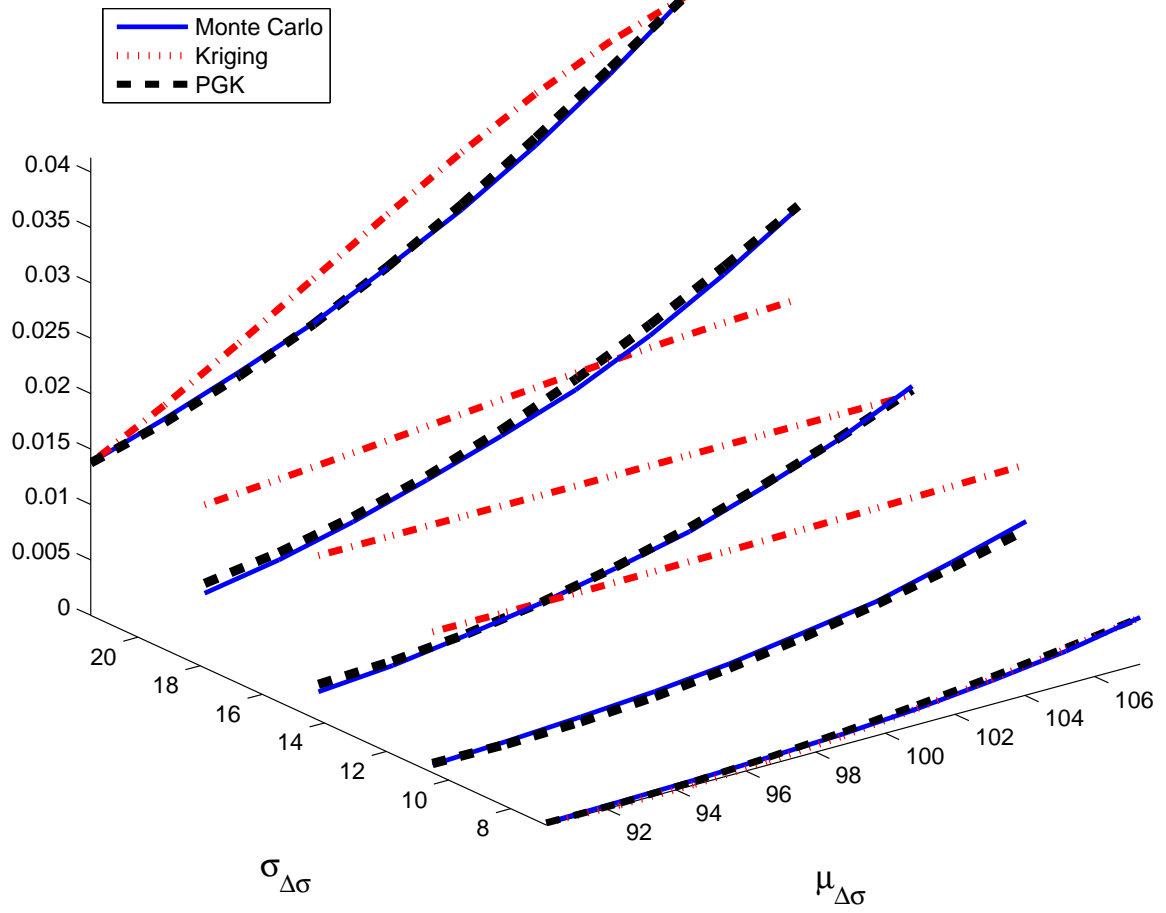


Figure 3.3: Kriging and PGK Approximation Comparison,  $\Delta\sigma$

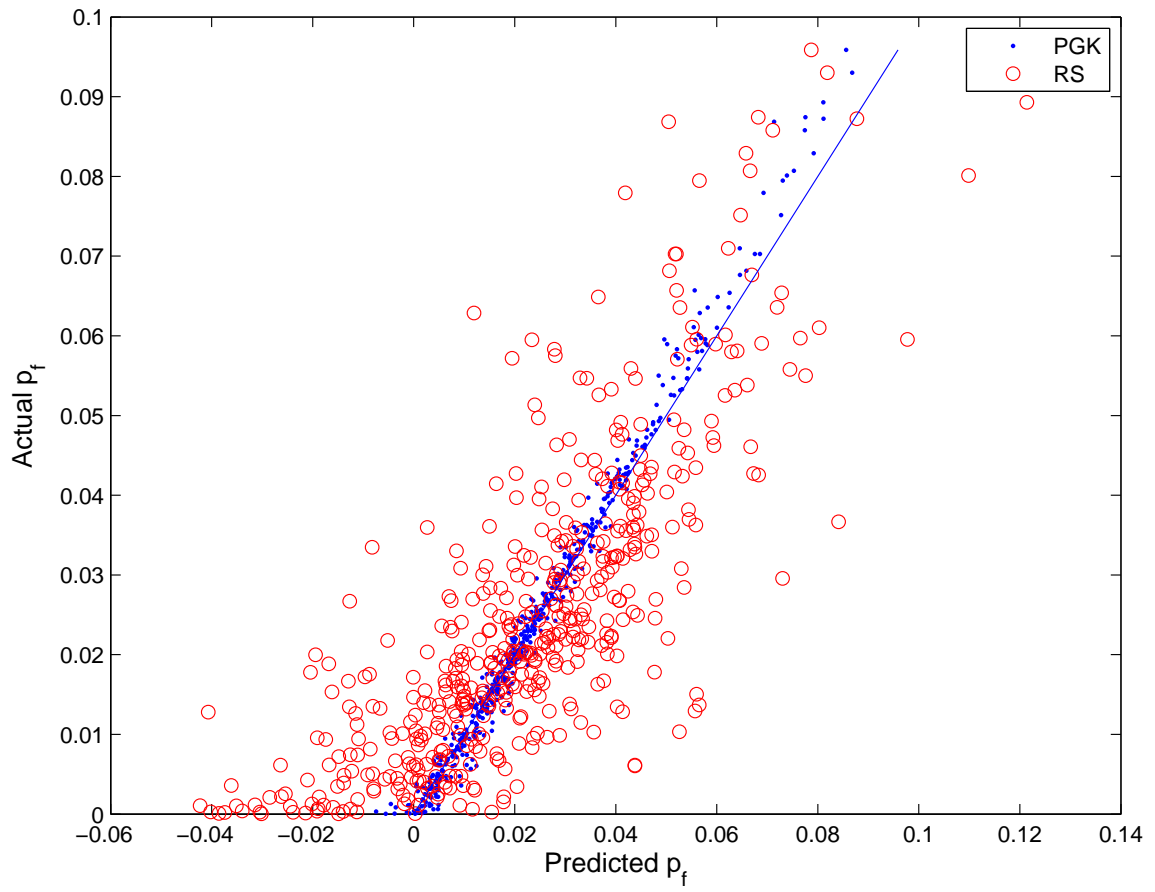


Figure 3.4: FCG: PGK and RS Predicted vs. MCS Actual

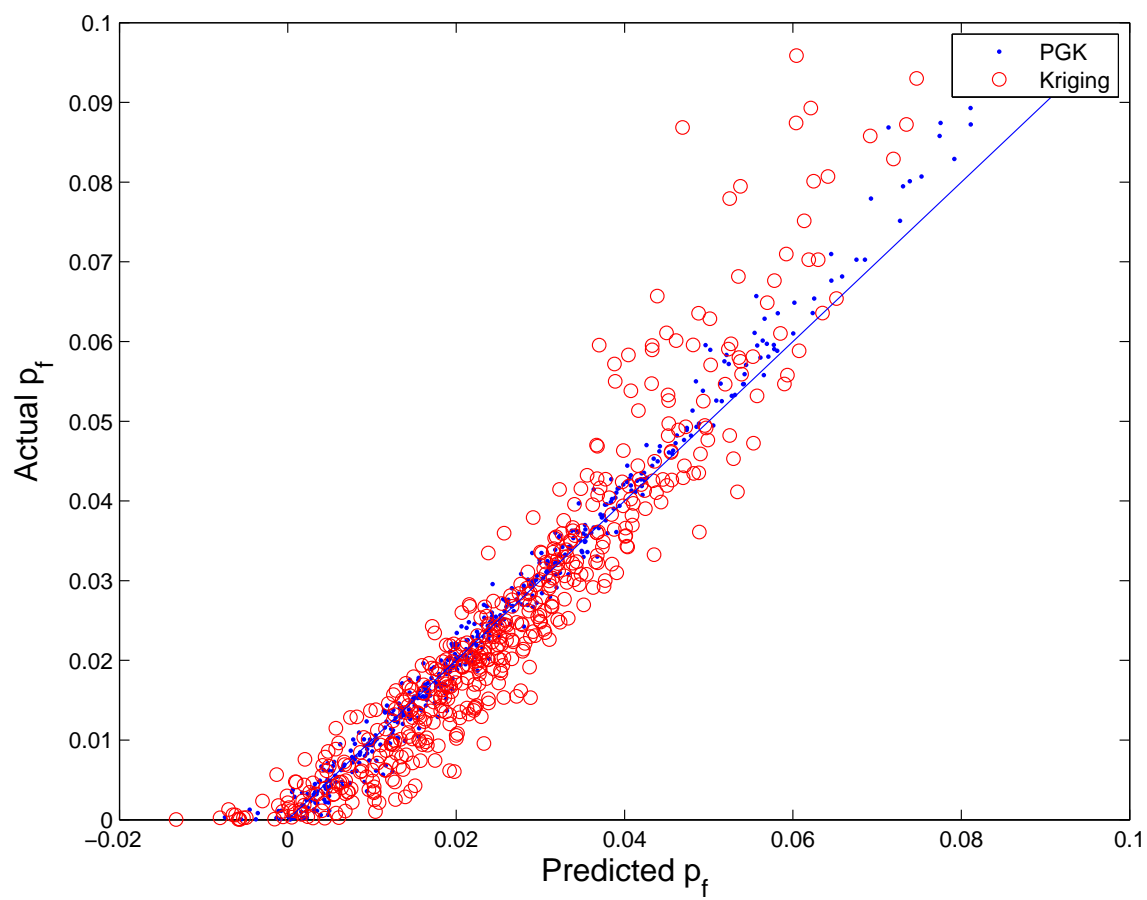


Figure 3.5: FCG: Kriging and RS Predicted vs. MCS Actual

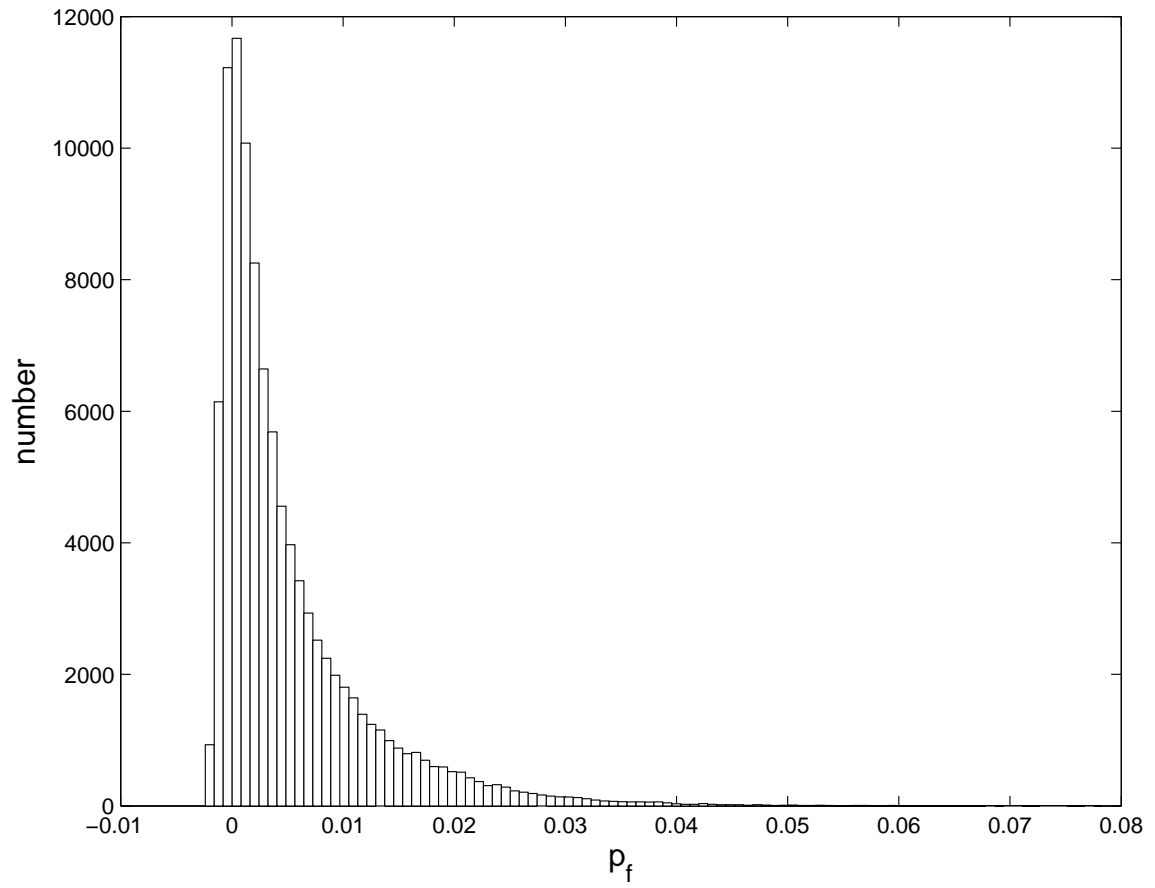


Figure 3.6: Fatigue Crack Growth Failure Probability Distribution

$UTS$ , ultimate tensile strength	$N(220000, 5000)$
$\omega$ , RPM	$N(21000, 1000)$
$R$ , outer radius	$N(24, 0.5)$
$R_o$ , inner radius	$N(8, .3)$
$MUF$ , material utilization factor	$N(0.925, 0.0722)$
$\rho$ , density	$U(0.28, .30)$

Table 3.4: Burst Margin Parameters

	$n_s$	$\bar{x}_{0.025}$	$\bar{x}$	$\bar{x}_{0.975}$	$s_{0.025}$	$s$	$s_{0.975}$
$UTS$ , ultimate tensile strength	15	214290	217610	220940	4392	5991	9.46
$\omega$ , RPM	15	20427	21011	21595	772	1055	1664
$R$ , outer radius	15	23.68	23.95	24.21	.3490	.4767	.7517
$R_o$ , inner radius	15	7.79	7.97	8.15	0.23	0.32	0.50
$MUF$ , material utilization factor	15	0.87	0.92	0.97	.071	.097	0.15

Table 3.5: Burst Margin Statistics

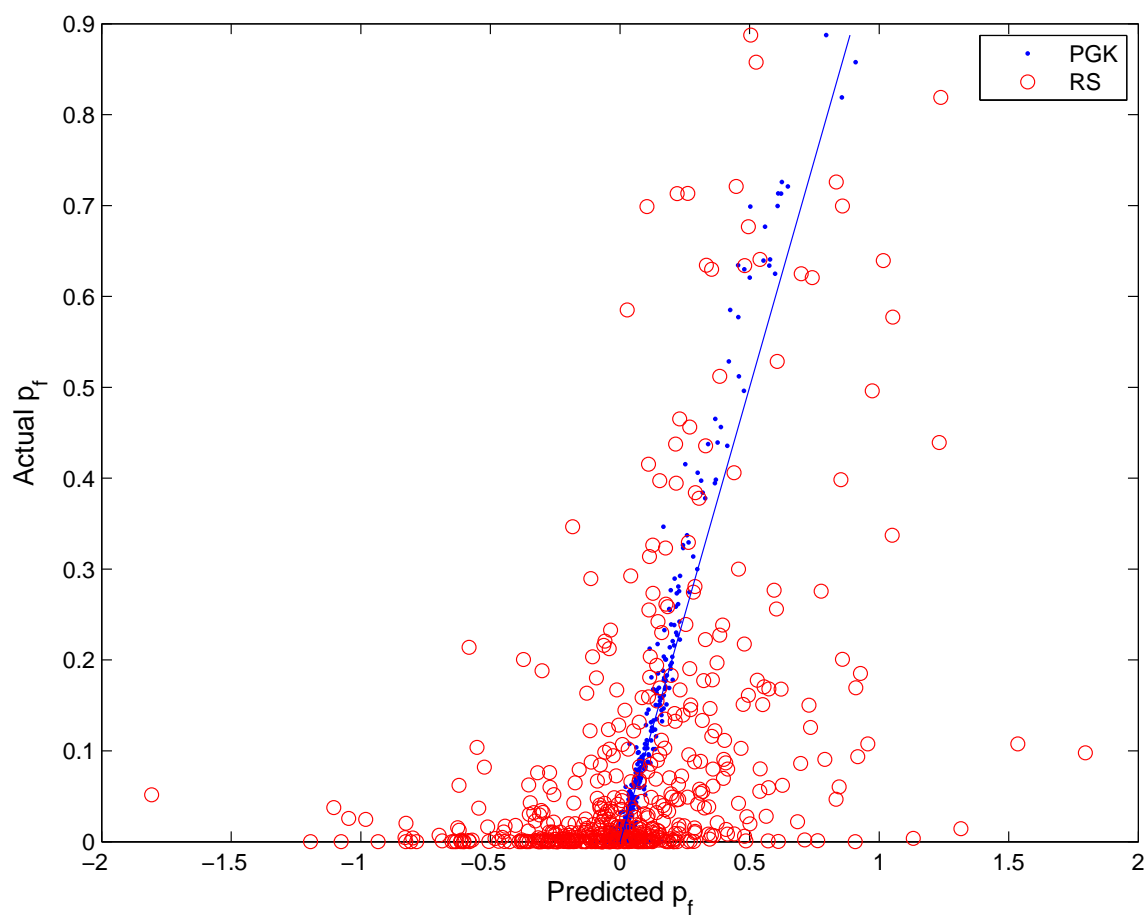


Figure 3.7: Burst Margin: PGK and RS Predicted vs. MCS Actual

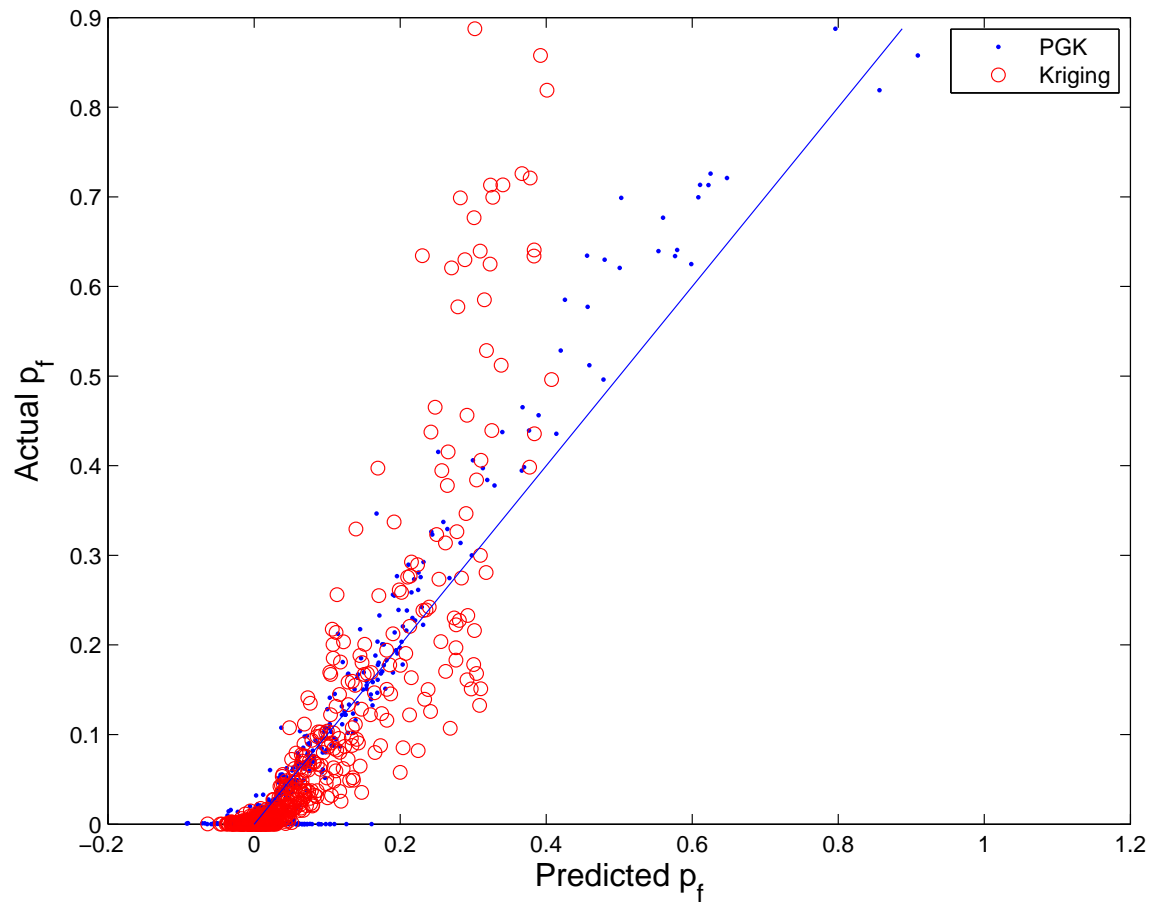


Figure 3.8: Burst Margin: PGK and Kriging Predicted vs. MCS Actual

# **4 Application of Component Mode Synthesis Methods for Modeling Geometric Mistuning in Integrally Bladed Rotors**

## **Abstract**

Reduced-order methods have been developed that rapidly predict mistuned rotor response by approximating mistuning with a nominal-mode basis and airfoil modal stiffness perturbation. Nominal-mode approximation assumes that airfoil geometric perturbations alter modal stiffness without affecting mode shape and that the mistuned response can be predicted by a summation of nominal modes. This work investigates the accuracy of that approximation and develops several Component Mode Synthesis based reduced-order mistuning models that explicitly account for geometric deviations using both nominal and non-nominal mode shape approximation approaches. The first represents the prevailing industry method and uses nominal-mode substructure reduction with airfoil substructure modal stiffnesses perturbed using geometrically-perturbed cantilevered airfoil finite element models. This approach demonstrates effective qualitative predictions that identify relative mistun-



ing amplification, but when compared to analytical results from a geometrically-perturbed integrally bladed rotor model, shows significant ( $\sim 20\%$ ) errors in maximum predicted mistuned response. For blade-to-blade response prediction at specific frequencies, dramatic ( $>100\%$ ) errors are demonstrated. The second approach uses nominal-mode substructure reduction and mistuned airfoil modal stiffness perturbations from a reduced-order modal method. The approximate airfoil model reduces computational time by 50% while enabling qualitative mistuning prediction. The third method uses nominal-mode substructure reduction, mistuned modal stiffnesses from geometrically-perturbed airfoil finite element models, and expands results with a non-nominal Craig-Bampton matrix for each airfoil. Though improvements in quantitative prediction of maximum response frequency and response amplitudes are found for all modes, the method was inconsistent. The fourth approach uses non-nominal mode substructure reduction and expansion using non-nominal Craig-Bampton matrices generated from geometrically-perturbed finite element models. This approach demonstrates excellent prediction of peak mistuning amplification and blade-to-blade response with prediction errors below 1%. A fifth approach uses reduced-order modal methods to approximate the non-nominal Craig-Bampton matrices. Use of these approximate mode shapes is found to significantly improve accuracy compared to the nominal-mode assumption but that overall performance is dominated by the accuracy of frequency approximation. It is concluded that for rapid qualitative analysis nominal-mode mistuning analysis with approximate mistuned modal stiffnesses should be used, for improved accuracy with additional computational expense approximate non-nominal mode mistuning analysis should be used, and with greater solution time and need for quantitative accuracy geometrically perturbed finite element model results should be used in non-nominal Craig-Bampton reduction and expansion.

## 4.1 Introduction

For integrally bladed rotor (IBR) forced response prediction a nominal analysis assumes that each airfoil is geometrically identical. This is sometimes referred to as a tuned analysis. While this was standard practice for many years, it is well-known that each airfoil has random geometric deviations within inspection tolerance limits. These variations are caused by manufacturing deviations and usage effects such as erosion, foreign object impacts, and airfoil blending repair operations. Such geometry deviations are responsible for variations in airfoil frequencies and mode shapes.

In the presence of random airfoil geometries, rotor cyclic symmetry breaks down, resulting in disruption of nodal diameter response and repeated root splitting. Instead of a single repeated root there will be  $n_b$ -blade, closely spaced natural frequencies. A single excitation frequency near the tuned repeated natural frequency will then excite multiple modes. Each mode's amplitude is a function of its proximity to the excitation frequency, the modal forcing of the mode, and modal damping. The superposition of modal response from the multiple excited modes can lead to modal energy localization in a small blade set. This localization can, and does, lead to forced response results significantly greater than an excitation of the tuned model. This is known as mistuned response amplification.

It is clear that mistuning is a stochastic phenomenon governed by geometry variations of each individual IBR. This complicates the tasks of quantifying IBR forced response and requires conservative design margins or predictions of the stochastic behavior. Stochastic behavior prediction is more valuable because reliability can be explicitly quantified and the effect of design changes can be explicitly determined. For instance, given a predicted distribution of mistuned response, new geometric tolerances could be established to reduce mistuning. A stochastic simulation requires multiple mistuning calculations, and therefore, reduced-order models (ROMs) for mistuning have been actively researched.

While early research studied lumped parameter models to define the basic principles of mistuning [3, 5, 6, 10, 13], more recent work has been based on using finite element model (FEM) based ROMs. A foundation for mistuning work that would come decades later was established by Craig and Bampton, almost the same year that the initial analytical mistuning studies were beginning [14]. The Craig and Bampton work defined an approach for model substructuring based on constraint modes at substructure interfaces and the fixed-boundary normal modes of the interior structures. The defined Craig-Bampton Component Mode Synthesis (C-B CMS) approach was computational efficient and easily implemented technique. Irretier would use the C-B CMS approach to model a simple 2-D mistuned bladed disk model and demonstrated the process of using a finite element method to produce required response substructures [15].

A rotor mistuning CMS solution technique, applicable to modern day design practice, was shown by Castanier, et al. [16]. The approach used cyclic-sector finite element predictions of modal quantities, stiffness, and mass matrices for use in a CMS approach that used disk-induced constraint modes. Use of disk-induced constraint modes limits interface degrees of freedom (DOF) and reduces the assembled substructure matrices size and solution time. Their approach assumes that mistuned response can be approximated by linear combination of tuned modes, limiting itself to perturbation of airfoil frequencies, and ignoring geometric mistuning effects on constraint modes and cantilevered substructure mode shapes. Results compared favorably to analytical case studies [17]. The analytical studies validated the method with a FEM that used airfoil Young's modulus perturbation to represent mistuning. As such, the airfoil substructures maintained their nominal mode shapes and the full models themselves were only an approximation of geometric mistuning. In the validation study, accuracy was degraded by excessive interface stiffness caused by the disk-induced constraint mode assumption and an iterative approach to artificially adjust mistuned modal stiffnesses was employed for solution improvement. The approach

has been widely used by the turbomachinery industry and software development led to the mistuning prediction software, named REDUCE. The approach is also referred to as a Component Mode Mistuning (CMM) approach. Later, the REDUCE CMS method was modified by Bladh, et al. to account for shroud interfaces [18].

Bladh et al. developed a Craig-Bampton CMS approach that used a Secondary Modal Analysis Technique (SMART) to further reduce assembled substructure matrices size [19, 20]. Because the approach is based on C-B CMS, the interface stiffness between substructures is more accurately represented. The resulting model will have a larger set of DOF compared to REDUCE, but the SMART approach conducts an eigenanalysis of the C-B reduced matrices to create a second reduced-basis. The SMART results are used in a mistuning projection technique to accurately predict mistuning with fewer DOF and a more accurate model of the constraint mode stiffness. As with REDUCE, validation was conducted with a full FEM that perturbed the Young's modulus for each airfoil to represent the mistuning.

Lim et al. investigated the mistuning impact of large geometric deformations caused by Foreign Object Damage (FOD) [21]. The solution approach uses CMS and divides the rotor into two substructures, a tuned bladed disk and the set of mistuned airfoils. In the formulation, all DOF in the mistuned airfoil substructure are treated as interface DOF. This leads to large ROMs when all the blades are geometrically mistuned. By considering a single FOD deformed airfoil, the number of model DOF is greatly reduced. The two model substructures are coupled through attachment modes created by applying unit forces to the interface region of the tuned bladed disk. The authors noted that these attachment modes can lead to matrix ill-conditioning and resulting numerical instability due to the fact that displacement values of the attachment modes are much less than those of normal modes. Also, the attachment and normal modes may not be independent. To overcome the numerical challenges caused by the attachment modes, Lim, et al. developed a ROM approach

based on the mode acceleration method based on static mode condensation [22]. The mistuned system is transformed to a reduced basis space of the tuned system modes and a set of static deflection shapes that account for the mistuning. These static deflection shapes can be obtained without the need to conduct a more expensive modal analysis. A single blade deformed by a FOD impact was considered to reduce the number of static analyses. Both papers were exceptional as the first to address geometric effects on a mistuned system.

An alternative to the CMS approach was developed by Yang and Griffin [27, 28]. Their approach created a reduced model through transformation of the full system model to a modal basis of tuned modes. In this case, the rotor is treated as a single structure and avoids the challenge of modeling substructure interface stiffness. The number of reduced DOF is determined by the retained tuned modes. The response of the mistuned system is approximated by a weighted sum of a subset of nominal modes, and mistuning is introduced by projecting the mistuning onto the retained nominal modes. For computational simplicity, their approach assumed Young's modulus mistuning and the stiffness perturbations are proportional to the airfoil frequency mistuning. This approach has been widely used by the turbomachinery industry and led to the Subset of Nominal Modes (SNM) mistuning prediction software. This model is attractive because it can be constructed from a cyclic sector finite element model, results in a small ROM, and simplifies disk-blade interface modeling. The method was demonstrated on a two-dimensional rotor model and, as with the prior mistuning ROMs, validation was conducted on a rotor FEM that represented mistuning through Young's modulus mistuning.

Sinha expanded the SNM approach for geometric mistuning and labeled the approach Multiple Modal Domain Analysis (MMDA) [32]. The approach represents the blade geometry variation through a spatial statistics model as shown by Garzon et al. [33]. The MMDA approach uses nominal system tuned modes and tuned modes of rotors having perturbed geometry based on the spatial statistical analysis. The spatial statistical analysis produces

a set of principal component modes that define the geometric deviations with a reduced basis. The perturbed geometries consist of the nominal geometry with the addition of each retained principal component mode. The ROM dimension is the number of tuned modes retained multiplied by the number of retained principal component modes. This is still an approximate basis for the airfoil mode shapes since the actual geometry of the airfoils is not used to generate the modal basis. The approach uses results from a cyclic sector analysis and sector DOF are transformed to the new basis through pre- and post-multiplying matrices. The approach was demonstrated on a geometrically-perturbed academic rotor and showed excellent accuracy for a single mode.

While an MMDA is an effective ROM, there can still be large computational costs associated with the transformation of physical sector DOF to the new basis, particularly when there are a large number of DOF in the disk. Tuned and mistuned stiffness matrices are used in the calculation and pre and post multiplications of these matrices by tuned modes and perturbed modes are required. For the 16 bladed rotor example in this work, the MMDA approach would require 544 matrix operations. When many several modes are retained with large DOF models, it can require significant computational time. The reduced order model resulting from this basis transformation, for the 16 bladed rotor example in this work, would require an  $800 \times 800$  full matrix eigenvalue problem compared to the  $2632 \times 2632$  reduced matrix from the C-B CMS methods in this work. The C-B matrices are 40% sparse which reduces computational time and the reduced order model construction is simplified, requiring only 34 matrix operations. The CMS approach also conducts many of its operations on the smaller airfoil substructure models which further reduce computational costs. Sinha's work also did not demonstrate the use of the nominal-mode approximation for the problem, and therefore did not fully demonstrate the need to account for non-nominal modes.

Reduced-order methods have been developed that rapidly predict mistuned rotor response by approximating mistuning with a nominal-mode basis and airfoil modal stiffness

perturbation. Nominal-mode approximation assumes that the geometry of each airfoil is identical and the geometric perturbations that alter modal stiffness do not perturb mode shape. This work investigates the accuracy of that approximation and develops several Component Mode Synthesis based reduced-order mistuning models that explicitly account for geometric deviations using both nominal and non-nominal mode shape approaches. The first represents the prevailing industry method and uses nominal-mode substructure reduction with airfoil substructure modal stiffnesses perturbation using geometrically-perturbed cantilevered airfoil finite element models. This approach demonstrates effective qualitative predictions that identify relative mistuning amplification but, when compared to analytical results from a full geometrically-perturbed integrally bladed rotor model, shows significant ( $\sim 20\%$ ) errors in maximum predicted mistuning amplification. For blade-to-blade response prediction at specific frequencies, dramatic ( $>100\%$ ) errors are demonstrated. The second approach uses nominal-mode substructure reduction and mistuned airfoil modal stiffness perturbations from reduced-order modal methods. The reduced-order airfoil model reduces computational time while enabling qualitative mistuning prediction. The third method uses nominal-mode substructure reduction, mistuned modal stiffnesses from geometrically-perturbed airfoil finite element models, and expands results with non-nominal Craig-Bampton matrix for each airfoil. Though improvements in quantitative prediction of maximum response frequency and response amplitudes are found for all modes, the method was inconsistent and is not elevated above a qualitative tool. The fourth approach uses non-nominal mode substructure reduction and expansion using non-nominal Craig-Bampton matrices generated from geometrically-perturbed finite element models. This approach demonstrates excellent prediction of peak mistuning amplification with prediction errors below 1%. A fifth approach uses reduced-order methods to approximate the non-nominal Craig-Bampton matrices. Use of these approximate mode shapes is found to significantly improve accuracy but that overall performance is dominated by accurate

frequency approximation. It is concluded that for rapid qualitative analysis, nominal-mode mistuning analysis with approximate mistuned modal stiffnesses should be used, for improved accuracy with additional computational expense approximate non-nominal mode mistuning analysis should be used, and with greater solution time and need for quantitative accuracy geometrically perturbed finite element model results should be used in non-nominal Craig-Bampton reduction and expansion.

The following section gives the mathematical description of the nominal and non-nominal mode approximations of mistuned response. The reduced-order approach to model geometric variations and the reduced-order substructure modal analysis approach are described in Subsection 4.2.2. These reduced-order modeling approaches are then demonstrated in Section 4.3 on an advanced IBR configuration.

## **4.2 Theory**

The first subsection describes the use of a C-B CMS approach for mistuning analysis using a nominal-mode approximation. The second section develops new nominal and non-nominal mode approaches to account for geometric mistuning.

### **4.2.1 Nominal-Mode Reduced-Order Mistuning Model**

Prior mistuning CMS ROM developments have assumed nominal-mode approximation of mistuned modes. Castanier et al. used a modified CMS approach of nominal cantilevered blade normal modes and disk-induced constraint modes. In their work, overly stiff results were obtained because of the constraint mode approximation that negatively impacted accuracy. Bladh et al. use a C-B approach which more accurately quantified constraint stiffness and used SMART for further model analysis. Validation of both approaches was conducted with rotor FEMs that represented mistuning by perturbation of Young's modulus.



Because of this, geometric effects were not explicitly considered and airfoil substructure mode shapes remained nominal.

Because of its accuracy, the C-B approach is the basis for further geometric mistuning model development and described in detail. The C-B approach is attractive for its ability to reduce computational time and memory required for large numerical models while still providing an exact solution if, in the limit, all modes are retained. Using this approach, an engine rotor is divided into one disk substructure and  $n_b$  blade substructures. The shared nodes between blades and disk are boundary nodes while those that remain are interior. The C-B method uses fixed-boundary normal modes and boundary constraint modes as the reduced basis. Each substructure is reduced independently and later coupled using a compatibility matrix.

The boundary constraint static modes are derived from a partitioned form of the static displacement equation. The matrix and vector quantities of the system of equations are partitioned by interior and boundary DOF. This leads to

$$\begin{bmatrix} k^{bb} & k^{bi} \\ k^{ib} & k^{ii} \end{bmatrix} \begin{bmatrix} u^b \\ u^i \end{bmatrix} = \begin{bmatrix} f^b \\ f^i \end{bmatrix} \quad (4.1)$$

where the superscripts  $b$  and  $i$  refer to the boundary and interior DOF. Static constraint modes are calculated by assuming that each boundary DOF has successive unit displacement, all other boundary freedoms are fixed, and interior freedoms are free. By assuming that forces on interior freedoms,  $f^i$ , are zero, the system of equations

$$k^{ib}u^b + k^{ii}u^i = 0 \quad (4.2)$$

allow for the solution of  $u^i$  as a function of  $u^b$

$$u^i = - [k^{ii}]^{-1} [k^{ib}] u^b = \Phi^c u^b \quad (4.3)$$

where  $\Phi^c$  is the constraint mode matrix.

The fixed-boundary normal modes of the substructure are computed by partitioning the mass matrix according to boundary and interior freedoms

$$\begin{bmatrix} m^{bb} & m^{bi} \\ m^{ib} & m^{ii} \end{bmatrix} \quad (4.4)$$

and solving the generalized eigenvalue problem

$$k^{ii} \Phi^n = \Lambda m^{ii} \Phi^n \quad (4.5)$$

where  $\Phi^n$  matrix of normal modes and  $\Lambda$  is the diagonal matrix of eigenvalues . Having both  $\Phi^c$  and  $\Phi^n$  enables transformation of the model's physical DOF,  $u$ , to a modal domain

$$u = \Phi^{cb} \alpha \quad (4.6)$$

where

$$\Phi^{cb} = \begin{bmatrix} I & 0 \\ \Phi^c & \Phi^n \end{bmatrix} \quad (4.7)$$

and

$$\alpha = \begin{bmatrix} \alpha^b \\ \alpha^i \end{bmatrix} \quad (4.8)$$

where  $\alpha^b$  are the modal coordinates of the constraint modes and  $\alpha^i$  are the modal coor-

ordinates of the fixed-boundary normal modes. The modal coordinates,  $\alpha^b$ , are equivalent to  $u^b$  because of the identity matrix in  $\Phi^{cb}$ . Transforming the substructure matrices from the physical domain to the modal domain reduces the matrix order to the sum of the number of retained constraint and fixed-boundary normal modes. This transformation reduces computational expense when the number of interior DOF are large, the number of retained modes is small, and number of interface DOF is small. The substructure stiffness matrix transforms to the C-B retained modes basis

$$\hat{k} = [\Phi^{cb}]^T k [\Phi^{cb}] = \begin{bmatrix} \hat{k}^{bb} & 0 \\ 0 & \hat{k}^{ii} \end{bmatrix} \quad (4.9)$$

where

$$\hat{k}^{bb} = k^{bb} + k^{bi} \Phi^c \quad (4.10)$$

and

$$\hat{k}^{ii} = [\Phi^n]^T k^{ii} [\Phi^n] \quad (4.11)$$

where  $\hat{k}^{ii}$  is the matrix of modal stiffnesses, i.e. a diagonal matrix of the system eigenvalues.

The reduced mass matrix of the substructure is

$$\hat{M} = [\Phi^{cb}]^T M [\Phi^{cb}] = \begin{bmatrix} \hat{m}^{bb} & \hat{m}^{bi} \\ \hat{m}^{ib} & \hat{m}^{ii} \end{bmatrix} \quad (4.12)$$

$$\hat{m}^{bb} = m^{bb} + [\Phi^c]^T m^{ib} + m^{bi} \Phi^c + [\Phi^c]^T m^{ii} [\Phi^c] \quad (4.13)$$

$$\hat{m}^{bi} = [\hat{m}^{ib}]^T = m^{bi} \Phi^n + [\Phi^c]^T m^{ii} [\Phi^n] \quad (4.14)$$

$$\hat{m}^{ii} = [\Phi^n]^T m^{ii} [\Phi^n] \quad (4.15)$$

where  $m^{ii}$  is the identity matrix because of the mass normalized  $\Phi^n$ . This completes the calculation of the reduced substructures matrices.

Coupling substructures requires that geometric compatibility is maintained at joined substructure boundaries. This requires

$$\alpha_b^1 = \alpha_b^2 = u_b = q_b \quad (4.16)$$

where the coupled substructure modal coordinates,  $\alpha$ , are transformed to a set of independent modal coordinates,  $q$ , through a matrix transformation  $S$

$$\begin{bmatrix} \alpha_i^1 \\ \alpha_b^1 \\ \alpha_i^2 \\ \alpha_b^2 \end{bmatrix} = Sq = \begin{bmatrix} I & 0 & 0 \\ 0 & 0 & I \\ 0 & I & 0 \\ 0 & 0 & I \end{bmatrix} \begin{bmatrix} q_i^1 \\ q_i^2 \\ u_b \end{bmatrix} \quad (4.17)$$

that ensures equality at coupled substructure boundary DOF. The above equation is for two joined substructures and can be extended for multiple interfaces.

For an  $n_b$ -bladed rotor system the assembled stiffness is

$$\hat{K} = \begin{bmatrix} \hat{k}_D^{ii} & \cdots & & 0 \\ \vdots & \hat{k}_1^{ii} & & \\ & & \ddots & \\ & & & \hat{k}_{n_b}^{ii} \\ 0 & & & & \hat{K}_{bb} \end{bmatrix} \quad (4.18)$$

where

$$\hat{K}_{bb} = S_D \hat{k}_D^{bb} S_D + \sum_{r=1}^{n_b} S_r \hat{k}_r^{bb} S_r \quad (4.19)$$

where and the summation occurs over each of the  $r$  substructures. The  $k_D^{ii}$  substructure references the disk substructure and 1 through  $n_b$  identifies each airfoil. The assembled mass matrix is

$$\hat{M} = \begin{bmatrix} \hat{m}_D^{ii} & \cdots & \cdots & 0 & M_D^{ib} \\ \vdots & \ddots & & & \vdots \\ \vdots & & \ddots & & \vdots \\ 0 & & & \hat{m}_{n_b}^{ii} & M_{n_b}^{ib} \\ M_D^{bi} & \cdots & \cdots & M_{n_b}^{bi} & M^{bb} \end{bmatrix} \quad (4.20)$$

$$M_r^{ib} = M_r^{bi} = \hat{m}_r^{ib} S_r \quad r = 1, \dots, n_b \quad (4.21)$$

$$M^{bb} = S_D \hat{m}_D^{bb} S_D + \sum_{r=1}^{n_b} S_r \hat{m}_r^{bb} S_r \quad (4.22)$$

and the summation occurs over each of the  $r$  substructures. This completes the assembly of the reduced-order system model. These matrices will be  $n_i \times n_i$  where  $n_i$  is the sum of the number of interface DOF and retained fixed-boundary normal modes for the system.

Solution of the reduced basis eigenproblem

$$\hat{K}\alpha_i = \lambda_i \hat{M}\alpha_i \quad i = 1, \dots, n_m \quad (4.23)$$

where  $\alpha_i$  is the  $i^{th}$  CMS mode. The expansion to the physical domain for each airfoil substructure is

$$u_k = \Phi_k^{cb} A_k \quad (4.24)$$

where  $A$  is the matrix of retained CMS eigenvectors for the  $k^{th}$  substructure and

$$A_k = \begin{bmatrix} A^b \\ A^i \end{bmatrix}_k \quad k = 1, \dots, n_b \quad (4.25)$$

and the  $k^{th}$  substructure C-B matrix is

$$\Phi_k = \begin{bmatrix} I & 0 \\ \Phi_k^c & \Phi_k^n \end{bmatrix}$$

for each of the  $k$  airfoil substructures.

To implement a CMM approach such as REDUCE, mistuning is modeled as a perturbation in airfoil substructure modal stiffness,  $\hat{k}_{n_b}^{ii}$ , which is equivalent to a perturbation of the cantilevered airfoil natural frequency

$$\left[ \hat{k}_{i,i}^{ii} \right]_k = (1 + \delta_{k,i}) \Lambda_{i,i}^0 \quad (4.26)$$

where  $\left[ \hat{k}_{i,i}^{ii} \right]_k$  is the modal stiffness for the  $i^{th}$  retained mode for the  $k^{th}$  airfoil substructure. The nominal airfoil eigenvalues are in the diagonal matrix  $\Lambda_{i,i}^0$  and the mistuning percentage for the  $k^{th}$  airfoil and  $i^{th}$  forms the matrix  $\delta_{k,i}$ . Because only modal stiffnesses

are perturbed, there is an assumption that the mistuned modes of a blade can be accurately approximated with a linear combination of tuned modes. In practice, the values of  $\delta_{k,i}$  are either prescribed or obtained through empirical measurement of airfoils variations and using their percentage difference from average. Capiez-Lernout and Soize developed a nonparametric model of random uncertainties for mistuned bladed disks for this parameter [40]. A follow-on effort by these authors modified these dispersions based on an estimate from three geometric parameters [41]. Past work has not linked  $\delta_{k,i}$  and explicit geometric variations and has not accounted for non-nominal mode effects. An approach to do so is defined in Subsection 4.2.2.

The nominal-mode approximation of the mistuned system assumes that  $\Phi^c$ ,  $\Phi^n$ ,  $k^{ib}$ ,  $\hat{m}^{bb}$ ,  $\hat{m}^{bi}$  are unchanged in the CMM model. Geometric variations will alter all of these quantities to some degree, which negatively impact the accuracy of the nominal-mode approach. The following section develops a set of approaches to explicitly model geometric deviations and account for non-nominal mode shapes of airfoil substructures.

## 4.2.2 Geometric Mistuning with Component Mode Synthesis

### Methods

Given that explicit modeling of geometric effects and the modal variations they induce are significant to accurate mistuning prediction, there is a need for an efficient geometric mistuning model. It is proposed that incorporating geometric variations in a C-B CMS solution will enable more accurate response prediction of a geometrically mistuned rotor. Several approaches will be defined in the subsections below. Common to each is the need to model airfoil geometry deviations in a reduced-basis. Retention of geometric deviations in the physical domain increase computational complexity as each airfoil surface can be defined by hundreds and sometimes thousands of node spatial coordinates. The approach described

reduces geometric definition to 15 coordinates for the example problem in Section 4.3.

Airfoil geometry can be collected using coordinate measurement machines that obtain spatial data through a geometry traversing probe. Each measured airfoil may provide thousands of data points. Efficiently modeling these variations for the following ROM developments is beneficial. Previous works have used PCA to model geometric deviations [96, 33]. PCA is attractive given its ease of implementation and minimized set of retained basis vectors that represent correlated geometry variations. In addition, the statistics from the analysis can be used to generate stochastic airfoil geometry models. The stochastic application of this approach has been demonstrated in prior works by Brown and Grandhi [97, 98].

PCA is implemented by storing  $n$  measured three-dimensional coordinate data points in vector  $\mathbf{x} \in \mathbb{R}^{3n}$ . A set of  $p$  measured airfoils results in matrix,  $\mathbf{X} \in \mathbb{R}^{3n,p}$ . Since it is of interest to understand the variations from the average blade, the mean value of each row is subtracted from each member of the row to give a matrix of measured deviations,  $\Delta\mathbf{X}$ , where each element is

$$\Delta x_{i,j} = x_{i,j} - \bar{x}_i \quad i = 1, 2, \dots, 3n; j = 1, 2, \dots, p \quad (4.27)$$

where  $\bar{x}_i$  is the average of the  $i^{th}$  row. It is important to note that the average,  $\bar{x}_i$ , is not necessarily the original design intent. Also, subtracting the row mean from each element makes the expected value of each row zero. The first-order covariance matrix of  $\Delta\mathbf{X}$ ,  $\Sigma_{\Delta X}$ , defines the statistical relationship between a measurement point deviation and all other points, and its eigensolution leads to eigenvectors that can be used to form a new subspace optimally representing variation. This is written in standard eigenproblem form

$$\Sigma_{\Delta X} \Psi = \Psi \mathbf{D} \quad (4.28)$$



where  $\mathbf{D}$  and  $\Psi$  are the eigenvalue and eigenvector matrices, respectively. The eigenvectors are the principal components modes of the measured data, and the eigenvalues are the principal component variances that indicate the data variance each principal component captures. Based on these eigenvalues, graphical and statistical methods can be used to retain a limited set of basis vectors. Also of importance, the principal components are orthogonal, and therefore, uncorrelated statistically. The PCA transforms a large set of correlated parameters into a small set of uncorrelated parameters.

Transformation of the measured deviations,  $\Delta\mathbf{X}$ , to the principal component basis requires the linear operation

$$\mathbf{Z} = \Psi^T[\Delta\mathbf{X}] \quad (4.29)$$

where the eigenvector matrix is multiplied by the deviation matrix to give the z-score matrix,  $\mathbf{Z} \in \mathbb{R}^{n_p \times p}$  with  $n_p$  the number of retained principal component modes. These scores are effectively regression coefficients for the new principal component basis and define the participation of each PCA mode in each measured geometry. The above algorithm, Eqs. 4.27-4.29, is the covariance method of PCA and the columns of  $\mathbf{Z}$  represent the Karhunen-Loeve transformation. The Karhunen-Loeve transformation is the representation of a stochastic process as a linear combination of orthogonal functions determined by the covariance function of the process. When the coefficients of the linear combination are determined through a statistical sample, this approach is known as PCA, or Proper Orthogonal Decomposition (POD), or the Hotelling transform. Statistical analysis of the z-scores enable definition of the stochastic parameters of the airfoil geometry model.

$$\tilde{x} = \bar{x} + \sum_{i=1}^p \xi_i z_i \quad (4.30)$$

where  $\tilde{x}$  a vector defining the random geometry,  $\bar{x}$  the nominal geometry, and  $\xi_i$  is a random

scalar drawn from the distribution of the  $z_i$  z-score distribution. This geometry model is used with the following methods to predict geometrically mistuned rotor response.

#### 4.2.2.1 Nominal-Mode Approximation with Geometrically-Perturbed FEM Airfoil Modal Stiffnesses

The first method uses C-B CMS, nominal-mode approximation (NMA) for airfoil substructures, and uses geometrically-perturbed FEMs to determine the eigenvalues ( $\lambda_{FEM}$ ) that are needed for  $\hat{k}_k^{ii}$ ,

$$\left[ \hat{k}_{i,i}^{ii} \right]_k = [\lambda_i]_k \quad (4.31)$$

where  $[\lambda_i]_k$  are from geometrically perturbed FEM. The CMS reduction remains in the nominal space with a nominal mode C-B for all  $k$  airfoil substructures.

$$\Phi_{NMA}^{cb} = \begin{bmatrix} I & 0 \\ [\Phi^c]^0 & [\Phi^n]^0 \end{bmatrix} \quad (4.32)$$

where the superscript 0 refers to the nominal substructure model. The reduced CMS eigenproblem is then

$$\hat{K}_{NMA} [\alpha_i]_{NMA} = \lambda_i \hat{M}_{NMA} [\alpha_i]_{NMA} \quad (4.33)$$

where the subscript  $NMA$  refers to the nominal mode approach. The expansion to physical space for this approach is then

$$u_k = [\Phi_{NMA}^{cb}]_k [A_{NMA}]_k \quad (4.34)$$

for each of the  $k$  substructures.

This approach is representative of the CMM (REDUCE) method available to the turbo-machinery industry. While representative, it does not use disk-induced constraint modes and therefore does not suffer excessive stiffness at the disk-airfoil substructure boundaries. Prior applications of the C-B CMS approach have not considered geometric mistuning, have not used geometrically-perturbed FEMs to provide modal stiffness perturbation, and not been compared to a geometrically-perturbed IBR FEM.

#### **4.2.2.2 Nominal-Mode Approximation with Approximate Airfoil Modal Stiffness Perturbation**

By approximating the modal stiffness variations caused by geometric deviations, the computational costs associated with creating airfoil substructures and  $\delta_{n_b, n_m}$  can be eliminated. Previous efforts have shown that airfoil eigenvalues can be accurately approximated with a Taylor Series approximation using first-order sensitivities [99]. Sensitivity calculations can be computationally expensive when calculated numerically via finite difference methods that require FEM evaluations for each design parameter. A semi-analytic method, as shown in Chapter 2, replaces the costly calculations of the process, i.e. decomposing the stiffness and mass matrix and solving the matrix eigenvalue problem.

While effective, the results from Chapter 2 showed a sensitivity of predicted gradient to finite difference step size used for perturbing mass and stiffness matrices. A numerical finite difference approach based on airfoil FEMs did not have this sensitivity and showed consistent gradient values regardless of step size. This indicates the linear relationship between geometric deviations and modal response for the range of deviations under consideration. A numerical finite difference approach would require significant computational time if conducted in the physical domain. The use of the reduced-order geometry model significantly reduces the number of required FEM solutions. Because of this and the insensitivity of gradients to step size, the numerical approach in the PCA mode space is used

for sensitivity calculations. The semi-analytic methods used in Chapter 2 are important for future research in multi-point approximation of modal response that would become impractical with a numerical finite difference approach. A suggested multi-point modal response approximation for future exploration is the gradient Kriging method used in Chapter 3.

The numerical sensitivity methods combined with the reduced-order geometry model results described earlier leads to the following principal component mode eigenvalue sensitivities

$$\frac{\partial \lambda_i^0}{\partial \psi_j} \approx \left( \frac{\lambda_i^{(0+\Delta\psi_j)} - \lambda_i^0}{\Delta\psi_j} \right) \quad (4.35)$$

where  $\lambda_i^0$  is the nominal eigenvalue,  $\lambda_i^{(0+\Delta\psi_j)}$  is the numerically perturbed value, and  $\Delta\psi_j$  is the percentage change (step-size) of the  $j^{th}$  principal component. As shown in Figure 2.15, the result is insensitive to a broad range of step-size.

For the nominal mode C-B CMS approach, an eigensensitivity-accelerated computation of Eq. 4.26 is

$$\left[ \tilde{k}_{i,i}^{ii} \right]_k = \lambda_i^0 + \sum_{j=1}^{n_p} \frac{\partial \lambda_i^0}{\partial \psi_j} \Delta [\psi_j]_k \quad (4.36)$$

where  $n_p$  are the number of principal component vectors. This method represents frequency variation and computational burden is effectively eliminated once the initial finite difference calculations are completed. The Craig-Bampton space eigenproblem with this approximation becomes

$$\tilde{\hat{K}}_{NMA} [\alpha_i]_{NMA} = \lambda_i \hat{M}_{NMA} [\alpha_i]_{NMA} \quad (4.37)$$

where the stiffness matrix reflects the approximation. Expansion continues with the nominal C-B matrix.

#### 4.2.2.3 Nominal-Mode Approach with Non-Nominal Mode Expansion

The prior two approaches address geometric effects on modal stiffness accurately, but neither considers non-nominal mode shape. The most attractive approach would be to use nominal-mode approximations to predict the CMS-basis modal response and only use non-nominal mode shape results during expansion to the physical domain. This would allow use of existing mistuning ROMs with a mode shape correction step during expansion. This assumes that the predicted  $\alpha$  from nominal-mode approximation and non-nominal mode approximation are similar.

In this approach the nominal mode approach is used to transform the physical substructures to the Craig-Bampton domain, coupled, and the resulting reduced system eigenproblem is

$$\hat{K}_{NMA} [\alpha_i]_{NMA} = \lambda_i \hat{M}_{NMA} [\alpha_i]_{NMA} \quad (4.38)$$

where the modal participation's have been computed using the nominal mode approximation,  $[\alpha_i]$ . Using this nominal-mode approach with non-nominal mode expansion (NMA-NNME), the expansion to the physical domain would include geometrically perturbed eigenvectors in a C-B matrix,

$$[\Phi_{NNMA}^{cb}]_k = \begin{bmatrix} I & 0 \\ \Phi_k^c & \Phi_k^n \end{bmatrix} \quad (4.39)$$

where the subscript  $NNMA$  refers to the use of geometrically perturbed airfoil substructures. The expansion to physical space for this approach is then

$$u_k = [\Phi_{NNMA}^{cb}]_k [A_{NMA}]_k \quad (4.40)$$

Should this approach be accurate, a reduced-order approximation of the modal quantities could improve solution times. Because the NMA with geometrically perturbed substructure expansion results show an improvement over nominal-mode expansion, but still have significant error, the approximation approach is not pursued.

#### 4.2.2.4 Non-Nominal Mode Approach with Geometrically-Perturbed FEM

##### Mode Shapes

While the above approaches gain efficiency using the nominal-mode approximation, some quantifiable error will be introduced. To reduce this error, a non-nominal mode approach (NNMA) with geometrically-perturbed FEM mode shapes ( $\phi_{FEM}$ ) are used in C-B CMS substructure development. In the limit, this approach will provide the exact solution. This is considered the use of a conventional analysis technique, C-B CMS, to the novel application of geometric mistuning.

In this approach the nominal mode approach is used to transform the physical substructures to the Craig-Bampton domain, coupled, and the resulting reduced system eigenproblem is

$$\hat{K}_{NNMA} [\alpha_i]_{NNMA} = \lambda_i \hat{M}_{NNMA} [\alpha_i]_{NNMA} \quad (4.41)$$

where the modal participations have been computed using the non-nominal mode approximation,  $[\alpha_i]_{NNMA}$ .

The expansion to physical space for this approach is then

$$u_k = [\Phi_{NNMA}^{cb}]_k [A_{NNMA}]_k. \quad (4.42)$$

Because only a subset of the IBR DOF are perturbed with airfoil mistuning, effective substructuring will lead to computational advantages. A large percentage, frequently over

50%, of the IBR DOF are located in the disk substructure of the IBR. Since this substructure is not altered during blade geometry perturbations, isolating the disk as a CMS substructure, enables a single solution of this large model for all successive solutions of  $\hat{K}\alpha_i = \lambda_i \hat{M}\alpha_i$ . Additional efficiencies are possible by using a disk cyclic symmetry analysis to efficiently create the C-B matrix for the disk substructure. Each blade is considered as a separate substructure and each can be efficiently modeled because of the relatively small number of DOF relative to the entire rotor.

With each airfoil being a separate substructure coupled to the larger disk substructure, additional efficiencies can be enabled through maximizing the value of each airfoil reduced-order substructure once it has been calculated. The value can be maximized by reusing the airfoil substructures to create multiple assembled mass and stiffness matrices by randomly selecting from a generated library of airfoil substructures. In this approach a reduced set of airfoil substructures are generated ( $\sim 100$ ) and are randomly sampled from  $n$  times where  $n$  is the number of IBR airfoils. This approach is similar to the statistical bootstrapping technique. Bootstrapping is the process of sampling from a small population of data where the bootstrap sample is some number smaller than the number of population samples. Because mistuning is heavily dependent on the pattern of mistuned blades around the rotor, this bootstrapping approach will accelerate prediction of the range of response. Accuracy of this approach is dependent on the number of bootstrapping samples and the assumption that the small bootstrap sample accurately represents the full rotor population. Previous research has shown that small samples of mistuned rotors can accurately represent the full population [8].

#### 4.2.2.5 Non-Nominal Mode Approach with Approximate Perturbed Mode Shapes

A NNMA with approximate airfoil substructure C-B matrices will reduce the computational time associated with the solution approach of the previous subsection. For the local approximation approach used in this chapter, a numerical approach is used to calculate constraint mode sensitivities

$$\frac{\partial [\phi_i^c]}{\partial \psi_j} \approx \left( \frac{[\phi_i^c]^{(0+\Delta\psi_j)} - [\phi_i^c]^0}{\Delta\psi_j} \right) \quad (4.43)$$

where  $\phi_i^c$  is the constraint mode for the  $i^{th}$  constraint mode. The approximate constraint mode for the  $k^{th}$  substructure is calculated using the Taylor series expansion

$$[\tilde{\phi}_i^c]_k = [\phi_i^c]^0 + \sum_{j=1}^{n_p} \frac{\partial [\phi_i^c]^0}{\partial \psi_j} \Delta [\psi_j]_k \quad (4.44)$$

where  $d[\psi_j]_k$  is the change in principal component mode for the  $k^{th}$  airfoil.

To explicitly account for geometric effects, the fixed-boundary normal modes,  $\Phi^n$ , must also account for modal variations. Each vector in  $\Phi^n$  should contain the eigenvectors of the random airfoil. Rapid prediction of these eigenvectors is possible using

$$[\tilde{\phi}_i^n]_k = [\phi_i^n]^0 + \sum_{j=1}^{n_p} \frac{\partial [\phi_i^n]^0}{\partial \psi_j} \Delta [\psi_j]_k \quad (4.45)$$

where the sensitivities of the substructure mode shapes are calculated numerically

$$\frac{\partial \phi_i^n}{\partial \psi_j} \approx \left( \frac{[\phi_i^n]^{(0+\Delta\psi_j)} - [\phi_i^n]^0}{\Delta\psi_j} \right). \quad (4.46)$$

A significant advantage to this method is that the sensitivities will be calculated for the blade-alone models rather than the cyclic symmetry models that, because of the repeated



roots, are difficult to accurately calculate.

With the ability to efficiently calculate random constraint and fixed-boundary normal modes the Craig-Bampton matrix is random

$$\tilde{\Phi}_k^{cb} = \begin{bmatrix} I & 0 \\ \tilde{\Phi}_k^c & \tilde{\Phi}_k^n \end{bmatrix} \quad (4.47)$$

which can be used to transform the perturbed physical domain mass and stiffness matrices to the modal domain. The physical domain matrices are also perturbed from nominal and their sensitivity can be computed numerically

$$\frac{\partial K}{\partial \psi_j} = \begin{bmatrix} \frac{\partial k^{bb}}{\partial \psi_j} & \frac{\partial k^{bi}}{\partial \psi_j} \\ \frac{\partial k^{ib}}{\partial \psi_j} & \frac{\partial k^{ii}}{\partial \psi_j} \end{bmatrix}$$

where each partition is numerically calculated. The variation in the mass matrix is identically determined.

With these sensitivities, random computation of the relevant reduced matrices is

$$\tilde{k}^{bb} = [k^{bb}]^0 + \sum_{j=1}^{n_p} \frac{k^{bb}}{\partial \psi_j} d\psi_j + \left[ [k^{bi}]^0 + \sum_{j=1}^{n_p} \frac{k^{bi}}{\partial \psi_j} d\psi_j \right] \tilde{\Phi}^c \quad (4.48)$$

$$\tilde{m}^{bb} = \left[ [m^{bb}]^0 + \sum_{j=1}^{n_p} \frac{m^{bb}}{\partial \psi_j} d\psi_j \right] + [\tilde{\Phi}^c]^T \left[ [m^{ib}]^0 + \sum_{j=1}^{n_p} \frac{m^{ib}}{\partial \psi_j} d\psi_j \right] + \dots$$

$$\dots \left[ [m^{bi}]^0 + \sum_{j=1}^{n_p} \frac{m^{bi}}{\partial \psi_j} d\psi_j \right] \tilde{\Phi}^c + [\tilde{\Phi}^c]^T \left[ [m^{ii}]^0 + \sum_{j=1}^{n_p} \frac{m^{ii}}{\partial \psi_j} d\psi_j \right] [\tilde{\Phi}^c] \quad (4.49)$$

$$\tilde{m}^{bi} = [\tilde{m}^{ib}]^T = \left[ [m^{bi}]^0 + \sum_{j=1}^{n_p} \frac{m^{bi}}{\partial \psi_j} d\psi_j \right] \tilde{\Phi}^n + \dots$$

$$\dots [\tilde{\Phi}^c]^T \left[ [m^{ii}]^0 + \sum_{j=1}^{n_p} \frac{m^{ii}}{\partial \psi_j} d\psi_j \right] [\tilde{\Phi}^n] \quad (4.50)$$

where  $\psi_j$  are from the PCA results. The random reduced matrix  $\tilde{k}^{ii}$  is calculated via eq. 4.36 and  $\tilde{m}^{ii}$  is always the identity matrix.

The eigenproblem of the reduced-order system

$$\tilde{K}_{NNMA} [\alpha_i]_{NNMA} = \lambda_i \tilde{M}_{NNMA} [\alpha_i]_{NNMA} \quad (4.51)$$

and the solution in physical space is

$$\tilde{u}_k = [\tilde{\Phi}_{NNMA}^{cb}]_k [A_{NNMA}]_k. \quad (4.52)$$

## 4.3 Results

The methods developed in the prior section are demonstrated on the Advanced Low Aspect Ratio Fan (ADLARF), Figure 4.1, which is representative of modern IBR designs. This IBR is sensitive to mistuning and has been rigorously studied under the GUIde (Government, University, Industry) consortium to fund research in turbomachinery forced response [90, 100]. Because airfoil geometry measurements are not available for this rotor, measured deviations from a representative industrial IBR fan stage are used. The applied deviations are identical to those used in a prior work developing blade-alone reduced order models [99]. An exaggerated geometrically perturbed airfoil, with deviations scaled by more than 100 times, is shown in Figure 4.2 to show the representative shape of the distortion. Without scaling for this figure, the true deviations would not be visible. Results from a geometrically perturbed 360-degree FEM provide the benchmark results for each of the mistuning approximation techniques.

The full rotor FEM, shown in Figure 4.3, uses 13952 linear hexahedral elements, 22784 nodes, 67776 active DOF, Ti-6-4 material properties, and is fixed in all directions at its aft flange as shown in Figure 4.4. Predicted modal responses are used in a modal harmonic forced response analysis with each airfoil loaded circumferentially at each airfoil's leading edge tip node. While not representative of in-flight loads, this does replicate conventional traveling wave bench testing procedures [101]. A constant damping ratio,  $\zeta$ , of 0.002 is used for the forced response calculations. Results are shown for in-phase loading, representing a zero nodal diameter forcing condition. Forced response results are investigated between 4 kHz and 6.5 kHz which showed three excited modes of interest. Table 4.1 shows the fixed-boundary resonant frequencies for the nominal airfoil geometry. The modes of interest in this analysis are modes eleven, thirteen, and seventeen (M11, M13, and M17). These were the first set of modes excited to a significant degree by the zeroth harmonic excitation that showed a difference between the nominal-mode approximation and full model. Based on the full rotor mistuned and tuned analyses, the mistuning amplification at these modes is 1.29x, 2.33x, and 1.22x. Tuned and geometrically perturbed fixed-boundary airfoil substructures are used for the CMS mistuning methods. Both the full rotor validation FEM and CMS airfoil substructures are constructed with a parametric model that retains element number and topology to ensure consistency for each geometrically perturbed airfoil. The full rotor models are constructed with a continuous mesh between airfoil and disk substructures. Modal results and structural matrices are output from a commercial FEM code and used in software algorithms written to implement the methods defined in the prior sections.

All mistuning methods are based on a C-B CMS solution composed of one disk substructure and 16 airfoils substructures. With the defined mesh density, the full FEM contains 67,776 DOF, leading to  $67,776 \times 67,776$  matrices. This is a coarse model compared to industry standard meshing practices, but useful for demonstrating the developed methods.

The CMS solution includes the airfoil substructures with 34 nodes at the disk-airfoil boundary, which leads to 102 boundary DOF per airfoil. Accounting for the entire rotor, there are 1632 total boundary DOF. To provide accurate results through a frequency range between 0 Hz – 6.5 kHz, 50 airfoil substructure cantilevered airfoil modes shapes and 200 disk substructure mode shapes were required. The number of retained modes was determined through a convergence between the full FEM and the CMS solution with a criteria set to have the maximum mistuning predictions to be within 1%. This led to a reduced-order CMS matrix size of  $2632 \times 2632$ .

Two types of results are considered in the following subsections. First, maximum rotor forced responses are considered that show the peak forced response of the IBR. These results give important response information over a wide range of frequencies. The second type of result is blade-to-blade forced response. These results are shown at the maximum forced response frequencies, selected from the maximum rotor forced response plots. The blade-to-blade results show if the developed methods are accurately predicting response at a local level. The results at the local level give a better indication of the methods ability to model the physics of mistuning. The results at the blade level are also significant for defining the statistics of stress variation as part of a probabilistic mistuning assessment.

#### **4.3.1 Nominal Mode Approach with Geometrically-Perturbed FEM Airfoil Modal Stiffnesses**

The first result case uses NMA- $\lambda_{FEM}$  for airfoil substructure reduction and geometrically mistuned airfoil FEMs to generate the eigenvalues used to determine modal stiffness input for  $\hat{k}_k^{ii}$ . Figure 4.5 compares the maximum rotor response, in inches, predicted by the NMA- $\lambda_{FEM}$  and the geometrically-perturbed IBR FEM between 4 kHz to 6.5 kHz. While differences exist, the NMA- $\lambda_{FEM}$  predicts mistuning with sufficient quality (predicting

the modes having low or high mistuning amplifications) that its capabilities as a qualitative design tool are evident. The FEM predicted mistuning amplifications for M11, M13, and M17 are 1.29x, 2.33x, and 1.22x, and NMA- $\lambda_{FEM}$  predicts 1.30x, 2.76x, and 1.43x. Quantitatively, errors between the two approaches are evident and are considered in detail by plotting additional M11, M13, and M17 results in Figures 4.6-4.17.

The expanded M11 results in Figure 4.6 show generally good agreement between the maximum rotor response predictions. The tuned peak is at 4319 Hz. with an amplitude of 0.009261 in., the maximum FEM peak is at 4331 Hz. with amplitude 0.01192 in. (1.29x), and NMA- $\lambda_{FEM}$  predicts the peak at 4319 Hz. with amplitude 0.01203 in. (1.30x). The nominal-mode approximation appears to have produced a very accurate result when considering overall IBR mistuning amplification, though with a 12 Hz. error in predicted peak frequency. Obvious differences in amplitudes exist at specific frequencies with the largest difference at 4319 Hz, where NMA- $\lambda_{FEM}$  predicts its largest response and overpredicts the FEM response by 16%. For a more detailed accuracy assessment, blade-to-blade amplitudes are plotted at three frequencies.

Figure 4.7 compares blade-to-blade amplitudes predicted from the FEM results at 4331 Hz. and the NMA- $\lambda_{FEM}$  results at 4319 Hz., i.e. the comparison at predicted peak mistuning frequencies. There are significant differences and NMA- $\lambda_{FEM}$  fails to accurately predict the pattern of mistuning amplification, underpredicting the peak responding blade 1 by 42% and overpredicting blade 10 by 98%. This error is driven by the difference in peak response frequencies, and shows that an attempt to predict blade-to-blade response with NMA- $\lambda_{FEM}$  at the peak mistuning frequency would result in large errors for M11.

Errors are less severe when comparing method results at the same frequency. Figure 4.8 compares results at the NMA- $\lambda_{FEM}$  predicted peak of 4319 Hz. At blade 1, NMA- $\lambda_{FEM}$  underpredicts by 10%, and at blade 10 NMA- $\lambda_{FEM}$  overpredicts peak response by a more reasonable 19%. It is also seen that NMA accurately predicts the mistuning response

pattern.

Figure 4.9 compares results at the FEM predicted peak of 4331 Hz., and again results look much more favorable than in Figure 4.7. For blade 1, NMA- $\lambda_{FEM}$  under predicts peak response by 6% and overpredicts blade 10 by 14%. As with Figure 4.8, the relative pattern of mistuning is accurately predicted.

It is encouraging and a credit to NMA- $\lambda_{FEM}$ , that for M11 the maximum IBR mistuning amplification was predicted within 1% and at specific frequencies the predicted blade response error was no greater than 20%. This does not mean that this error is negligible. A 20% overprediction of response could negatively impact a design in terms of excessive margin that would be realized in increased weight or reduced performance. The NMA- $\lambda_{FEM}$  also mispredicts the maximum peak frequency, and the prediction at 4319 Hz. would be incorrectly identified as the peak mistuning pattern. The accuracy of predicting IBR mistuning amplification is not as accurate for the M13 and M17 results.

Figure 4.10 compares the predicted peak rotor response for NMA- $\lambda_{FEM}$  and FEM for M13. The tuned response peak is at 4814 Hz. with amplitude 0.006215 in., the mistuned FEM peak is at 4793 Hz. with amplitude 0.01454 in. (2.33x), and the NMA- $\lambda_{FEM}$  peak is at 4796 Hz. with amplitude 0.01716 in. (2.76x). The NMA- $\lambda_{FEM}$  has overpredicted the FEM predicted maximum mistuning amplitude by 18%. This error is of sufficient magnitude that it could negatively impact IBR design decisions. The results also show a much smaller difference between predicted maximum response frequency, 3 Hz., which would suggest based on the M11 results that the blade-to-blade response at predicted peak frequencies would be similar.

Figure 4.11 compares the blade-to-blade results at both methods' predicted response peaks, and unlike the M11 results, the location of the maximum blade is predicted correctly. However, also unlike the M11 results, there are significant errors in the prediction of blade-to-blade response. Blade 2 underpredicts by 27%, blade 9 is overpredicted by 18%,

and blade 15 overpredicts by 149%. In general, blade mistuning sequence is predicted accurately with the exception of blade 15, which is significantly overpredicted. Based on the M11 results, these errors might be reduced when a comparison between methods is made at the same frequencies.

Figure 4.12 compares results at the FEM predicted maximum response frequency, 4793 Hz., and blade 2 underpredicted by 25%, blade 9 overpredicts by 17%, and blade 15 overpredicts by 146%. A very minor reduction in error was achieved at the 4793 Hz. comparison. The results at the NMA- $\lambda_{FEM}$  predicted maximum frequency, 4796 Hz., in Figure 4.13 show similar results to Figures 4.11-4.12 with only a minor change to error magnitude. Similar results were produced because of the small, 3 Hz., difference in peak frequency predicted by the full FEM and NMA- $\lambda_{FEM}$  models. It is important that in all cases the mistuning pattern was incorrectly predicted, primarily because of the significant error at blade 15.

Use of NMA- $\lambda_{FEM}$  for M13 shows the need for improved mistuning modeling approaches. While it does qualitatively predict IBR mistuning amplification, the 18% error in predicted maximum IBR mistuning and the 146% error in predicting the blade 15 response could negatively impact a design's weight and performance. The errors on specific blades could create problems when predicting the statistics of mistuned response. For example, results for M13 would show a distribution of response with higher probabilities of large response because of the significant overprediction of the blade 15 response. Further research in the statistics predicted with the NMA- $\lambda_{FEM}$  approach compared to the the FEM approach are therefore recommended.

Figure 4.14 compares NMA- $\lambda_{FEM}$  and FEM predicted maximum rotor response for M17. The tuned response peak is at 6487 Hz. with amplitude 0.009109 in., the mistuned FEM peak is at 6473 Hz. with amplitude 0.01108 in. (1.22x), the NMA- $\lambda_{FEM}$  peak is at 6497 Hz. with amplitude 0.01304 in. (1.43x). The NMA- $\lambda_{FEM}$  result has overpredicted

the FEM result by 18%. The figure also shows that the predicted rotor resonant response peak adjacent to the maximum peak, at 6449 Hz., is significantly overpredicted by 84%. This error is significant and shows a limitation of NMA- $\lambda_{FEM}$ .

Continuing the analysis of M17, Figure 4.15 compares the blade-to-blade results at both methods' predicted peaks. The location of the maximum blade, blade 2, is not predicted correctly by NMA- $\lambda_{FEM}$  which predicts the maximum at blade 15. Instead, it underpredicts the peak at blade 2 by 29%, and overpredicts blade 15 by 59%. There is also a 46% underprediction of airfoil 9 and 49% underprediction of blade 10. There is a 24 Hz. difference in the methods' predicted peaks, so as with M11, it is possible that results will improve when methods are compared at the same frequencies.

Results at the frequency peak predicted by full FEM, 6473 Hz., are shown in Figure 4.16. Similar results to those in Figure 4.15 are found with blade 2 underpredicted by 35%, blade 15 overpredicted by 49%, 45% underprediction of blade 9, and 43% underprediction of blade 10. Results at the frequency peak predicted by NMA- $\lambda_{FEM}$ , 6497 Hz., shown in Figure 4.17, show the larger overpredictions with a 90% overprediction at blade 15. In each figure, the pattern of mistuning is not correctly predicted.

In summary, the NMA- $\lambda_{FEM}$  approach did not reliably predict the peak responding airfoil location, predicted maximum rotor mistuned amplification with significant errors ( $\sim 20\%$ ), and showed dramatic errors in blade-to-blade response predictions ( $>100\%$ ). This error can have ramifications on probabilistic calculations which consider not just the peak blade, but all blades on the rotor [98]. A nominal-mode approximation does qualitatively, identifying high and low mistuning amplifications, represent the mistuned response of a geometrically mistuned rotor to a degree that enables its useful application in design. But as a quantitative tool, the approach could lead to inaccurate design decisions. A suggest scenario would be a mistuning screening be conducted with the a nominal-mode approach and for critical modes near design constraints, a more accurate method such as developed



in Subsection 4.2.2.4 and 4.2.2.5 should be applied.

The NMA- $\lambda_{FEM}$  approach uses FEMs of geometrically-perturbed airfoils to provide modal stiffness perturbations. These finite element simulations contribute to the computational time required for the solution. Reducing the solution time associated with the modal stiffness perturbation would benefit the design process and enable a more thorough exploration of the mistuned response given a fixed computational budget. The following subsection applies approximate modal methods to predict substructure mistuning to reduce the computation cost of the approach while retaining its qualitative prediction capability.

### **4.3.2 Nominal Mode CMM with Approximate Airfoil Modal Stiffness Perturbation**

The prior subsection illustrated the ability of NMA- $\lambda_{FEM}$  to qualitatively predict mistuned amplifications, but was based on geometrically-perturbed airfoil FEMs to provide modal stiffness perturbations. This section uses the approximate the airfoil modal eigenvalue prediction approach described in Subsection 4.2.2.2 to generate the mistuned modal stiffnesses at virtually no computational cost. These results will determine if the errors introduced by the approximations negatively impact the qualitative prediction capability. Results comparing the approximations of geometrically-perturbed cantilevered airfoil frequencies are shown followed by their impact on predicted mistuned forced response with a nominal mode approach.

Figure 4.18 compares predicted blade-to-blade frequencies for M11 from the full geometrically-perturbed airfoil FEM,  $\omega_{FEM}$ , and the approximate approach,  $\omega_a$ , described in Subsection 4.2.2.2. The approximate model qualitatively represents the FEM results well, demonstrating the ability to capture the high and low frequency airfoils and the overall pattern of frequency variation. The FEM predicted range from minimum to maximum frequency is

157 Hz., the average difference between approximate and FEM predictions is 3.2 Hz., and the maximum difference is 8.2 Hz. at blade 9. The predicted frequencies from the FEM and approximate method are then used to predict the mistuned M11 frequency response.

Figure 4.19 shows three rotor frequency response functions (FRF) for M11 that compare  $NMA-\lambda_{FEM}$ ,  $NMA-\lambda_a$ , and the FEM results. The offset in FRF peaks caused by the errors in the approximate model are evident at several peaks. While many of the peaks predicted by either NMA solution have nearly the same amplitude, there is a significant difference at the peak frequency predicted by  $NMA-\lambda_{FEM}$ , 4318 Hz. At this frequency,  $NMA-\lambda_a$  predicts 0.009247 and  $NMA-\lambda_{FEM}$  0.01203, a 30% increase in predicted response. This variation in response is caused by the small variations in frequency shown in Figure 4.18. This large mistuned forced response variation demonstrates the impact of eigenvector sensitivity in the presence of a system with closely spaced frequencies. While generally well known that mistuning is sensitive to frequencies, the literature does not explore how sensitive it is and these results provide a realistic demonstration. Despite the demonstrated sensitivities, the results do not significantly change the qualitative accuracy of the  $NMA-\lambda_a$  prediction and are therefore concluded to be acceptable to qualitatively predict mistuned response. The  $NMA-\lambda_a$  underpredicts peak mistuned amplification by 2.9% and  $NMA-\lambda_{FEM}$  overpredicts by 1%. Analysis of the M13 provides additional evidence to support this finding.

Figure 4.20 compares predicted blade-to-blade frequencies for M13 from the full geometrically-perturbed airfoil FEM,  $\omega_{FEM}$ , and the approximate approach. Again,  $\omega_a$  shows excellent qualitative prediction of  $\omega_{FEM}$ . The FEM predicted range from minimum to maximum frequency is 118 Hz., the average difference between approximate and FEM predictions is 1.45 Hz., and the maximum difference is 7.2 Hz. at blade 11. The predicted frequencies from the FEM and approximate method are then used to predict the mistuned M13 frequency response.

Figure 4.21 plots maximum rotor response FRFs for M13 from the different modal stiffness models and the FEM result. The NMA- $\lambda_a$  overpredicts peak mistuned amplification by 12.6% and NMA- $\lambda_{FEM}$  overpredicts by 18%. This apparent improvement in accuracy is a function of the input frequency error and error induced by the nominal mode approximation, not a improvement in the physics-based modeling. At the second large peak in the response at 4867 Hz., a significant difference is again seen between the two input frequency arrangements, with the NMA- $\lambda_a$  solution overpredicting the NMA- $\lambda_{FEM}$  peak by 43%. Despite these quantitative differences in mistuned frequencies, the NMA- $\lambda_a$  qualitatively predict the mistuned amplification. The following M17 results continue to support this claim.

Figure 4.22 compares predicted blade-to-blade frequencies for M17 from the IBR FEM and the approximate approaches. Again, the approximate modal results show excellent modal stiffness prediction accuracy. The FEM predicted range from minimum to maximum frequency is 195 Hz., the average difference between approximate and FEM predictions is 8.9 Hz., and the maximum difference is 30.1 Hz. at blade 9. The predicted frequencies from the FEM and approximate method are then used to predict the mistuned M13 frequency response.

Figure 4.23 plots maximum rotor response FRFs for M17 from the models. Again, a clear difference is seen between the methods. The difference in predicted maximum mistuning response is small, with NMA- $\lambda_a$  overpredicts peak mistuned amplification by 15.1% and NMA- $\lambda_{FEM}$  overpredicts by 18.0%. The NMA- $\lambda_a$  results continue to overpredict the second highest FRF peak at 6449 Hz. by a significant margin. The improvement in NMA- $\lambda_a$  not a physics-based improvement, rather a fortunate result based on the input approximate frequencies and errors in the nominal mode approximation.

From these results, it can be concluded that approximate predictions of mistuned modal stiffnesses can be used to qualitatively predict mistuned response. Use of approximations

eliminate the solution cost for airfoil modal stiffness perturbation and therefore increases design tool throughput. Results from M13 and M17 reinforce the extreme sensitivity of mistuning predictions to modal stiffness input and indicate that for use of approximate methods in a quantifiably accurate prediction would require near exact approximations. This finding will recur in Subsection 4.3.5. As in the prior subsection, the method does not provide a quantitatively accurate result, showing that geometric deviations must be considered in more than airfoil modal stiffness perturbation. The following section applies a simplified approach to account for non-nominal mode shapes for the prediction of mistuned forced response.

### 4.3.3 Nominal Mode Approach with Non-nominal Mode Expansion

Incorporation of non-nominal mode shape information into the mistuning calculation can significantly increase computational costs. The results in this subsection are based on the method developed in Subsection 4.2.2.3 that uses nominal mode reduction of substructures, solution of the coupled substructures in the nominal domain, and expansion in the non-nominal domain. This approach assumes that the modal solution in the C-B basis is not sensitive to the difference in nominal and non-nominal substructures. This non-nominal mode expansion approach is annotated NMA-NNME- $\lambda_{FEM}$ . These results are based on using geometrically-perturbed airfoil FEMs to predict modal stiffness variation.

Figure 4.24 compares the M11 maximum rotor response results from NMA- $\lambda_{FEM}$  and NMA-NNME- $\lambda_{FEM}$ . The most significant change from NMA- $\lambda_{FEM}$  to NMA-NNME- $\lambda_{FEM}$  is that the latter predicts the peak mistuned response frequency within 1 Hz., whereas the NMA- $\lambda_{FEM}$  predicted peak is 12 Hz. higher. This difference results in NMA- $\lambda_{FEM}$  incorrectly predicting the maximum mistuning blade-to-blade response pattern, as shown

in Figure 4.7. Figure 4.24 shows that there has been some improvement in the predictions with the results of NMA-NNME- $\lambda_{FEM}$  generally closer to the FEM results, in particular for the 2<sup>nd</sup> – 6<sup>th</sup> and peaks. Predicted maximum response error has increased slightly with a NMA-NNME- $\lambda_{FEM}$  overprediction by 10% compared to the underprediction of 6% by NMA- $\lambda_{FEM}$  at the FEM predicted maximum response frequency. The blade-to-blade response data will give further detail on the effect of the NMA-NNME- $\lambda_{FEM}$  method.

Figure 4.25 shows the NMA- $\lambda_{FEM}$  and NMA-NNME- $\lambda_{FEM}$  results at the NMA-NNME- $\lambda_{FEM}$  predicted peak frequency, 4332 Hz., and the FEM results at its predicted peak frequency for M11, 4331 Hz. Unlike the results of Figure 4.7, the NMA-NNME predicts the mistuning pattern accurately. Because the NMA-NNME predicted the peak frequency and predicted the blade-to-blade mistuning sequence it appears that NMA-NNME is a qualitative improvement over NMA- $\lambda_{FEM}$  for M11. There is still uncertainty to whether this is an effect of error introduced by the non-nominal mode expansion or an actual physics-based improvement in the method. Analysis of M13 will provide further data to make a conclusion.

Figure 4.26 shows the NMA- $\lambda_{FEM}$  and NMA-NNME- $\lambda_{FEM}$  maximum rotor response results at M13, and its FRF shows the same form as that predicted with NMA- $\lambda_{FEM}$ . The predicted peak amplitude has dropped from 0.01716 in. to 0.01638 in., representing a reduction of error from 18% to 13% when compared to the FEM results. It is also observed that the error with the NMA-NNME- $\lambda_{FEM}$  method increased at the large peak at 4868 Hz. Analysis of predicted blade-to-blade response data gives further insight to the NMA-NNME- $\lambda_{FEM}$  solution.

Figure 4.27 compares the blade-to-blade response of NMA- $\lambda_{FEM}$  and NMA-NNME- $\lambda_{FEM}$  prediction at the full FEM predicted maximum response frequency. The improvement in predicted maximum response is seen at blade 9 while there is an even larger improvement in the prediction of the blade 15 response. There are significant improvements

at blades 3, 5, and 6 which are low response modes. While not demonstrating itself as a quantitative tool, there is an improvement with NMA-NNME- $\lambda_{FEM}$ . Because this figure shows improvements at several blades without significant increases in error at any blade, indicates that the NMA-NNME- $\lambda_{FEM}$  has enabled a physics-based improvement. A final mode is analyzed to support this conclusion.

Figure 4.28 compares the maximum rotor response results at M17 using NMA- $\lambda_{FEM}$  and NMA-NNME- $\lambda_{FEM}$ . Peak amplitude predicted by NMA-NNME- $\lambda_{FEM}$  has dropped from 0.01304 in. with NMA- $\lambda_{FEM}$  to 0.01190 in., a reduction in overprediction of the FEM results from 18% to 7.4%. The NMA-NNME- $\lambda_{FEM}$  approach is still clearly overpredicting the second FRF peak, but by a smaller percentage than NMA- $\lambda_{FEM}$ . Error does increase with the NMA-NNME- $\lambda_{FEM}$  away from the peak response at the 6300 Hz. Despite this, because of the reduction in error at the peak response, the results indicate an improvement in predictive accuracy. The blade-to-blade results provide more insight to the M17 results.

Figure 4.29 shows the blade-to-blade response predictions for the three methods at the FEM predicted maximum response frequency. The NMA-NNME- $\lambda_{FEM}$  solution shows improved results at blades 11, 13 and 15. There are also decreases in accuracy using NMA-NNME- $\lambda_{FEM}$ , notably at airfoils 7-10. Accuracy at the peak responding blade 2 was not appreciably changed nor has the approach enable the correct prediction of the mistuning sequence. For M17 use of NMA-NNME- $\lambda_{FEM}$  has not rigorously demonstrated that any reduction in errors are from physics-based improvements to the model.

It is concluded that the NMA-NNME- $\lambda_{FEM}$  approach is an improvement in nominal-mode predictions for some modes but, given the remaining errors and uncertainties in physics-based improvements, does not move the approach beyond a qualitative tool. The additional expense in computing the perturbed C-B matrix is therefore not necessarily compensated by a sufficient improvement in result. Its use would be dependent on cost to implement and the need for some level of qualitative improvement.

A brief analysis of the CMS results is included to identify the cause of the remaining error in the NMA-NNME- $\lambda_{FEM}$  solution. The NMA-NNME- $\lambda_{FEM}$  approach is based on the assumption that the predicted C-B basis eigenvectors,  $q$ , are not impacted by the difference between nominal and non-nominal basis vectors. To investigate this, Figure 4.30 plots the M13 cantilever blade mode participation of blade 9 for the nominal and non-nominal mode CMS solutions. It is noted that the order of the modes in the plot is inverted, i.e. the 50<sup>th</sup> mode is the 1<sup>st</sup> blade mode. It is seen that both approaches predict the same general trend of modal participation values, but with variations in magnitude. These variations in magnitude are the cause of the remaining error between in the NMA-NNME approach and full model result. This shows that for more accurate predictions, the non-nominal mode shape effects should be accounted for in the C-B basis eigenproblem, not just the expansion phase.

#### **4.3.4 Non-Nominal Mode Approach with Geometrically-Perturbed FEM Mode Shapes**

This section shows results for the NNMA method developed in Section 4.2.2.4. This represents the most accurate approach and, as will be described in Section 4.4, is more computational expensive than the other approximate methods. Each airfoils substructure is constructed with geometrically-perturbed FEM modal results for both nominal and constraint modes and the coupled solution is expanded in the non-nominal domain. To achieve near exact prediction of the FEM response, the NNMA results here were based on retaining 200 disk modes and 50 airfoil modes.

Figure 4.31 shows the NNMA maximum rotor response solution compared to the FEM and a near perfect fit is seen across the frequency range of interest. More detailed FRF results are shown for M11, M13, and M17 in the remainder of this subsection that show the accuracy of NNMA.

Figure 4.32 provides the more detailed rotor results at M11. The predicted peak using NNMA is 0.01188 in. which is a 0.03% difference between it and the FEM predicted peak. There are small errors at the two peaks adjacent to the maximum peak and these are both below 2.5 % error. Figure 4.33 shows the blade-to-blade amplitude results at the peak resonant condition, the same for both predictions, and the mistuning pattern is clearly predicted accurately.

Figure 4.34 shows the maximum rotor response results at M13 and again the NNMA predicted peak is 0.01469 in. which is a 1% over prediction of the FEM results. Though not shown, the blade-to-blade results show accurate prediction of the mistuning pattern.

Figure 4.35 shows the maximum rotor response result for M17 and again the NNMA predicted amplitude is 0.01121 in., an overprediction of 1%. As with the other modes, blade-to-blade predicted mistuning patterns are predicted accurately. This section demonstrates the excellent accuracy of the NNMA method and the usage of explicit geometric measurements to accurately predict mistuned response.

While there is a significant reduction in solution time compared to a IBR FEM, there is a significant increase in solution time compared to nominal mode approaches. The following section describes the results of using approximate frequency and mode shape predictions for airfoil substructures. This approach will reduce computational cost of NNMA with an impact on accuracy described in the following section.

### **4.3.5 Geometric Component Mode Mistuning with Approximate Perturbed Mode Shapes**

This section demonstrates the approximation of the airfoil substructure non-nominal mode shapes as described in Subsection 4.2.2.5. This is annotated as NNMA- $\lambda_a$ - $\phi_a$ . This approximation reduces the solution time required for mistuned response prediction but may



negatively impact accuracy.

Initial application of approximate mode shapes to the C-B matrix led to computational errors that required modification of the algorithm. The computational errors were caused by the approximate mode shapes leading to a non-positive definite mass matrices, specifically from the off-diagonal submatrices of the reduced mass matrix generated from Eq. 4.50. An investigation was conducted to determine and eliminate the errors, beginning with quantifying the accuracy of the mode shape approximations.

The Modal Assurance Criterion (MAC) is used to show the accuracy of the mode shape approximations. The MAC is calculated

$$MAC_{n_b, n_m} = \frac{\left( \tilde{\phi}_{n_b, n_m}^T \phi_{n_b, n_m} \right)^2}{\left( \tilde{\phi}_{n_b, n_m}^T \tilde{\phi}_{n_b, n_m} \right) \left( \phi_{n_b, n_m}^T \phi_{n_b, n_m} \right)} \quad (4.53)$$

where  $\tilde{\phi}_{n_b, n_m}$  and  $\phi_{n_b, n_m}$  are the approximate and FEM mode shapes. The MAC gives a scalar value that quantifies the linear relationship between the two vectors, 0 for orthogonal vectors and 1 for identical vectors. The MAC plot for the modal approximations for each of the 16 airfoils for the first twenty modes is shown in Figure 4.36. The MAC values are shown as a matrix of shaded boxes with their values shown by the contour bar. It is seen that very good accuracy is achieved with the approximations with no MAC value lower than 0.991. Conversely, Figure 4.37 shows the MAC values for modes 21-40. Here we see significant errors for several of the modes including 22, 32, and 33. It is not unexpected that approximation accuracy degrades at high frequency mode shapes as it was shown in Chapter 2 that approximation error increases with increasing mode.

To remove the approximation error at higher order modes, in this case those between 21 and 50, a nominal mode approximation for those modes is used. This hybrid approach uses non-nominal approximations for modes 1-20 and nominal mode approximation between 21 and 50. Because the modal participation for each substructure in the high order modes is

very small, shown in Figure 4.30, the nominal mode approximation should not significantly impact the solution.

With the hybrid approach, there are still numerical errors with the approximate mode shapes that give non-positive definite substructure mass matrices. The approximate mode shapes are only approximately mass normalized and approximately orthogonal with respect to the substructure mass and stiffness matrices. Transforming the substructure matrices to the reduced modal space therefore introduces off diagonal terms into the reduced matrices that are not present when using the true substructure mode shapes. Reorthogonalizing the approximate vectors with respect to each other is possible with a Gram-Schmitt approach but this may substantially change the mode shapes so that they no longer represent an efficient basis set.

Modifications are made to the method in Subsection 4.2.2.5 to correct for the use of approximately mass normalized and orthogonal mode shapes. First, the approximate mode shapes are mass normalized with respect to the mass matrix with the scale factor

$$s_{n_b, n_m} = \sqrt{\frac{1}{\tilde{\phi}_{n_b, n_m}^T M_{n_b} \tilde{\phi}_{n_b, n_m}}} \quad (4.54)$$

for each airfoil mode. Figure 4.38 illustrates the lack of approximate mode mass normality for an airfoil substructure transformed mass matrix. The figure is a 3-D bar chart that shows the value of the reduced mass matrix using the first 20 approximate modeshapes. Mass normalized vectors would give a diagonal of ones, while it can be clearly seen at modes 16 and 17 values that exceed this. It can also be seen in the figure that off diagonal terms, particularly at the modes 16 and 17, have non-zero values that would be expected if the approximate mode shape were orthogonal with respect to the stiffness and mass matrix. Because of the approximate mode shape's lack of orthogonality,  $m_{ii}$  is assumed to be the expected identity matrix. The  $k_{ii}$  matrix is also created from the approximate

frequency predictions,  $\omega_a$ , rather than the use of the approximate mode shapes to transform the stiffness matrix to the modal basis. Given these modification, the solution can be carried out across the frequency range of interest.

Figure 4.39 displays the FRF predicted from NMA- $\lambda_a$  and NNMA- $\lambda_a-\phi_a$  for M11. The NNMA- $\lambda_a-\phi_a$  overpredicts maximum mistuned response by 0.5%, compared to the NMA- $\lambda_a$  underprediction of 2.9%. Several other peaks are more accurately predicted with NNMA- $\lambda_a-\phi_a$ , including the first, second, fourth, ninth and tenth peaks. Other peaks are nearly unaffected, including the sixth and eleventh peak. It is also noted that inclusion of the approximate non-nominal modes has not reduced the error at the sixth peak, indicating that its error could be largely driven by the error in the approximate frequency input. The M11 results give evidence that the NNMA- $\lambda_a-\phi_a$  approach is quantitatively more accurate than NMA- $\lambda_a$ .

The results in Figure 4.39 include errors from both frequency and mode shape approximations. To remove this confounding effect, the exact FEM frequencies,  $\omega_{FEM}$ , are used with the approximate non-nominal mode shapes for the M11 results in Figure 4.40. The figure shows excellent NNMA- $\lambda_{FEM}-\phi_a$  FRF peak predictions across the frequency range with some overprediction at the two highest peaks. The first, third, fourth, fifth, sixth, ninth and tenth peaks are all predicted more accurately when compared with the NMA- $\lambda_{FEM}$  results. The result at the sixth peak shows the most encouraging results, with the NNMA- $\lambda_{FEM}-\phi_a$  predicting the peak within .002%. Conversely, the non-nominal mode approach has increased prediction error at the eighth peak. Given that all other peaks are more accurately predicted, the NNMA- $\lambda_{FEM}-\phi_a$  is a quantitative improvement compared to NMA- $\lambda_{FEM}$ .

A final analysis of M11, Figure 4.41, compares the predicted response using the approximate frequencies,  $\omega_a$ , and both approximate non-nominal modes and FEM non-nominal modes. The plot isolates the error introduced by the approximate non-nominal mode shapes

given the  $\omega_a$  frequencies. In all but one peak, the difference between the solutions is very small, only the second largest peak shows an appreciable difference. This demonstrates the effectiveness of approximate non-nominal mode shapes and gives evidence that accurate frequency approximation methods are more critical to accurate mistuning modeling. Analysis of the remaining modes gives further evidence on usage of approximate non-nominal mode shapes.

Figure 4.42 displays the FRF predicted from the NMA- $\lambda_a$  compared to the NNMA- $\lambda_a$ - $\phi_a$  for M13. For this mode there is a more significant difference between predicted FRFs, with the nominal mode approach predicting a single dominant peak while the non-nominal approach predicts two nearly equal peaks. NNMA- $\lambda_a$ - $\phi_a$  underpredicts the maximum amplitude by 9.0% while NMA- $\lambda_a$  overpredicts by 12.8%. Before considering these results further, the solution is performed using the exact frequencies.

Figure 4.43 illustrates the NNMA- $\lambda_{FEM}$ - $\phi_a$  and NMA- $\lambda_{FEM}$  solutions. A significant improvement using the NNMA- $\lambda_a$ - $\phi_a$  is shown. Rotor mistuned amplification error is reduced from the NMA- $\lambda_{FEM}$  value of 18.0% to 4.3%. At the second large response peak at 4867 Hz. NMA- $\lambda_{FEM}$  shows 22.4% underprediction while the NNMA- $\lambda_{FEM}$ - $\phi_a$  reduces error to an overprediction of 4.7%. When accurate frequencies are supplied to the NNMA- $\lambda_{FEM}$ - $\phi_a$  and NMA- $\lambda_{FEM}$  approaches, the improvement in the non-nominal approach is clear. These results reinforce the importance of accurate frequency approximation and the value of approximate non-nominal mode shape results.

To continue investigating the error caused by the approximate non-nominal mode shapes, the results using  $\lambda_a$  with both approximate non-nominal,  $\phi_a$ , and FEM non-nominal mode shapes,  $\phi_{FEM}$ , are shown in Figure 4.44. It is seen that use of the FEM non-nominal mode shapes increases underprediction of the FEM response, just as with use of the approximate non-nominal mode shapes. Use of the FEM non-nominal mode shapes underpredicted FEM results by to 8.7%. The NNMA- $\lambda_a$ - $\phi_a$  results closely match the NNMA- $\lambda_a$ - $\phi_{FEM}$

results whereas the NMA- $\lambda_a$  results in Figure 4.42 significantly overpredict them. Again, this shows the importance of accurate frequency input for mistuning modeling. A final mode is investigated to demonstrate the capabilities of NNMA- $\lambda_a$ - $\phi_a$ .

Figure 4.45 shows the FRF predicted from NNMA- $\lambda_a$ - $\phi_a$  for M18 compared with NMA- $\lambda_a$ . Though there is a increase in overprediction, 21.0% versus 14.3% for NMA- $\lambda_a$ , it demonstrates an improved ability to predict the magnitude of the second peak at 6448 Hz. which the NMA- $\lambda_a$  overpredicted by 44.0%. The NNMA- $\phi_a$  overpredicts the second peak by 5.2%. These encouraging results are followed by the assessment using the actual frequencies,  $\omega_{FEM}$ , with the solution approaches.

When the exact FEM frequencies are used in the NNMA- $\lambda_{FEM}$ - $\phi_a$  solution, Figure 4.46, the prediction in peak rotor response drops to 18.0% and the second peak prediction error drops to 2.4%. The NMA- $\lambda_{FEM}$  error, Figure 4.14, increase to 18% and overpredict the second peak by 59.2%. As demonstrated in M11 and M13, use of the actual airfoil frequencies and approximate non-nominal mode shapes more accurately predicted response than NMA- $\lambda_{FEM}$ .

Finally, Figure 4.47 shows the FRF results with  $\lambda_a$  for both NNMA- $\phi_a$  and NNMA- $\phi_{FEM}$ . Use of the FEM mode shapes with the approximate frequencies shows and improvement in accuracy with overprediction dropping to 10.5%. The results do show, when compared to the NMA- $\lambda_a$  results in Figure 4.45 that NNMA- $\lambda_a$ - $\phi_a$  more accurately predicts to FEM force response result.

Use of approximate non-nominal mode shapes in the construction of airfoil substructure C-B matrices significantly improves the accuracy of the mistuning prediction when compared to nominal mode approximation. It is found that the error in approximate frequencies plays the largest role in accuracy. This shows that future efforts should focus on improved frequency approximation. This reduces the challenge since the approximation of frequency, a scalar, is not as complex as approximation of mode shape, a vector. While not as accurate

as using exact FEM frequencies and mode shapes shown in the previous section but, in situations where computational speed may be desired over accuracy, the approximate method should be considered for application.

## 4.4 Computational Time

Figure 4.48 illustrates the time required for three mistuning solution approaches, FEM, C-B CMS, and approximate C-B CMS . Results are from the extraction of 100 mistuned modes which enables prediction of approximately a 1,000 Hz. range of frequency. As more mistuned modes are extracted the coupled substructure solution becomes a more significant portion of the CMS solution and eventually dominates the airfoil substructure solution. In practical applications, detailed analysis of a critical mode region would look at a relatively small range, which the 1,000 Hz. range of this solution time comparison considers. Each result is normalized by the total FEM solution time. The results do not include the time to construct the reduced disk substructure, which is similar in time to the FEM solution if the full rotor disk model is used. It's inclusion in the CMS solution times makes a single mistuning calculation with CMS unattractive. This computational cost is greatly reduced when a cyclically symmetric disk sector is used to generate the reduced disk substructure model. In either case, the purpose of the developed C-B models is for multiple mistuning pattern solutions and with each iteration the solution time of the reduced disk substructure becomes less significant. With these assumptions, the CMS solution showed a 50% reduction in solution time while the approximate C-B CMS solution showed a 69% reduction.

The C-B solution time results show that the construction time for airfoil substructures is nearly equal to the coupled substructure modal solution. This demonstrates the value of using reduced-order methods for their computation. The results showed the need for improved approximation methods for airfoil substructures, but in their absence there are

still approaches to reduce airfoil substructure solution time. First, the CMS approach is well suited for parallel processing and each airfoil substructure can be solved independently on a separate node. Second, once these substructures are created, they can be reused in alternate mistuning patterns by rotating the substructures to different rotor locations.

Though significantly more efficient than a FEM solution, the solution time of the CMS methods are substantially larger than nominal-mode mistuning methods. The larger cost is caused by the retention of a large number of airfoil modes (50), disk modes (200), and the C-B assumption on constraint modes. In prior mistuning efforts a much smaller number of airfoil modes is considered, typically a single mode shape and much reduced set of disk modes. Use of fewer modes in the geometrically perturbed rotor problem showed significant errors in the prediction which were deemed unacceptable. A detailed convergence study would be valuable to determine appropriate levels of mode retention given an allowable error budget. The need to retain the large number of modes demonstrates how mistuning impacts the mode shapes at the system level and is not simply a summation of a small set of retained modes.

Computational time could also be reduced by investigating the use of alternate constraint mode methods such as employed by REDUCE. In REDUCE, the constraint modes are found from the displacements on a massless airfoil models from the disk mode shapes. While the original results from REDUCE showed that this approach resulted in overly stiff response, it is possible that the inclusion of substantially more disk-induced constraint modes would reduce this effect. Reduction of constraint modes is an area worthy of further work.

## 4.5 Conclusions

Reduced-order methods have been developed that rapidly predict mistuned rotor response by approximating mistuning with a nominal-mode basis and airfoil modal stiffness perturbation. Nominal-mode approximation assumes that the geometry of each airfoil is identical and the geometric perturbations that alter modal stiffness do not perturb mode shape. This work investigates the accuracy of that approximation and develops several Component Mode Synthesis based reduced-order mistuning models that explicitly account for geometric deviations using both nominal and non-nominal mode shape approaches. The first represents the prevailing industry method and uses nominal-mode substructure reduction with airfoil substructure modal stiffnesses perturbed using geometrically-perturbed cantilevered airfoil finite element models. This approach demonstrates effective qualitative predictions that identify relative mistuning amplification but, when compared to analytical results from a geometrically-perturbed integrally bladed rotor model, shows significant ( $\sim 20\%$ ) errors in maximum predicted mistuning amplification. For blade-to-blade response prediction at specific frequencies, dramatic ( $>100\%$ ) errors are demonstrated. The second approach uses nominal-mode substructure reduction and mistuned airfoil modal stiffness perturbations from reduced-order modal methods. The reduced-order airfoil model reduces computational time while enabling qualitative mistuning prediction. The third method uses nominal-mode substructure reduction, mistuned modal stiffnesses from geometrically-perturbed airfoil finite element models, and expands results with a non-nominal Craig-Bampton matrix for each airfoil. Though improvements in quantitative prediction of maximum response frequency and response amplitudes are found for all modes, the method was inconsistent. The fourth approach uses non-nominal mode substructure reduction and expansion using non-nominal Craig-Bampton matrices generated from geometrically-perturbed finite element models. This approach demonstrates excellent



prediction of peak mistuning amplification and blade-to-blade response with prediction errors below 1%. A fifth approach uses reduced-order modal methods to approximate the non-nominal Craig-Bampton matrices. Use of these approximate mode shapes is found to significantly improve accuracy compared to the nominal-mode assumption but that overall performance is dominated by accurate frequency approximation. It is concluded that for rapid qualitative analysis, nominal-mode mistuning analysis with approximate mistuned modal stiffnesses should be used, for improved accuracy with additional computational expense approximate non-nominal mode mistuning analysis should be used, and with greater solution time and need for quantitative accuracy, geometrically perturbed finite element model results should be used in non-nominal Craig-Bampton reduction and expansion.

Mode	Hz.	Mode	Hz.
1	370.72	<i>11</i>	<b>4320.8</b>
2	1118.8	12	4660.5
3	1230.4	13	<b>4820.2</b>
4	1833.3	14	4914.6
5	2029.0	15	5454.1
6	2432.9	16	6315.8
7	2800.4	17	<b>6449.1</b>
8	3159.7	18	6627.1
9	3423.9	19	6799.8
10	3610.3	20	6989.4

Table 4.1: ADLARF Nominal Airfoil Frequencies

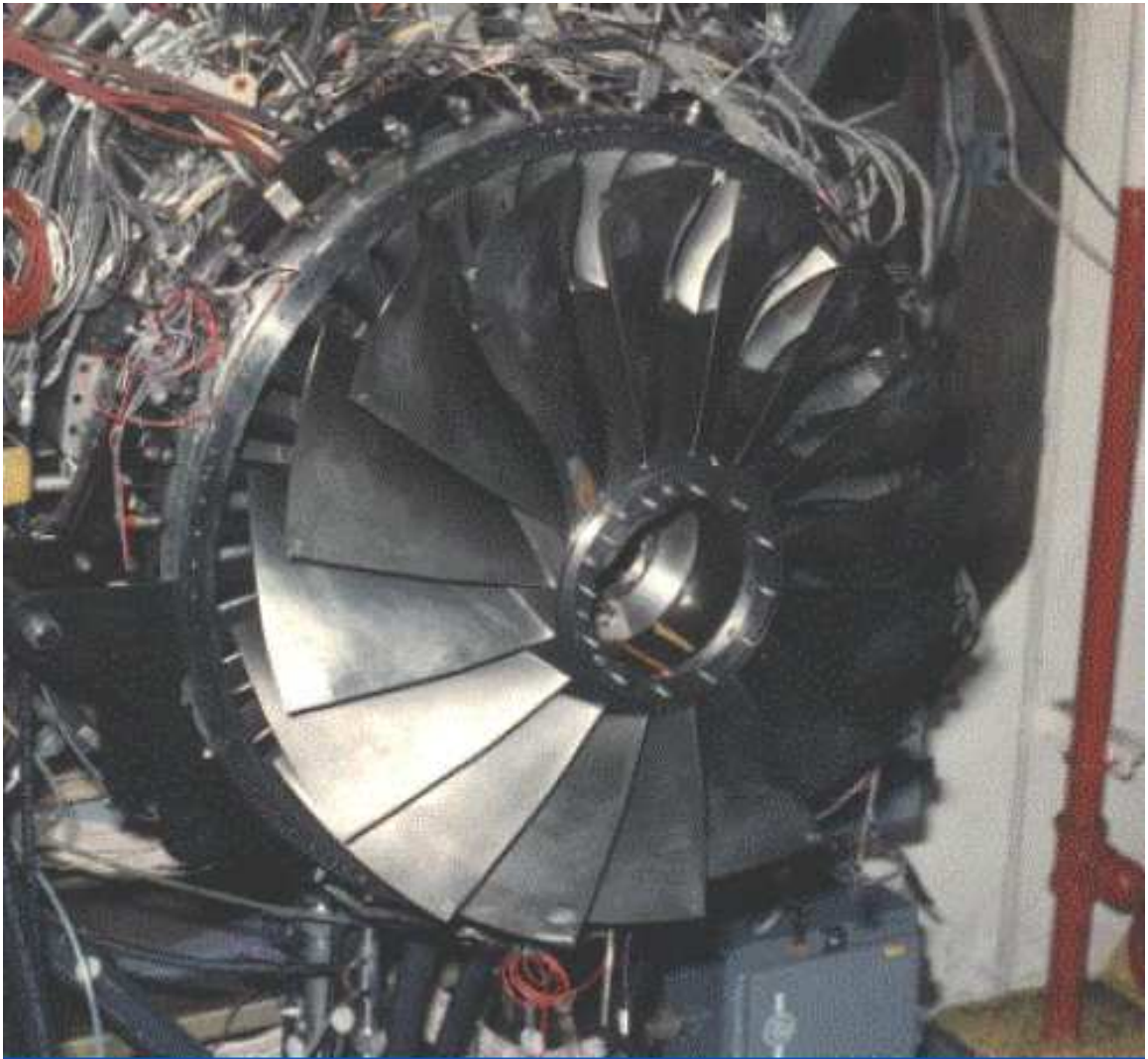


Figure 4.1: ADLARF Rotor

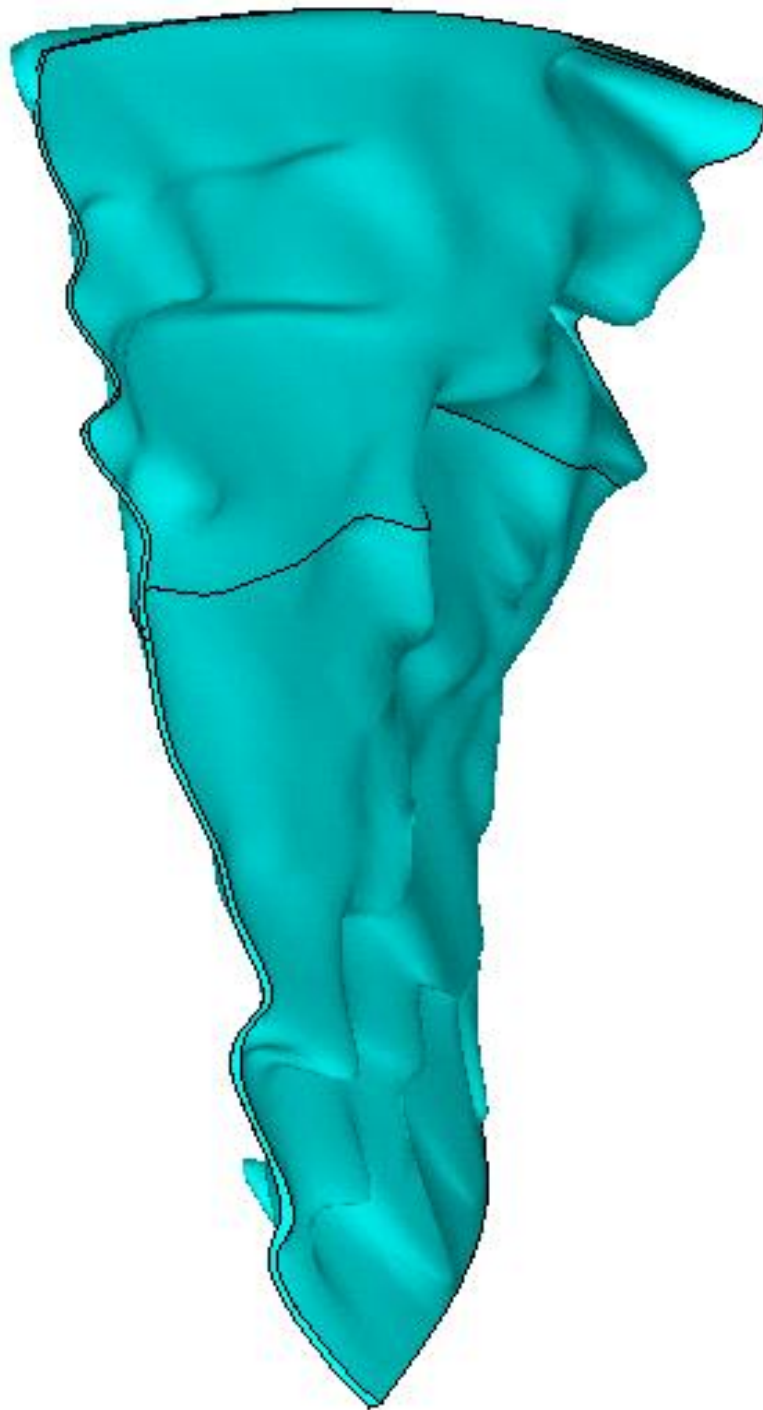


Figure 4.2: Geometrically Perturbed Airfoil Substructure (100x Magnification)

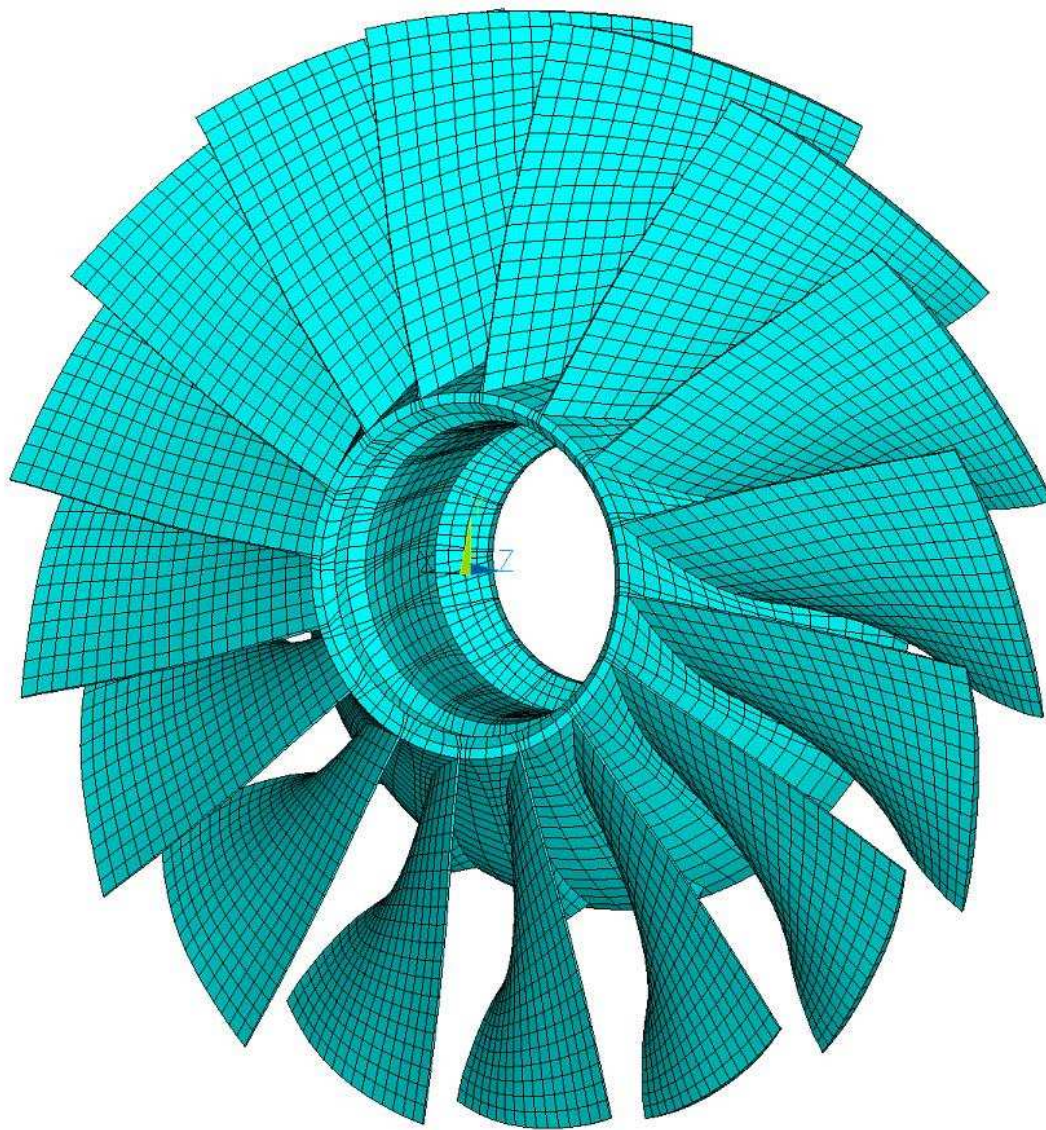


Figure 4.3: ADLARF Rotor FEM



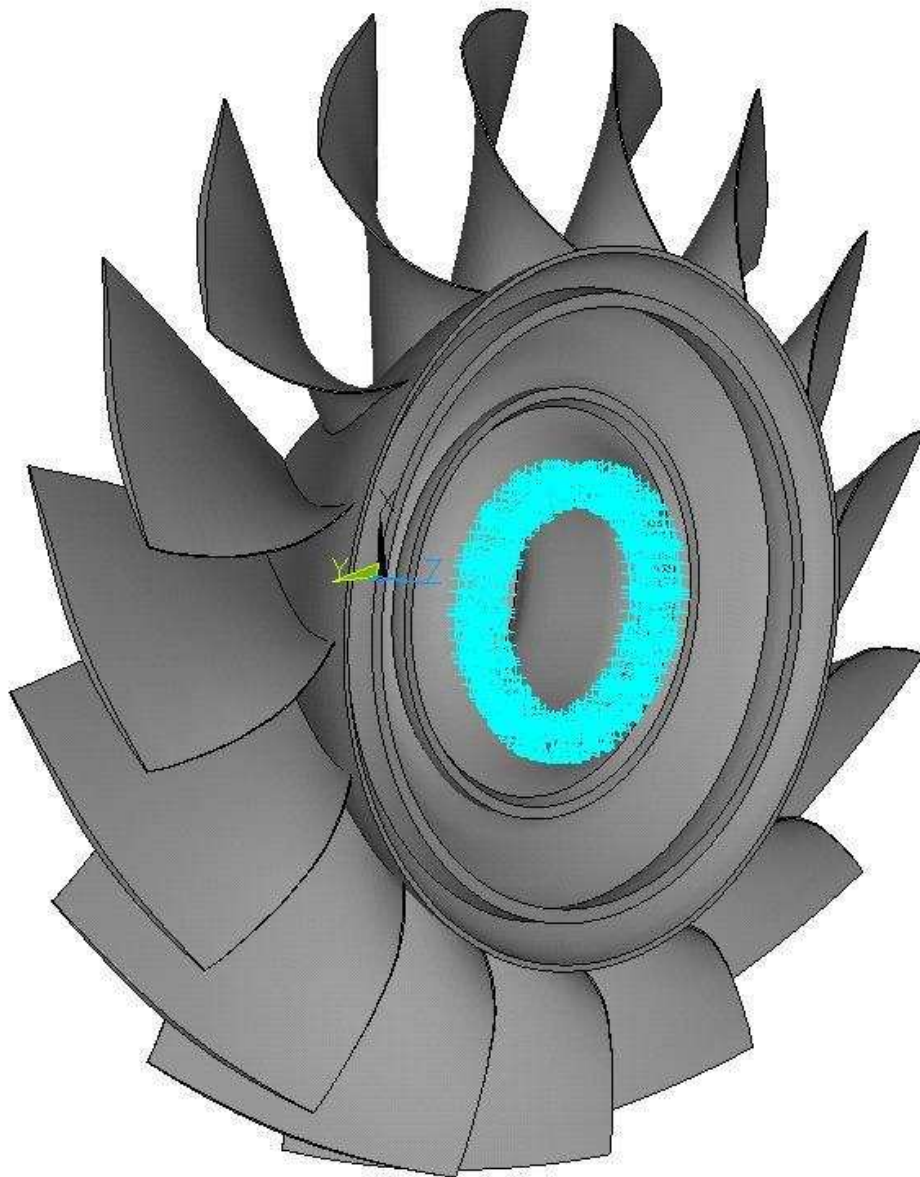


Figure 4.4: ADLARF Model Aft Flange Boundary Conditions

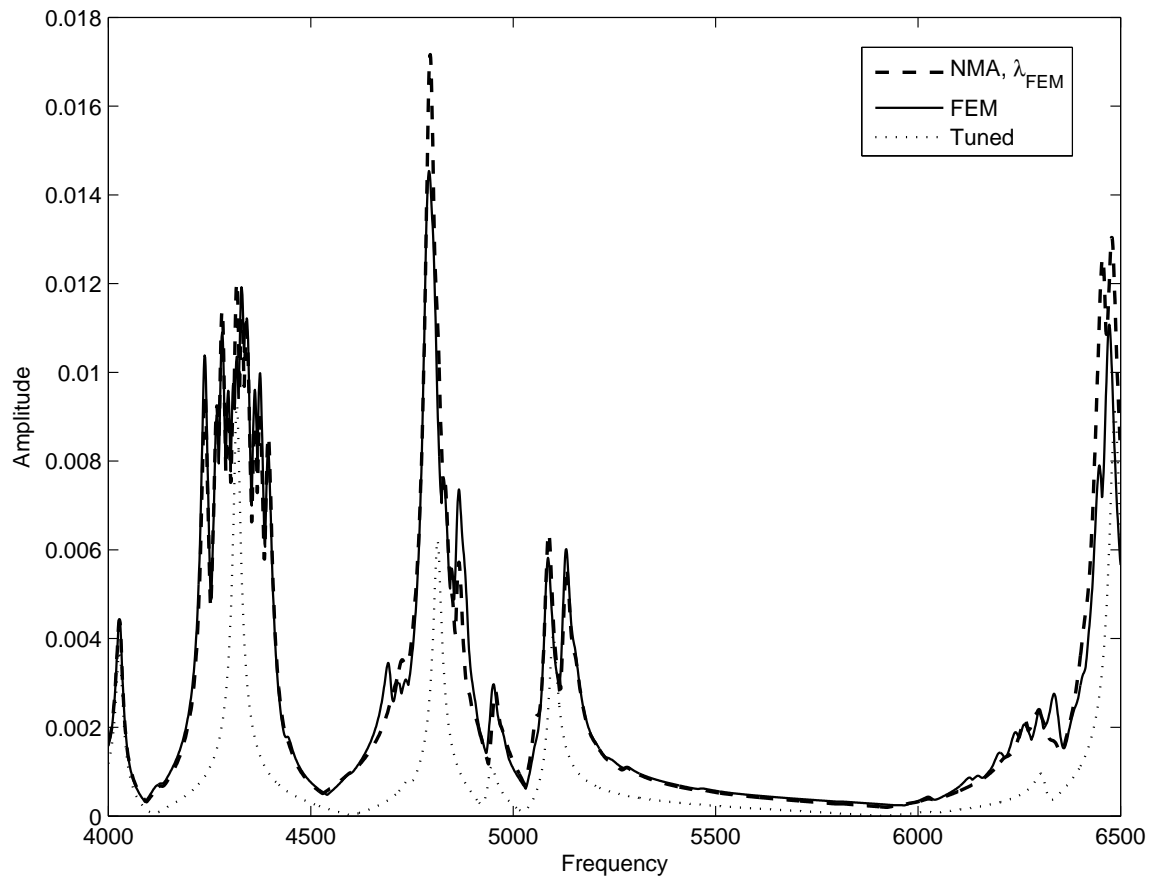


Figure 4.5: NMA-  $\lambda_{FEM}$  versus FEM Maximum Forced Response Prediction

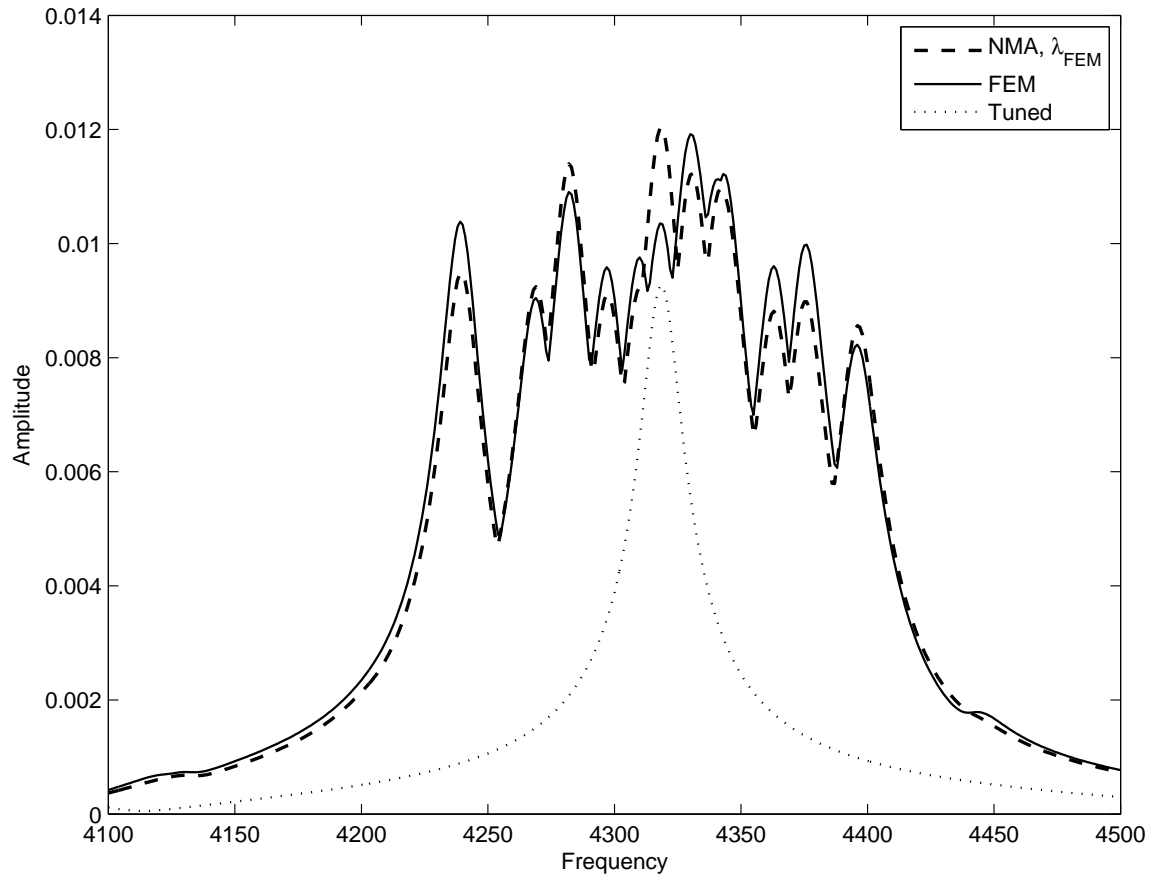


Figure 4.6: NMA  $-\lambda_{FEM}$  versus Full Model Maximum Forced Response - Mode 11



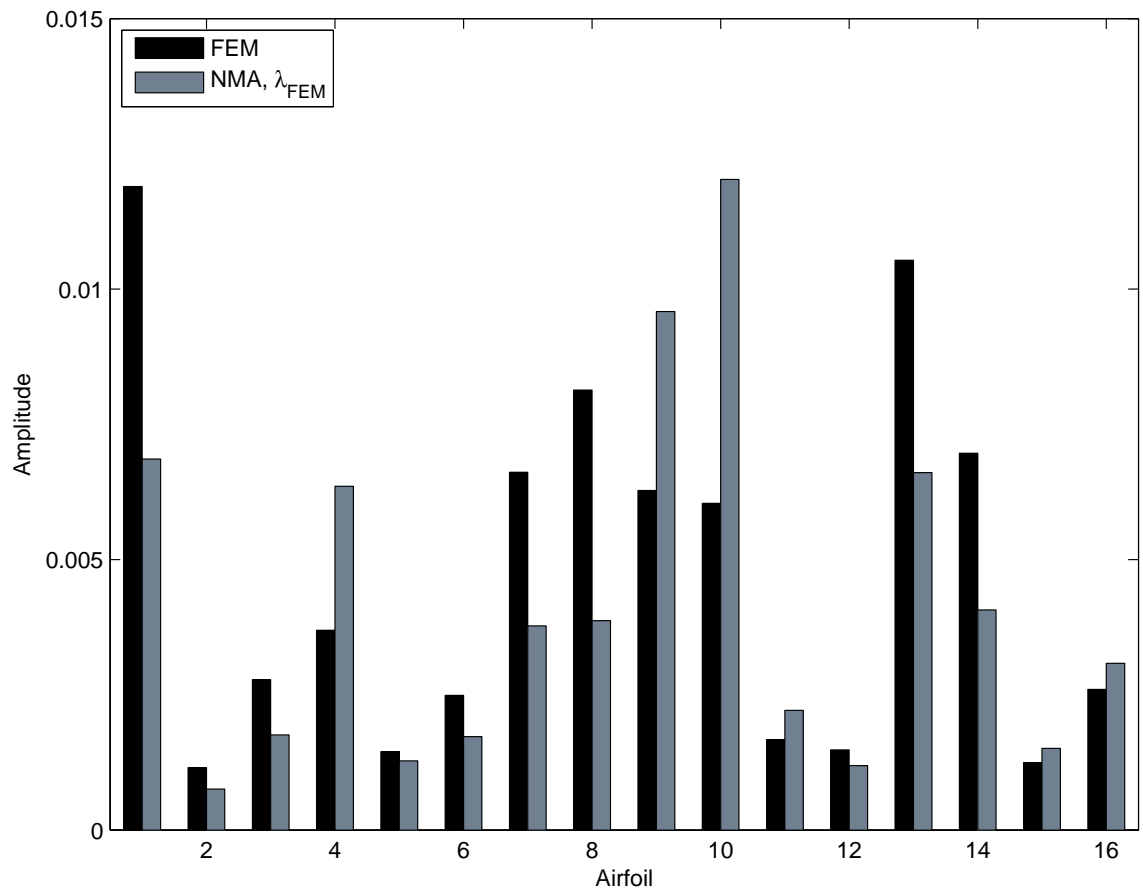


Figure 4.7: Blade-to-Blade Response at Maximum Response at Peaks - Mode 11

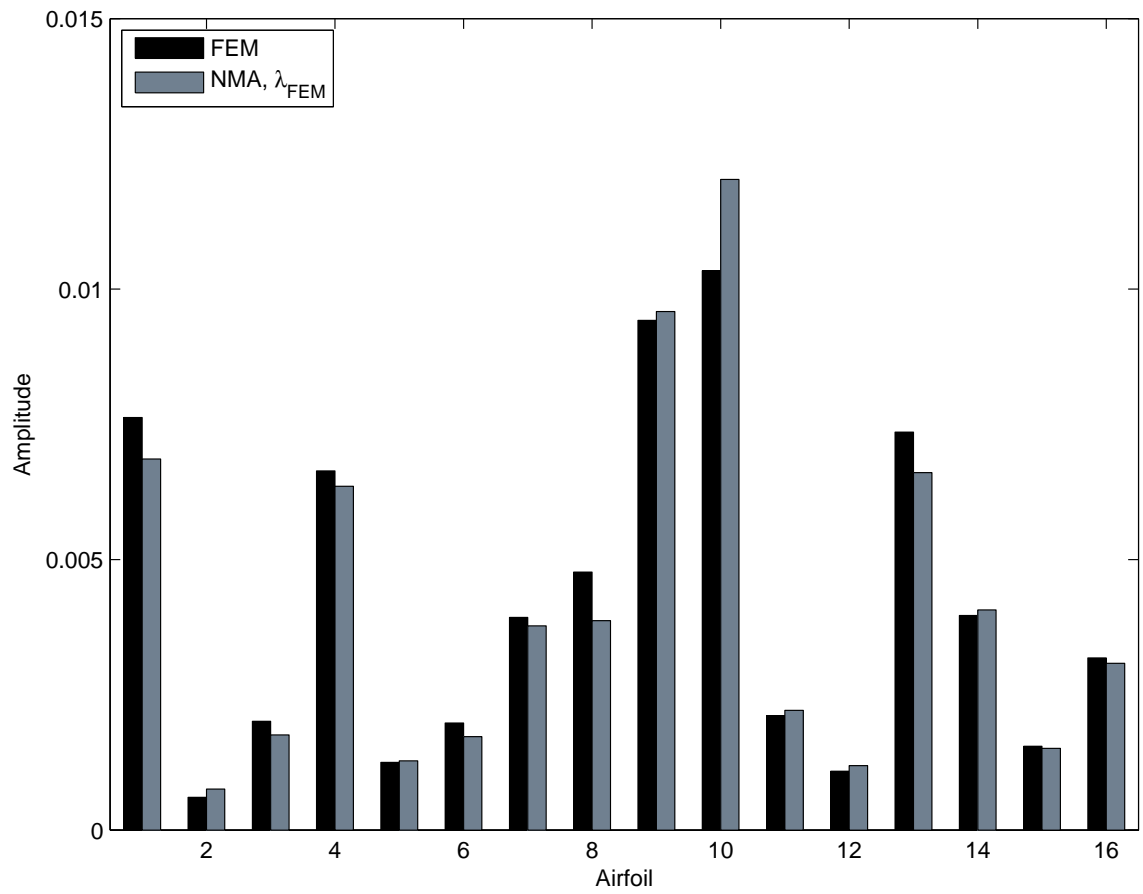


Figure 4.8: Blade-to-Blade Response at Maximum Response at 4319 Hz. - Mode 11

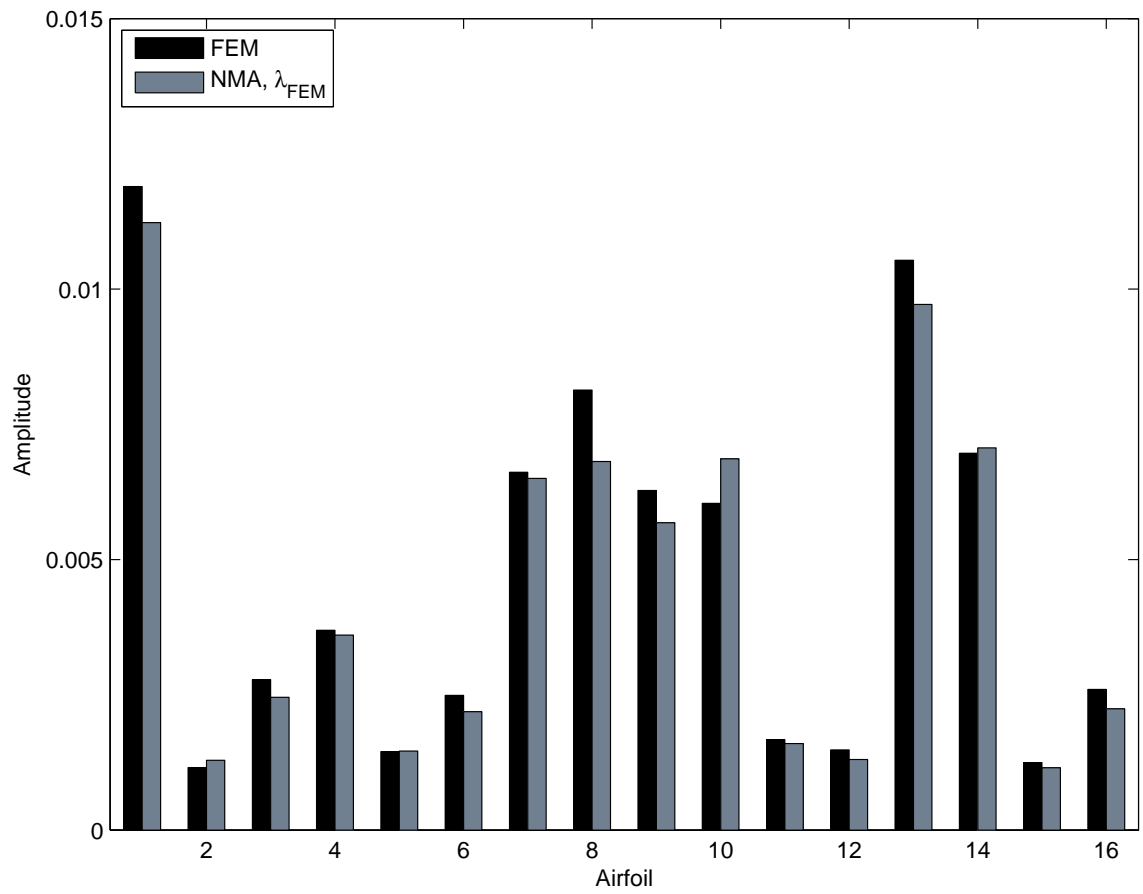


Figure 4.9: Blade-to-Blade Response at Maximum Response at 4331 Hz. - Mode 11

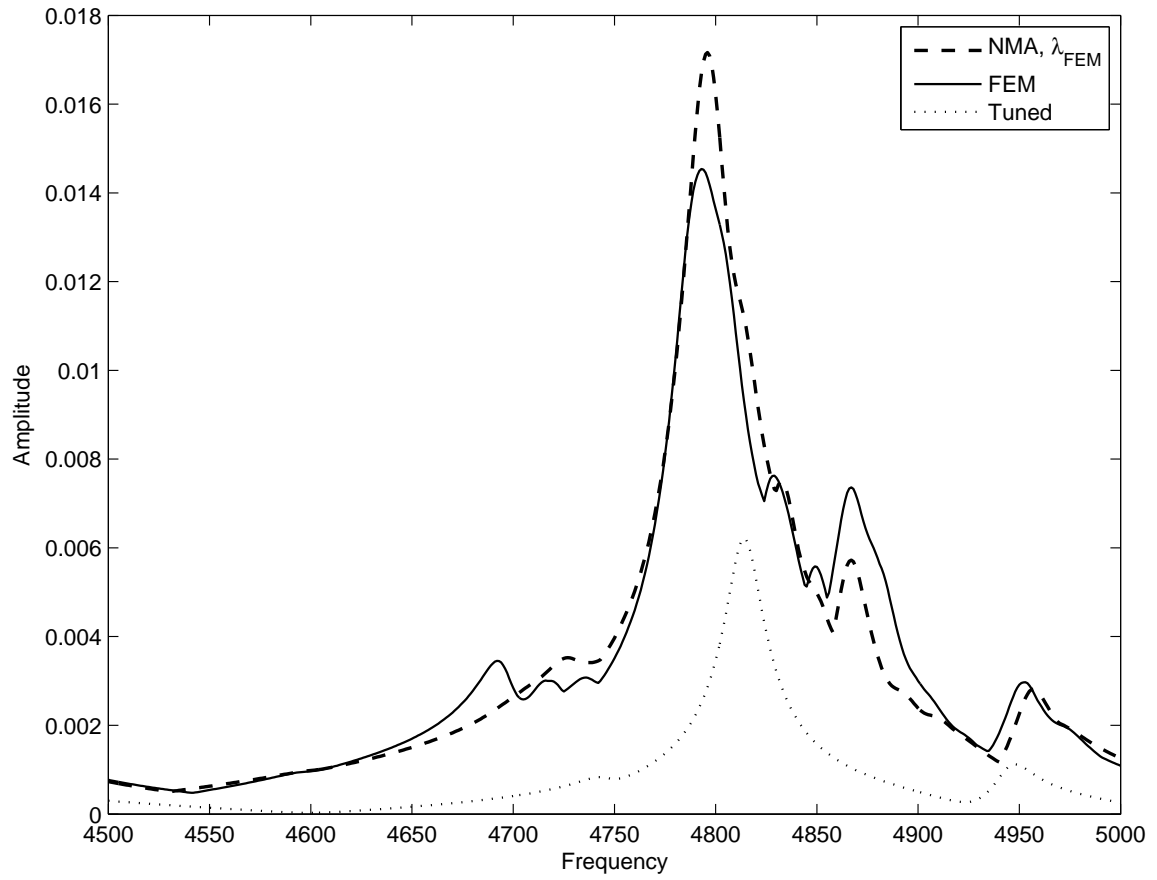


Figure 4.10: NMA-  $\lambda_{FEM}$  versus Full Model Maximum Forced Response - Mode 13

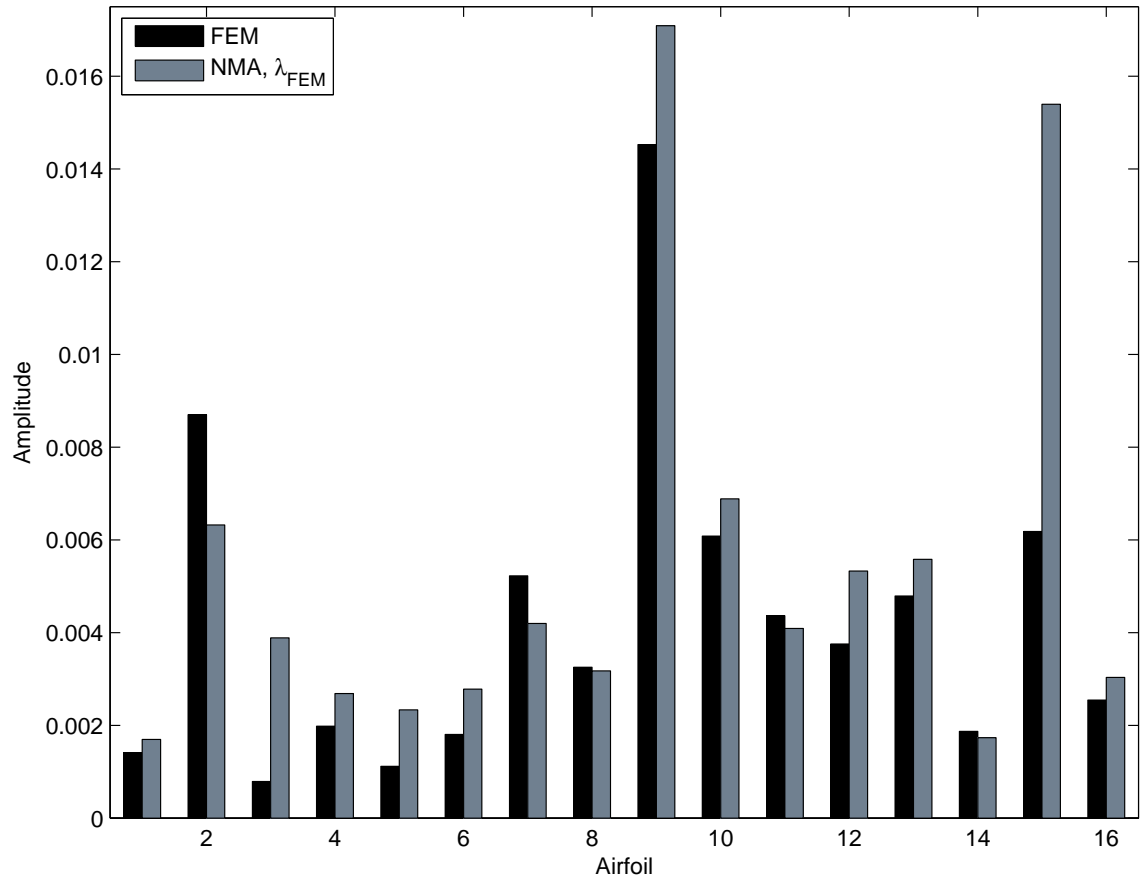


Figure 4.11: Blade-to-Blade Response at Maximum Response at Peaks- Mode 13

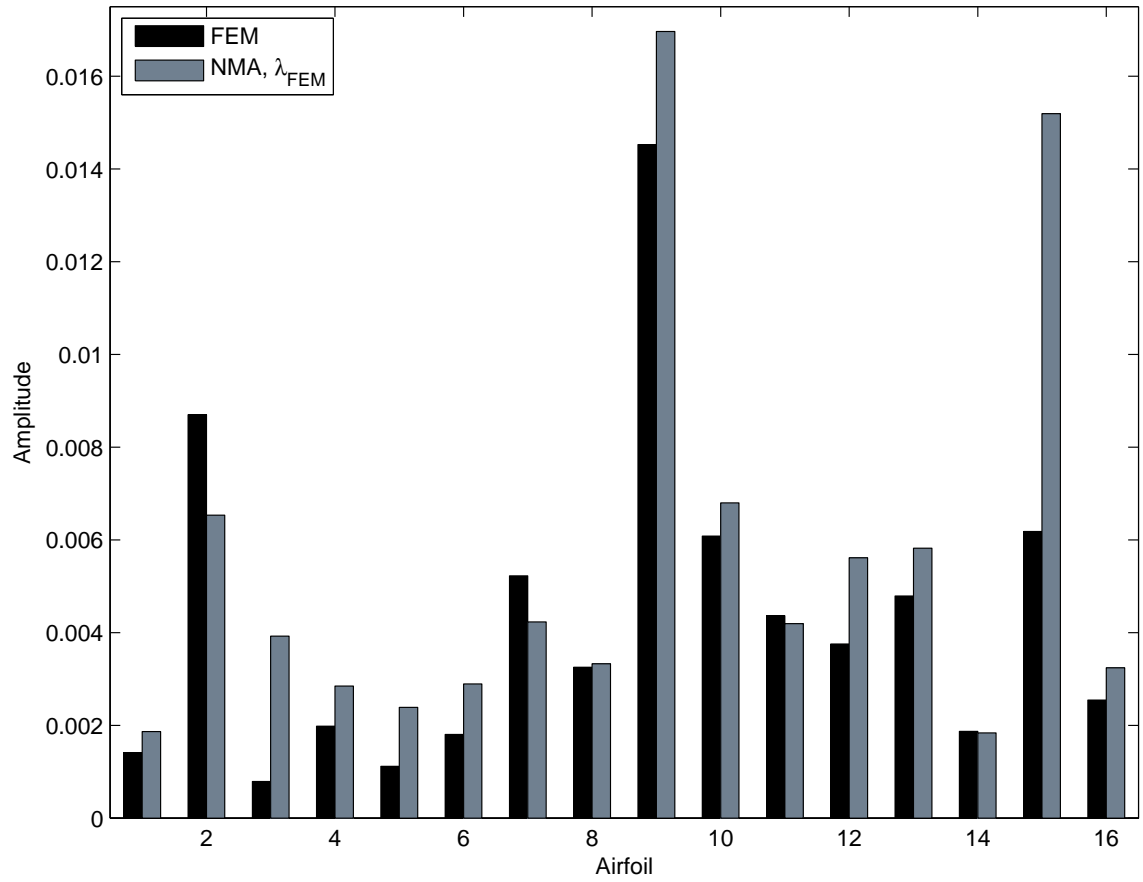


Figure 4.12: Blade-to-Blade Response at Maximum Response at 4794 Hz. - Mode 13

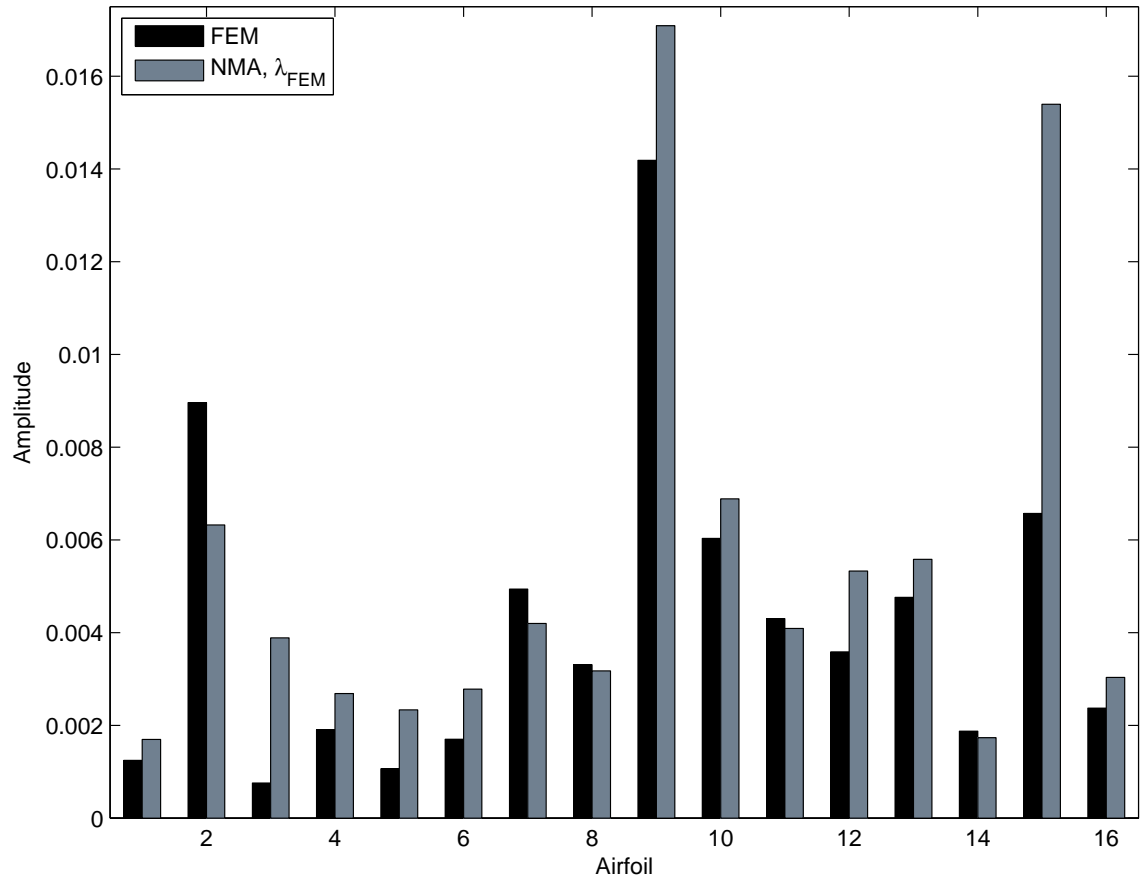


Figure 4.13: Blade-to-Blade Response at Maximum Response at 4797 - Mode 13

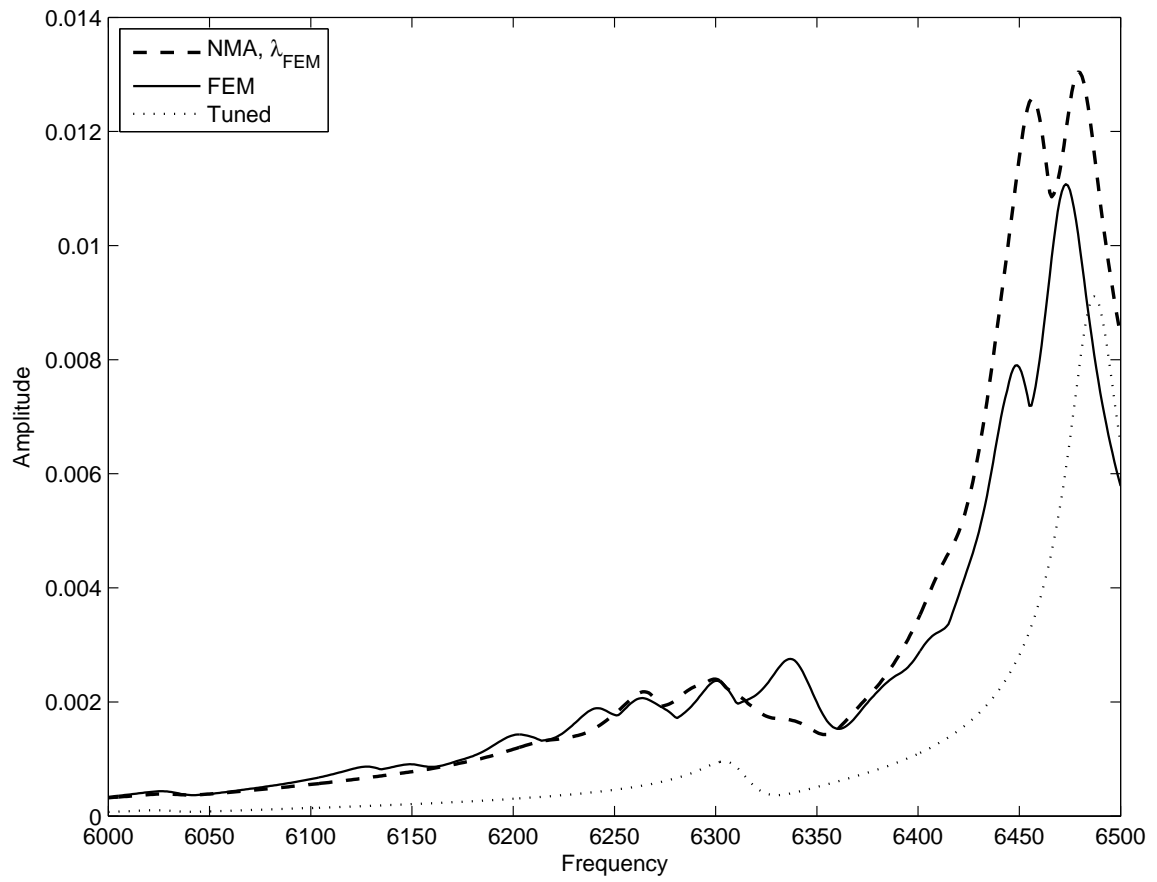


Figure 4.14: NMA-  $\lambda_{FEM}$  versus Full Model Maximum Forced Response - Mode 17



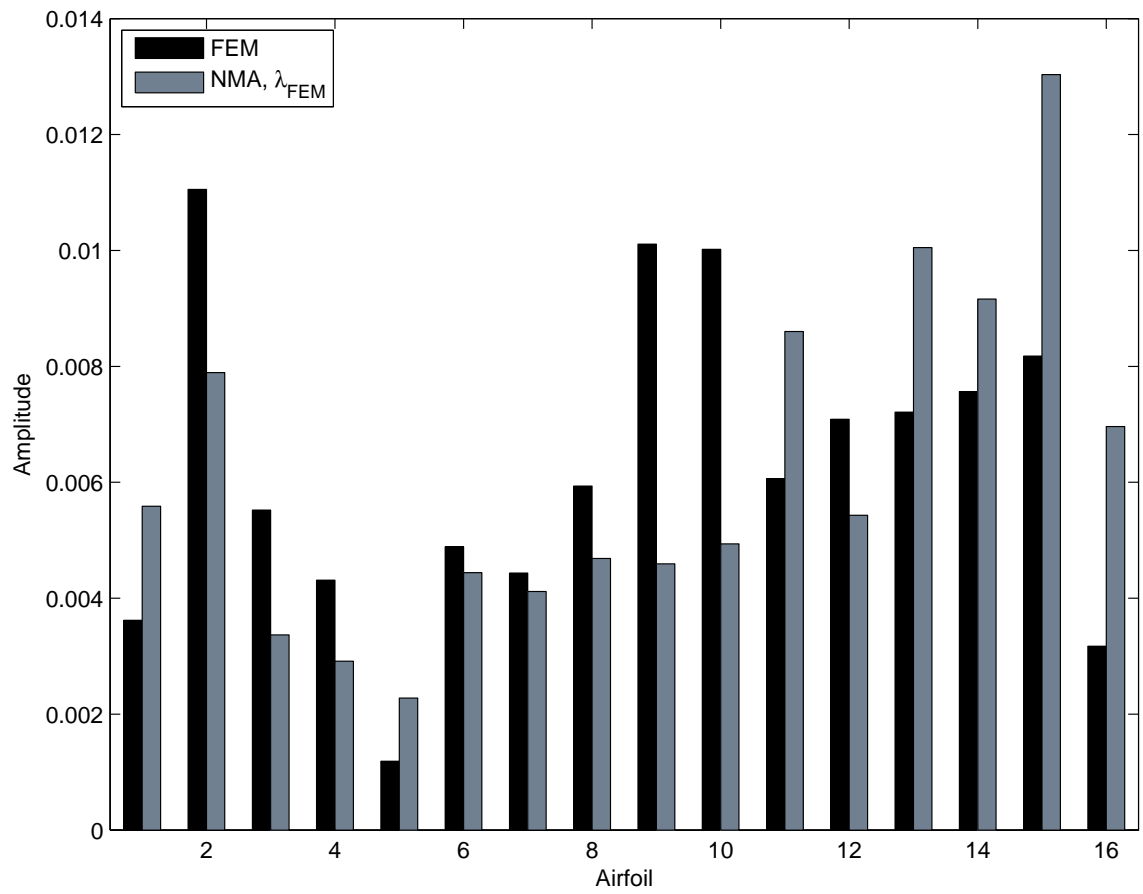


Figure 4.15: Blade-to-Blade Response at Maximum Response at Peaks - Mode 17

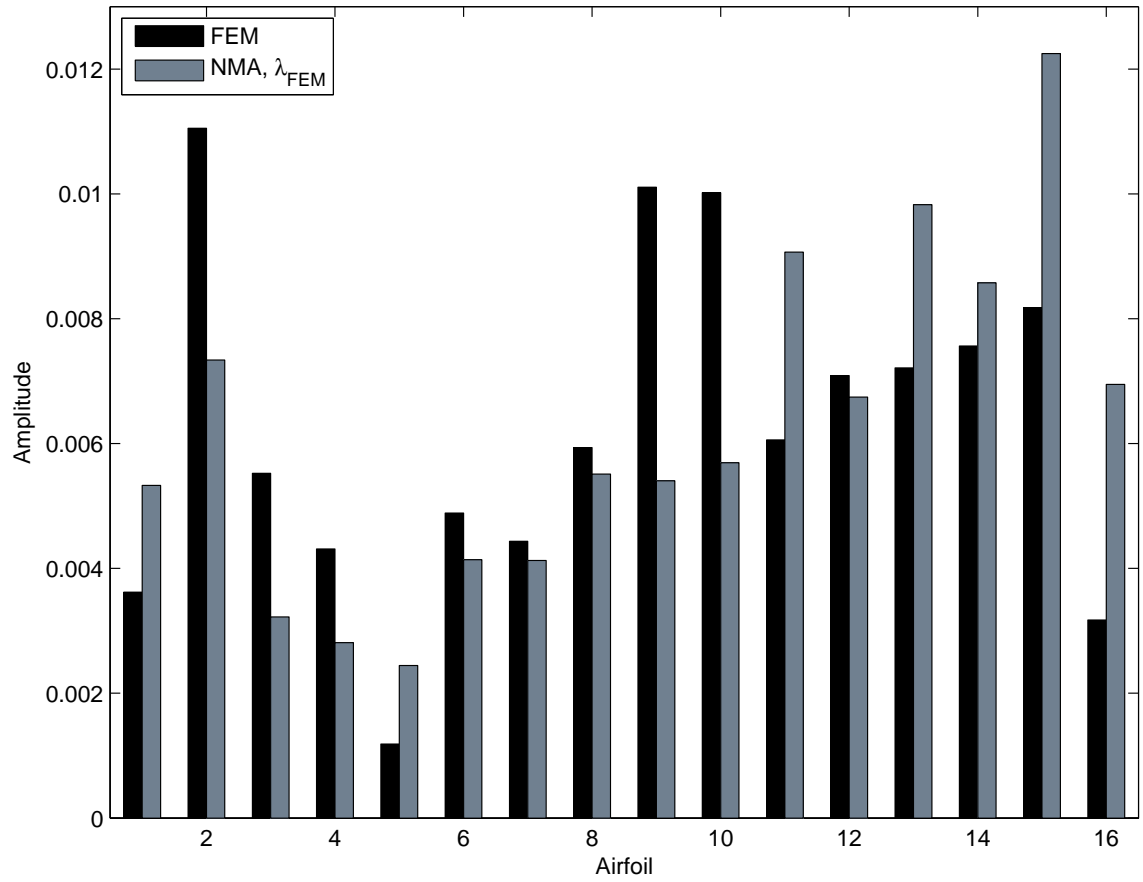


Figure 4.16: Blade-to-Blade Response at Maximum Response at 6474 Hz. - Mode 17

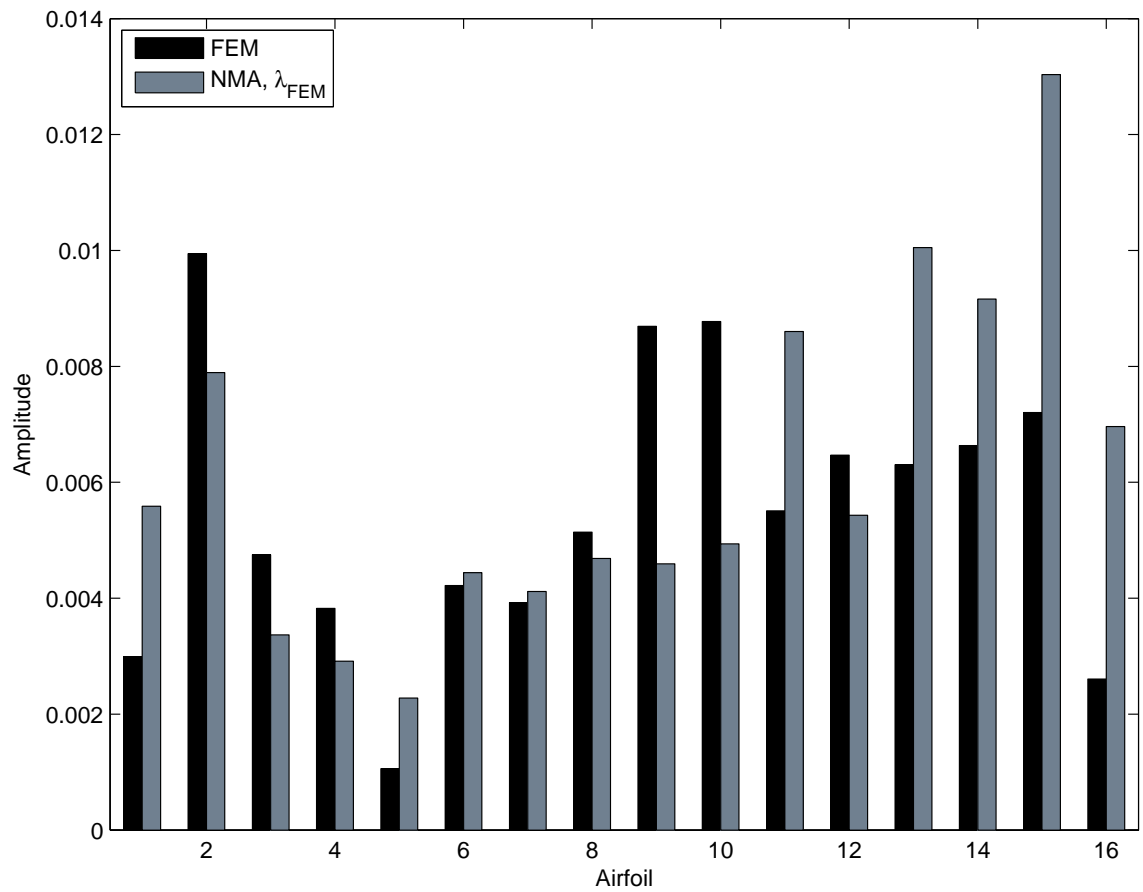


Figure 4.17: Blade-to-Blade Response at Maximum Response at 6480 - Mode 17

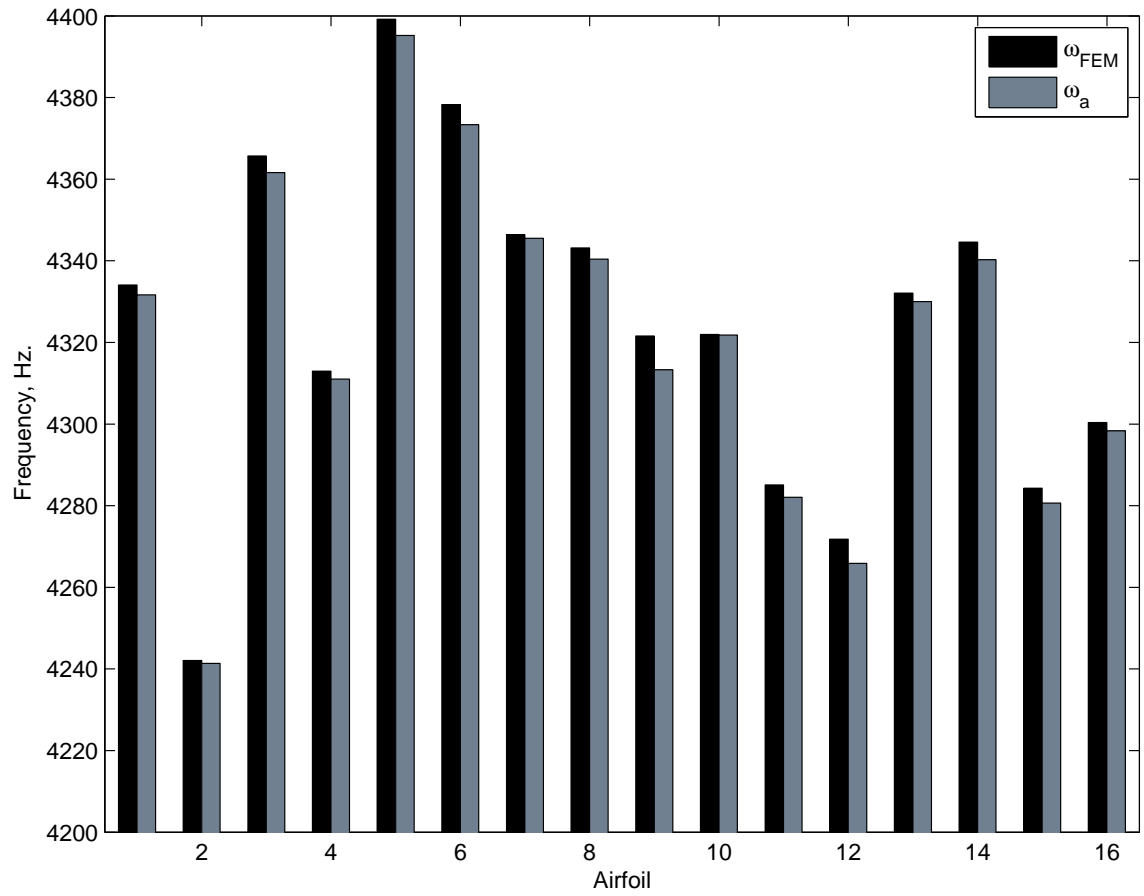


Figure 4.18: Modal Stiffness Approximation Results - Mode 11

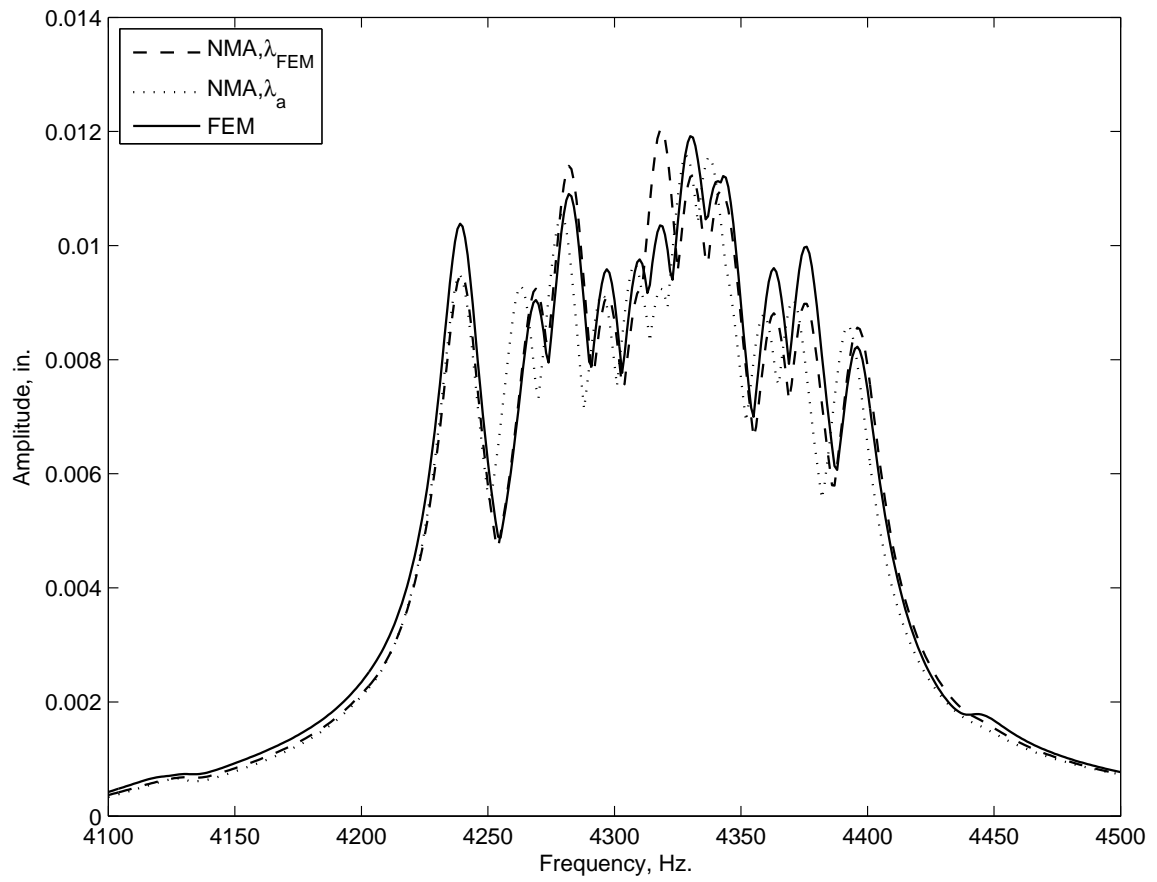


Figure 4.19: Comparison of Approximate NMA Approaches - Mode 11

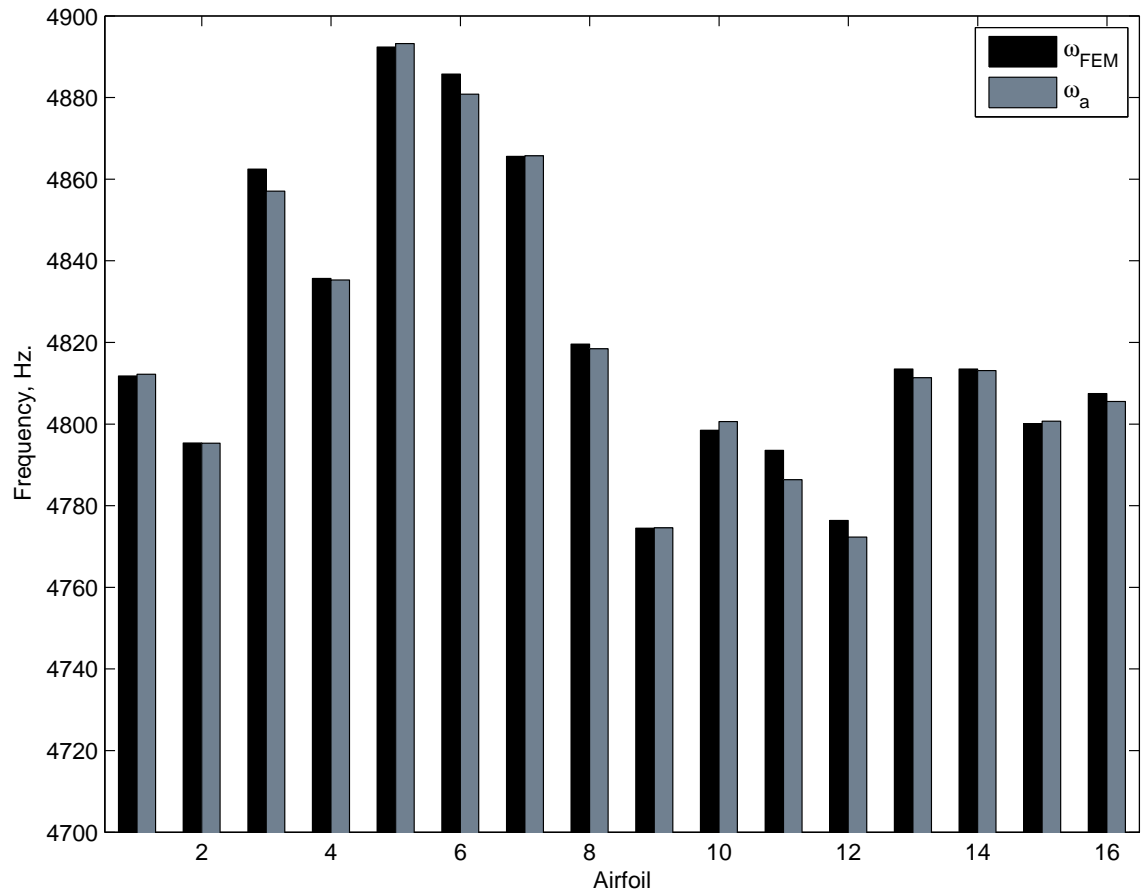


Figure 4.20: Modal Stiffness Approximation Results - Mode 13

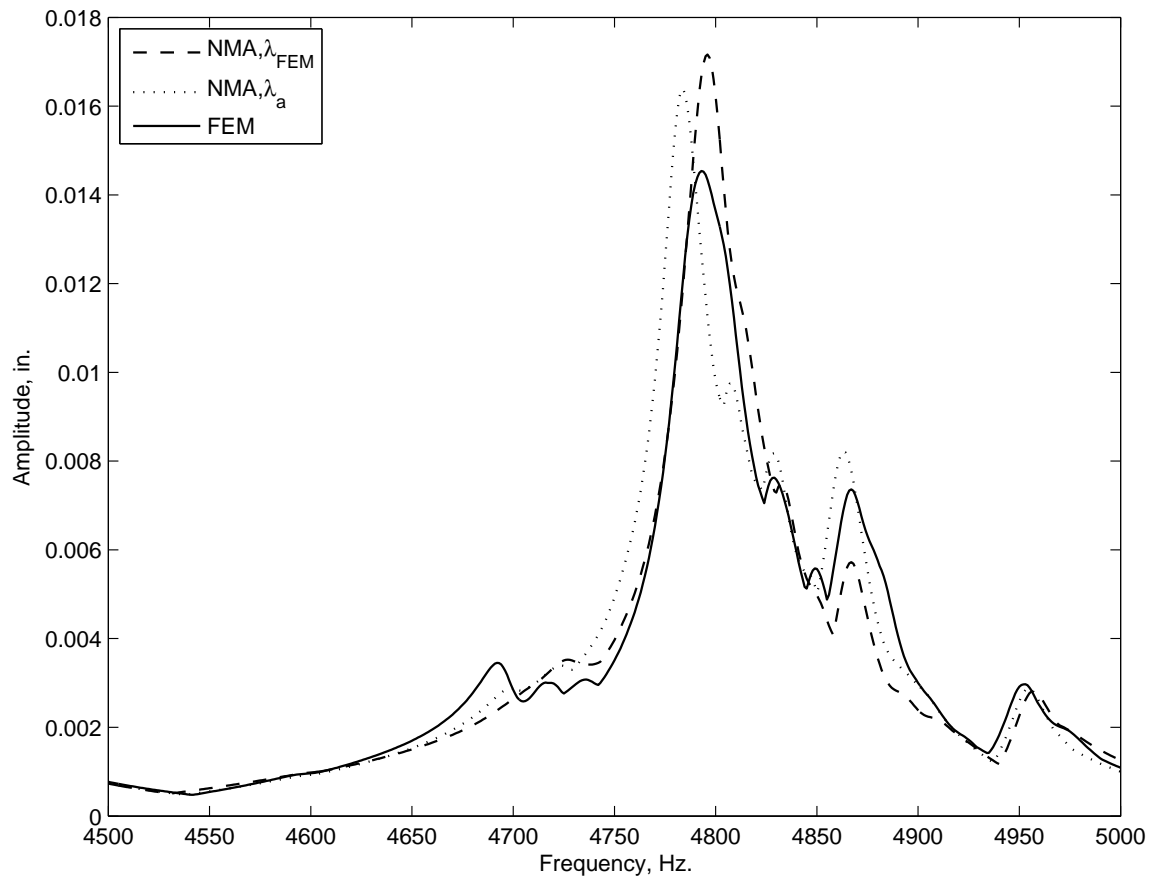


Figure 4.21: Comparison of NMA Approaches - Mode 13

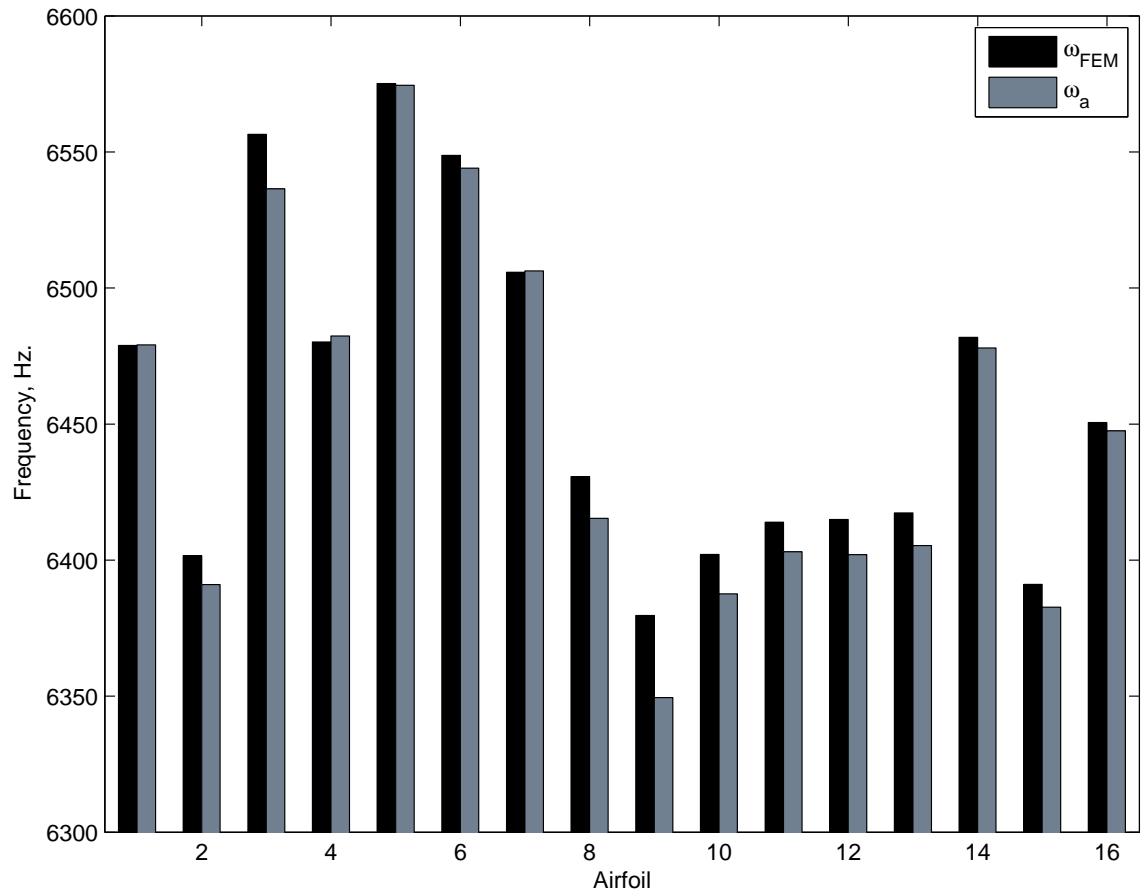


Figure 4.22: Modal Stiffness Approximation Results - Mode 17



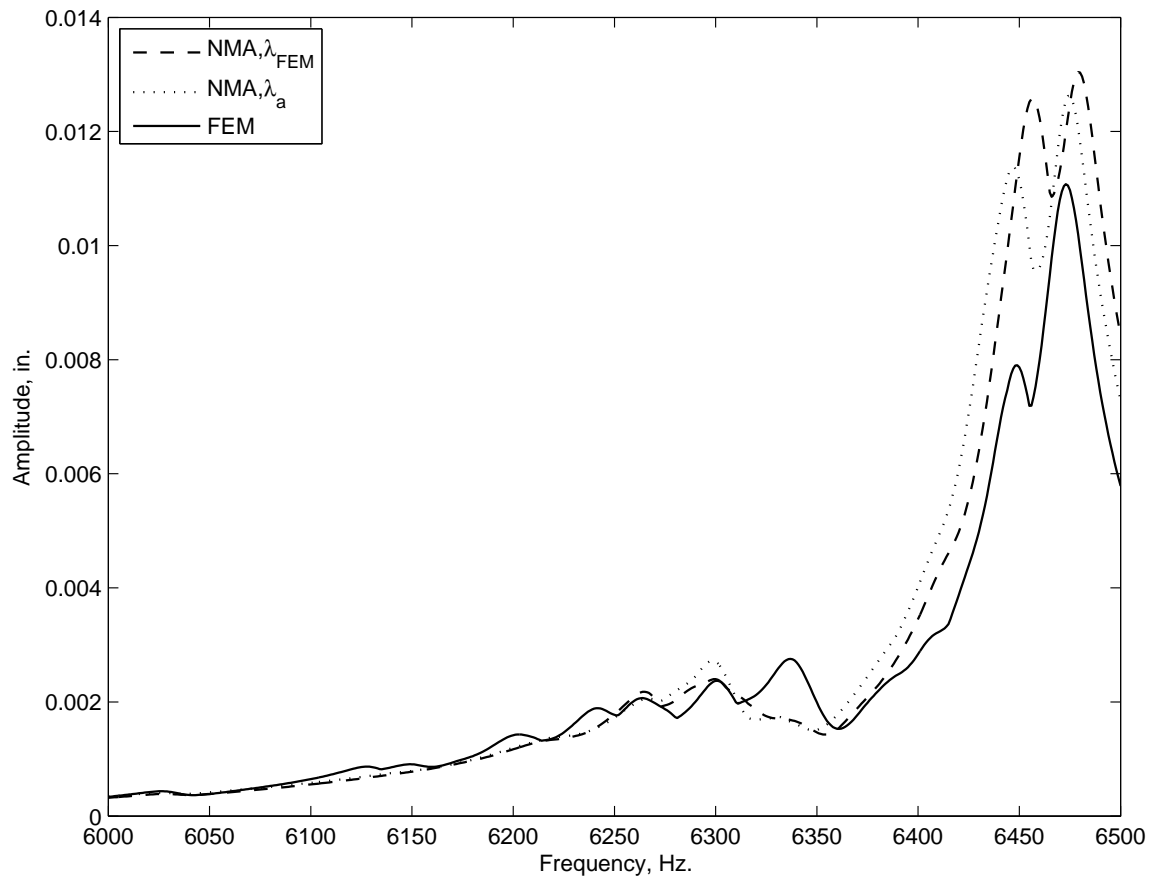


Figure 4.23: Comparison of NMA Approaches - Mode 17

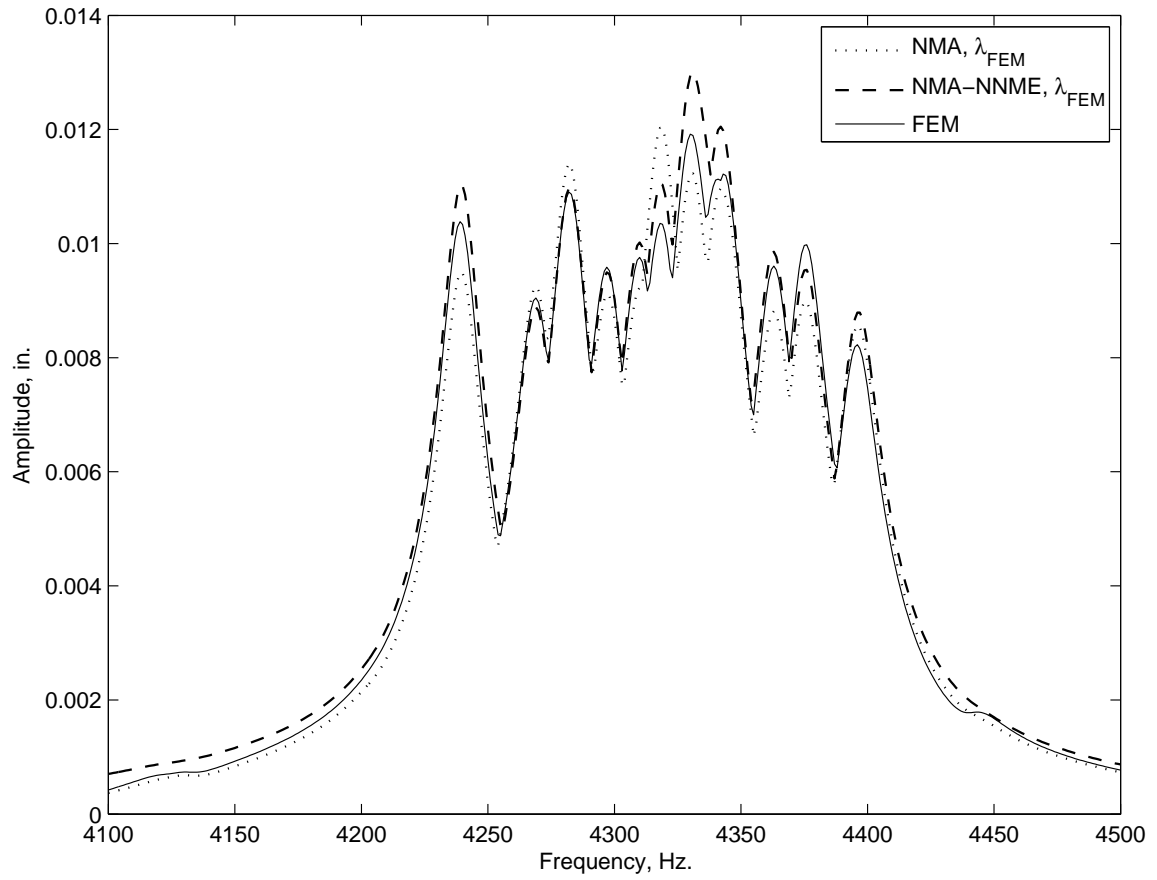


Figure 4.24: Comparison of NMA- $\lambda_{FEM}$  and NMA-NNME- $\lambda_{FEM}$  Results - Mode 11

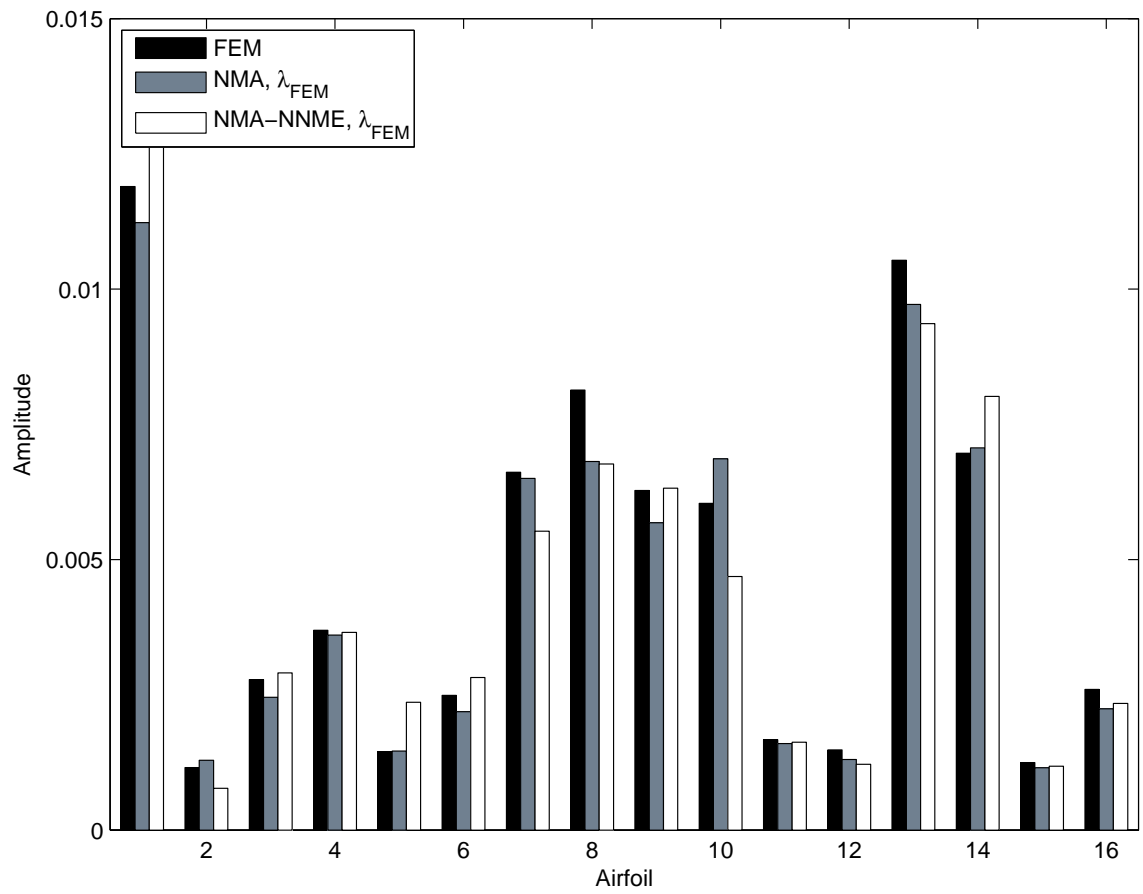


Figure 4.25: Blade-to-Blade NMA- $\lambda_{FEM}$  versus NMA-NNME- $\lambda_{FEM}$  Results - Mode 11

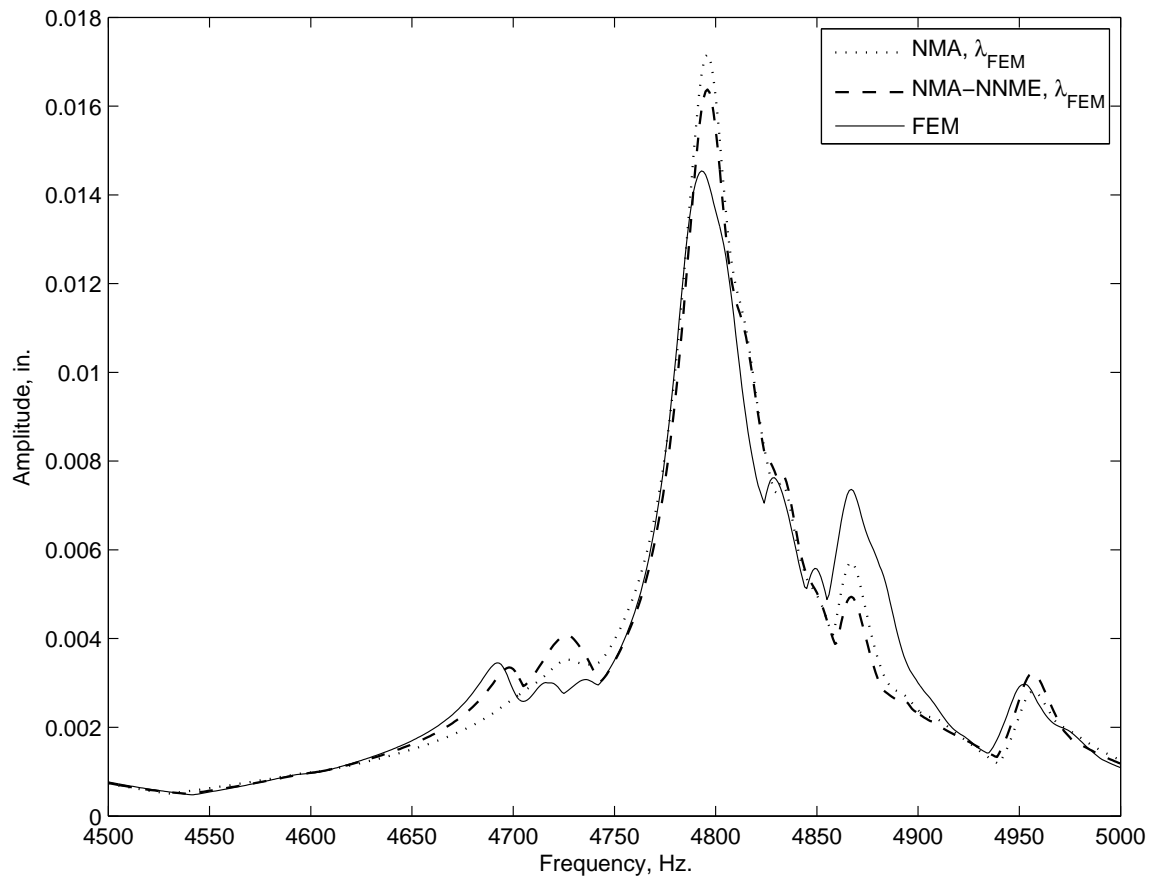


Figure 4.26: NMA- $\lambda_{FEM}$  versus NMA-NNME- $\lambda_{FEM}$  Maximum Forced Response Results- Mode 13

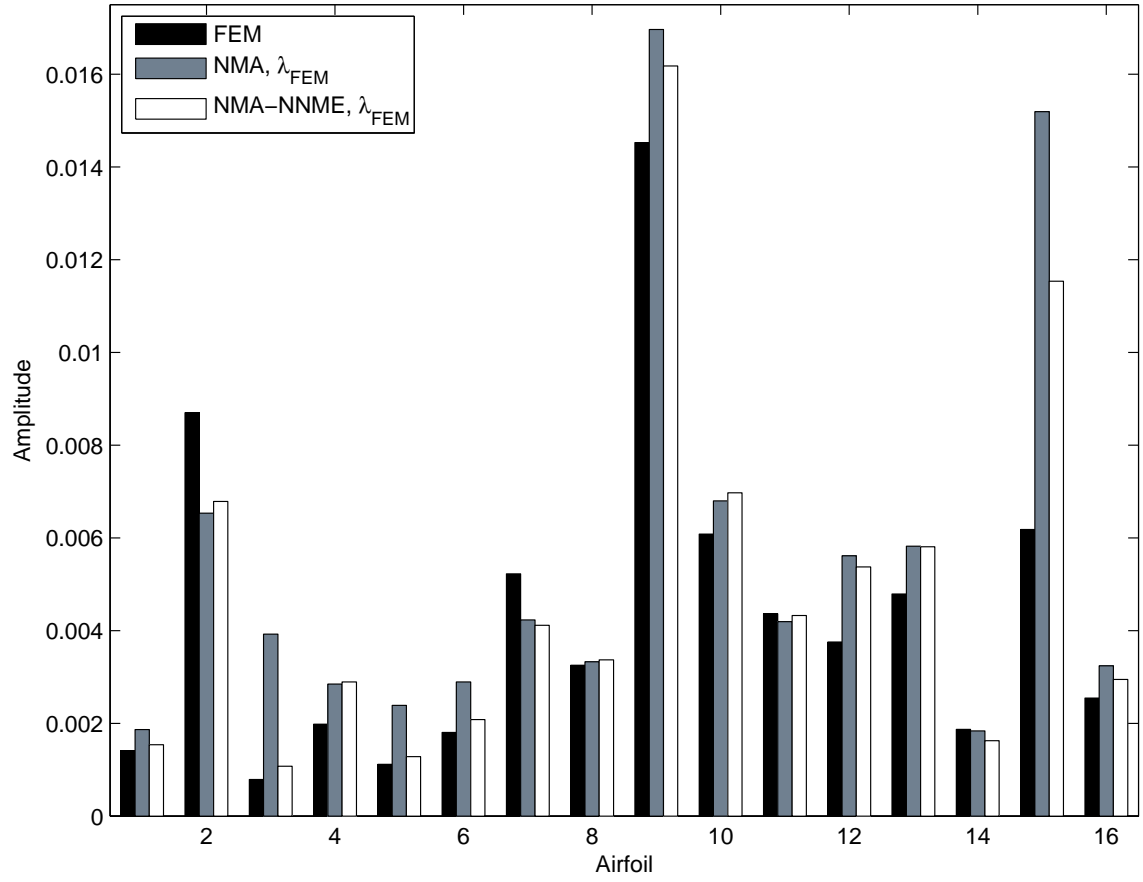


Figure 4.27: NMA- $\lambda_{FEM}$  versus NMA-NNME-  $\lambda_{FEM}$  Blade-to-Blade Results - Mode 13

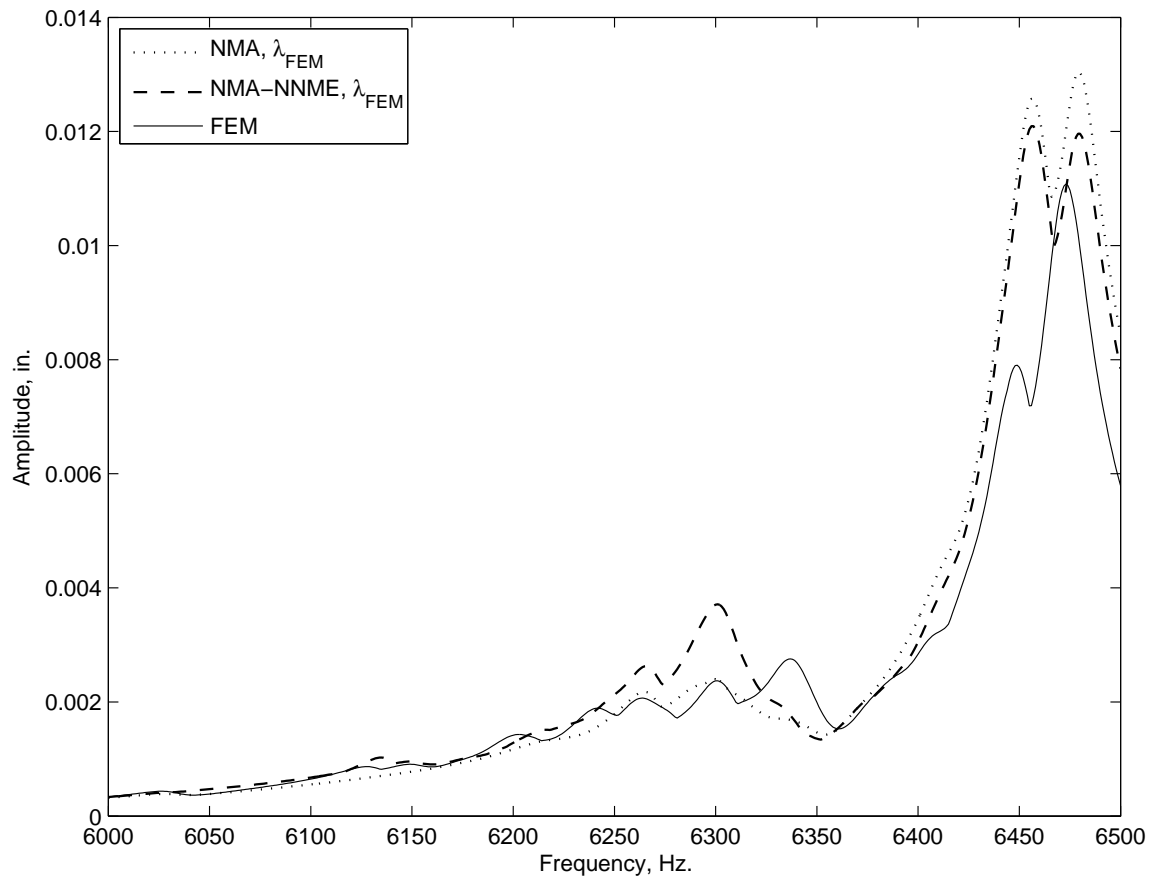


Figure 4.28: NMA- $\lambda_{FEM}$  versus NMA-NNME- $\lambda_{FEM}$  Maximum Forced Response Results  
- Mode 17

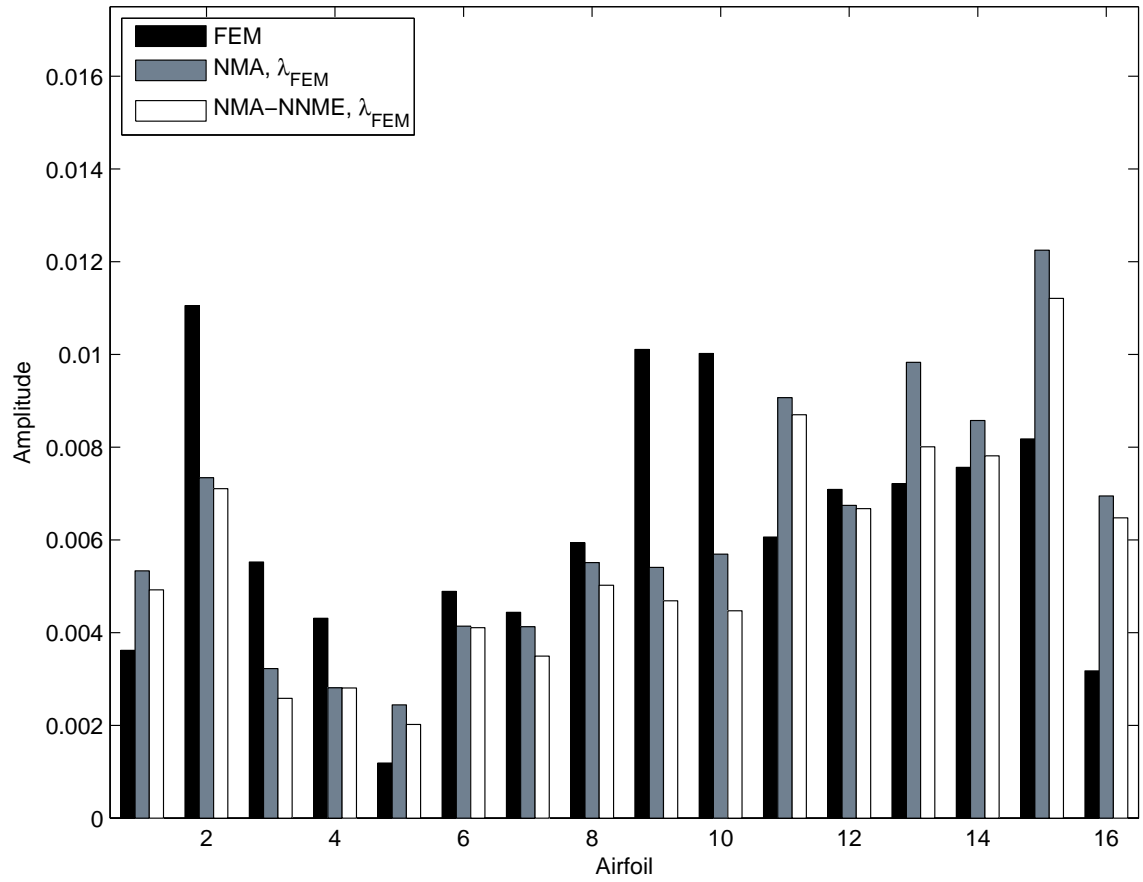


Figure 4.29: NMA- $\lambda_{FEM}$  versus NMA-NNME- $\lambda_{FEM}$  Blade-to-Blade Results - Mode 17

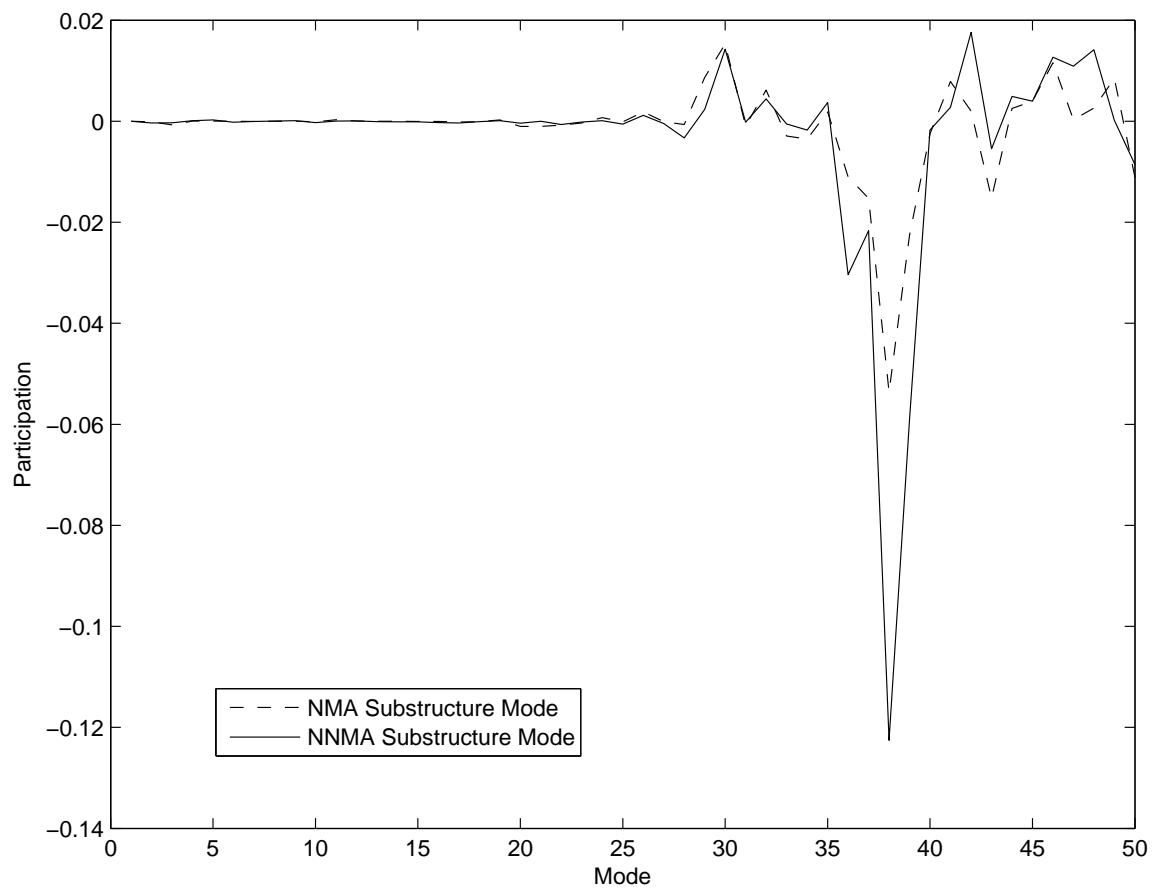


Figure 4.30: CMS  $A_k$  Vector Nominal vs. Non-Nominal - Blade 9 - M13



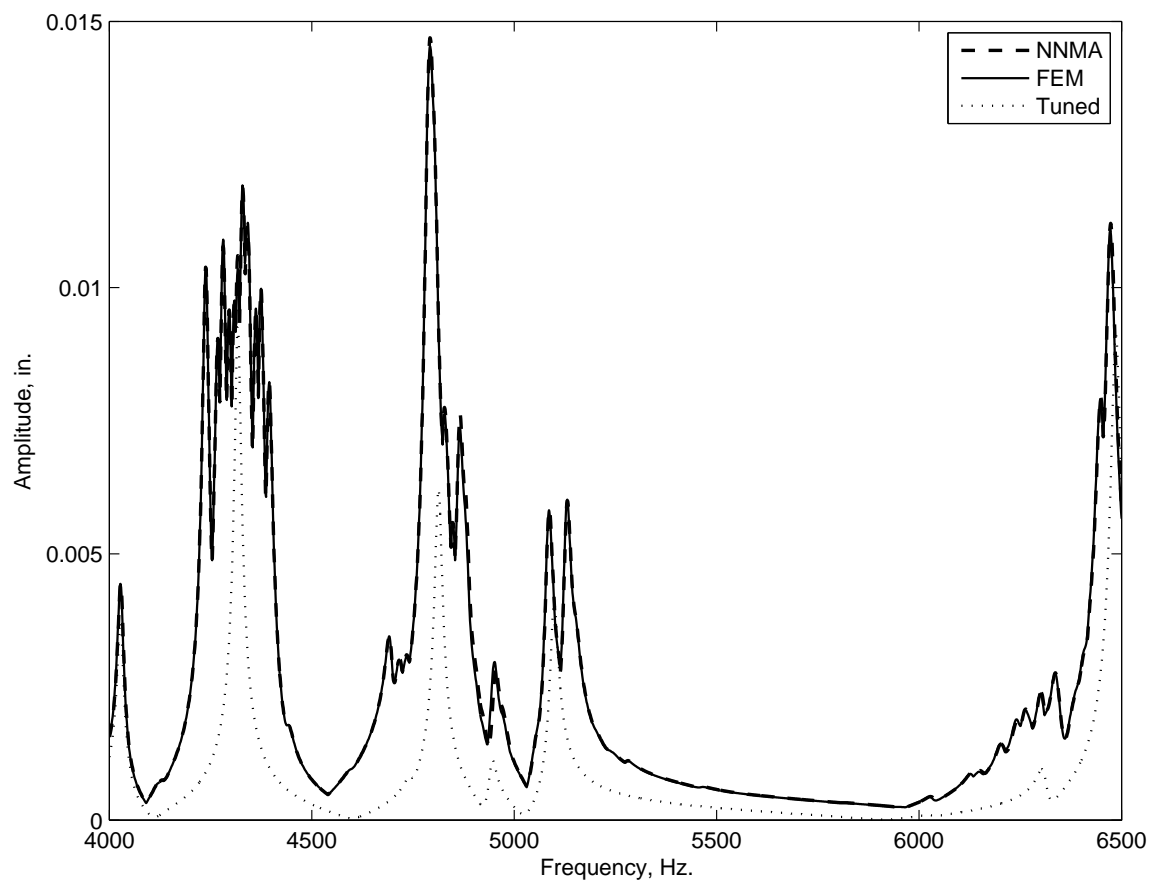


Figure 4.31: NNMA versus FEM Maximum Forced Response Results

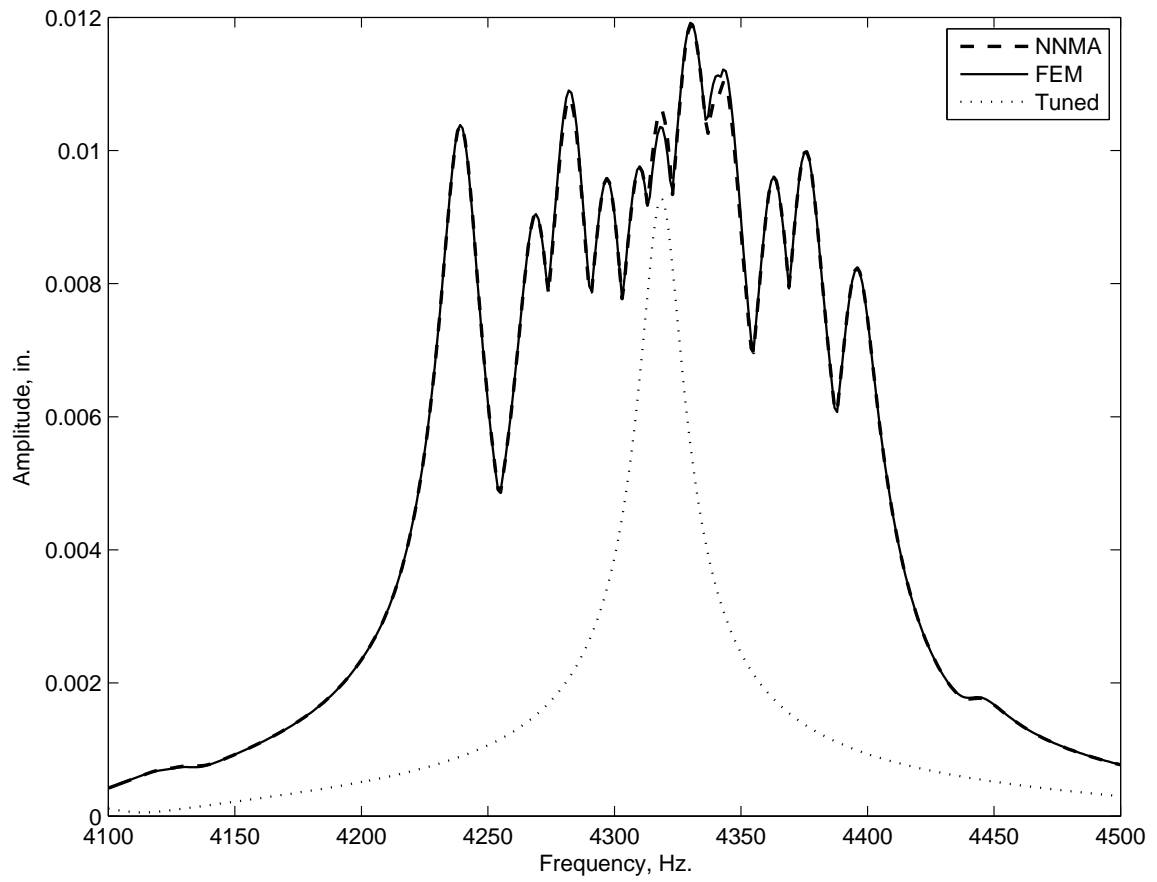


Figure 4.32: NNMA versus FEM Maximum Forced Response Results- Mode 11

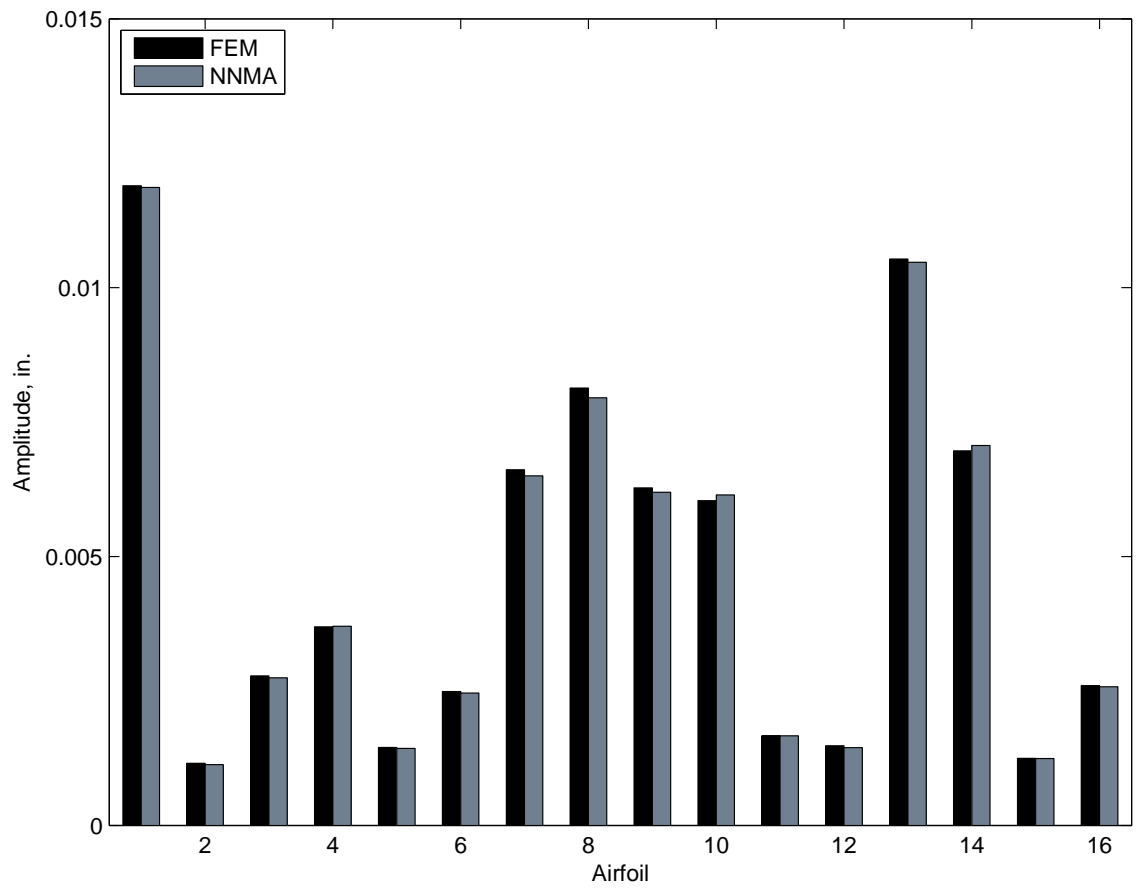


Figure 4.33: Blade-to-Blade NNMA Response Comparison at Maximum Response- Mode 11

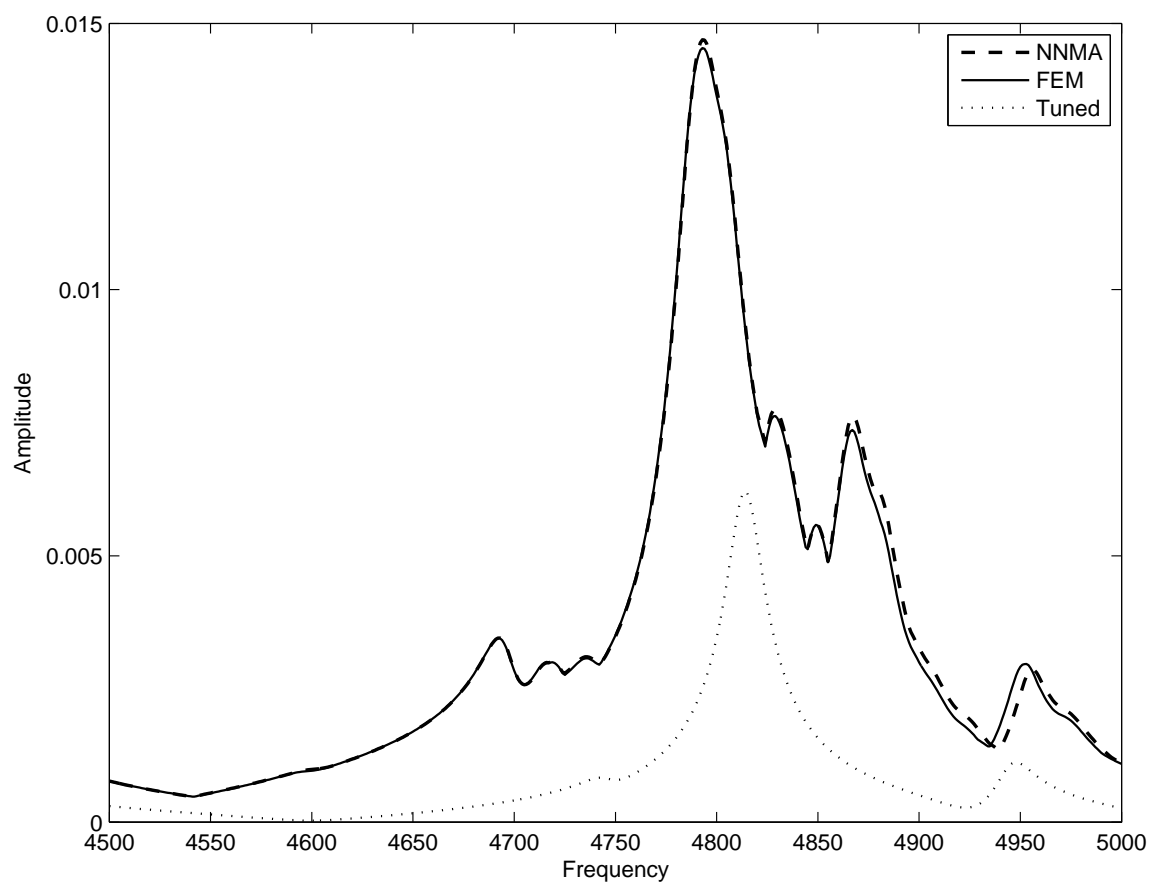


Figure 4.34: NNMA versus FEM Maximum Forced Response - Mode 13

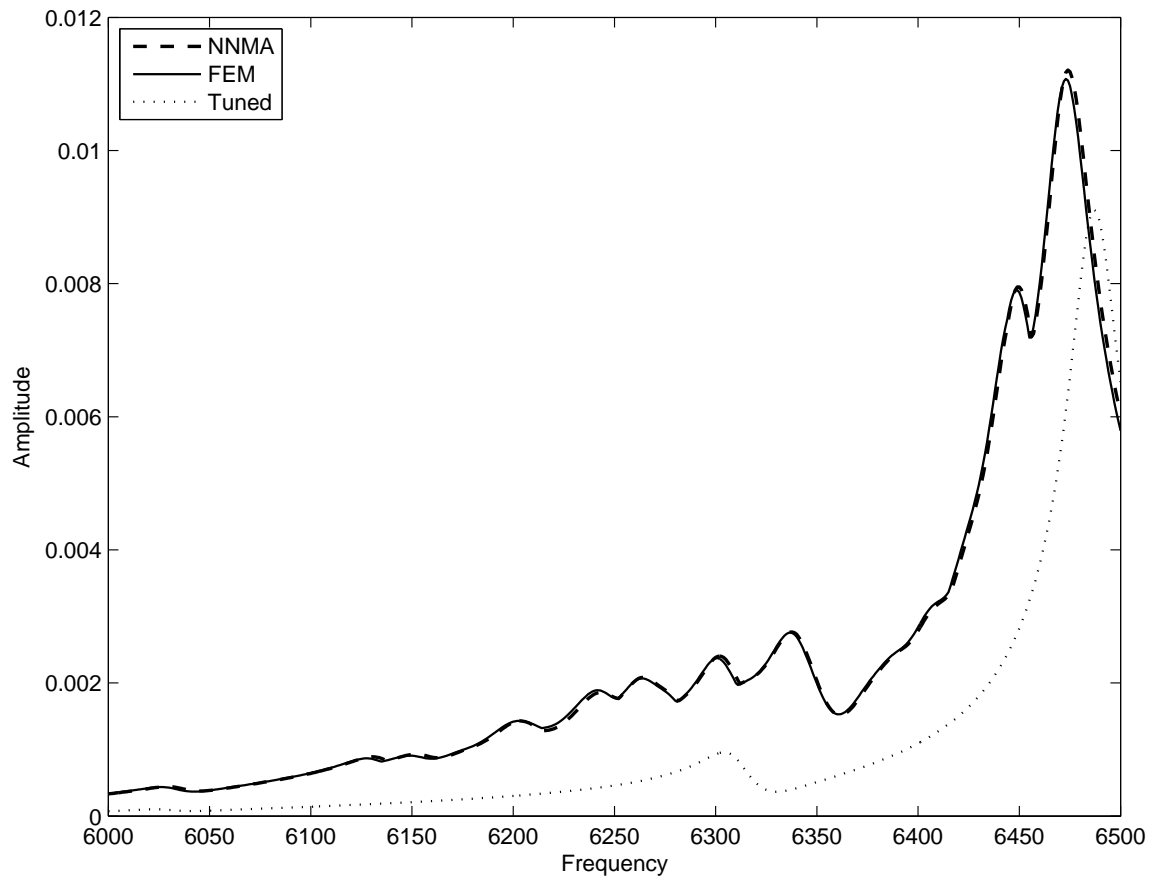


Figure 4.35: NNMA versus FEM Maximum Forced Response - Mode 17

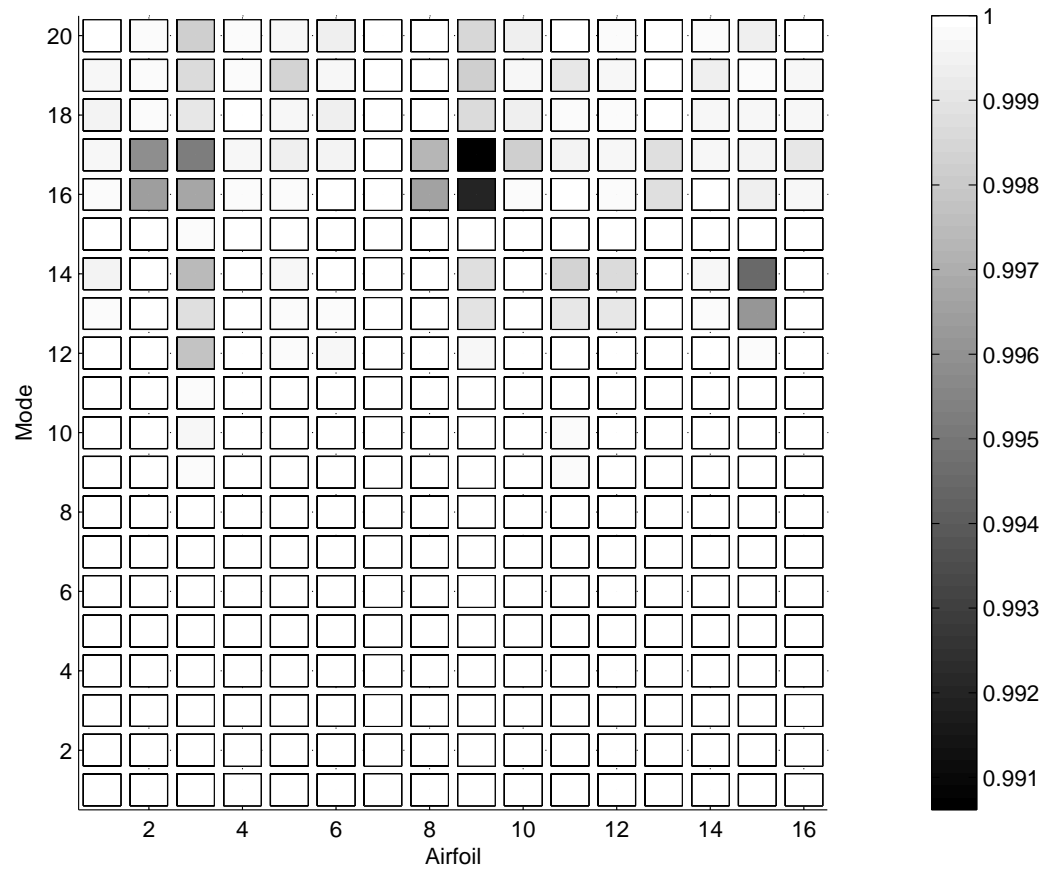


Figure 4.36: Approximate Mode Shape MAC Values (Modes 1-20)

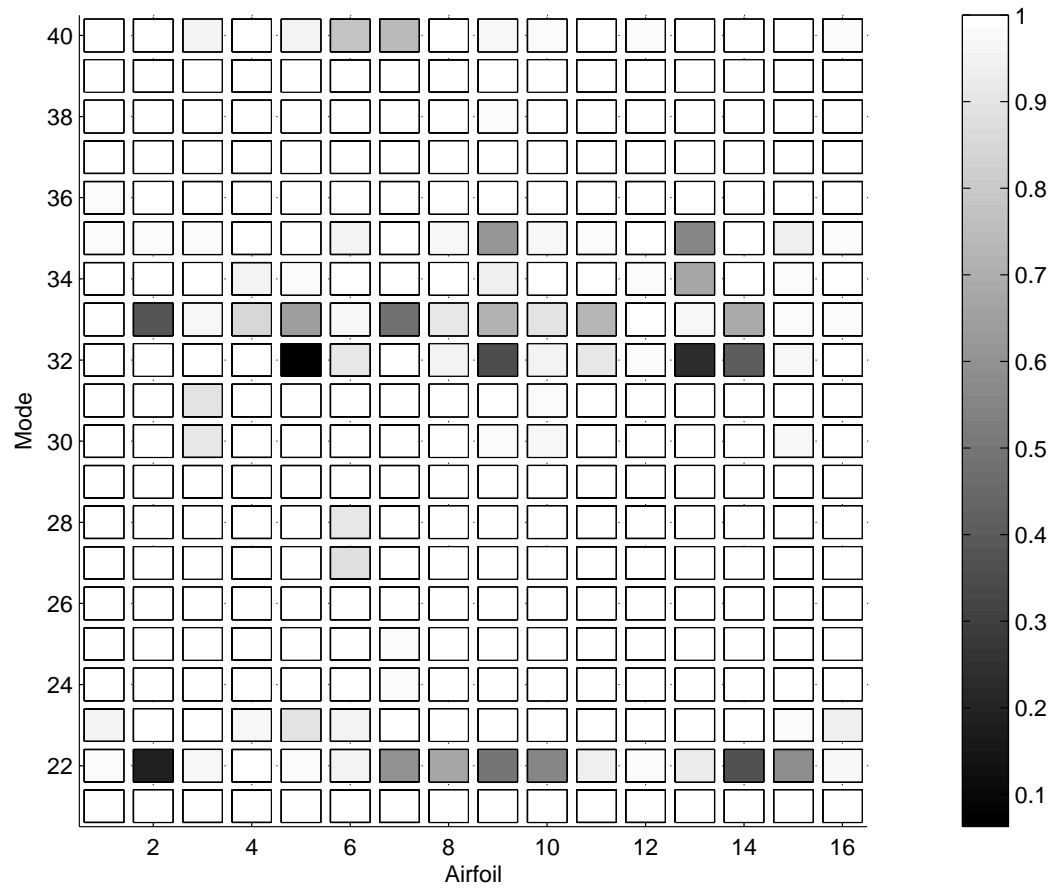


Figure 4.37: Approximate Mode Shape MAC Values (Modes 21-40)

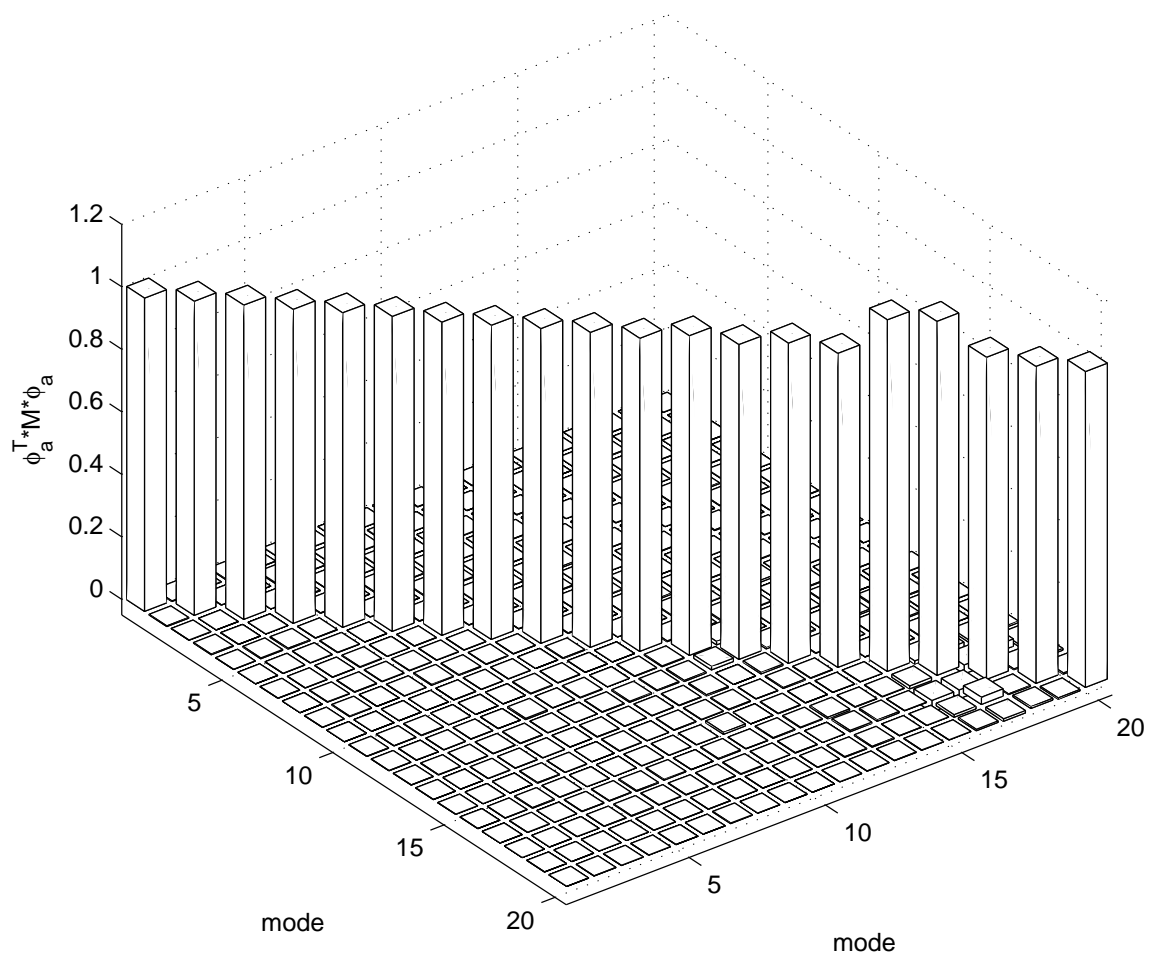


Figure 4.38: Reduced Airfoil Substructure Mass Matrix



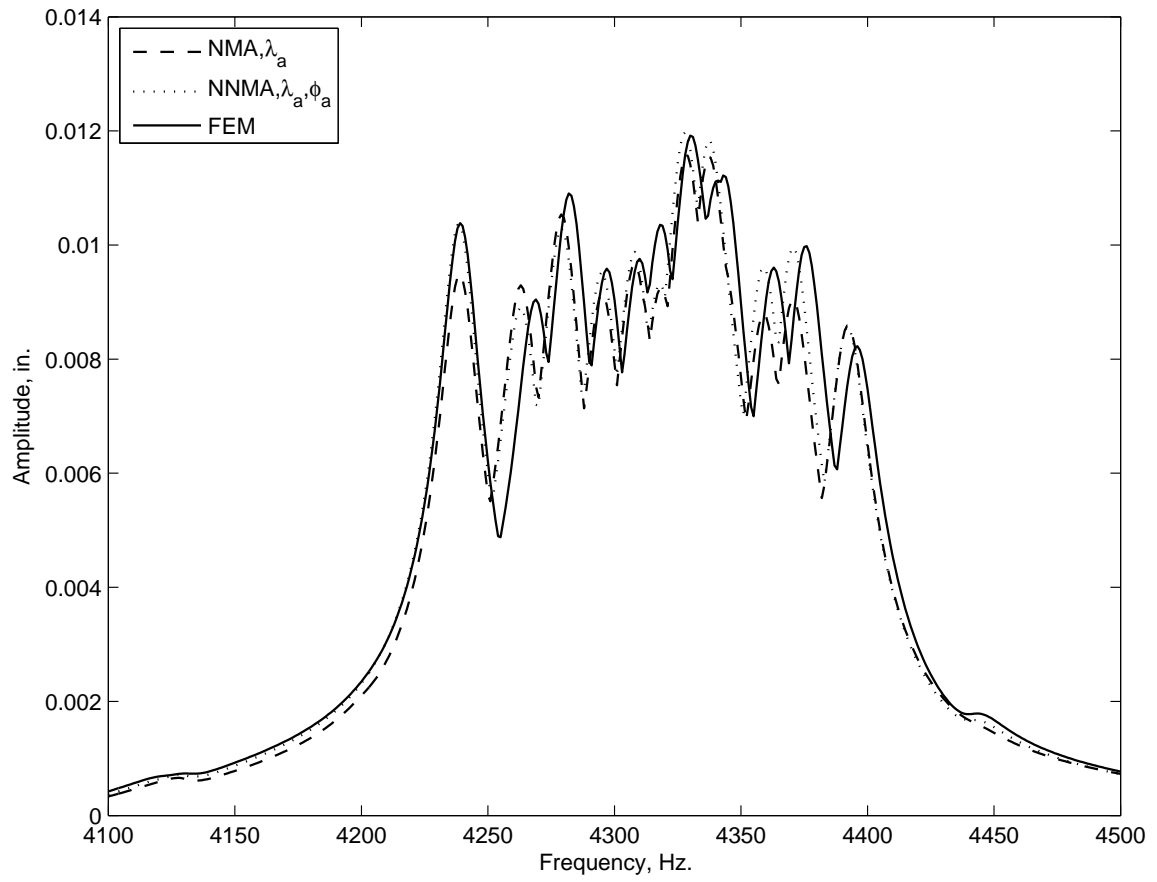


Figure 4.39: NNMA- $\lambda_a$ - $\phi_a$  versus NMA- $\lambda_a$  Maximum Forced Response Results- Mode 11

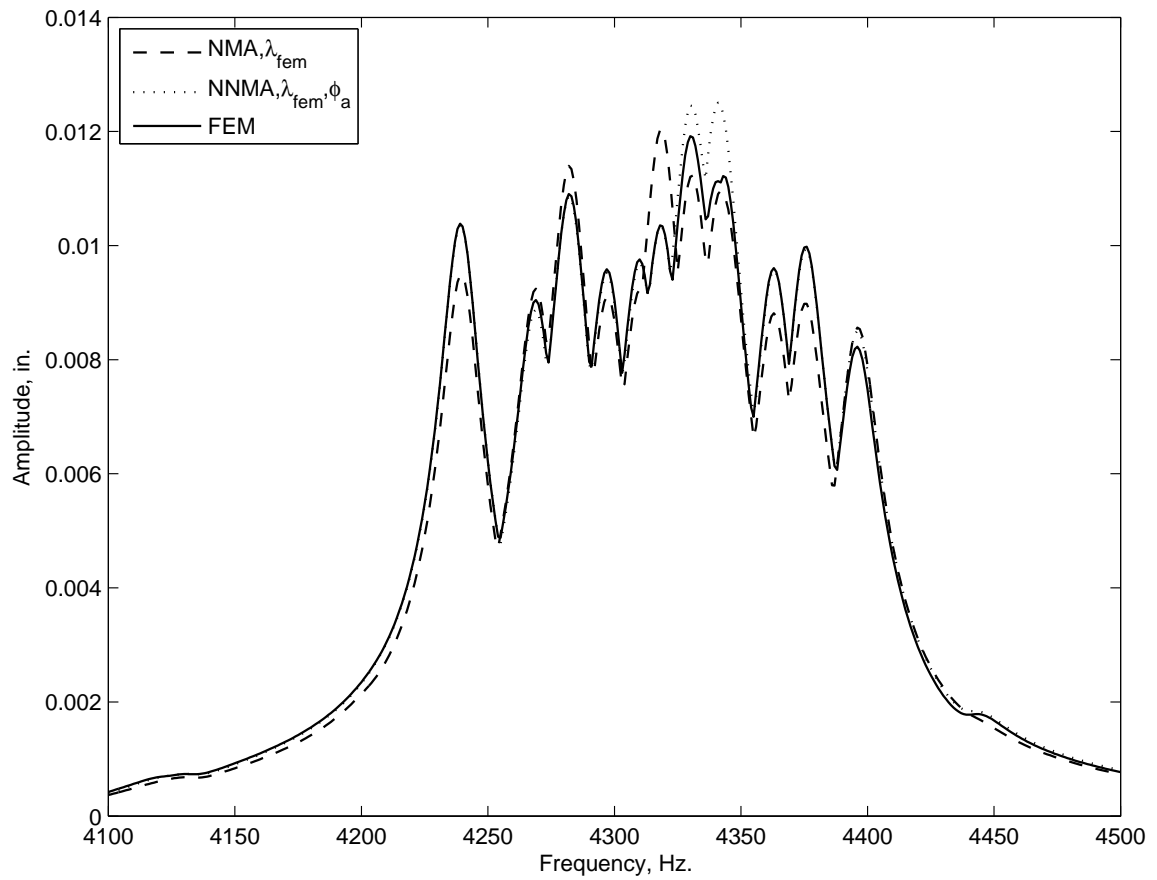


Figure 4.40: NNMA- $\lambda_{FEM}-\phi_a$  versus NMA- $\lambda_{FEM}$  Maximum Forced Response Results-Mode 11

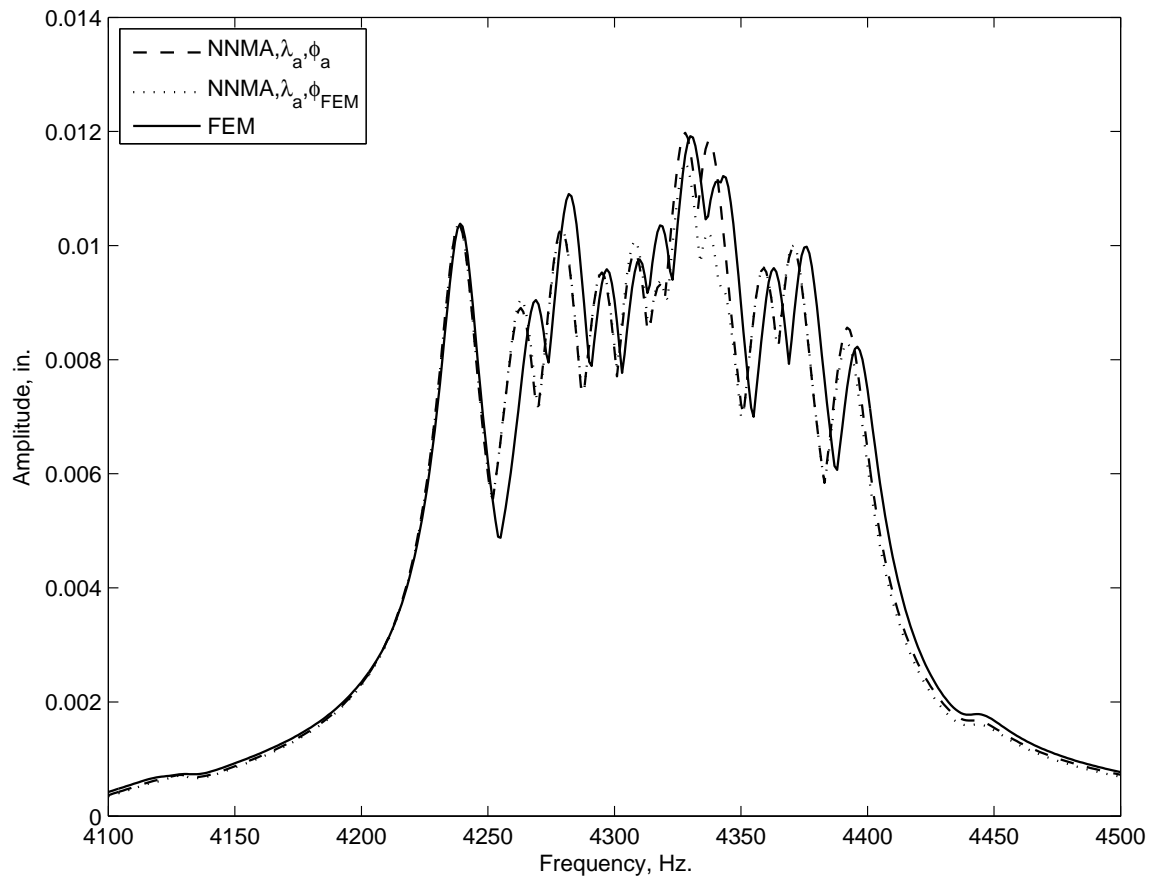


Figure 4.41: NNMA- $\lambda_a$ - $\phi_a$  versus NNMA- $\lambda_a$ - $\phi_{FEM}$  Maximum Forced Response Results-Mode 11

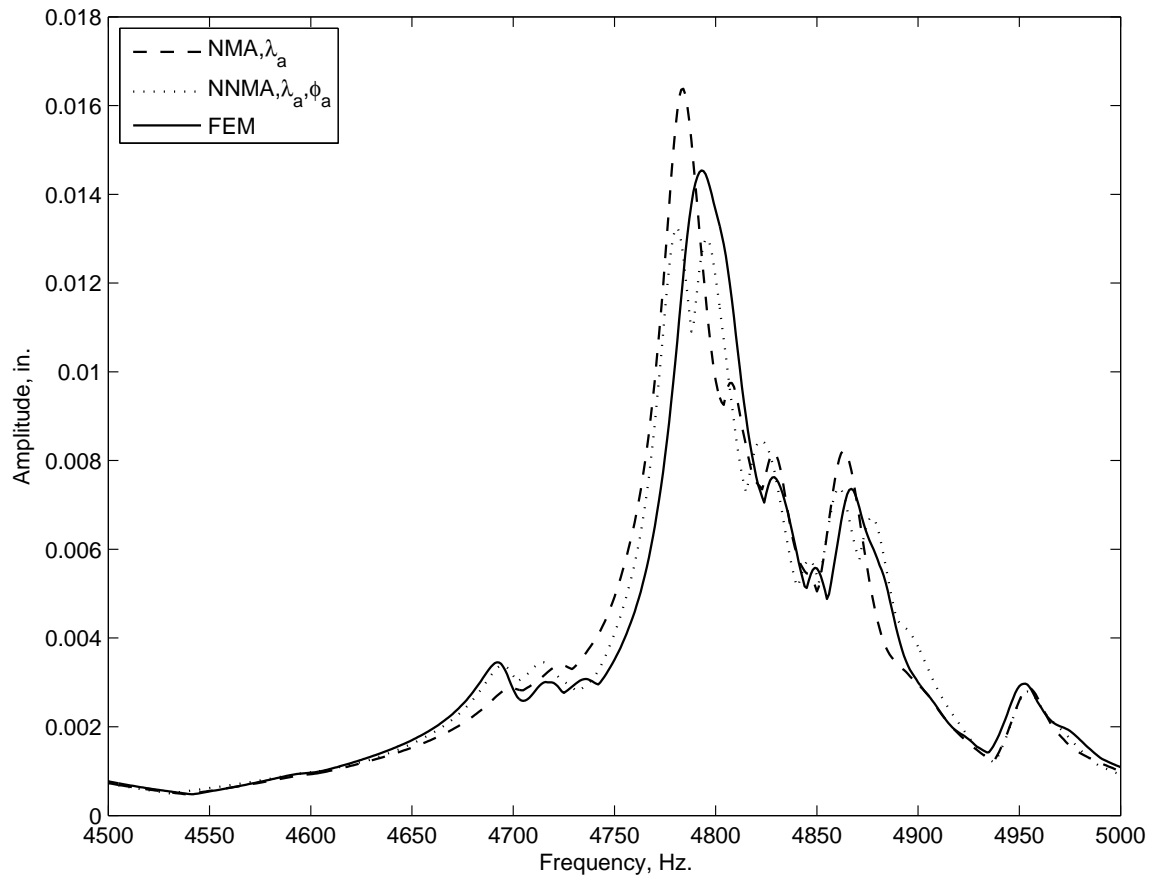


Figure 4.42: NNMA- $\lambda_a$ - $\phi_a$  versus NMA- $\lambda_a$  Maximum Forced Response Results- Mode 13

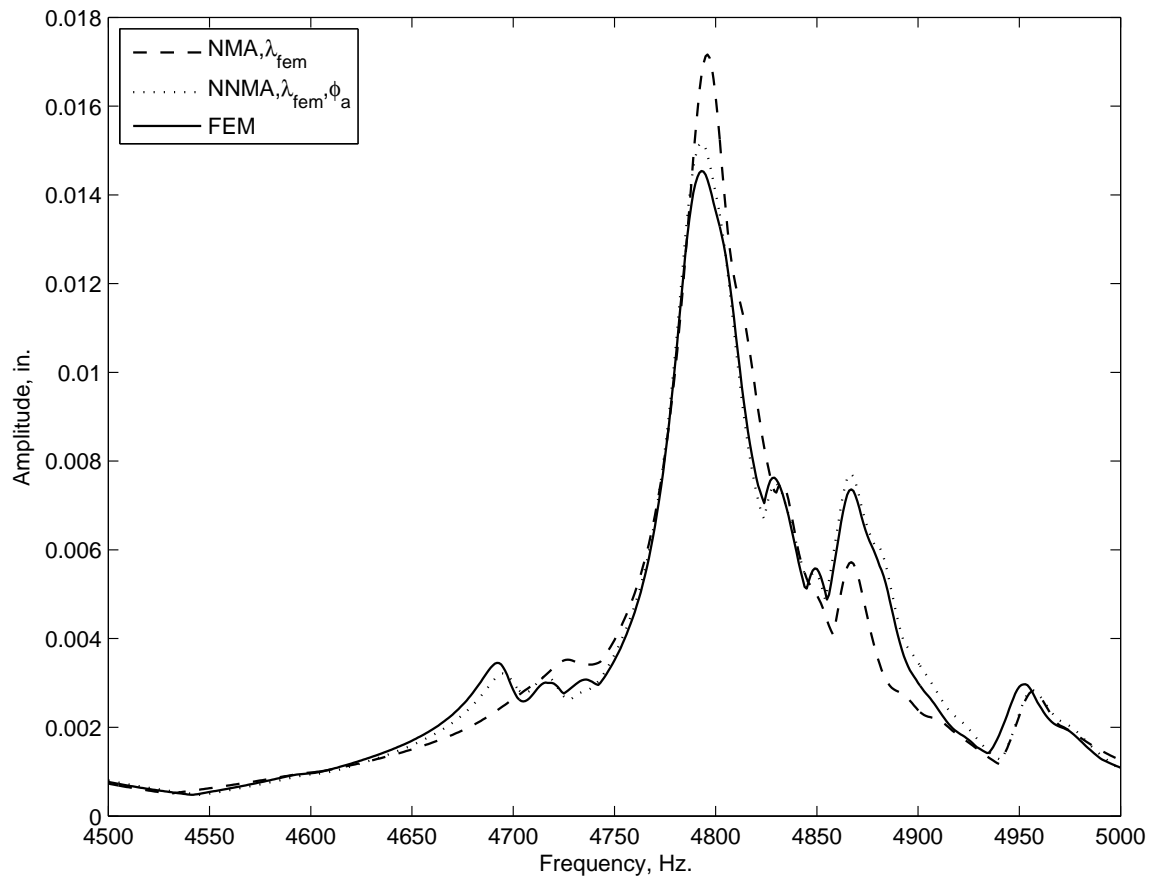


Figure 4.43: NNMA- $\lambda_{FEM}-\phi_a$  versus NMA- $\lambda_{FEM}$  Maximum Forced Response Results- Mode 13

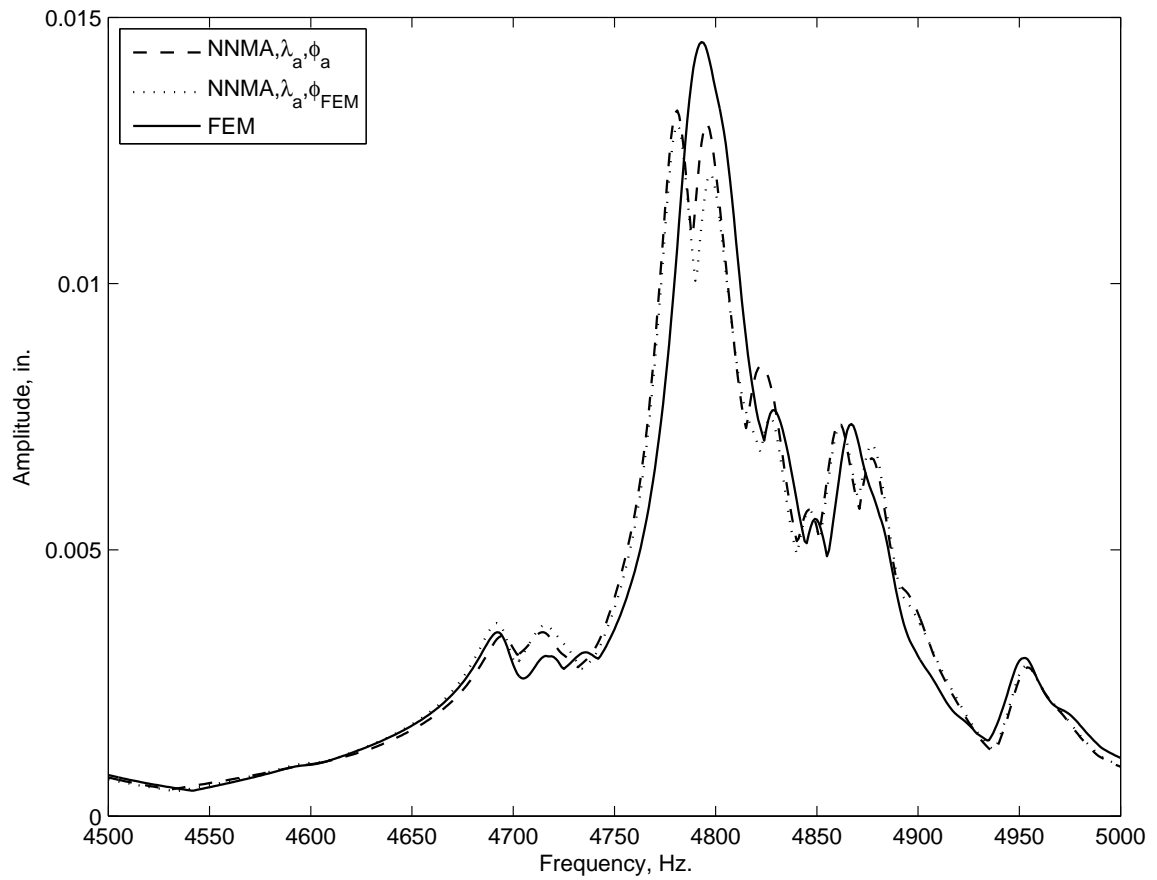


Figure 4.44: NNMA- $\lambda_a$ - $\phi_a$ , versus NNMA- $\lambda_a$ - $\phi_{FEM}$  Maximum Forced Response Results- Mode 13

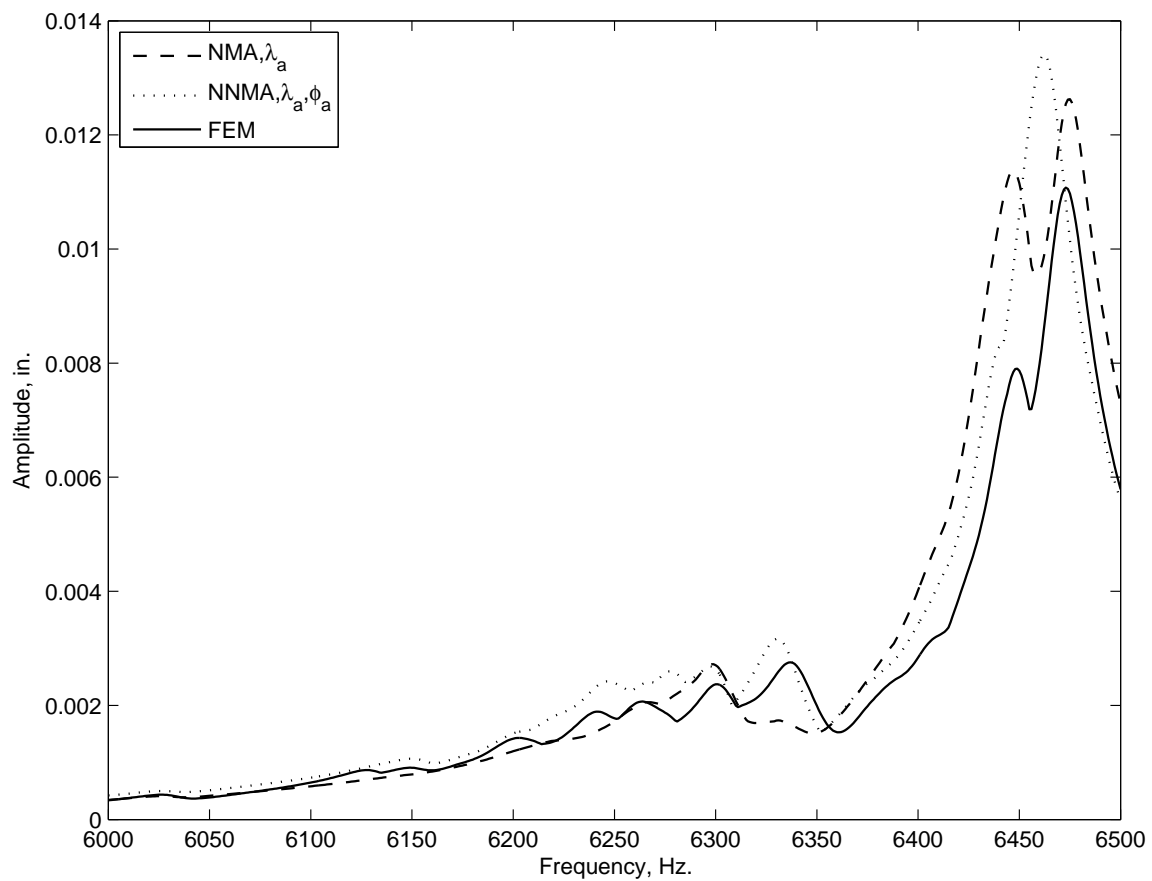


Figure 4.45: NNMA- $\lambda_a$ - $\phi_a$  versus NMA- $\lambda_a$  Maximum Forced Response Results- Mode 18

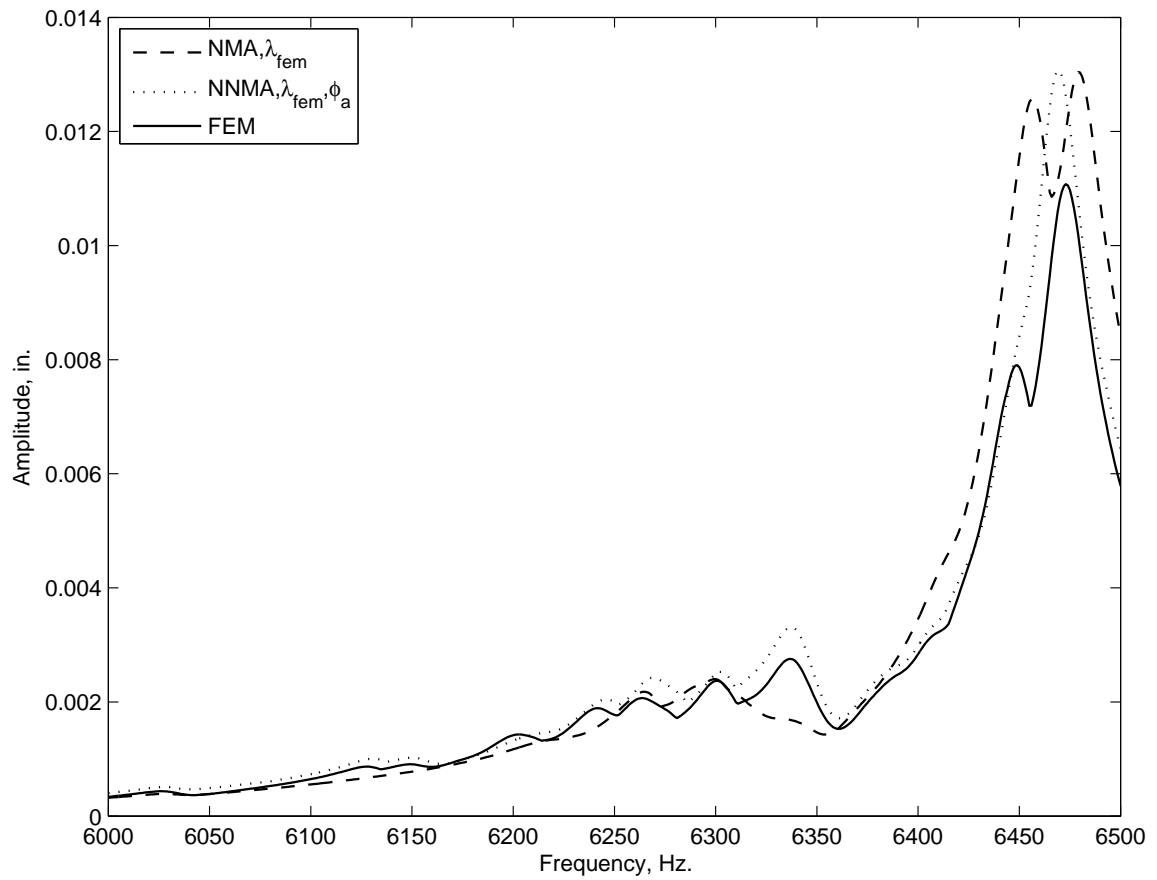


Figure 4.46: NNMA- $\lambda_{FEM}-\phi_a$  versus NMA- $\lambda_{FEM}$  Maximum Forced Response Results- Mode 18



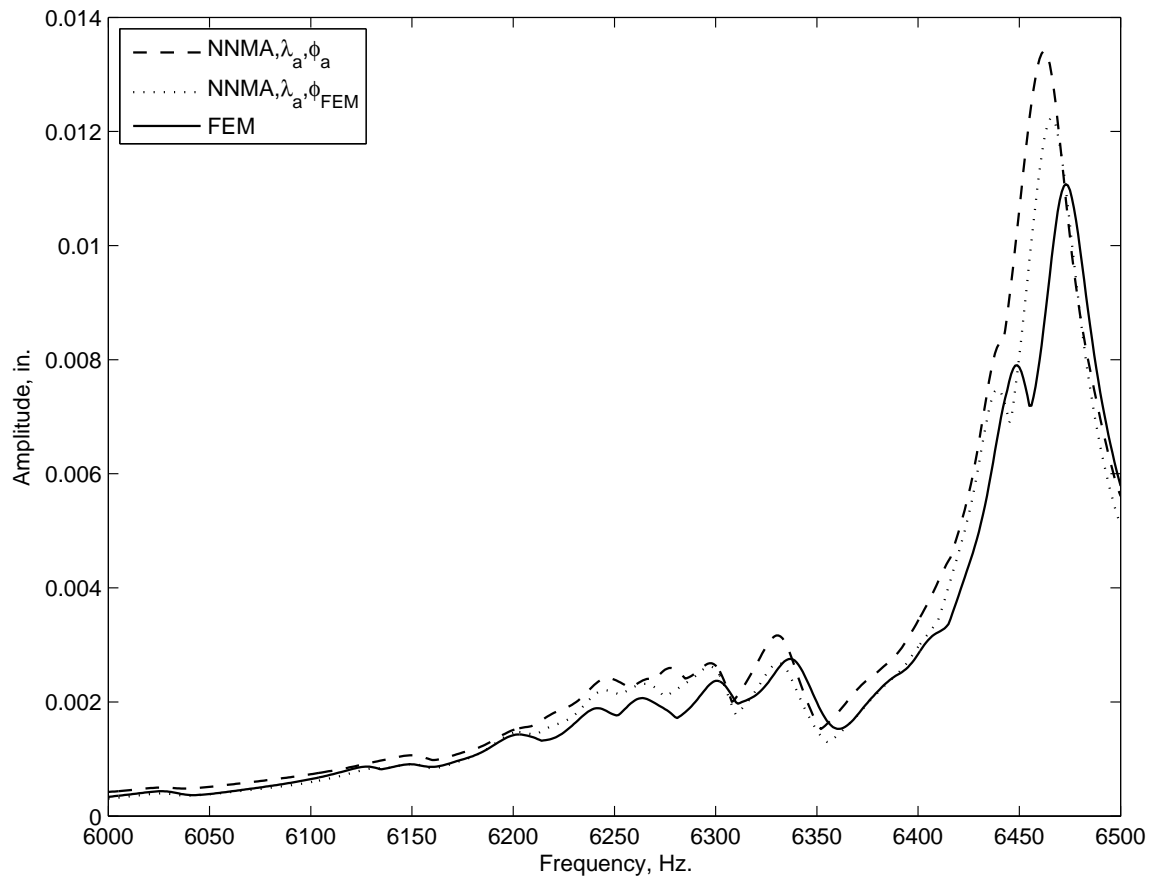


Figure 4.47: NNMA- $\lambda_a$ - $\phi_a$ , versus NNMA- $\lambda_a$ - $\phi_{FEM}$  Maximum Forced Response Results- Mode 18

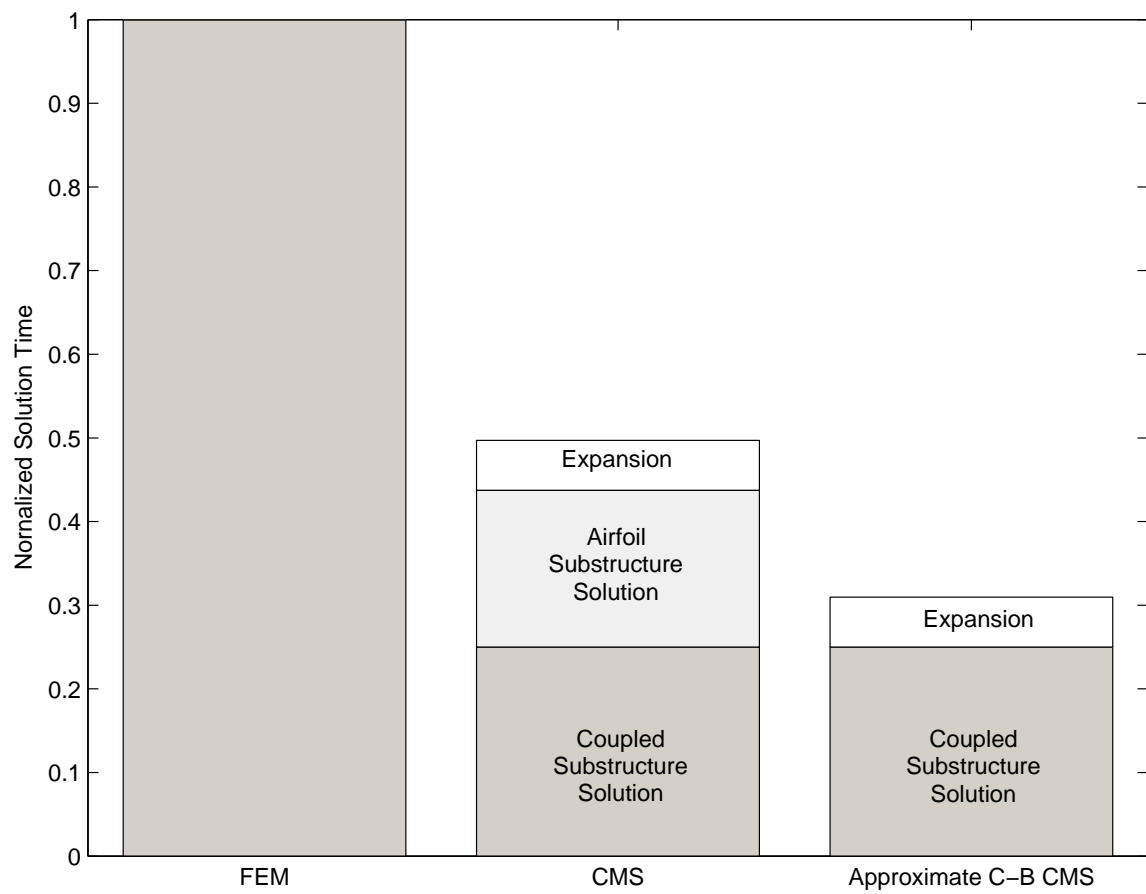


Figure 4.48: Solution Time Comparison

## 5 Conclusion

Design of structural components is constrained by both iteration time and prediction uncertainty. Iteration time refers to the computation time each simulation requires and controls how much of the design space can be explored given a fixed period. A comprehensive search of the space leads to more optimum designs. Prediction uncertainty refers to both irreducible uncertainties, such as caused by material scatter, and reducible uncertainty, such as simulation error of the physics-based model. In the presence of uncertainty, conservative safety factors and design margins are used to ensure reliability, but these negatively impact component weight and design life. This research investigated three areas to improve both iteration time and model uncertainty quantification for turbomachinery design.

The first developed an error-quantified reduced-order model that predicts the effect of geometric deviations on airfoil forced response. The model is composed of a Taylor series expansion using first-order semi-analytical sensitivities and a linear regression of a discrepancy measure onto airfoil geometric parameters. The discrepancy measure consisted of a comparison between the Taylor series approximation and the full finite element model result of a small set of training models. This error-quantified approximation shows significant improvements in accuracy compared to existing methods, because of its bias correction and description of random error. The results of this model were used later in the dissertation as input into the non-nominal mode mistuning model. Several areas of future research are possible,

1. Demonstration of model error quantification through linear regression of discrepancy to design parameters for a wider range of problems,
2. Development of an model error quantification approach for vector quantities,
3. Improved modal and forced response approximation through higher order sensitivities,
4. Improved modal and forced response approximation through gradient Kriging,
5. Application model error quantification approach on discrepancy between model and empirical results.

The second research area developed a Probabilistic Gradient Kriging approach to efficiently model the failure probability prediction uncertainty caused by small sample statistics. It was shown that the Probabilistic Gradient Kriging approach is significantly more accurate for a given number of training points when compared to conventional Kriging and polynomial regression approaches. It was found that statistical uncertainty from small sample sizes leads to orders of magnitude variation in predicted failure probabilities. Several areas of future research are possible,

1. Use of higher order sensitivities in the PGK approximation,
2. Demonstration of PGK as a surrogate surface for reliability optimization,
3. Develop approach to use initial set of training site function values and gradients to select new sites in likely regions of interest,
4. Apply gradient Kriging to other engineering problems, e. g. airframe structures and aerodynamics,

5. Develop a new surface approximation approach that uses gradients and function values, but does not require the assumptions of a Gaussian stochastic process,

The third research area developed non-nominal and nominal mode Component Mode Synthesis methods for reduced-order modeling of the geometric effects on rotor mistuning. Existing reduced-order methods approximate mistuning with a nominal-mode, or design intent, basis and airfoil modal stiffness perturbation. This assumption introduces a quantifiable error. It is shown that the nominal-mode approach can produce significant errors whereas the non-nominal approach accurately predicts blade-to-blade mistuned response. Several areas of future research are possible,

1. Use of GPM CMM to determine manufacturing tolerances, both large and small, that reduce mistuned response,
2. Compare the predicted distribution of mistuned response from nominal mode and non-nominal mode methods to determine if qualitative ability of nominal method is sufficient for probabilistic analysis,
3. Incorporate disk-induced constraint modes as an approach to reduce the quantity of interface DOF,
4. Compare GPM CMM approach to the MMDA method,
5. Experimental study of geometric mistuning.

# Bibliography

- [1] T. M. Bartsch, “High cycle fatigue science and technology program,” Tech. Rep. AFRL-PR-WP-TR-2002-2060, Air Force Research Laboratory, AFRL/RZTS, May 2002.
- [2] D. S. Whitehead, “Effect of mistuning on the vibration of turbomachinery blades induced by wakes,” *Journal of Mechanical Engineering Science*, vol. 8, no. 1, pp. 15–21, 1966.
- [3] D. J. Ewins, “The effects of detuning upon the forced vibrations of bladed disks,” *Journal of Sound and Vibration*, vol. 9, no. 1, pp. 65–79, 1969.
- [4] K. W. Jones, “Mistuning for minimum maximum bladed disk forced response,” in *40th AIAA/ASME/SAE/ASEE Joint Propulsion Conference and Exhibit, AIAA-2004-3755*, (Fort Lauderdale, FL), 11-14 July 2004.
- [5] R. C. F. Dye and T. A. Henry, “Vibration amplitudes of compressor blades resulting from scatter in natural frequencies,” *Journal of Engineering for Power*, vol. 91, pp. 182–188, 1969.
- [6] L. E. El-Bayoumy and A. V. Srinivasan, “Influence of mistuning on rotor-blade vibrations,” *AIAA Journal*, vol. 13, no. 4, pp. 460–464, 1975.

- [7] G. Sogliero and A. V. Srinivasan, "Fatigue life estimates of mistuned blades via a stochastic approach," *AIAA Journal*, vol. 17, no. 3, pp. 318–323, 1980.
- [8] S. Y. Lee, M. P. Castanier, and C. Pierre, "Assessment of probabilistic methods for mistuned bladed disk vibration," in *Proceedings of the 46th AIAA/ASME/ASCE/AHS/ASC Structures, Structural dynamics, and Materials Conference, AIAA-2005-1990*, (Austin, TX), 18-21 April 2005.
- [9] K. R. V. Kaza and R. E. Kielb, "Effects of mistuning on bending-torsion flutter and response of a cascade in incompressible flow," *AIAA Journal*, vol. 20, no. 8, pp. 1120–1127, 1982.
- [10] J. H. Griffin and T. M. Hoosac, "Model development and statistical investigation of turbine blade mistuning," *Journal of Vibration, Acoustics, Stress, and Reliability*, vol. 106, pp. 204–210, 1984.
- [11] D. Afolabi, "The frequency response of mistuned bladed disk assemblies," in *Vibration of Blades and Bladed Disk Assemblies* (R. E. Kielb and N. F. Rieger, eds.), pp. 15–21, New York, NY: ASME, 1985.
- [12] J. H. Griffin, "On predicting the resonant response of bladed disk assemblies," *Journal of Engineering for Gas Turbines and Power*, vol. 110, no. 1, pp. 45–50, 1988.
- [13] S. T. Wei and C. Pierre, "Localization phenomena in mistuned assemblies with cyclic symmetry part 1: Free vibrations," *Journal of Vibration, Acoustics, Stress, and Reliability*, vol. 110, no. 4, pp. 429–438, 1988.
- [14] R. R. Craig and M. C. C. Bampton, "Coupling of substructures for dynamic analyses," *AIAA Journal*, vol. 6, no. 7, pp. 1313–1319, 1968.

- [15] H. Irretier, “Spectral analysis of mistuned bladed disk assemblies by component mode synthesis,” in *Vibrations of Bladed Disk Assemblies*, pp. 115–125, New York, NY: ASME, 1983.
- [16] M. P. Castanier, G. Ottarsson, and C. Pierre, “A reduced-order modeling technique for mistuned bladed disks,” *Journal of Vibration and Acoustics*, vol. 119, no. 3, pp. 439–447, 1997.
- [17] R. Bladh, C. Pierre, M. P. Castanier, and M. J. Kruse, “Dynamic response predictions for a mistuned industrial turbomachinery rotor using reduced-order modeling,” *Journal of Engineering for Gas Turbines and Power*, vol. 124, no. 2, pp. 311–324, 2002.
- [18] R. Bladh, M. P. Castanier, and C. Pierre, “Reduced order modeling and vibration analysis of mistuned bladed disk assemblies with shrouds,” *Journal of Engineering for Gas Turbines and Power*, vol. 121, no. 3, pp. 515–522, 1999.
- [19] R. Bladh, M. Castanier, and C. Pierre, “Component mode based reduced order modeling techniques for mistuned bladed disks part 1: Theoretical model,” *Journal of Vibration and Acoustics*, vol. 123, no. 1, pp. 89–99, 2001.
- [20] R. Bladh, M. P. Castanier, and C. Pierre, “Component mode based reduced order modeling techniques for mistuned bladed disks part 2: Application,” *Journal of Engineering for Gas Turbines and Power*, vol. 123, no. 1, pp. 100–108, 2001.
- [21] S.-H. Lim, R. Bladh, M. P. Castanier, and C. Pierre, “A compact, generalized component mode mistuning representation for modeling bladed disk vibration,” in *Proceedings of the 44th AIAA/ASME/ASCE/AHS/ASC Structures, Structural dynamics, and Materials Conference, AIAA-2003-1545*, (Norfolk, VA), 7-10 April 2003.



- [22] S.-H. Lim, M. P. Castanier, and C. Pierre, "Vibration modeling of bladed disks subject to geometric mistuning and design changes," in *Proceedings of the 45th AIAA/ASME/ASCE/AHS/ASC Structures, Structural dynamics, and Materials Conference, AIAA-2004-1686*, (Palm Springs, CA), 19-22 April 2004.
- [23] E. P. Petrov, K. Y. Sanliturk, and D. J. Ewins, "A new method for dynamic analysis of mistuned bladed disks based on the exact relationship between tuned and mistuned systems," *Journal of Engineering for Gas Turbines and Power*, vol. 124, no. 3, pp. 586–597, 2002.
- [24] E. P. Petrov and D. J. Ewins, "Analysis of the worst mistuning patterns in bladed disk assemblies," *Journal of Turbomachinery*, vol. 125, no. 4, pp. 623–631, 2003.
- [25] M. T. Yang and J. H. Griffin, "A reduced-order approach for the vibration of mistuned bladed disk assemblies," *Journal of Engineering for Gas Turbines and Power*, vol. 119, no. 1, pp. 161–167, 1997.
- [26] C. H. Menq, J. H. Griffin, and J. Bielak, "Effects of mistuning on the forced vibration of blades with mechanical coupling," *Journal of Vibration, Acoustics, Stress, and Reliability in Design*, vol. 108, no. 2, pp. 50–55, 1986.
- [27] M.-T. Yang and J. H. Griffin, "A reduced-order model of mistuning using a subset of nominal system modes," *Journal of Engineering for Gas Turbines and Power*, vol. 123, no. 4, pp. 893–900, 2001.
- [28] M. T. Yang and J. H. Griffin, "A normalized modal eigenvalue approach for resolving modal interactions," *Journal of Engineering for Gas Turbines and Power*, vol. 119, no. 3, pp. 647–650, 1997.
- [29] D. M. Feiner and J. H. Griffin, "A fundamental model of mistuning for a single

- family of modes,” *Journal of Engineering for Gas Turbines and Power*, vol. 124, no. 4, pp. 597–605, 2002.
- [30] D. M. Feiner and J. H. Griffin, “Mistuning identification of bladed disks using a fundamental mistuning model - part 1: Theory,” *Journal of Turbomachinery*, vol. 126, no. 1, pp. 150–158, 2004.
- [31] D. M. Feiner and J. H. Griffin, “Mistuning identification of bladed disks using a fundamental mistuning model - part 2: Application,” *Journal of Turbomachinery*, vol. 126, no. 1, pp. 159–165, 2004.
- [32] A. Sinha, “Reduced-order model of a bladed rotor with geometric mistuning,” in *Proceedings of the ASME Turbo Expo 2007: Power for Land, Sea and Air, GT2007-27276*, (Montreal, Canada), 14-17 May 2007.
- [33] V. E. Garzon and D. L. Darmofal, “Impact of geometric variability on axial compressor performance,” *Journal of Turbomachinery*, vol. 125, no. 4, pp. 692–703, 2003.
- [34] A. Sinha, “Calculating the statistics of forced response of a mistuned bladed disk assembly,” *AIAA Journal*, vol. 24, no. 11, pp. 1797–1801, 1986.
- [35] S. T. Wei and C. Pierre, “Statistical analysis of the forced response of mistuned cyclic assemblies,” *AIAA Journal*, vol. 28, no. 5, pp. 861–868, 1990.
- [36] M. P. Mignolet, C. C. Lin, and B. H. LaBorde, “A novel limit distribution for the analysis of randomly mistuned bladed disks,” *Journal of Turbomachinery*, vol. 123, no. 2, pp. 388–394, 2001.
- [37] C. C. Lin and M. P. Mignolet, “An adaptive perturbation scheme for the analysis

- of mistuned bladed disks,” *Journal of Engineering for Gas Turbines and Power*, vol. 120, no. 1, pp. 153–160, 1997.
- [38] M. T. Bah, P. B. Nair, A. Bhaskar, and A. J. Keane, “Forced response statistics of mistuned bladed disks: A stochastic reduced basis approach,” *Journal of Sound and Vibration*, vol. 263, no. 2, pp. 377–397, 2003.
- [39] A. Sinha, “Computation of the statistics of forced response of a mistuned bladed disk assembly via polynomial chaos,” *Journal of Vibration and Acoustics*, vol. 128, no. 4, pp. 449–457, 2006.
- [40] E. Capiez-Lernout and C. Soize, “Nonparametric modeling of random uncertainties for dynamic response of mistuned bladed disks,” *Journal of Tubomachinery*, vol. 126, no. 4, pp. 610–618, 2004.
- [41] E. Capiez-Lernout, C. Soize, J. P. Lombard, C. Dupont, and E. Seinturier, “Blade manufacturing tolerances definition for a mistuned industrial bladed disk,” *Journal of Engineering for Gas Turbines and Power*, vol. 127, no. 3, pp. 621–628, 2005.
- [42] G. Scarselli and L. Lecce, “Non-deterministic approaches for the evaluation of the mistune effects on the rotor dynamics,” in *Proceedings of the 45th AIAA/ASME/ASCE/AHS/ASC Structures, Structural dynamics, and Materials Conference, AIAA-2004-1748*, (Palm Springs, CA), 19-22 April 2004.
- [43] B. K. Choi, J. Lentz, A. J. Rivas-Guerra, and M. P. Mignolet, “Optimization of intentional mistuning patterns for the reduction of the forced response effects of unintentional mistuning: Formulation and assessment,” *Journal of Engineering for Gas Turbines and Power*, vol. 125, no. 1, pp. 442–454, 2003.

- [44] J. Li, M. P. Castanier, C. Pierre, and S. L. Ceccio, “Experimental monte carlo mistuning assessment of bladed disk vibration using forcing variation,” in *Proceedings of the 47th AIAA/ASME/ASCE/AHS/ASC Structures, Structural dynamics, and Materials Conference*, May 2006.
- [45] A. Gelman, J. B. Carlin, H. S. Stern, and D. B. Rubin, *Bayesian Data Analysis*. New York, NY: Chapman I& Hall, 1995.
- [46] F. C. Hadipriono, “Fuzzy sets in probabilistic structural mechanics,” in *Probabilistic Structural Mechanics Handbook* (C. J. Sundararajan, ed.), pp. 280–316, New York, NY: Chapman I& Hall, 1995.
- [47] G. Shafer, *A Mathematical Theory of Evidence*. Princeton, NJ: Princeton University Press, 1976.
- [48] Y. Ben-Haim, *Information Gap*. London, UK: Academic Press, 2001.
- [49] B. H. Thacker, M. C. Anderson, P. E. Senseny, and E. A. Rodriguez, “The role of nondeterminism in model verification and validation,” *International Journal of Materials and Product Technology*, vol. 25, no. 1, pp. 144–163, 2006.
- [50] M. C. Kennedy and A. O’Hagan, “Bayesian calibration of computer models,” *Journal of the Royal Statistical Society, Series B, Methodological*, vol. 63, pp. 425–464, 2001.
- [51] H. O. Madsen, S. Krenk, and N. C. Lind, *Methods of Structural Safety*. Englewood Cliffs, NJ: Prentice-Hall, 1986.
- [52] Y. T. Wu, O. H. Burnside, and T. A. Cruse, “Probabilistic methods for structural response analysis,” in *Computational Mechanics of Probabilistic and Reliability*

*Analysis* (W. K. Lie and T. Belytschko, eds.), p. Chapter 7, Lausanne, Switzerland: Elmepress International, 1989.

- [53] S. Choi, R. V. Grandhi, and C. R. A., *Reliability-based Structural Design*. London: Springer, 2006.
- [54] W. J. Sacks, T. J. Michell, and H. P. Wynn, “Design and analysis of computer experiments,” *Statistical Science*, vol. 4, no. 4, pp. 409–453, 1989.
- [55] O. Ditlevsen, “Model uncertainty in structural reliability,” *Structural Safety*, vol. 1, no. 1, pp. 183–190, 2003.
- [56] P. Thoftt-Christensen and Y. Murotsu, *Application of Structural System Reliability Theory*. Berlin, GE: Springer Verlag, 1986.
- [57] K. F. Alvin, “Method for treating discretization error in nondeterministic analysis,” *AIAA Journal*, vol. 38, no. 5, pp. 910–916, 2000.
- [58] L. F. Richardson, “The approximate differences of physical problems involving differential equations with an application to the stresses in a masonry dam,” *Transactions of the Royal Society of London, Series A*, vol. 210, pp. 307–357, 1910.
- [59] P. J. Roache, *Verification and Validation in Computational Science and Engineering*. Albuquerque, NM: Hermosa, 1998.
- [60] D. C. Kammer, K. F. Alvin, and D. S. Malkus, “Combining metamodels with rational function representations of discretization error for uncertainty quantification,” *Computational Methods in Applied Mechanics and Engineering*, vol. 191, pp. 1367–1379, 2002.

- [61] J. C. Helton, “Uncertainty and sensitivity analysis in the presence of stochastic and subjective uncertainty,” *Journal of Statistical Computation and Simulation*, vol. 57, pp. 3–76, 1997.
- [62] H. R. Bae, R. V. Grandhi, and R. A. Canfield, “Epistemic uncertainty quantification techniques including evidence theory for large scale structures,” *Computers I& Structures*, vol. 82, pp. 1101–1112, 2004.
- [63] R. W. Logan, C. K. Nitta, and S. K. Chidester, “Uncertainty quantification during integral validation: Estimating parametric, model form, and solution contributions,” in *Proceedings of the 47th AIAA/ASME/ASCE/AHS/ASC Structures, Structural Dynamics, and Materials Conference, AIAA-2006-1923*, (Newport, RI), 1-4 May 2006.
- [64] G. C. Fraccone, M. Ruzzene, V. Volovoi, P. Cento, and C. Vining, “Assessment of uncertainty in response estimation for turbine engine bladed disks,” *Journal of Sound and Vibration*, vol. 317, pp. 625–645, 2008.
- [65] T. K. Hasselman, K. C. Yap, G. W. Wathugala, and M. C. Anderson, “A top-down method for uncertainty quantification and predictive accuracy assessment,” in *Proceedings of the 46th AIAA/ASME/ASCE/AHS/ASC Structures, Structural Dynamics, and Materials Conference, AIAA-2005-1903*, (Austin, TX), 18-21 April 2005.
- [66] P. Vinai, R. Macian-Juan, and R. Chawla, “A statistical methodology for quantification of uncertainty in best estimate code physical models,” *Annals of Nuclear Energy*, vol. 34, pp. 628–640, 2007.
- [67] J. R. Red-Horse and A. S. Benjamin, “A probabilistic approach to uncertainty quantification with limited information,” *Reliability Engineering I& System Safety*, vol. 85, pp. 183–190, 2003.

- [68] S. Vittal and P. Hajela, “Conf dence intervals for reliability estimated using response surface methods,” in *Proceedings of the 9th AIAA/ISSMO Symposium on Multidisciplinary Analysis and Optimization*, AIAA-2002-5475, (Atlanta, GA), 4-6 Sep, 2002.
- [69] W. R. Gilks, S. Richardson, and D. J. Spiegelhalter, *Markov Chain Monte Carlo in Practice*. New York, NY: Chapman I& Hall, 1996.
- [70] A. Der Kiureghian and P. L. Liu, “Structural reliability under incomplete probability information,” *Journal of Engineering Mechanics*, vol. 112, no. 1, pp. 85–104, 1986.
- [71] P. H. Wirshing, “Error (or conf dence) bounds for distribution functions resulting from statistical sampling error,” in *In Probabilistic Structural Analysis Methods (PSAM), 2nd annual report Appendix D, Southwest Research Institute, NASA Contract NAS3-24389*, (San Antonio, TX), Nov 1986.
- [72] Y. T. Torng and B. H. Thacker, “Conf dence bounds assessment for probabilistic structural reliability analysis,” in *Proceedings of the 33rd AIAA/ASME/ASCE/AHS/ASC Structures, Structural Dynamics, and Materials Conference*, AIAA-92-2409, (Dallas, TX), 13-15 Apr 1992.
- [73] Y. T. Torng and B. H. Thacker, “An efficient probabilistic scheme for constructing structural reliability conf dence bounds,” in *Proceedings of the 34th AIAA/ASME/ASCE/AHS/ASC Structures, Structural Dynamics, and Materials Conference*, AIAA-93-1627, (La Jolla, CA), 19-22 Apr 1993.
- [74] S. R. Mehta, T. A. Cruse, and S. Mahadevan, “Conf dence bounds assessment for probabilistic structural reliability analysis,” in *Proceedings of the 34th AIAA/ASME/ASCE/AHS/ASC Structures, Structural Dynamics, and Materials Conference*, AIAA-93-1377, (La Jolla, CA), 19-22 Apr 1993.

- [75] S. Venkataraman, R. R. Sirimamilla, S. Mahadevan, V. Nagpal, B. Strack, and S. S. Pai, “Calculating confidence bounds for reliability index to quantify effect of distribution parameter uncertainty,” in *Proceedings of the 48th AIAA/ASME/ASCE/AHS/ASC Structures, Structural Dynamics, and Materials Conference, AIAA-2007-1940*, (Honolulu, Hawaii), 23-26 April, 2007.
- [76] A. K. Karamchandani, P. Bjerager, and C. A. Cornell, “Methods to estimate parametric sensitivity in structural reliability analysis,” in *Probabilistic Methods in Civil Engineering, Proceedings of the 5th ASCE Specialty Conference*, (Blacksburg, VA), pp. 86–89, 25-27 May, 1988.
- [77] R. E. Melchers and M. Ahammed, “A fast approximate method for parameter sensitivity estimation in monte carlo structural reliability,” *Computers and Structures*, vol. 82, pp. 55–61, 2004.
- [78] V. Picheny, N. H. Kim, R. T. Haftka, and J. Peters, “Conservative estimation of probability of failure,” in *Proceedings of the 11th AIAA/ISSMO Multidisciplinary Analysis and Optimization Conference, AIAA-2006-7038*, (Portsmouth, Virginia), 6-8 Sep, 2006.
- [79] T. A. Cruse and J. M. Brown, “Confidence interval simulation for systems of random variables,” *Journal of Engineering for Gas Turbines and Power*, vol. 129, no. 3, pp. 836–842, 2007.
- [80] B. J. Bichon, J. M. McFarland, and S. Mahadevan, “Using bayesian inference and efficient global reliability analysis to explore distribution uncertainty,” in *Proceedings of the 49th AIAA/ASME/ASCE/AHS/ASC Structures, Structural Dynamics, and Materials Conference, AIAA-2008-1712*, (Schaumburg, Il), 7-10 April 2008.



- [81] B. J. Bichon, M. S. Eldred, L. P. Swiler, S. Mahadevan, and J. M. McFarland, "Multimodal reliability assessment for complex engineering applications using efficient global optimization," in *Proceedings of the 48th AIAA/ASME/ASCE/AHS/ASC Structures, Structural Dynamics, and Materials Conference, AIAA-2007-1946*, (Waikiki, HI), 23-26 April 2007.
- [82] I. T. Jolliffe, *Principal Component Analysis*. New York, NY: Springer Verlag, 1986.
- [83] R. L. Fox and M. P. Kapoor, "Rates of change of eigenvalues and eigenvectors," *AIAA Journal*, vol. 6, no. 12, pp. 2426–2429, 1968.
- [84] M. I. Friswell, "The derivatives of repeated eigenvalues and their associated eigenvectors," *Journal of Vibration and Acoustics*, vol. 118, no. 3, pp. 390–397, 1996.
- [85] P. J. Roache, K. Ghia, and F. White, "Editorial policy statement on the control of numerical accuracy," *Journal of Fluids Engineering*, vol. 108, no. 1, p. 2, 1986.
- [86] A. M. WAAS, "Editorial policy statement on numerical accuracy and experimental uncertainty," *AIAA Journal*, vol. 37, no. 1, p. 9, 1999.
- [87] R. T. Haftka and Z. Gurdal, *Elements of Structural Optimization*. Norwell, MA: Kluwer Academic, 3rd ed., 1992.
- [88] S. E. Gorrell and M. W. Davis, "Application of a dynamic compression system model to a low aspect ratio fan: Casing treatment and distortion," in *Proceedings of the 29th AIAA/ASME/ASCE/AHS/ASC Structures, Structural dynamics, and Materials Conference, AIAA-93-1871*, (Monterey, CA), 28-30 June 1993.
- [89] C. Breard, M. Vahdati, A. I. Sayma, and M. Imregun, "An integrated time-domain aeroelasticity model for the prediction of fan forced response due to inlet distortion,"

*Journal of Engineering for Gas Turbines and Power*, vol. 124, no. 1, pp. 196–208, 2002.

- [90] S. R. Manwaring, D. C. Rabe, C. B. Lorence, and A. R. Wadia, “Inlet distortion generated forced response of a low aspect ratio transonic fan,” *Journal of Turbomachinery*, vol. 119, no. 4, pp. 665–676, 1997.
- [91] D. G. Krige, “A statistical approach to some mine valuations and allied problems at the witwatersrand,” Master’s thesis, University of Witwatersrand, Johannesburg, South Africa, 1951.
- [92] T. J. Santner, B. J. Williams, and W. I. Notz, *Design and Analysis of Computer Experiments*. New York: Springer, 2003.
- [93] H. Chung and J. J. Alonso, “Using gradients to construct cokriging approximation models for high-dimensional design optimization problems,” in *Proceedings of the 40th AIAA Aerospace Sciences Meeting and Exhibit, AIAA-2002-0317*, (Reno, NV), 14-17 Jan 2002.
- [94] W. Liu and S. M. Batill, “Gradient-enhanced response surface approximations using kriging models,” in *Proceedings of the 9th AIAA/ISSMO Symposium on Multidisciplinary Analysis and Optimization, AIAA-2002-5475*, (Atlanta, GA), 4-6 Sep 2002.
- [95] A. Karamchandani and C. A. Cornell, “Sensitivity estimation within first and second order reliability methods,” *Structural Safety*, vol. 11, pp. 95–107, 1992.
- [96] J. M. Brown, J. C. Slater, and R. V. Grandhi, “Probabilistic analysis of geometric uncertainty on modal response,” in *Proceedings of the ASME Turbo Expo 2003: Power for Land, Sea and Air, GT2003-38557*, (Atlanta, GA), 13-16 June 2003.

- [97] J. M. Brown and R. V. Grandhi, “Probabilistic analysis of geometric uncertainty on blade alone force response,” in *Proceedings of the ASME Turbo Expo 2004: Power for Land, Sea and Air*, GT2004-53959,, (Reno, Vienna, Austria), 14-17 June 2004.
- [98] J. M. Brown and R. V. Grandhi, “Probabilistic high cycle fatigue assessment process for integrally bladed rotors,” in *Proceedings of the ASME Turbo Expo 2007: Power for Land, Sea and Air*, GT2005-69022, (Reno, NV), 6-9 June 2005.
- [99] J. M. Brown and R. V. Grandhi, “Reduced-order model development for airfoil forced response, article id 387828,” *International Journal of Rotating Machinery*, vol. 11, 2008.
- [100] D. C. Rabe, A. Boles, and P. Russler, “Influence of inlet distortion on transonic compressor blade loading,” in *Proceedings of the 31st AIAA/ASME/SAE/ASEE Joint Propulsion Conference*, AIAA-95-2461, (San Diego, CA), 10-12 July 1995.
- [101] K. W. Jones and C. J. Cross, “Traveling wave excitation system for bladed disks,” *Journal of Propulsion and Power*, vol. 19, no. 1, pp. 134–141, 2003.